Measured and Simulated Electron Thermal Transport in the Madison Symmetric Torus Reversed Field Pinch

by

Joshua Adam Reusch

A dissertation submitted in partial fulfillment of the

requirements for the degree of

Doctor of Philosophy

(Physics)

at the

University of Wisconsin – Madison

2011

Abstract

New high time resolution measurements of the evolution of the electron temperature profile through a sawtooth event in high current reversed-field pinch (RFP) discharges in the Madison Symmetric Torus (MST) have been made using the enhanced capabilities of the multipoint, multi-pulse Thomson scattering system. This system is now capable of providing data at 21 spatial locations and 30 time points per discharge making it one of, if not the, most advanced diagnostic of its type in the world. The dramatic improvements in the quality and quantity of the electron temperature data provided by this diagnostic have enabled the determination of the magnetic equilibrium and the thermal transport at previously unrealizable levels of confidence and time resolution. The electron thermal diffusion χ_e in particular is found to vary by more than two orders of magnitude in core region of the plasma over the course of the sawtooth cycle.

This wealth of experimental data is then compared directly to simulations run at experimentally relevant parameters. This includes zero β, single fluid, nonlinear, resistive magnetohydrodynamic (MHD) simulations run with the aspect ratio, resistivity profile, and Lundquist number ($S \sim 4 \times 10^6$) of high current RFP discharges in MST. These simulations display MHD activity and sawtooth like behavior similar to that observed in the MST. This includes both the sawtooth period and the duration

of the sawtooth crash, which is distinctly different from simulations of the sawteeth in tokamaks which require two fluid effects in order to get this time scale correct. The radial shape of the magnetic mode amplitudes, scaled to match edge measurements made in MST, are then used to compute the expected level of thermal diffusion due to parallel losses along diffusing magnetic field lines, $\chi_{MD} = v_{\|} D_{mag}$. The evolution of the D_{mag} profile was determined for over 20 sawteeth so that the ensemble averaged evolution could be compared to the sawtooth ensembled data from MST. The resulting comparison to the measured χ_e shows that χ_{MD} is larger than χ_e at most times even though χ_{MD} should represent the minimum possible thermal diffusion in MST. However, if electrons are trapped in a magnetic well they cannot carry energy along the diffusing magnetic field lines and thus χ_{MD} should be reduced by the circulating particle fraction in order to be compare with the experimental measurements. This reduction brings χ_{MD} to within uncertainty of χ_e in the mid radius at most times throughout the sawtooth cycle. In the core, the measured χ_e is greater than χ_{MD} leading up to and including the sawtooth crash, suggesting other transport mechanisms such as temperature flattening due to magnetic islands, may be important or even dominant transport mechanisms at this time. Additionally, in a separate simulation in which the pressure field was evolved self consistently assuming Ohmic heating and anisotropic thermal conduction, a direct comparison of the measured temperature to the simulated temperature is made. Interestingly, while the equilibrium temperature profile evolution is only in moderate agreement with measurements, there is striking agreement between character and time evolution of the simulated temperature fluctuations to those recently measured in MST.

Acknowledgements

There are a great many people that have had a hand, directly or indirectly, in making this work possible and making my time here in Madison as enjoyable as it has been educational.

First and foremost, I have to thank the incredibly talented and dedicated faculty and staff at MST. In particular to Jay Anderson for teaching me the ways of MSTFit, John Sarff and Karsten McCollam for many a fruitful conversation about MST, and Dalton Schnack for helping me to understand the wonders of DEBS, though everyone at MST has contributed in many ways, both small and large, to my understanding of plasma physics and my general enjoyment of these eight years spent in Wisconsin. Thanks to the many past and present graduate students who have kept life interesting and kept the research wheels turning at MST, especially my office mates of so many years: Dan Clayton, Matt Miller, and Tim Tharp. It is truly not the same without you guys. I also owe a great debt of gratitude to the Thomson scattering folks, especially the original group of Dan Den Hartog, Rob O'Connell, Mike Borchardt, and Hillary Stephens who helped me to understand both the Thomson scattering diagnostic and plasma physics in general.

I would like to thank my mentors Daniel Den Hartog and Cary Forest. Dan has been a guide, mentor, and builder of many a fantastic diagnostic. The fast Thomson laser is a thing of beauty and the data it will produce will be a game changer. I cannot thank you enough for your help through the years. I will never forget the image of you striking a flash lamp arc with a Tesla coil. What a day! And to my adviser, Cary Forest, the builder of many a beautiful experimental device, for always turning my failures into new and interesting features and my confusion into science. Your enthusiasm is infectious. May you never run out of ideas!

While my research experience here has been fantastic, my academic experience has also been great. In particular E&M with Bob Joynt and quantum mechanics with C.C. Lin. And of course, the host of plasma physics professors, Chris Hegna, Carl Sovinec, Jim Callen, and (on a few memorable occasions) Stewart Prager, just to name a few.

I would like to thank a whole host of friends. Many thanks to Hillary, Nick, and Lola for many fun times and to Hillary in particular for put up with me for all those years while in the trenches working on Thomson scattering. To the Lancors: Brian, Rachael, and Ben. We will miss you, but Boston will treat you well. Drop a few R's for me. To Dave Burke for many a great conversation. Your enthusiasm and work ethic are admirable. So many ideas, so little time! Also, my old roommate Homer Wolfe. What can I say, Batavia is too far, it's time to move back to Madison. We have an extra room, pack the truck.

Many thanks to my wife who's love and support has sustained me throughout much of my graduate career. From arguments over Jackson homework to endless discussions of stochastic transport, not to mention optical microscopy and ultrasound, you have been invaluable in helping me wrap my head around physics. Thanks for putting up with me, I couldn't have done it without you. And to my beautiful daughter Lilith, thank you for helping me edit my thesis. I love you, now go to sleep.

Last but not least, I owe everything to my family. So many thanks to my parents, Jim and Donna Reusch, who's love and guidance has shaped me as a person and set me on this path. And to my sister, Jessica Reusch, who is in the midst of her own graduate school struggles. I am so glad you are here in Madison, you will make it, persevere.

Contents

List of Tables

List of Figures

Chapter 1

Introduction

Matter in the plasma state exists throughout the universe, from the vast and tenuous plasma of the interstellar medium to the dense hot plasmas that make up the stars, to the mundane plasmas in fluorescent light bulbs and plasma TV screens. They are invaluable as tools for everything from cutting huge pieces of steel to nano fabrication with many potential uses still in development. Arguably one of the greatest of these potential uses is the possibility of using high temperature plasmas for controlled thermonuclear fusion; a clean, nearly limitless source of energy. While the potential is great, the challenge is equally great and, as such, the physics of high temperature plasmas continue to be the focus of a great deal of experimental and theoretical research.

The primary motivation of this work is to improve the understanding of heat transport in a particular type of magnetically confined laboratory plasma, namely the toroidal reversed field pinch (RFP). A deeper understanding of the transport mechanisms active in this configuration may one day facilitate its use as a controlled thermonuclear fusion energy source. The RFP configuration is of particular interest for fusion power generation because the amount of thermal energy that can be contained with a given externally applied magnetic field (i.e. the plasma β) is relatively high and the effective plasma resistance is sufficient that it is possible for an RFP reactor to be Ohmically heated to ignition, mitigating the need for expensive and complicated auxiliary heating[1]. These two factors make an RFP reactor relatively simple and inexpensive to build and maintain.

While increasing our understanding of heat transport in RFP plasmas is important for furthering the goal of fusion energy, it is also important because the mechanisms that govern the heat transport in this type of plasma are also likely to be important in many other laboratory and astrophysical plasmas. Thus, this work is also motivated by the expectation that a deeper understanding of the transport in the RFP will improve the understanding of transport mechanisms in plasmas in general. In particular, this thesis explores and attempts to quantify the effect of magnetic fluctuation induced transport[2] in standard RFP discharges in the Madison Symmetric Torus (MST)[3].

The low safety factor in MST allows for a large number of overlapping magnetic tearing modes to be resonant inside the plasma. These overlapping modes cause the magnetic field lines to become tangled to the point that their trajectories are no longer deterministic, but become stochastic in nature. The charged particles that make up the plasma, and the heat that they carry, travel much more rapidly along field lines than they do across field lines. However, because these field lines wander stochastically, heat is transported rapidly across the minor radius and out of the plasma.

Predicting and understanding thermal transport in a stochastic magnetic field is the focus of a great deal of research in both laboratory and astrophysical plasmas[4, 5, 6, 7, 8, 9]. In any toroidal magnetic confinement device, overlapping magnetic perturbations can lead to tangled magnetic fields and stochastic transport. In astrophysics, the turbulent motion of the plasma, for example in galaxy clusters, can generate tangled magnetic fields on vast scales.

In their seminal work on the subject, Rechester and Rosenbluth suggest a method for quantifying the stochastic diffusion of the magnetic field lines in laboratory plasmas[5]. More recently, this method has been extended to astrophysical plasmas where an additional reduction in the thermal transport due to trapped particles was suggested[6, 10]. Interestingly, the Rechester-Rosenbluth model often predicts thermal transport that is significantly larger than measured in laboratory plasmas[7, 9]. One possible explanation for this is that trapped particles, which cannot carry heat along the diffusing field lines out of the system[6], are generally ignored in this type of analysis. The MST is ideally suited for investigating this effect as the trapped particle fraction is of order 50% across much of the minor radius[11], and the magnetic field is stochastic throughout most of the plasma volume[7]. Furthermore, quasi-periodic bursts of magnetohydrodynamic (MHD) activity known as sawteeth cause the degree of stochasticity to vary substantially in both time and space.

Measuring magnetic fluctuation induced transport has previously been done in MST. Past work used insertable probes that were capable of directly measuring the parallel heat flux in the plasma edge in MST[12]. This work was able to show that magnetic fluctuation induced transport can account for the majority of the heat transport in the edge regions of the plasma. Probes, however, cannot be used in the core regions of the plasma, nor even in the edge regions of high current plasmas, as the high temperatures tend to rapidly destroy the probes. For transport measurements in the inner regions of high current plasmas, non invasive diagnostics must be used.

The first internal profile measurements of the electron thermal transport in high current MST discharges were presented in Biewer, *et al.*[7, 13]. These measurements were made possible by Thomson scattering measurements of the radial profile of the electron temperature $T_e(r)$ with the ruby Thomson system on MST. To date, there are no non-invasive diagnostic techniques for directly measuring the heat flux, but because all other sources and sinks of energy were measured, conservation of energy was used to compute the heat flux. From this, the thermal transport coefficients were determined. Biewer, *et al.*, also included an attempt at quantifying the level of stochastic transport through the use of a combination of measurement and MHD simulation performed with the DEBS code[14]. The results of this comparison indicated that the thermal transport in MST was consistent with magnetic diffusion driven transport. However the uncertainty in the measurement was too large to draw any strong conclusions about the exact agreement. Additionally, this comparison was only made at a single time point. The large variation in both the simulated and measured magnetic mode amplitudes over the course of the sawtooth cycle suggest that the dominant transport mechanisms may well change in time. To gain a full understanding of the effect of stochastic transport on standard plasmas in MST, one must make this comparison over the full sawtooth cycle. The limited diagnostic and computational capabilities of the time made such a comparison impossible.

The single-point, single-pulse ruby Thomson scattering system on MST has now been replaced with a new multi-point, multi-pulse system that I helped to both install and upgrade to its current capabilities. This electron temperature diagnostic is now one of, if not the, most sophisticated diagnostic of its type in the world and represents a significant advance in high time resolution electron temperature measurements of high β plasmas, which are inaccessible to such measurement techniques as electron cyclotron emission (ECE). It is capable of measuring the temperature profile at 21 radial locations and 30 time points in a single discharge. Furthermore, the light source and detection hardware have been improved yielding a significantly higher signal to noise ratio, allowing single shot temperature fits even in the edge most locations (r/a$\sim$ 0.9). Due to these improvements, as well as the improvements in many of the other diagnostics on MST, the electron transport can now be determined with a time resolution and with a degree of confidence that was previously impossible. In addition to the diagnostic improvements, improvements mainly in the speed of computer processors have allowed me to run force free simulations with the DEBS code at values of Lundquist number matching those of high current standard discharges in MST ($S \sim 4 \times 10^6$). Not only that, these simulations were allowed to evolve for many sawteeth so that the sawtooth ensembled result can be compared to measurement. Ensemble averaging many simulated sawtooth events not only gives a much better sense of the typical sawtooth behavior but also make a much more compelling comparison to the sawtooth ensembled experimental data.

While the comparison of measured data to force free simulations can give significant insight into the evolution of the magnetic equilibrium and the important transport mechanisms active in the plasma, such a comparison to the transport is cumbersome. A much more straight forward comparison can be made if transport is simulated such that the simulated temperature can be compared directly to the measured temperature. The DEBS code used in Biewer, *et al.*, is also capable of running in a mode in which the pressure is self consistent evolved, and has been successfully used to model the heat transport in the RFP in the past, but those simulations were not performed at the aspect ratio or Lundquist number of MST, nor were they concerned with direct comparison to temperature measurements[15, 16, 17]. I have revisited this type of simulation, running at parameters that more closely match those of MST, so that both the measured temperature profile evolution and the evolution of the temperature fluctuations, which have now been measured on MST[18], can be directly compared to this simulation.

1.1 Outline and Summary of Key Results

As indicated, improvements in the Thomson scattering system and stronger computing power allow for a better and more complete comparison between the heat transport in MST to that obtained using simulated data, in addition to a better understanding of the physics dominating the transport throughout a sawtooth cycle. To these ends, the research presented in this thesis consists of a substantial set of experimental measurements of high current RFP discharges made in the MST as well as nonlinear MHD simulations designed to match MST parameters as closely as possible. These two projects, lead to four main results. The high time resolution Thomson scattering data show that the electron thermal diffusion changes by several orders of magnitude over the course of the sawtooth cycle. The simulations reproduce the equilibrium behavior in MST well including the sawtooth period and the duration of the sawtooth crash. Comparing the simulated and measured data shows that the simulations only match the measured thermal transport when the trapped particle fraction is taken into account. Lastly, simulations also reproduce temperature fluctuations that have previously been measured in MST[18].

A significant amount of this thesis was written to aide those that follow to reproduce and extend this work, so those familiar with MST may not want to read it in its entirety. The following summary explains the layout of this thesis with specific references to those sections containing key results in addition to a description of what is discussed in each chapter. For those less familiar with MST and RFP physics, the remainder of this chapter contains additional background information about MST as well as sawteeth and magnetic stochasticity.

Chapter 2 contains a detailed description of the multi-point multi-pulse Thomson scattering system on MST. This chapter also includes a discussion of the physical phenomenon of Thomson scattering, how that phenomenon is used in MST to find the electron temperature, and a detailed description of the hardware used in the system. *In section 2.4 I showcase the vastly improved capabilities of the Thomson scattering system using both ensemble averaged data from high current standard plasmas and single shot data from a variety of different discharge conditions.*

In chapter 3, a detailed description of how the magnetic equilibrium is determined from measurements is presented. This is followed by the presentation of the sawtooth evolution of the kinetic and magnetic profiles of interest for transport analysis for the case of a 400 kA standard plasma. The sawtooth evolution of the poloidal β, global energy confinement time, and a low resolution electron thermal diffusion profile are then presented and discussed. *In section 3.3.2 I present the sawtooth evolution of* *the electron thermal diffusion χ_e and find that χ_e in the core changes by two orders of magnitude through the sawtooth cycle, reaching a maximum at the sawtooth crash and a minimum shortly after the crash.*

In chapter 4, a set of force free (also referred to as zero β), nonlinear, resistive MHD simulations are presented. The primary purpose of these simulations was to determine the level of stochastic transport in these 400 kA MST plasmas. To do this, the magnetic perturbations inside the plasma need to be determined. This has been modeled using simulations performed at parameters that match experimental parameters as possible. This included running the simulations at a Lundquist number that matches that of MST as well as using a measured resistivity profile. Two resistivity profiles types were used: a Spitzer resistivity and a neoclassical resistivity model. A detailed comparison of the equilibrium evolution of these simulations to the equilibrium evolution of MST plasmas found in chapter 3 is presented. One striking feature of this comparison is that the duration of the sawtooth crash matches that observed in MST without the need for anomalous resistivity or two fluid effects, which is in contrast to simulations of sawteeth in tokamaks. This culminates in the comparison of the measured χ_e to that predicted by the Rechester and Rosenbluth model χ_{RR} and that due to magnetic diffusion χ_{MD}, which is found by direct tracing of the magnetic field lines. *Section 4.5, shows the result that the transport predicted from field line tracing over predicts χ_e unless trapped particles are taken into account. After the sawtooth crash, it becomes clear that the base level of heat transport in the core region is due to magnetic diffusion reduced by the circulating particle fraction (about a factor of 2). However, in the time leading up to the sawtooth, there must be substantial additional* *sources of heat transport to explain the large value of the measured χ_e at this time.*

In chapter 5, finite β simulation which incorporates Ohmic heating and anisotropic thermal conduction are presented. While the zero β simulations can tell us a great deal about the evolution of the equilibrium fields and the MHD modes that help drive that evolution, they don't directly tell us anything about the temperature evolution. Furthermore, the complex interplay between the heat transport, the equilibrium magnetic fields, and the fluctuations that modify, and are modified by, both of these is lost. In this chapter the simulated temperature profile evolution is presented and is found to be in moderate agreement with equilibrium measurements. *In section 5.1.2, a comparison between the simulated and measured temperature fluctuations is made, and striking agreement is found.*

In the last chapter, chapter 6, conclusions and future work are discussed.

1.2 Additional Background

This section present some additional background material for those less familiar with MST. This is by no means an exhaustive introduction to MST. The goal is simple to introduce and explain some of the common terminology in the hopes that it will help to avoid some confusion in later chapters.

1.2.1 The Madison Symmetric Torus

The Madison symmetric torus is a large reversed field pinch with a major radius of $R = 1.5$ m and a minor radius $r = 0.52$ m. MST has a unique design in which the vacuum vessel, primary plasma facing component, single turn toroidal field coil, and close fitting conducting boundary are all simultaneously provided by a 5 cm thick

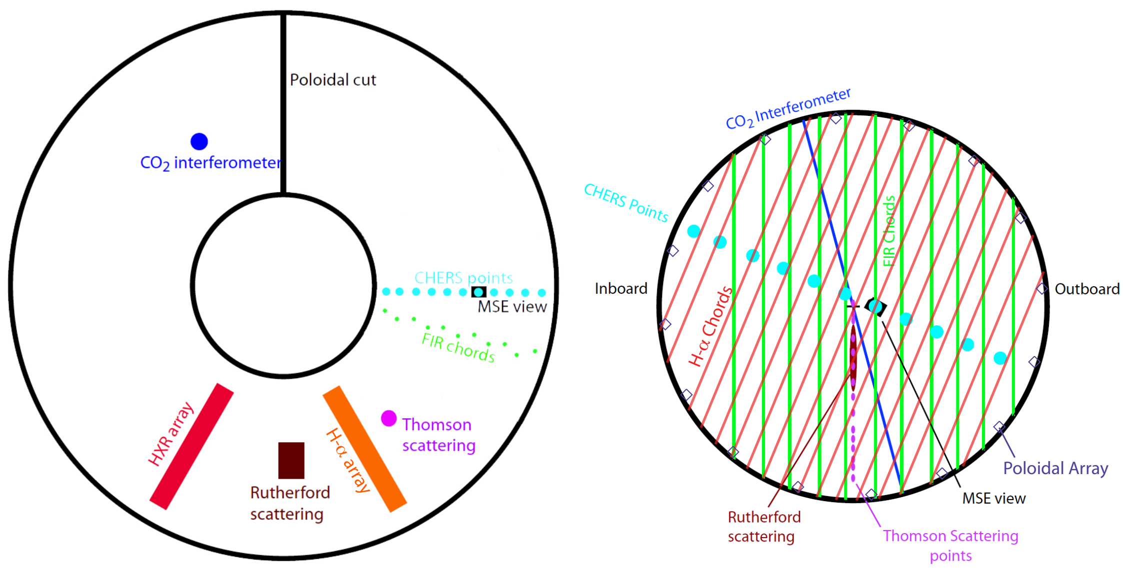

Figure 1.1: Toroidal (left) and poloidal (right) cross sections of the diagnostic coverage of MST used in this work.

aluminum shell. The resistive time of the shell is long enough that it is expected to appear to the plasma as an ideal boundary on the time scale of the plasma discharge[19]. Furthermore, in order to reduce error fields at the boundary and provide a more ideal boundary condition, the size of the port holes used for diagnostic access is very limited. While this is good for the stability of the plasma, it provides a challenge for diagnostic design. Despite this limitation, MST is host to a substantial diagnostic set including some of the most advanced diagnostics of their type in the world. One such diagnostic is the multi-point multi-pulse Thomson scattering system discussed in chapter 2. Figure 3.1 shows the layout and field of view for the diagnostics used in this work. Note that while this is a fairly complete list, it is not exhaustive as there are several diagnostics installed on MST that were not used in this analysis.

In RFP terminology there are two important parameters for describing the magnetic equilibrium, the reversal and pinch parameters. The target values for these parameters for this work were a reversal parameter $F = B_\phi(a)/\langle B_\phi \rangle \approx -0.2$ and a pinch parameter $\Theta = B_\theta(a)/\langle B_\phi \rangle \approx 1.7$. This set of parameters results in an electron temperature of about 350 eV, an ion temperature of about 250 eV, and a magnetic field of about 0.4 T on axis. These parameters represent one of the most typical set of run parameters used in MST and a good target for assessing the typical behavior of standard RFP discharges in MST.

1.2.2 Sawteeth in MST

A typical MST discharge can be broken into three parts: the current ramp, current flattop, and current decay phases. During the current ramp, the average toroidal field increases while the toroidal field at the wall decreases (see figure 1.2). This decrease is likely due to magnetic relaxation where the high degree of MHD activity at plasma startup drives the plasma towards a minimum energy state. This phenomena of field reversal was first explained by J.B. Taylor as the plasma relaxing towards a minimum energy state with the additional constraint that global magnetic helicity is conserved[20, 21]. Once the field at the wall reverses sign, the plasma starts to exhibit quasi-periodic sawtooth oscillations. These sawtooth oscillation, which have long been observed in the RFP configuration[22, 23, 24], persist throughout the current flattop phase of the discharge, ceasing in the ramp down phase when the externally applied current drive has been turned off.

In addition to being periodic, a closer analysis of the sawtooth evolution of the MHD activity shows that there are three phases to the sawtooth oscillation. The first phase is a slow rise phase in which the MHD activity, the amplitudes of the

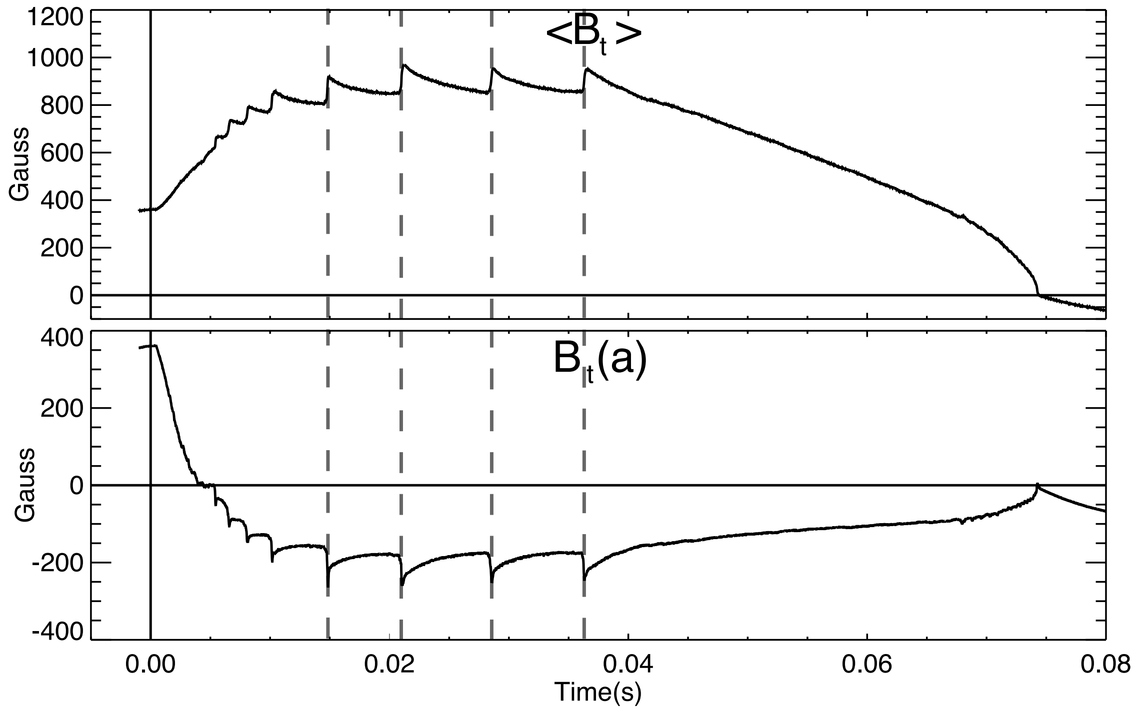

Figure 1.2: The average toroidal field (top) and the toroidal field at the wall (bottom) for a single discharge. Note that the current flattop starts just after the sawtooth at 15 ms and ends just after the sawtooth at 37 ms.

core modes in particular, increase slowly. The second is the sawtooth crash (dashed lines in figure 1.2) in which all of the magnetic mode amplitudes (as measured at the edge of the plasma) grow rapidly. In this phase the toroidal flux increases rapidly and equilibrium modeling shows that the current density is redistributed inside the plasma, with the toroidal current density being reduced in the core and the poloidal current enhanced in the mid-radius. Finally, there is the quiescent phase where all of the modes get relatively small and the MHD activity is reduced to some nominal minimum value. Figure 1.3 shows the RMS amplitude for the core resonant poloidal mode number m=1 modes as well as the mode spectrum at two different times in the sawtooth cycle. This apparent resetting of the MHD activity that occurs with each

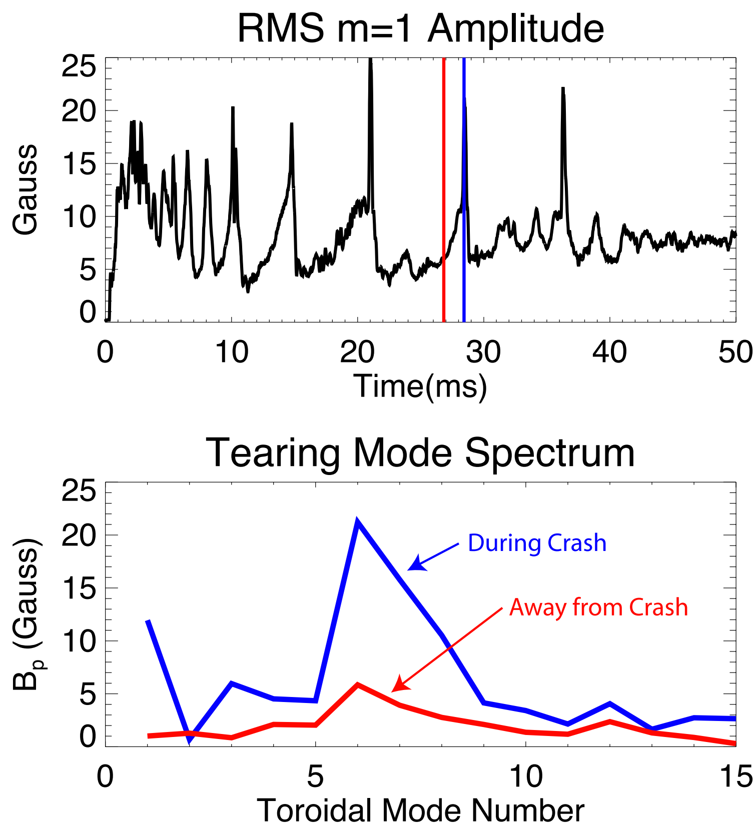

Figure 1.3: RMS m=1 amplitude (top) and m=1 mode spectra for toroidal mode numbers n=1 through 15 (bottom) from edge magnetic pickup coil data. Notice that at the crash all of the modes increase substantially.

sawtooth is mimicked on many of the diagnostic measurements made in MST. This feature of the sawtooth oscillation makes these sawtooth crashes good markers in time around which data can be ensemble averaged to yield the canonical sawtooth behavior for a given set of discharge parameters[25]. Most of the work presented in this thesis, from both the experiment and MHD simulations, involves averaging data from many sawteeth in this way.

1.2.3 Magnetic Stochasticity in MST

The magnetic perturbations measured at the edge of MST are generally resonant somewhere inside the plasma. At the resonant location, a magnetic island can form. In the periodic cylinder approximation for the toroidal geometry, the resonance condition for which a perturbation will not be damped by the natural restoring force of the magnetic field lines is $\mathbf{k} \cdot \mathbf{B} = mB_\theta/r + nB_\phi/R = 0$. By rearranging this expression we can identify the safety factor as $q = m/n = -rB_\phi/RB_\theta$ (note that while B_θ is formally negative, the sign is often dropped for convenience). The equilibrium magnetic field profile for the standard RFP discharge results in a relatively low safety factor. A typical q profile for MST is shown in figure 1.4 and is about 0.2 on axis and decreases until crossing zero near the edge. The toroidal field is largely self generated and scales with current and thus, the resulting safety factor is relatively constant with current.

The safety factor is important as it indicates the location and number of the magnetic perturbations that will be resonant inside the plasma. In general, the modes with the lowest poloidal and toroidal number are the most dangerous to confinement and any RFP will not only have nearly all the $m = 1$ modes resonant inside the plasma, in addition to all of the $m = 0$ modes, which will be resonant at the point where the toroidal field crosses zero, or the reversal surface. As these modes grow in amplitude they can create magnetic islands which can overlap and cause the magnetic field lines to become tangled. The magnetic field line trajectories, rather than being deterministic, become stochastic but can be described by a diffusion coefficient of their own. As will be discussed in detail later, this makes the radial heat transport a doubly diffusive process where not only do particle collisions cause heat to be transported across field lines and down the temperature gradient, but the field lines themselves are diffusing radially, adding a parallel component to the radial transport. The left plot in figure 1.4 shows a representative safety factor profile for MST parameters. The island widths $\Delta_{mn} = 4\sqrt{r_{mn}|\tilde{b}_{rmn}|/\left(nB_\theta|q'_{mn}|\right)}$ for many of the resonant modes are also shown in the left plot. The right hand plot shows the island overlap or 'stochasticity' parameter $s = \left(\Delta_{mn} + \Delta_{m'n'}\right)/\left(2|r_{mn} - r_{m'n'}|\right)$. Clearly the degree of stochasticity varies significantly across the minor radius of MST. Furthermore, since the island width is dependent on the mode amplitude and the stochasticity is dependent on the island widths, it is clear that the degree of stochasticity should increase as the mode amplitudes increase. This means that the degree of stochasticity not only varies with radius, but will also vary substantially though the sawtooth cycle.

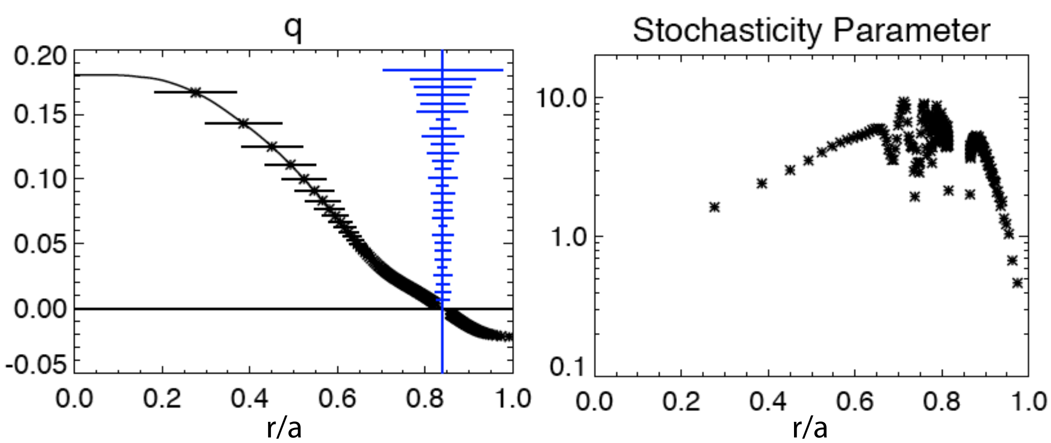

Figure 1.4: Safety factor profile with many of the m=1 and m=0 island widths overplotted (left) and the stochasticity parameter for the m=1 modes (right).

REFERENCES

[1] Bodin, H. and Newton, A. Reversed Field Pinch Research. *Nuclear Fusion* **20**(10), 1255 (1980).

[2] Prager, S. C. Transport and fluctuations in reversed field pinches. *Plasma Physics and Controlled Fusion* **32**(11), 903 (1990).

[3] Dexter, R. N., Kerst, D. W., Lovell, T. W., Prager, S. C., and Sprott, J. C. The Madison Symmetric Torus. *Fusion Technol.* **19**(1), 131–139 (1991).

[4] Rechester, A. B. and Stix, T. H. Magnetic Braiding Due to Weak Asymmetry. *Phys. Rev. Lett.* **36**(11), 587–591 Mar (1976).

[5] Rechester, A. B. and Rosenbluth, M. N. Electron Heat Transport in a Tokamak with Destroyed Magnetic Surfaces. *Physical Review Letters* **40**(1), 38–41 (1978).

[6] Chandran, B. D. G. and Cowley, S. C. Thermal Conduction in a Tangled Magnetic Field. *Phys. Rev. Lett.* **80**(14), 3077–3080 Apr (1998).

[7] Biewer, T. M., Forest, C. B., Anderson, J. K., Fiksel, G., Hudson, B., Prager, S. C., Sarff, J. S., Wright, J. C., Brower, D. L., Ding, W. X., and Terry, S. D.

Electron Heat Transport Measured in a Stochastic Magnetic Field. *Phys. Rev. Lett.* **91**(4), 045004 (2003).

[8] Baldi, A., Forman, W., Jones, C., Nulsen, P., David, L., Kraft, R., and Simionescu, A. CHANDRA Observations of the Galaxy Group AWM 5: Cool Core Reheating and Thermal Conduction Suppression. *Astrophysical Journal* **694**(1), 479–491 March (2009).

[9] Park, G., Chang, C. S., Joseph, I., and Moyer, R. A. Plasma transport in stochastic magnetic field caused by vacuum resonant magnetic perturbations at diverted tokamak edge. *Physics of Plasmas* **17**(10), 102503 (2010).

[10] Chandran, B. D. G., Cowley, S. C., Ivanushkina, M., and Sydora, R. Heat Transport Along an Inhomogeneous Magnetic Field. I. Periodic Magnetic Mirrors. *The Astrophysical Journal* **525**(2), 638 (1999).

[11] Anderson, J. K., Forest, C. B., Biewer, T. M., Sarff, J. S., and Wright, J. C. Equilibrium reconstruction in the Madison Symmetric Torus reversed field pinch. *Nuclear Fusion* **44**, 162–171 (2004).

[12] Fiksel, G., Bengtson, R. D., Cekic, M., Den Hartog, D. J., Prager, S. C., Pribyl, P., Sarff, J., Sovinec, C., Stoneking, M. R., Taylor, R. J., Terry, P. W., Tynan, G. R., and Wootton, A. J. Measurement of magnetic fluctuation-induced heat transport in tokamaks and RFP. *Plasma Physics and Controlled Fusion* **38**(12A), A213 (1996).

[13] Biewer, T. M. *Electron Thermal Transport in the Madison Symmetric Torus.* PhD thesis, University of Wisconsin at Madison, (2002).

[14] Schnack, D. D., Barnes, D. C., Mikic, Z., Harned, D. S., and Caramana, E. J. Semi-implicit magnetohydrodynamic calculations. *Journal of Computational Physics* **70**(2), 330 – 354 (1987).

[15] Sovinec, C. R. *Magnetohydrodynamic Simulations of Noninductive Helicity Injection in the Reversed-Field Pinch and Tokamak*. PhD thesis, University of Wisconsin at Madison, 1150 University Ave., Madison, WI, 53706, (1995).

[16] Scheffel, J. and Schnack, D. D. Confinement Scaling Laws for the Conventional Reversed-Field Pinch. *Phys. Rev. Lett.* **85**(2), 322–325 Jul (2000).

[17] Scheffel, J. and Schnack, D. Numerical studies of confinement scaling in the conventional reversed field pinch. *Nuclear Fusion* **40**(11), 1885–1896 (2000).

[18] Stephens, H. D., Den Hartog, D. J., Hegna, C. C., and Reusch, J. A. Electron thermal transport within magnetic islands in the reversed-field pinch. *Physics of Plasmas* **17**(5), 056115 (2010).

[19] Fitzpatrick, R., Guo, S., Den Hartog, D., and Hegna, C. Effect of a resistive vacuum vessel on dynamo mode rotation in reversed field pinches. *Physics of Plasmas* **6**(10), 3878–3889 Oct. (1999).

[20] Taylor, J. B. Relaxation of Toroidal Plasma and Generation of Reverse Magnetic Fields. *Physical Review Letters* **33**(19), 1139–1141 Nov (1974).

[21] Taylor, J. Relaxation and magnetic reconnection in plasmas. *Review of Modern Physics* **58**(3), 741–763 July (1986).

[22] Wurden, G. A. Soft x-ray array results on the ZT-40M reversed-field pinch. *Physics of Fluids* **27**(3), 551–554 (1984).

[23] Prager, S. C., Almagri, A. F., Assadi, S., Beckstead, J. A., Dexter, R. N., Den Hartog, D. J., Chartas, G., Hokin, S. A., Lovell, T. W., Rempel, T. D., Sarff, J. S., Shen, W., Spragins, C. W., and Sprott, J. C. First results from the Madison Symmetric Torus reversed field pinch. *Physics of Fluids B: Plasma Physics* **2**(6), 1367–1371 (1990).

[24] Hokin, S., Almagri, A., Assadi, S., Beckstead, J., Chartas, G., Crocker, N., Cudzinovic, M., Den Hartog, D. J., Dexter, R., Holly, D., Prager, S., Rempel, T., Sarff, J., Scime, E., Shen, W., Spragins, C., Sprott, C., Starr, G., Stoneking, M., Watts, C., and Nebel, R. Global confinement and discrete dynamo activity in the MST reversed-field pinch. *Physics of Fluids B: Plasma Physics* **3**(8), 2241–2246 (1991).

[25] Chapman, J. T. *Spectroscopic Measurement of the MHD Dynamo in the MST Reversed Field Pinch*. Doctor of philosophy, University of Wisconsin at Madison, 1150 University Ave., Madison, WI, 53706, (1998).

Chapter 2

Measuring the Electron Temperature Profile Evolution in MST

This chapter contains a discussion of the physics of Thomson scattering and how it is used as a diagnostic on MST. Significant time is spent detailing the system design and operation. The structure of the chapter is as follows: first, there is a brief discussion of Thomson scattering theory, followed by a detailed description of the physical layout of the system and a discussion of calibration and fitting. Finally, some example data is shown for a few different types of plasmas.

2.1 Thomson Scattering Theory

Thomson scattering is the process in which a photon is absorbed by a free charge and reemitted. Essentially, the electric field of the photon accelerates the free charge, in this case an electron although Thomson scattering off ions can also be done, causing it to emit a photon and thus it is the incident photon energy that was absorbed that is reemitted. This photon will have the same wavelength as the incident photon in the rest frame of the electron, but its direction of emission will have a dipole probability distribution. Figure 2.1 shows the incident and emitted photon scattering off an electron, which means that the intensity of the emitted light has a $\sin^2\chi$ distribution where χ is the angle formed between the plane formed by the incident and scattered k vectors and the acceleration vector of the electron (i.e. the electric field vector of the incident photon). θ is the angle between the incident and scattered k vectors and is commonly referred to as the scattering angle.

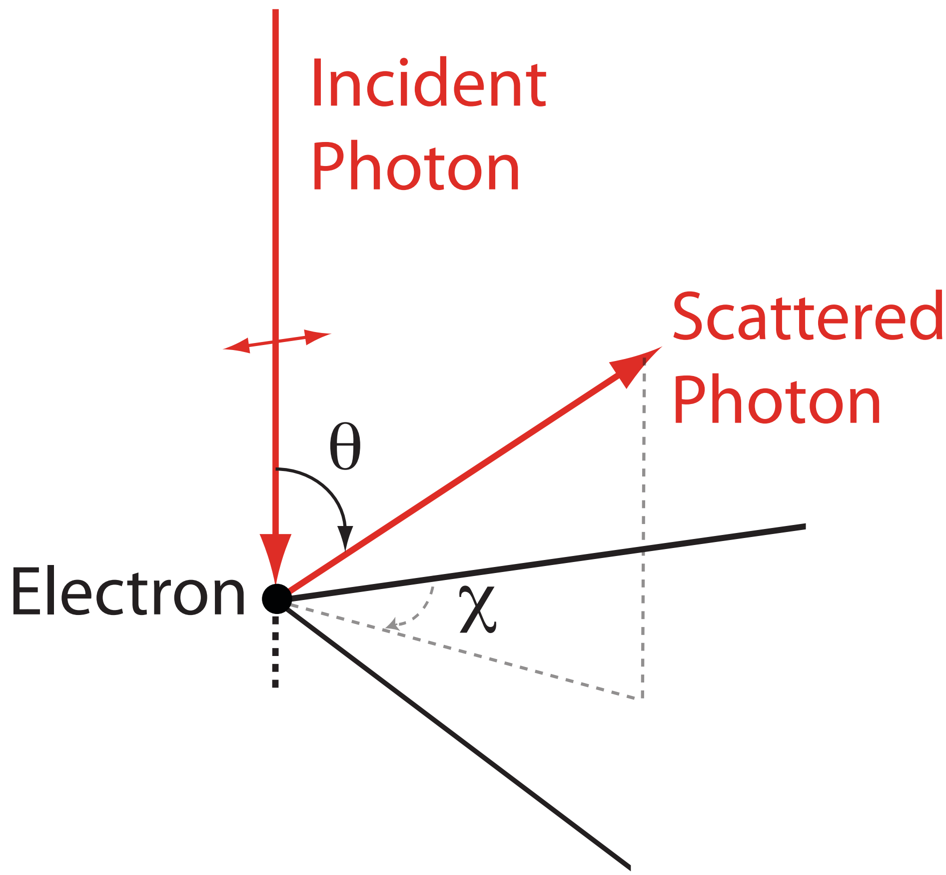

Figure 2.1: The incident laser light is absorbed and reemitted at the same wavelength by the electron. The scattering angle, θ, is defined as the angle between the incident photon and the scattered photon in the plane formed by the wave vectors of these two photons. The angle between this plane and the electric field of the incident photon is labeled as χ and the emission intensity has a $\sin^2\chi$ distribution.

In reality, we are concerned with the scattering of many photons off many electrons. The total amount of power scattered by a given number of electrons in a given cross sectional area is related to the incident energy flux from the photon source I (energy/time/area) and the number of electrons in that area N_e.

$$P_{total} = \sigma_{Thomson} I N_e \tag{2.1}$$

The Thomson scattering cross section is well known to be

$$\sigma_{Thomson} = \frac{8\pi}{3}\left(\frac{e^2}{4\pi\epsilon_0 m_e c^2}\right)^2 = 6.65 \times 10^{-29} m^2 \tag{2.2}$$

where the term in parenthesis is the classical electron radius. Clearly, the Thomson scattering process in extremely inefficient, even if one could collect all the scattered photons produced. In plasmas, the incident light source is often a linearly polarized short pulse laser. These lasers have high instantaneous power, which increases the Thomson scattered power, and short duration, which makes the scattered light pulse easy to distinguish from the background. The wavelength of the emitted light will match the absorbed light in the rest frame of the particle, which means that in the lab frame the emitted light will be shifted with respect to the laser light by an amount related to its velocity. This effect can be thought of as a simple Doppler shift of the wavelength of the scattered light. This approximation turns out to be good all the way to relativistic speeds.

One further consideration is the direction of motion of the charged particle that is doing the scattering. Functionally, the scattered light is not collected everywhere, rather it is collected at a single location. Since the input light is also fixed, conservation of momentum dictates the speed and direction of the electrons that a real diagnostic will be sensitive to. Conservation of momentum can be written as $\mathbf{k_i} + \mathbf{k_e} = \mathbf{k_s}$ where $\mathbf{k_i}$ is the incident k vector of the laser light, $\mathbf{k_e}$ is the electron k vector, and $\mathbf{k_s}$ is the k vector of the scattered photon. The angle between $\mathbf{k_i}$ and $\mathbf{k_s}$ is the scattering angle, θ.

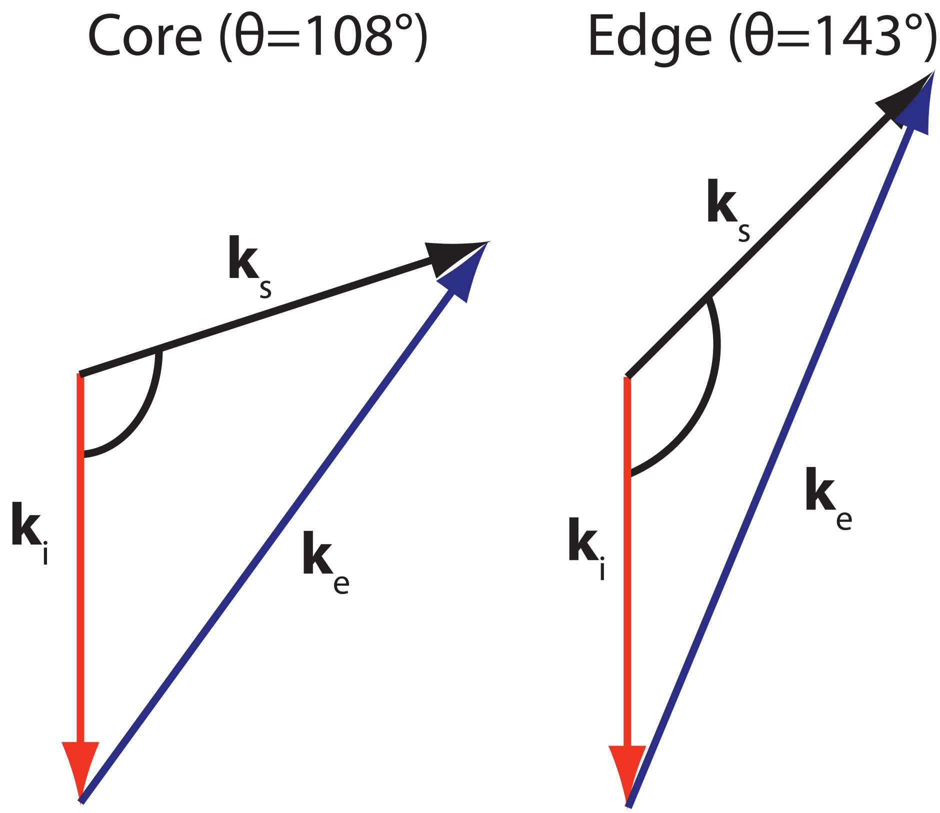

Figure 2.2: k diagrams for two scattering angles. Each radial location for the multipoint Thomson scattering system on MST measures light scattered at a different scattering angle.

Again, while these pictures give a good sense of the behavior of a single photon scattering off a single electron, plasmas are made up of a large number of free charges with a range of velocities in the lab frame. Approximating the electron distribution as a Maxwellian allows the number of Thomson scattered photons emitted per wavelength to be computed. If the velocity gets high enough then relativistic effects become important and will skew the spectrum of resulting light as the distribution function itself become skewed. The scattered power per wavelength, or spectral power density, has been calculated analytically[1] taking into account these relativistic effects, and the approximations used for the analytic calculations have been shown to hold for electron temperatures up to 100 keV[2]. It should be noted that the relativistic corrections become important at less than 1 keV. The polarization of the scattered light can also be modified by relativistic effects, though this does little to change the shape of the scattered spectrum, rather it can change the intensity of the scattered light and thus must be taken into account before any attempt at measuring the density with this effect is made[3]. The parameter that is of practical importance for the use of the Thomson scattering phenomena as a temperature and density diagnostic is the number of photons scattered per unit solid angle as a function of electron temperature, density, and wavelength. The spectral density function $S(\epsilon, \theta)$ is linearly proportional to the number of photons emitted as a function of wavelength and is approximately described by the Selden equation (Equation 2.3).

$$S\left(\epsilon,\theta\right) = c\left(\alpha\right) e^{-2\alpha B(\epsilon,\theta)} / A\left(\epsilon,\theta\right) \tag{2.3}$$

where

$$
\begin{aligned}
A \quad (\epsilon, \theta) &= (1+\epsilon)^3 \sqrt{2\left(1-cos\theta\right)\left(1+\epsilon\right)+\epsilon^2} \\
B \quad (\epsilon, \theta) &= \sqrt{1+\frac{\epsilon^2}{2\left(1-cos\theta\right)\left(1+\epsilon\right)}}-1 \\
c \quad (\alpha) &= \sqrt{\frac{\alpha}{\pi}}\left(1-\frac{15}{16}\alpha^{-1}+\frac{345}{512}\alpha^{-2}+...\right) \qquad \text{for } \alpha \gg 1
\end{aligned}
$$

and $\alpha \equiv \frac{1}{2}\frac{m_e c^2}{kT_e}$, $\epsilon = \frac{\lambda_s}{\lambda_i} - 1$, and θ is the scattering angle. For the MST case, θ varies from about 108° to about 143°. While this expression is not an exact solution to the scattered power for a relativistic distribution function, it has been shown to be in very good agreement in the range of temperatures seen on MST, which are typically in the tens to hundreds of electron volt range and to date, are always less than 3 keV. It should be noted that the expression for the Thomson scattering cross section is the classical expression which, while nicely related to the classical electron radius, neglects the quantum mechanical effect of electron recoil. This is the so called Compton effect and has been taken into account in the derivation of equation 2.3. It should also be noted that this equation yields the scattered power density and that the total scattered power, and thus the total number of scattered photons, will scale linearly with incident light intensity, so the absolute density simply scales the whole distribution up and down.

2.2 Hardware and Physical Layout

Given this understanding of the underlying principles and considerations of the physical mechanisms of the Thomson scattering process, the details of their implementation on MST will now be discussed. The multi-point Thomson scattering diagnostic on MST has been operational since 2003 and has the capability of providing multiple radial profiles of electron temperature per discharge. This system has proven to be very versatile and has produced high quality data over the full range of MST operating conditions. The system design allows for the study of not only a wide range of plasma conditions, but also a wide range of plasma phenomena. It has been used to evaluate diverse scenarios ranging from equilibrium temperature evolution throughout the discharge to high frequency temperature fluctuations. This includes transient events such as the profile evolution through sawteeth and during enhanced confinement (EC) periods[4]. All of this is done while overcoming the challenges of small viewing ports and the remote location of the laser head.

This diagnostic has been incrementally improved and upgraded since those first measurements were made in 2003. The installation, operation, and improvement of a diagnostic this complex requires a team of people of which I am but one member. The Thomson scattering team on MST consists of five to ten people at any one time. It is lead by Daniel Den Hartog and has included several members of MST staff as well as several graduate and undergraduate students. The initial installation was done by myself and fellow graduate student Hillary Stephens with the help and guidance of Rob O'Connell and Mike Borchardt. Later upgrades were made with the help of graduate students Adam Falkowski, Ming Yang, and Eli Park as well as the several undergraduate students who have helped out over the years. The initial data was collected with one laser pulse supplying data at three radial locations through the use of a set of three oscilloscopes. Over the course of two years the system was brought up to the initial design spec of 21 spatial points and two time points[5, 6, 7] (one time point per laser per discharge). Further upgrades increased the number of time points from 2 to 30 and expanded the temperature range that a subset of the radial points are sensitive to from 2 keV to 10 keV. The data collection system has also undergone major changes over the years. The following section will go through the current hardware setup though the upgrades that have been made to the system will also be mentioned when pertinent.

2.2.1 Laser Light Path

2.2.1.1 The Laser System

The laser head is the origin of the pulse of incident photons used for Thomson scattering. For posterity, this section contains many of the technical specifications and some of the operational principles of these lasers. The lasers are housed in a separate room from the main MST experimental hall and are over 15 m from the first point of interest inside the vacuum vessel (see Figure 2.3). The system currently uses two Spectron SL858 Nd:YAG lasers that are operated at the fundamental wavelength of 1064 nm and have a 9 ns pulse duration (FWHM). Both lasers have a pointing stability of 75 μrad, a beam divergence of 0.5 mrad, and output beam diameters of 1.25 cm [8]. Originally, these lasers were an off the shelf design capable of producing 3 J per pulse in a 2 Hz mode, or up to 1.3 J per pulse in a 50 Hz mode with a top hat beam profile. In a series of upgrades made between 2007 and 2009 both the Pockel cell driver and the laser power supplies replaced, greatly enhancing the amount of data produced each shot and the reliability of that data.

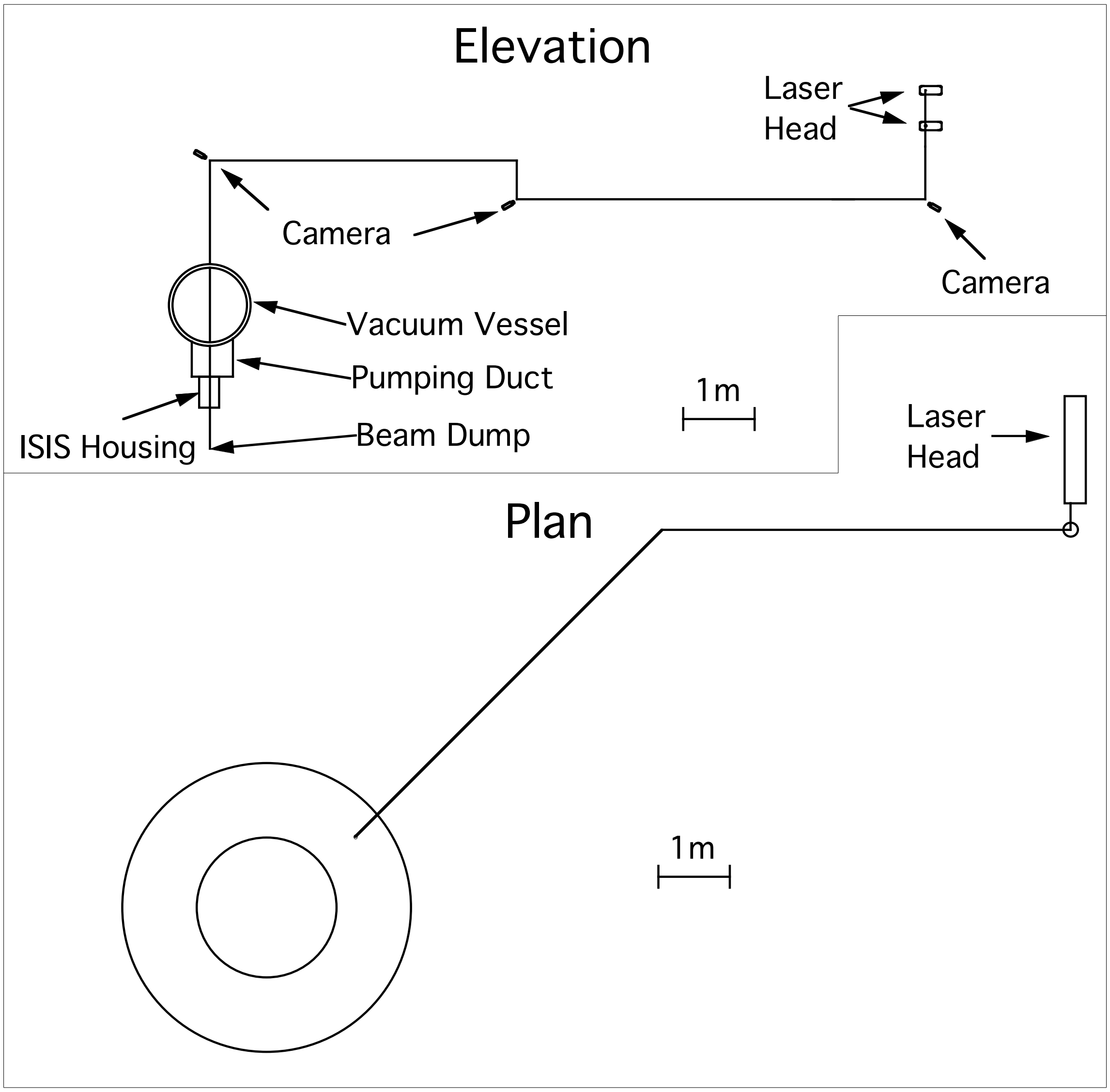

Figure 2.3: The entire system layout is shown here in both an elevation and overhead view. The laser beam has to pass under a public hallway and across the MST machine area before finally being directed down through the vacuum vessel.

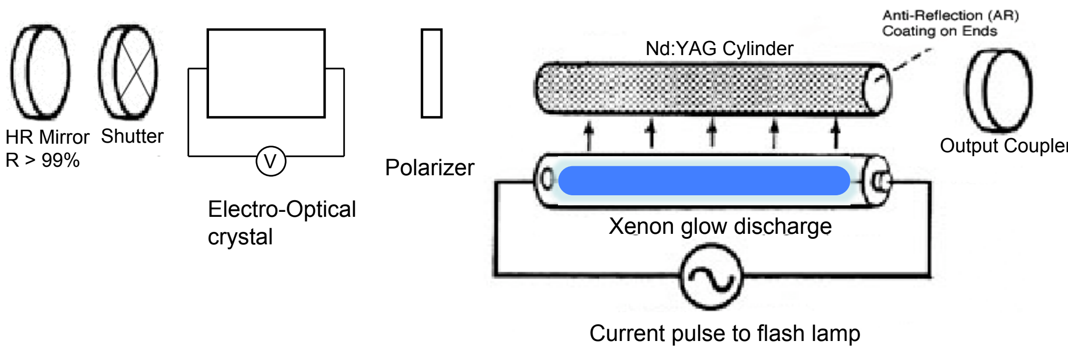

Figure 2.4: Cartoon of a Q-switched laser oscillator.

In order to fully understand the significance of these upgrades one must first understand the basic operating principles of these lasers. These are high pulse power Q-switched lasers. The key component to these lasers is the Pockel cell, or Q-switch, which is an electro-optical crystal that has the property that it can alternately act as a quarter wave plate, a half wave plate, or window depending on the voltage applied across it. In order to form the laser pulse, the laser rod is optically pumped with xenon arc discharge flash lamps. These lamps excite electrons in the laser rod into a metastable energy level with a relatively long decay time. The electrons will spontaneously emit a photon with a wavelength of 1064 nm as the electron drops from the metastable second excited state into the first excited state. As this photon passes through the rod it stimulates the emission of photons from other electrons in this metastable energy level that have the same wavelength and direction as the initial photon. Once the photon exits the laser rod it is absorbed by a polarizer, mirror, quarter wave plate combination (see figure 2.4). This means the Q, or efficiency, of the cavity is very low because all of the emitted photons are lost. The rod is pumped until this loss of excited electrons balances the number of electrons being excited by the flash lamps. This population of excited electrons is relatively high because the amount of stimulated emission is very small as the spontaneously emitted photons only get to make one pass through the rod before they are absorbed. For the Spectron system it takes about 140 μs from the time flash lamp arc starts till the maximum number of exited electrons is achieved. Another way to think of this is that the maximum possible amount of optical energy is now stored in the laser rod. A large voltage (about 5 kV) is then applied to the Pockel cell changing it from essentially a window to a quarter wave plate. This means that the light that was going through the polarizer, mirror, quarter wave plate combination is now going through a polarizer, mirror, half wave plate combination and horizontally polarized light can now pass freely back and forth through the laser rod. With each pass these horizontally polarized photons stimulate the emission of other horizontally polarized photons and the total number of photons grow rapidly. This means the Q of the cavity is now relatively high. The Pockel cell allows the Q to be changed rapidly and thus it is often called a Q-switch. The stored energy in the rod is rapidly depleted and a 9 ns laser pulse is produced. After about 40 ns the voltage on the Pockel cell is returned to zero and the Q of the cavity is low again. This allows the laser rod to be re-pumped, but now the laser rod starts with some number of excited electrons and the flash lamps are operating at full output, so the saturation level is achieved in less time. In the Spectron system this re-pumping takes about 80 μs. This means that multiple laser pulses at the same energy can be generated in a single flash lamp pulse.

The original Pockel cell driver for these lasers only allowed one laser pulse per flash lamp pulse but, in 2007, the lasers were upgraded with a new set of Pockel cell drivers manufactured by Bergmann Meßgeräte Entwicklung KG (part number ds11d/KD*P). The new drivers greatly reduced electrical noise generated when the laser is Q-switched, substantially improving the data quality due to the reduction in electrical pickup on the data signals. These new drivers are also able to generate multiple high voltage pulses in a row with a pulse to pulse separation of tens of microseconds thus allowing multiple laser pulses per flash lamp pulse. Due to the physical characteristics of the Pockel cell used in these lasers (Cleveland Crystals Impact 10) the minimum pulse to pulse time is about 40 μs, however, as discussed above, there is a functional limit of 80 μs due to the physical characteristics of the laser rod and flash lamp combination used.

The original pulse forming network (PFN) for the laser ran the flash lamps for about 200 μs and the Pockel cell upgrade allowed the generation of two pulses per laser per discharge instead of one. At the end of 2008 the laser power supplies were switched over to run the new QXF54 power supplies and Flash Lamp Power Supply Control System (FLPSCS) that were designed and built by the Physical Sciences Laboratory (PSL) for the Fast Thomson system that is currently under development. The new supplies use an insulated gate bipolar transistor (IGBT) based system. This system is capable of producing high power flash lamp pulses with a wide range of pulse durations and can be re-triggered at about a 1 kHz repetition rate. When this is combined with the upgraded Pockel cell driver, the system can be run in a mode in which bursts of high repetition rate pulses are produced every millisecond. A pulse to pulse time of 80 μs translates to about 12.5 kHz and the two lasers can be interleaved giving an effective 25 kHz burst of pulses every millisecond for several milliseconds. Alternately, one laser pulse per flash lamp pulse can be produced for up to 15 pulses per laser which translates to 15 ms of data in the standard 2 kHz mode[9, 10]. Functionally, it is the heat load on the walls of the flash lamps that limit the number of pulses that can be produced per discharge as there is very little cooling that is done during the 80 ms long MST plasma. However, since the time between plasma discharges is a minimum of two minutes, the system has ample time to cool down completely between shots.

The two lasers are independently triggered by a compact reconfigurable I/O (cRIO) module from National Instruments which has a 25 ns resolution and less than 10 ns channel to channel jitter. This module triggers both the flash lamps and the Pockel cells using different time loops to ensure that the Pockel cell is fired at consistent time with respect to the beginning of the flash lamp pulse. Figure 2.5 shows the current vs. time for the eight flash lamps as well as the Pockel cell triggers for the two lasers. Notice that the first trigger happens about 140 μs after the pulse begins while the later pulses have a Δt of 80 μs. The power and operating mode of each of the two lasers is independently and remotely controlled using a Labview GUI and is quite versatile. That said, we typically operate in one of two modes which both yield 15 pulses per discharge per laser at 2 J. The first mode interleaves the two lasers firing at 1 kHz continuous for an effective 2 kHz repetition rate. This mode is used for looking at the long time scale equilibrium evolution of the plasma and allows most of the current flat top to be measured in a single shot. The second mode is a 25 kHz effective pulse burst mode that is used primarily for fluctuation measurements, though, using the ensemble techniques discussed in the next chapter, the data from many shots can be combined to yield equilibrium data as well. Figure 2.6 shows the energy per pulse for 15 pulses

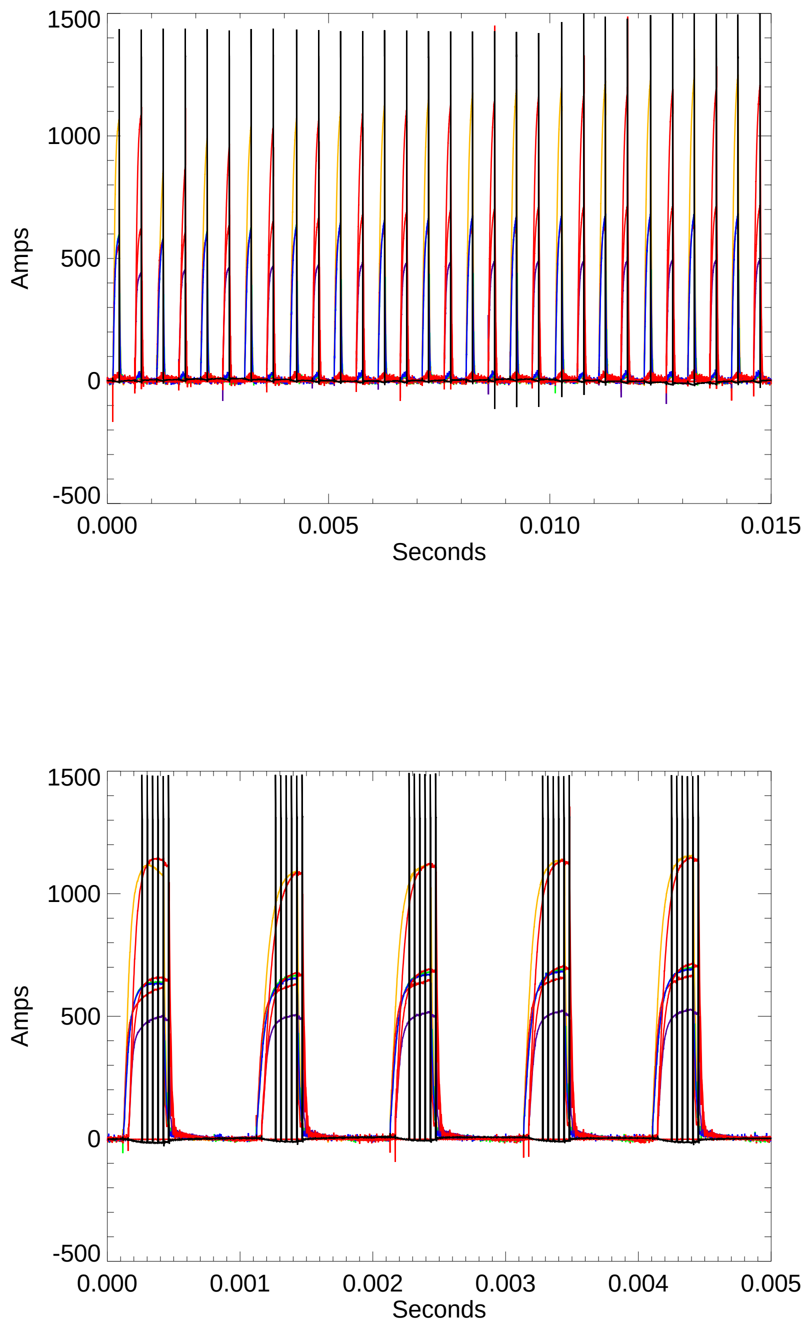

Figure 2.5: Current traces (colored) and Pockel cell triggers (black) for the 8 flash lamps in the two lasers firing in 2 kHz mode (top plot) and 25 kHz mode (bottom plot).

in 1 kHz and 12.5 kHz mode. The fall off of the pulse energy in the 1 kHz operation is assumed to be due to capacitor bank droop and changes in the flash lamp impedance as it heats up. As the impedance changes the power output from the lamp drops and thus the maximum stored optical energy obtained in the laser rod also drops.

2.2.1.2 Beam Line

The two lasers are stacked vertically and the light pulse is directed 15 m, using five mirror stages, to the first point of interest in the center of the MST vacuum vessel. The light paths of the two lasers converge over the length of the beam line such that their path through the sampling volume (from the geometric center of MST to the bottom of the inner vacuum vessel wall, along the geometric axis) are nearly identical.

The optical components of the beam line include a half wave plate, five 90° turning mirrors, a focusing lens, two vacuum windows at the Brewster angle, and a three stage beam dump (see Figure 2.3). A half wave plate from CVI (QMPM-1064-15-2-R20) is used to rotate the horizontally polarized laser light by about 20° in order to maximize the amount of light Thomson scattered in the direction of the collection optics. Recall that the scattering intensity goes like $\sin^2\chi$ so this change should increase the scattered light by about 12%, though this value has not as yet been confirmed with measurement. The angle of rotation is determined by rotating horizontally polarized 1064 nm light from a laser diode at the beginning of the beam line until it is aligned to the toroidal direction of MST at the entrance vacuum window. The high power turning mirrors that direct the beam down to the machine are designed to reflect 1064 nm unpolarized light with an incidence angle of 45° (CVI Y1-2037-45)

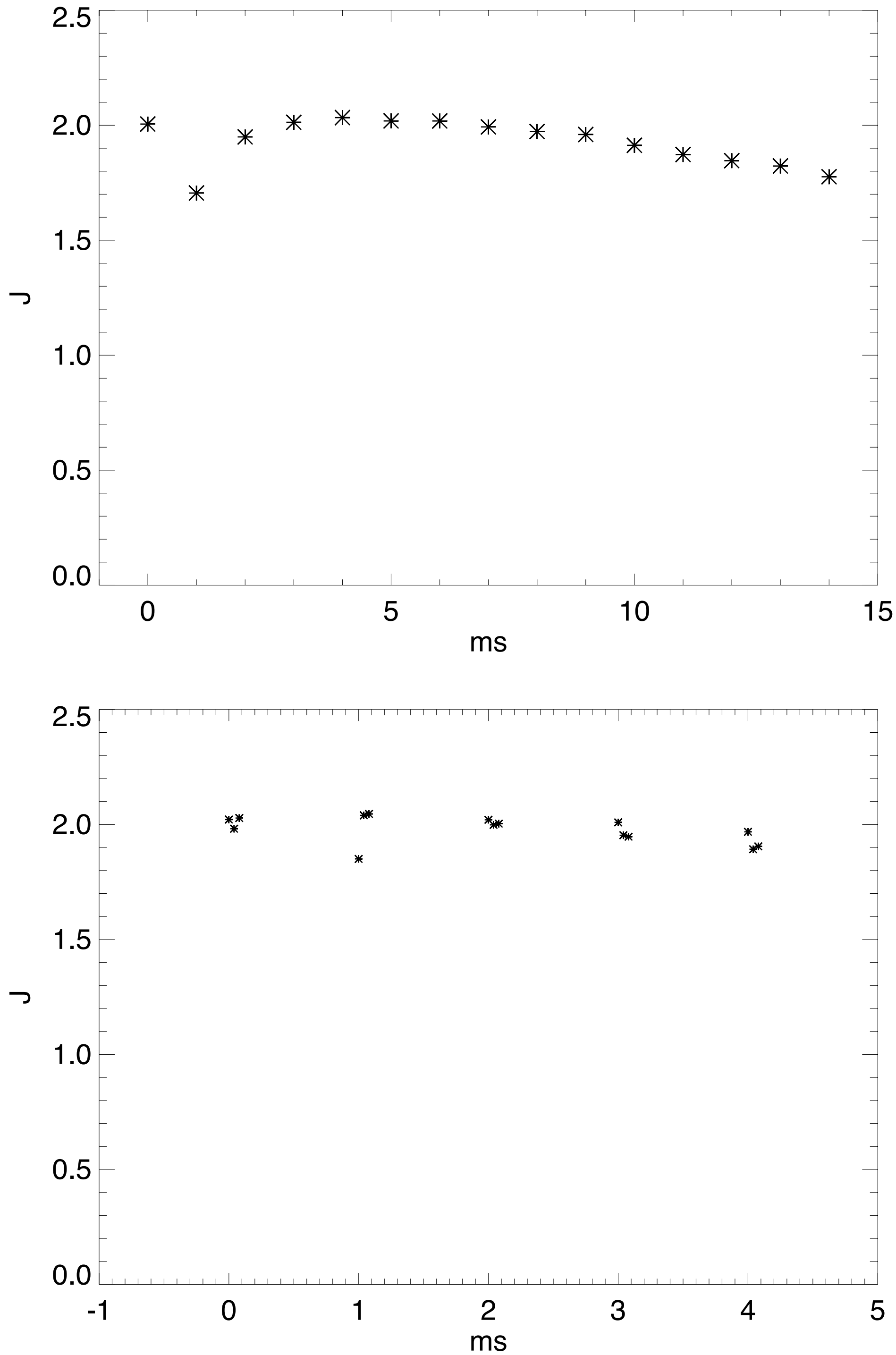

Figure 2.6: Laser power vs. time for 15 pulses at 1 kHz (top plot) and 15 pulses in 3 pulse bursts (bottom plot). Notice that the second pulse in the top plot and the first pulse in the second burst in bottom plot are relatively low. This may be due to the simmer boost circuit used on these lasers.

and have a damage threshold of 15 J/cm^2 in 20 ns. Hot spots in the beam exceed this damage threshold when the lasers are run at full power (3 J/pulse), and thus the lasers are run below full power to avoid damaging the mirrors. The focusing optic is an AR coated plano-convex lens with a focal length of 2.03 m at 1064 nm (CVI part number PLCX-50.8-1030.2-C-1064) and the same damage rating as the mirrors. The vacuum boundary windows are made of glass and set at the Brewster angle. The oval windows are sized such that they have a circular cross section of 3.8 cm when viewed in the direction of propagation of the laser. The entrance Brewster window is at the end of a 1 m stainless steel tube which ensures that the power density on the window remains low. The beam exits the machine through the pumping manifold[11] (or pumping duct) and another stainless steel tube and Brewster window. The beam then enters a beam dump consisting of two stages of absorbing glass and a stack of razor blades[12]. Bench tests have shown that approximately 90% of the laser beam power is absorbed by the first stage stage of the beam dump, which consists of two stacked pieces of blue green filter glass (Hoya G530 topped by Hoya C500). The remaining 10% of the laser light is reflected into a second stage of filter glass which absorbs most of the remaining light. Any reflected light from the second stage is dumped into a stack of closely spaced razor blades (see Figure 2.7) where the remaining energy is dissipated. It should be noted that in order to maximize the absorbed power at each stage, each piece of filter glass should be set at the appropriate Brewster angle for it's index of refraction. In practice the performance of the beam dump is not significantly effected by small deviations in this angle and therefore, for ease of construction, all of the surfaces were set to the same angle with respect to the incident laser beam. The beam line is fully enclosed by a set of light tight aluminum boxes connected by four inch diameter schedule 40 PVC tube which protects the optics from dust and damage as well as providing a layer of safety for MST personnel.

2.2.2 Alignment

Alignment of the two Nd:YAG laser beams in the near field is done with co-linear 670 nm laser diodes. However, due to the low reflectivity of the high power mirrors in this wavelength range, the red lasers become undetectable after the third turning mirror. One solution is to use high power dichroic mirrors (such as CVI YD-2037-45). However, these mirrors have a lower damage threshold than the single wavelength mirrors and the afore mentioned hot spots in the beam exceed this threshold at relatively low pulse energy. In order to overcome this, we use the dichroic mirrors with the co-linear alignment laser diodes for the initial optical alignment of the system. We can align these lasers a fiducial beam path set by the insertable integrating sphere (ISIS), shown in Figure 2.8, which resides in the pumping duct during normal MST operation but can be inserted vertically all the way to the geometric center of the machine. This integrating sphere has a pin hole so that the incident laser light is fiber coupled and the incident power is measured by a radiometer. The beam position is adjusted until the measured power is maximized along the entire path of the integrating sphere. (In practice this is rarely done as it time consuming and in general if both beams are passing cleanly through the vacuum vessel then the beam position can be optimized by maximizing the scattered signal during plasma operation.)

Once the positions of the the alignment diodes have been optimized, the position

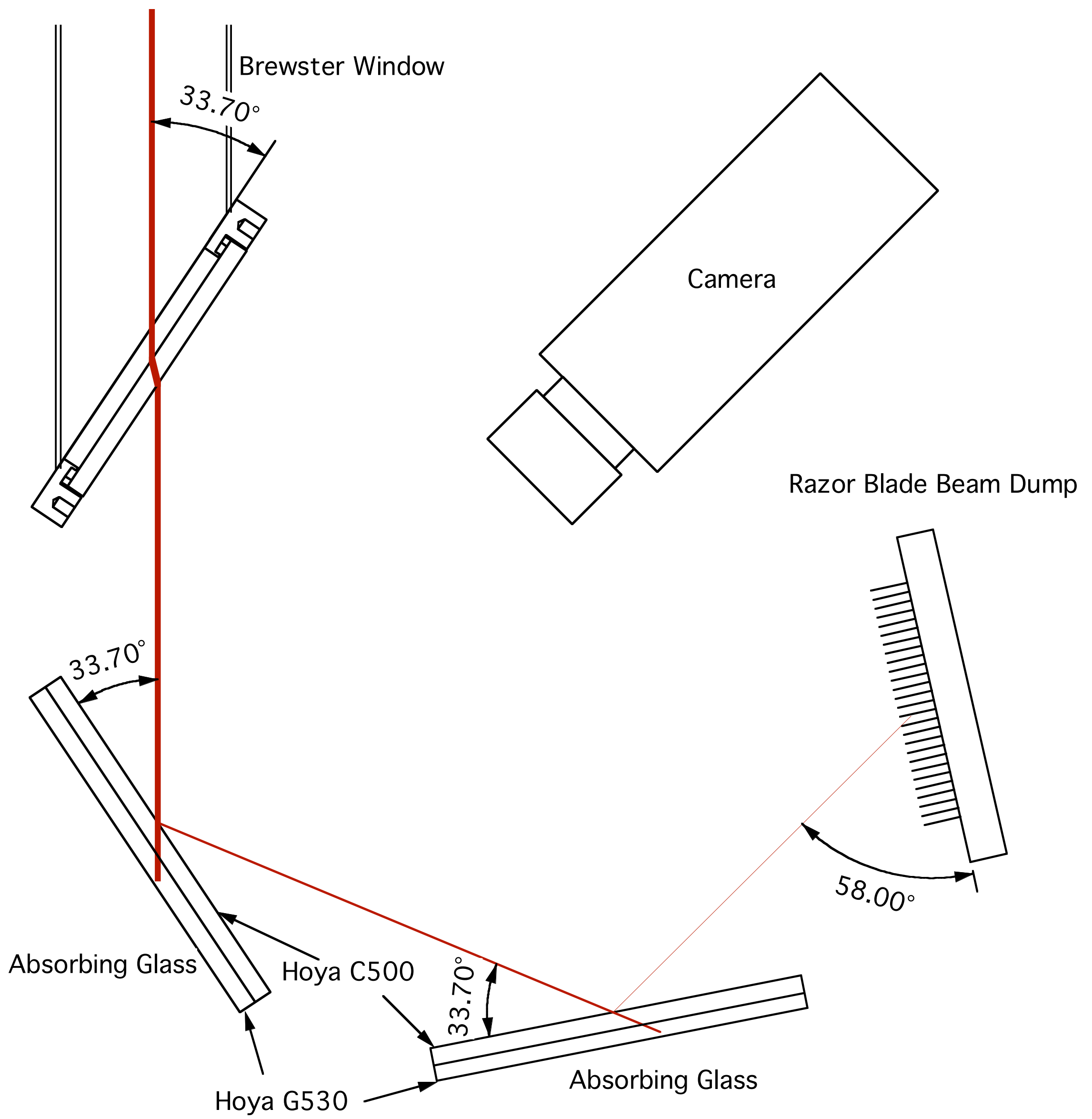

Figure 2.7: The beam dump consists of two stages of absorbing glass and a set of closely spaced razor blades that effectively absorbs the power from the two Nd:Yag lasers. A CCD camera monitors the beam position on the first stage of the beam dump.

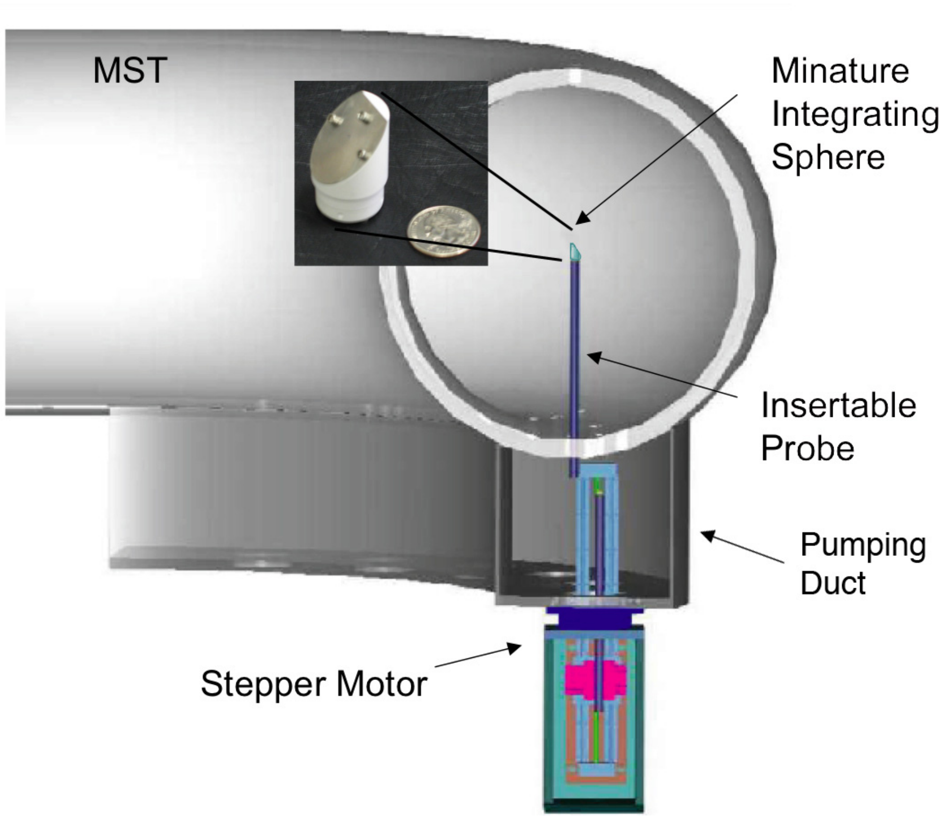

Figure 2.8: ISIS travels along the beam path in the vacuum vessel allowing fine alignment of both the fiber optics and the laser position. Figure courtesy of Mike Borchardt.

of the associated 1064 nm laser spots are recorded on three of the turning mirrors and the first stage of the beam dump using a set of four PULNIX TM-6702 CCD cameras. The lasers are fired at relatively low power to ensure the dichroic mirrors are not damaged. When the lasers are fired, a small amount (less than 1%) of the laser light passes through the mirror and is imaged by the CCD (Figure 2.9). Pictures of the beam are taken using a NI-IMAQ 1409 PCI frame grabber. Once the position of each beam is recorded for each camera, the first stage turning mirrors are swapped out with high power single frequency mirrors. The swap can not be done in a way that ensures there is no deviation in the beam position, and the first stage mirrors have the most

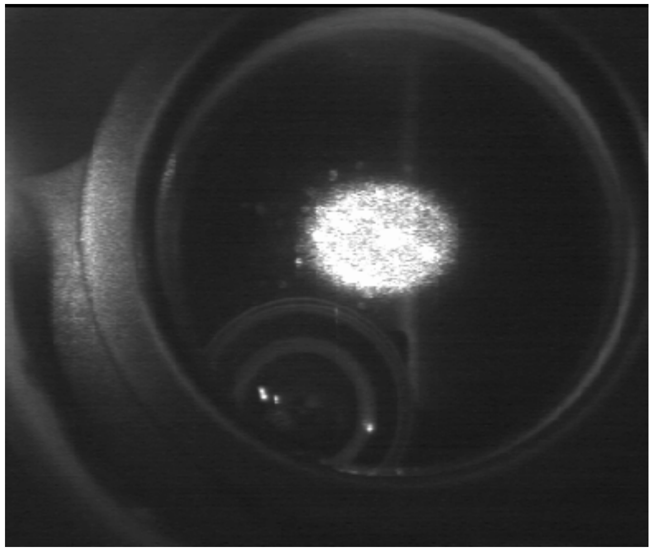

Figure 2.9: A small fraction of the total beam energy is lost at each turning mirror. This comparably small amount of light is easily detectable by the CCD cameras. For this example, only one of the two lasers was fired.

dramatic effect on the beam position. The alignment is then checked using the now much dimmer alignment lasers and then re-optimized using the camera system. The mirrors are swapped out one at a time and the beam position re-optimized until all the mirrors have been replaced with high power mirrors. Once this alignment is set, the beam position tends to be relatively stable and this "rough" alignment will not need to be repeated unless the beam line has been disturbed.

At the beginning of each day the beams are aligned to the recorded spots on the turning mirrors and the first stage of the beam dump. The beam alignment is set and maintained using New Focus Piezoelectric motorized mirror mounts (part number 8732). Each mirror mount in the beam line is controlled independently through a Labview program. This level of control is important because the beam position does drift throughout the day (generally most apparent in the afternoon). This effect is much more prevalent in the summer than in the winter. In the summer the beam will drift by two to four centimeters in the course of a day if left uncorrected, while it tends to be much more stable in the winter and thus it is believed that this drift is due almost entirely to nonuniform thermal expansion of the building. Currently the beam is monitored and adjusted manually at the beginning of the day, and then the alignment is maintained using an automated alignment program[13].

2.2.3 Laser Safety System

Since the Thomson scattering system uses Class IV lasers that are separated from the MST machine area, substantial design effort was put into the creation of an interlock system that would be both functional and adhere to the ANSI Z136 safety standard. The laser head is far removed from the MST control room and the main machine area entrance, thus it is impossible to immediately determine the operational status of the laser head. The only way to guarantee that laser light cannot reach the machine area while people are working is to power down the lasers by physically turning the power off to the system. This is impractical as the laser power supplies are on a different floor than the main control room and experimenters often need machine access between shots. Even if this were not the case, it would still cause unreasonable wear on the laser system to power cycle it often. In order to maximize the safety of MST personnel while maintaining a high degree of machine area accessibility and limiting the wear on the laser power supplies we have implemented a multilayered set of safety systems.

The first, and most straight forward, safety system is simply that the lasers are run in a single pulse mode as opposed to a continuous mode as with the Thomson scattering systems on other machines[14, 15]. This means that the lasers should not even fire unless actively triggered, thus creating an inherent layer of safety for this diagnostic. A second, passive, layer of safety is to ensure that the beam line is completely enclosed. This has been done using PVC piping to enclose the beam line and aluminum boxes to enclose the turning mirrors. Every access point to the beam line enclosure either requires tools to open or is interlocked with micro switches that cut the power to the laser head if opened. There are, however, windows that view the inside of the vacuum vessel and thus there is a possibility of light getting out of the machine with only a single reflection. For this reason a third layer of protection was added. This third layer of protection is a mechanical shutter in the beam line that automatically closes whenever the machine area is accessed, ensuring that no light from the laser room can pass down into the machine area. This way, if there was a spurious trigger to the laser system while people were in the machine area, there are two separate physical barriers in place to protect them from harm.

In order to ensure that the laser system can not be energized while people are in the laser room working, a search system has been implemented. For the laser to be able to fire, one must ensure that there is no one inside the laser room and then press a button inside indicating that they have completed a search of that area. Pressing the button bypasses the laser room door micro-switch for ten seconds. In that time, they have to exit the room, close the door behind them, and press the search complete button outside the room. Once the search is complete the lasers can be powered on. As part of the standard operating procedure the door to the laser room is locked after the search is completed and, when the lasers are powered on, a white flashing light over the door indicates that there is a possibility of laser emission inside the laser room. If, despite these warnings, the door is opened, the lasers immediately power down.

In order to keep from losing functionality with the increased safety we have added a controlled bypass to the safety system. In this mode, the main beam line is closed off using the mechanical shutter and, as part of the bypass procedure, a metal plate is placed in the beam line adding a second barrier. With the beam line enclosed and blocked off we can safely run the lasers for maintenance and beam profile diagnosis without the need to restrict access to the MST machine area.

2.2.4 Light Detection System

2.2.4.1 Collection Optics

One of the design goals of MST was to minimize field errors due to currents flowing in the conducting shell[11]. Portholes generate field errors and the maximum acceptable field error sets the maximum porthole size at 11.4 cm in diameter. For reference, the minor radius of MST is 52 cm and the major radius is 150 cm. This size constraint poses a significant challenge for the collection optics. In order to maximize the entendue, the inner wall of the MST was chamfered to reduce vignetting for the core and edge positions (see Fig. 2.10). Even though this porthole is relatively small, the field error generated by it is still large enough that a significant interaction of the plasma with the first element of the lens was observed. In order to minimize damage to the lens a limiter was installed around the porthole. The vacuum window is part of the lens assembly and, during operation, the lens itself is moved into position past a

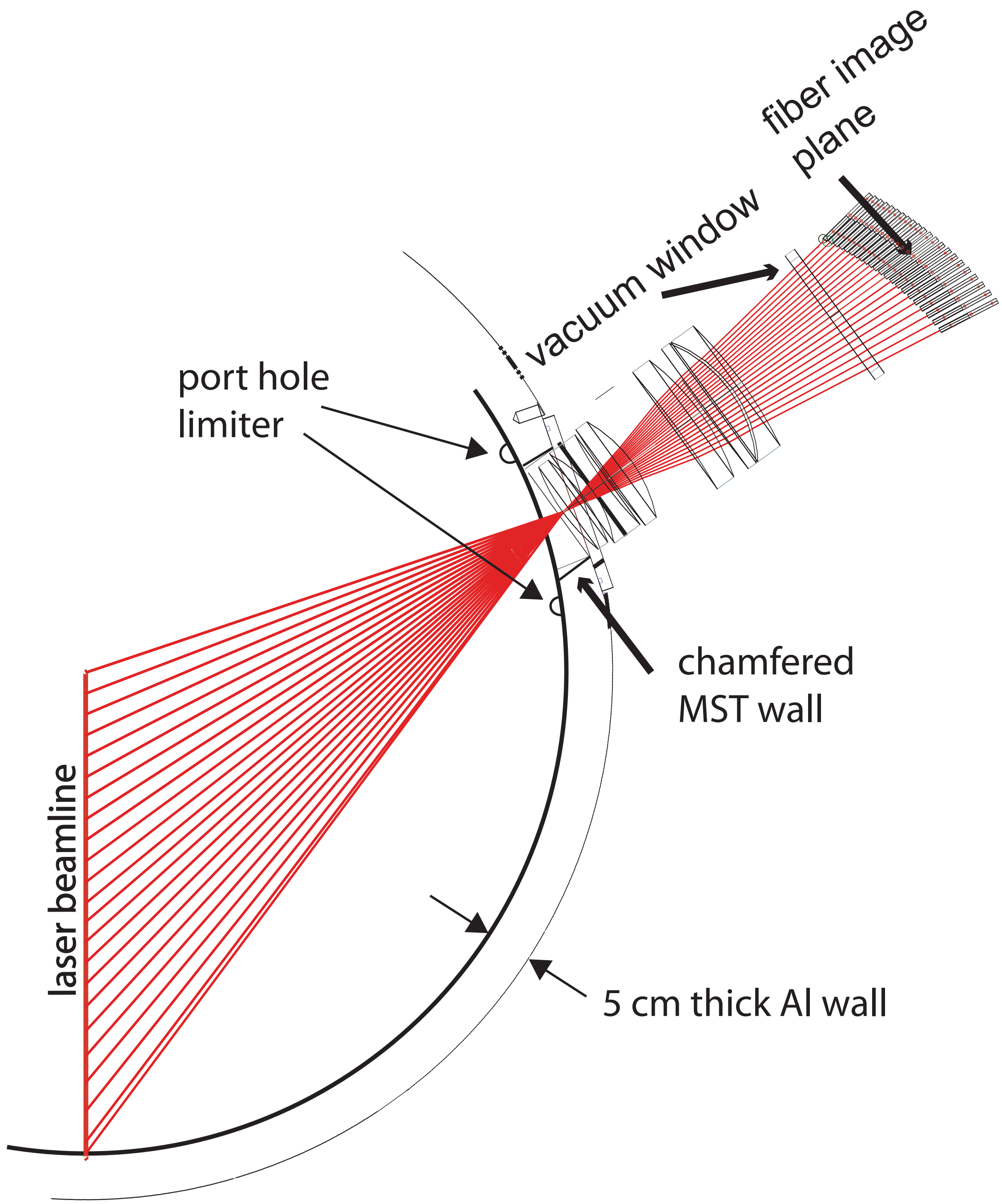

Figure 2.10: The vacuum vessel wall was chamfered to reduce vignetting of the core and edge positions. Most of the material that needed to be removed was on the bottom, inner part of the port, but there was some removed from the top part of the port as well. Also note the limiter, which was installed around the port to minimize plasma-lens interaction.

gate valve. Two bellows are used to maintain a neutral volume change to keep vacuum forces low on the movable part of the assembly. A double pillow block traverse is used (Fig. 2.11). The lens is a seven element split-triplet design, shown in Fig. 2.12. It

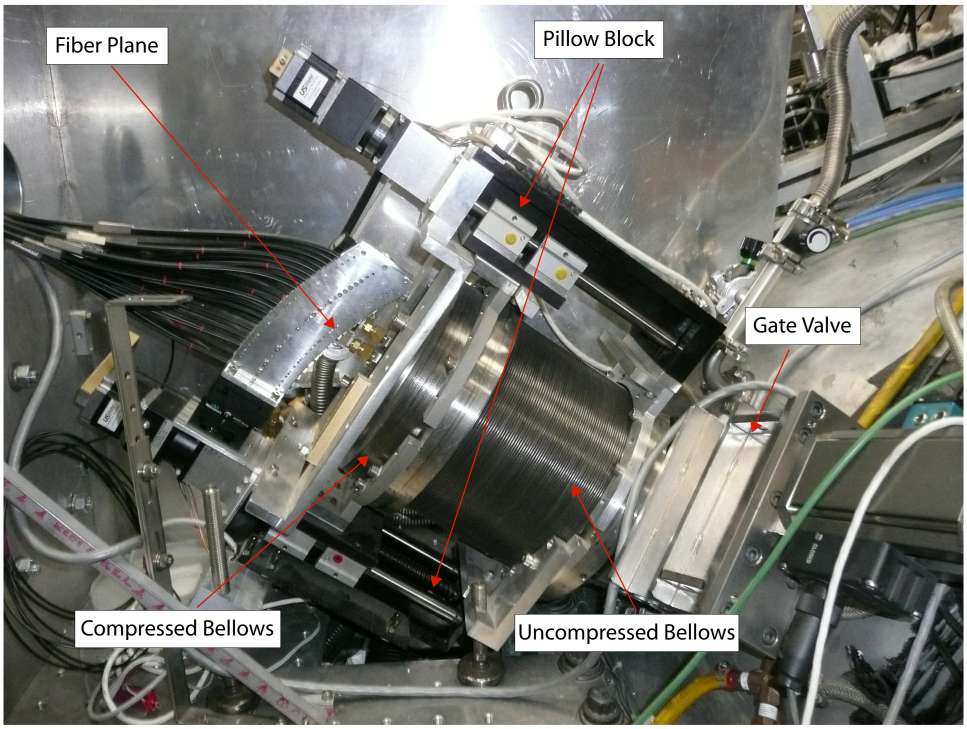

Figure 2.11: A pair of bellows are used to allow the lens to move into position without changing the volume under vacuum.

has a front element aperture of 102 mm diameter, an overall transmission of > 0.8 from 750 nm to 1064 nm, an r.m.s. spot radius of < 100 μm, an effective focal length of 214 mm, and demagnification that ranges from 4.2 at the edge to 2.7 in the core. The strands of each fiber bundle are arranged to have a rectangular front face that is 4.8 mm tall which, given the demagnification of the lens, translates to about a 2 cm radial extent in the edge and about 1.3 cm in the core[6].

The Thomson scattered light is collected using 21 incoherent fiber bundles. The

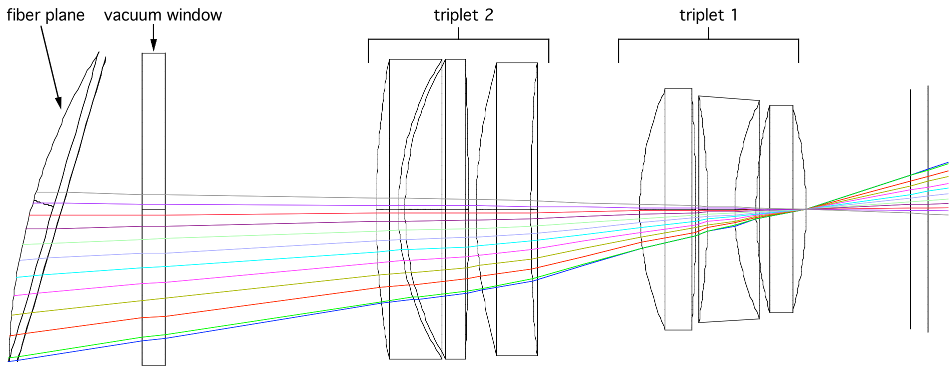

Figure 2.12: The seven element lens was designed by Wright Scientific to optimize collected light along the beam path given the porthole size constraint.

fiber bundles occupy 21 of the 34 possible positions in the fiber optic mount, which is curved to match the image plane of the lens (Figure 2.11). Each fiber bundle is made from 119 fibers each of which has as core diameter of 0.210 mm, giving a total light collecting area of 4.1 mm^2. Each fiber is 18 m long and the square imaging end (4.8 mm $\times$ 1.7 mm active area, fiber jackets not stripped) converts to a 6.35 mm diameter plug (3.1 mm active diameter, jackets not stripped). The fiber bundles run parallel to the beam line back to the laser room where they are coupled to a set of polychromators.

The position of the fiber optic mount is adjusted in order to place it on the image plane. This is done in two stages. First, a visible laser (usually a 632 nm HeNe) is coupled to ISIS such that light is emitted from the pinhole. This light source creates a visible spot on a ground glass concave segment that has the same curvature as the fiber optic mount and is mounted to the translation stage for the fiber optic mount. The position of the ground glass is adjusted until it matches the image plane of the lens. Once the position of the ground glass matches the image plane fairly closely it is replaced with the fiber optic mount and the visible laser is replaced with the 100 mW 1064 nm CW laser. At this point we simply adjust the fiber position until the signal level in our light detection system is maximized for all 21 fiber optics.

2.2.4.2 Polychromators

MST's substantial range of operating space requires a very versatile light detection system. Furthermore, the desire to use this system for turbulence studies requires that it have high time resolution (< 200 ns). The chosen system is a set of polychromators with spectral channels equipped with avalanche photodiodes (APDs). There are two outputs on each APD amplifier module that can be digitized. The so called DC signal, which is the direct amplified signal from the APD, and the AC signal, which this the DC signal with a 100 ns rolling subtraction. Currently, only the DC output of each APD is analyzed to determine the amount of scattered light in each channel. Directly digitizing the DC signal allows rapid changes in the background light, which often occur near sawteeth, to be correctly accounted for. For all the work presented in this thesis, the DC signal was digitized by a set of 1 G-sample per second Acqiris digitizers[7]. While these digitizers have high time resolution, they only have an 8 bit depth. In order to account for the large swings in background light, some of the channels had to be assigned a large dynamic range giving very little bit resolution to the actual laser pulse. In 2009, the system was upgraded with a set of Stück digitizers. These are 100 MHz, 16 bit digitizers with a fixed dynamic range that covers nearly the entire available range of outputs of the APD amplifier modules (0 to -2.5 V). These digitizers have been swapped with the Acqiris digitizers to record the DC signal and we have found they they have sufficient time resolution to be used in determining the electron temperature in the same way as the old system. The AC signal is now digitized by the Acqiris digitizers. In the near future, the DC signal will be used to find the background light level while the AC signal will only be sensitive to the Thomson scattered photons generated by the laser pulse. The combination of these two systems should improve the accuracy and decrease the uncertainty in the the electron temperature measurement.

Thomson scattered light is coupled to 21 polychromators each used to measure a separate radial location in the plasma. The polychromators are the same as those used on DIII-D[16], General Atomic Polychromator Model GAPB-1064-4-1K. Fifteen are equipped with 4 spectral channels over a range of 868 nm to 1065 nm (see figure 2.13 for a schematic view of one of these polychromators). The remaining six are fully equipped with 8 spectral channels over a range of 715 nm to 1065 nm. Each spectral channel is equipped with a General Atomics APD module. The first channel in each polychromator measures scattered light at the laser wavelength (1064 nm +/- 1.5 nm) and is currently overwhelmed by stray light. Therefore, there are 3 and 7 spectral channels available for electron temperature measurements. Transmission curves have been measured over the appropriate ranges for each polychromator[6]. The 4 channel polychromators are designed to be able to measure temperatures between 10 eV and 2 keV, whereas the 8 channel polychromators can measure electron temperatures up to 10 keV. In addition to the increased temperature range the 8-channel polychromators also have the capability of distinguishing non-Maxwellian temperature distributions that have been observed in other machines[17] and may be present in certain MST plasma conditions. In the near future all the remaining 4 channel polychromators will be upgraded to 6 channels to extend the range of temperatures they are sensitive to up to 5 keV.

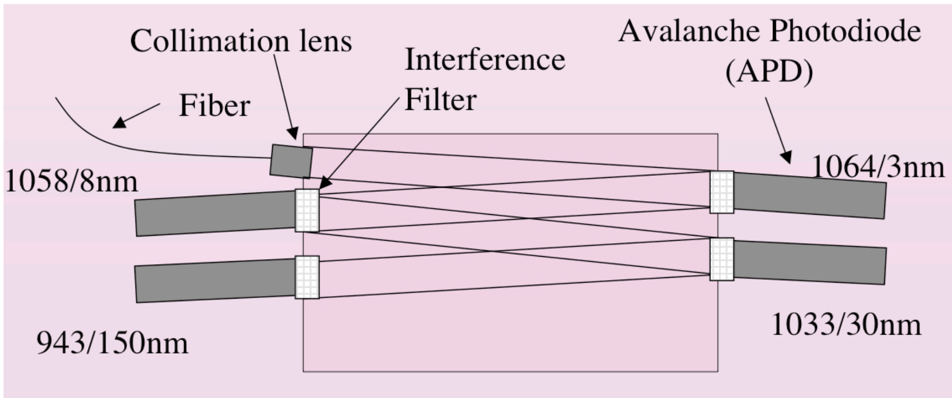

Figure 2.13: Schematic view of the 4 channel polychromator layout along with the wavelength range of each of the notch filters. Figure courtesy of H.D. Stephens.

2.2.4.3 Detectors

Each polychromator spectral channel is equipped with a PerkinElmer C30956E avalanche photodiode (APD) for light detection. Two different amplifier modules constructed by General Atomics are used[18]. The first amplifier module (1999 construction) is used with all 4 channel polychromators and three of the six 8 channel polychromators. The remaining three polychromators use the second amplifier module (2006 construction).

The two amplifier modules are similar in design but have key differences in construction and operation. These modules are described in detail in ref. [19] but, for completeness, a summary is presented here. Both amplifiers require +/-8 V input power, both have a pulsed and DC output and a four step DC gain selection (again, currently only the DC coupled output is used, though the combination of both AC and

DC signals will soon be implemented). Several differences in the two constructions exist. The first difference is the op amp used in the input stage; the 2006 construction amplifiers use LMH6624 (low-noise voltage-feedback surface-mount), whereas the 1999 construction amplifiers use CLC425 (low-noise voltage-feedback DIP, with adjustable supply current/bandwidth). As originally constructed the 2006 modules had a higher bandwidth and a gain of about 2.2 times the 1999 modules, though noise pickup and oscillation in the 2006 modules made operation difficult. Modifications were made to the 2006 modules to lower the gain, shield noise pickup and stabilize oscillations. A new set of modules are currently under development which are very similar to the first generation modules. Once these are complete, the entire system will be upgraded to 6 channels, extending the range of temperatures the system is sensitive to.

2.2.4.4 Environmental Control and Monitoring

The gain of the APDs is highly dependent on temperature and applied bias voltage. For example at 22° C a temperature change of just 0.5° C can change the gain by 1%. Similarly, a 5 V deviation in the applied bias voltage from the recommended voltage will change an APD's gain by approximately 6%. It is therefore important to both monitor and keep constant the temperature and applied bias voltage during calibration and during regular operation.

The detectors are located in an air-conditioned clean room to keep the ambient air temperature and humidity constant. During regular operation the APD modules are mounted on polychromators that are water cooled with an external chiller. The APD modules are then cooled by conduction with the polychromators. The temperature of each polychromator is monitored with a thermocouple attached to the top of the polychromator box. Individual polychromator temperature measurements are recorded with a Labview program and can be checked throughout any day the system is in operation for consistency. These measurements show that the temperature variation of any given polychromator is $< 0.12°$ C with many below $0.06°$ C.

Bias voltage for the APDs is supplied with a serial combination of power supplies located externally to the clean room. The bias voltages are fed through to the detector modules via panels in the ceiling. Each panel has voltages between 275 V and 425 V in 5 V increments with the bias voltage for each APD fixed inside the panel. The highest bias voltage is monitored on each panel for consistency. A change in any 5 V increment will be represented as a change in the maximum bias voltage.

The APD amplifier modules require +8 V and -8 V inputs. If these drop below a certain threshold the amplifiers do not work. These inputs are also provided by a power supply external to the clean room and fed thru the ceiling via the same panels and monitored at each panel. It should be noted that at present these are checked sporadically, but are not yet regularly monitored or recorded.

2.3 Calibration and Data Processing

The calibration of the system is talked about in detail in references [6, 19] so, once again, only the highlights will be discussed here. Multiple parts of the system must be calibrated in order to obtain an accurate measurement and uncertainty estimate. First the APD's must be absolutely calibrated to determine the gain, quantum efficiency (QE), and noise enhancement factor F, which describes the noise above Poisson statistical noise. This has been done by absolutely calibrating one of the APD modules and cross calibrating the rest of the modules to that one. While this calibration is generally only done for at a single wavelength, the wavelength dependence has also been checked and is small over the range of interest. Once the absolute calibration has been done for each APD module, each polychromator must be calibrated to exactly determine the transmission function for each notch filter in the polychromator. This is done using the combination of a white light source which emits light at fairly flat intensity across a large wavelength range, and a monochromator which selects out a narrow bandwidth of that wavelength range at a time. This method replaces an older method which used an optical parametric oscillator (OPO) which has a broad, tunable wavelength. The OPO system was originally used for spectral and in-situ calibration, but turned out to produce a large range of pulse intensities at each wavelength. As the OPO crystal aged, this pulse to pulse variation increased and calibration using this source became unnecessarily challenging and is no longer used. Once the APD and polychromator modules are calibrated, the number of photons in each wavelength bin, N, as well as the uncertainty in that number of photons $\sqrt{N * F * QE}$, can be accurately determined.

A separate, but also critical, calibration that must also be done is to determine the physical location of the scattering volume inside the MST vacuum vessel. This "radial" calibration is done using the ISIS system described earlier. Here a 100 mw continuous output 1064 nm diode pumped Nd:YVO_4 laser (Lasermate GMF-1064-100FBC2) is fiber coupled into the integrating sphere in the ISIS system and scanned up the beam path at a known rate. The location of a light gate at the bottom of MST is set such that its output changes state when the pinhole in the integrating sphere is level with the bottom of MST (r/a=1). By digitizing both the light gate signal and the APD signal from the modules centered on the laser wavelength, along with knowledge of the velocity of the integrating sphere from the ISIS stepper motor, the exact radial position and extent of each scattering volume can be determined. An example of the result of this calibration is shown in figure 2.14. This information is obviously important for understanding the shape of the temperature profile, but it also has a nontrivial contribution to the expected spectral density function through the scattering angle θ as described by equation 2.3 at the beginning of the chapter. Since the collection optics for all 21 radial points are in one location, the scattering angle changes from one point to the next. With the scattering angle determined the electron temperature can accurately be found.

One final consideration that should be made is that the pitch of the magnetic field in the RFP also changes dramatically with radius, so this system samples a mix of the parallel and perpendicular temperatures. This mix changes with radius from nearly perpendicular in the core to a mix of parallel and perpendicular at the edge. Some work has been done to determine the impact of this and it is generally expected that in standard plasmas the temperature is sufficiently isotropic that this geometric effect is unimportant.

This brings us to the data processing. The DC voltage trace recorded for each APD is fit to a characteristic pulse shape for that APD. The first step in this process is to identify the exact time of the laser pulse in the digitized signal. This is done by summing the 3 or 7 voltage traces for the 4 or 8 channel poly respectively, and then finding the first index above a threshold value. This has proven to be a very robust way of finding the time of the pulse as long as the digitization time window is sufficiently

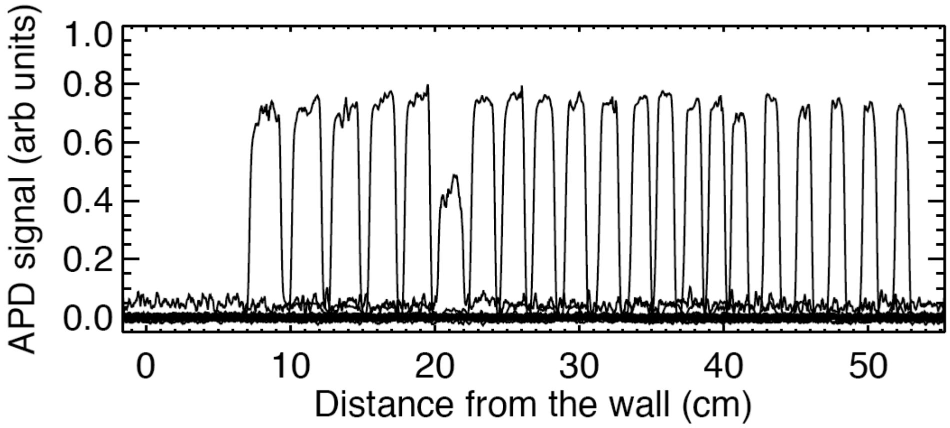

Figure 2.14: APD signal vs vertical position of each of the 21 fiber optic views. Note that the x-axis is the vertical distance from the wall rather than radius. The plasma radius is nearly continuously covered from about 9 cm in all the way to the geometric center of the machine.

small (generally 1 to 2 μs). The background is then removed by performing a quadratic fit to the signal 100 ns before and after the scattered light pulse, which has a width of about 100 ns. Once the background is removed, the remaining voltage trace is fit to a characteristic pulse shape. The fitting constant that multiplies the characteristic pulse is directly proportional to the number of scattered photons collected by the APD. This method very effectively shields the resulting photon count from electronic noise[7].

Once the number of photons per wavelength bin (i.e. per APD) is known, the electron temperature and density can be determined. This is done by performing a two parameter fit using the Selden equation (Equation 2.3) as a forward function. Again, the Selden equation provides an approximation for the number of Thomson scattered photons emitted for a given temperature and density as a function of wavelength assuming a relativistic Maxwellian distribution. This approximation has been shown to be very accurate over the range of temperatures that this diagnostic is sensitive to. In fact, numerical work done by Matoba, *et al.*, in reference [2] shows good agreement up to 100 keV, though recent work done at MST suggests that Matoba, *et al.*, contained an error and the approximation actually has an error greater than 5% above 5 keV[20]. None the less, this approximation is very good for the temperature range of interest in MST, which is always below 3 keV and, for this work, is generally below 400 eV. The system is currently not calibrated for density measurements so only a relative density can be determined. Some attempt to cross calibrate this diagnostic with other density diagnostics has been made, but has thus far proven impossible due to variations in both laser power and alignment. However, the density is functionally just a scale factor in the fitting procedure, and thus the temperature is unaffected by this lack of calibration. The most likely temperature that would yield the data from the polychromators is found using a Baysean method described in [21, 19].

2.4 Time Evolution of the Electron Temperature Profile

With this apparatus and analysis we are now able to measure the electron temperature profile as a function of time in a single shot. Figures 2.15 and 2.16 show the time evolution of the electron temperature profile in three different plasma types. Figure 2.15 shows the temperature for an enhanced confinement period as well as a standard plasma at the same low density high current plasmas. Figure 2.16 shows the same information for a PPCD plasma at 380 kA and moderate density. While these figures are a striking example of the kind of high quality temperature data this system can now produce, data from multiple shots can also be ensembled together to give the temperature evolution at high time resolution. Figure 2.17 shows the temperature evolution at a core and edge point for a large ensemble of 400 kA shots. The error

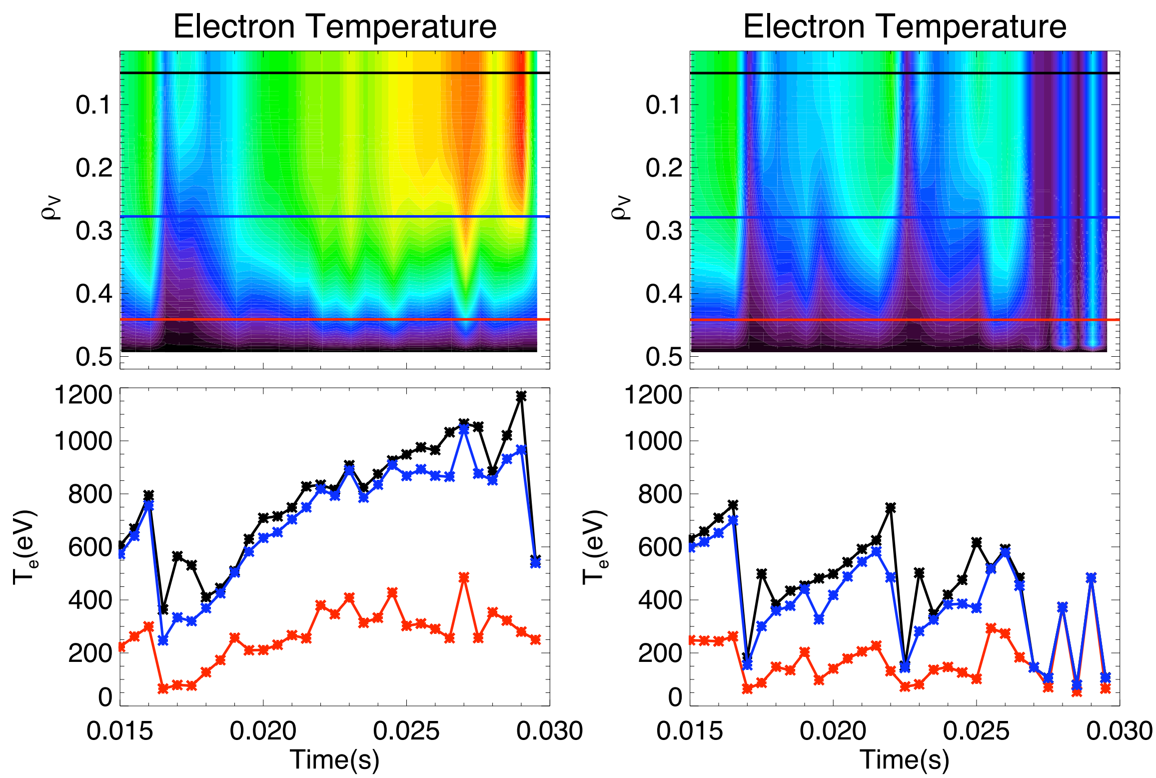

Figure 2.15: Temperature evolution for a low density enhanced confinement (left side) and low density standard (right side) at 470 kA. The top plots are contour plots and show the time evolution of the temperature profile while the bottom plots are the time evolution of the temperature at three points marked by the horizontal lines on the top plots.

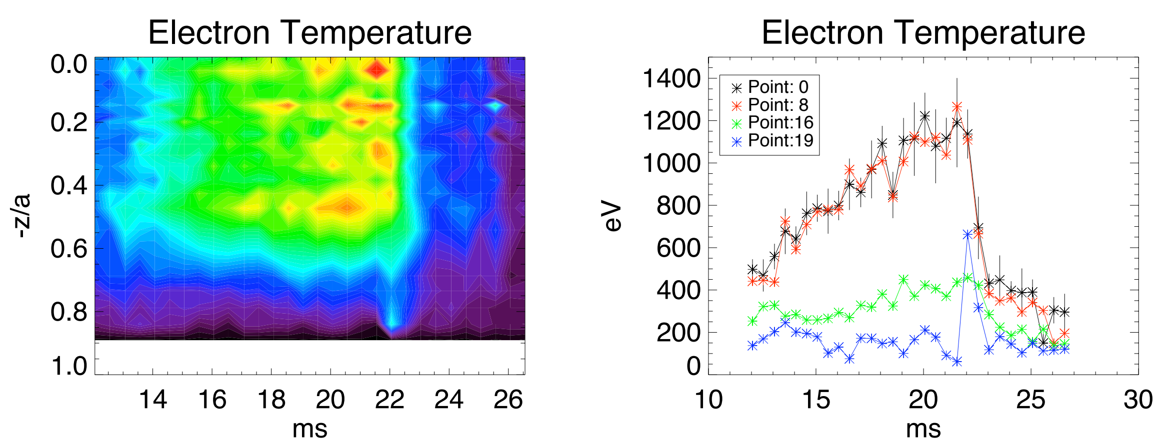

Figure 2.16: Contour plot and time evolution for a 380 kA PPCD discharge. The PPCD period ends at 22.5 ms.

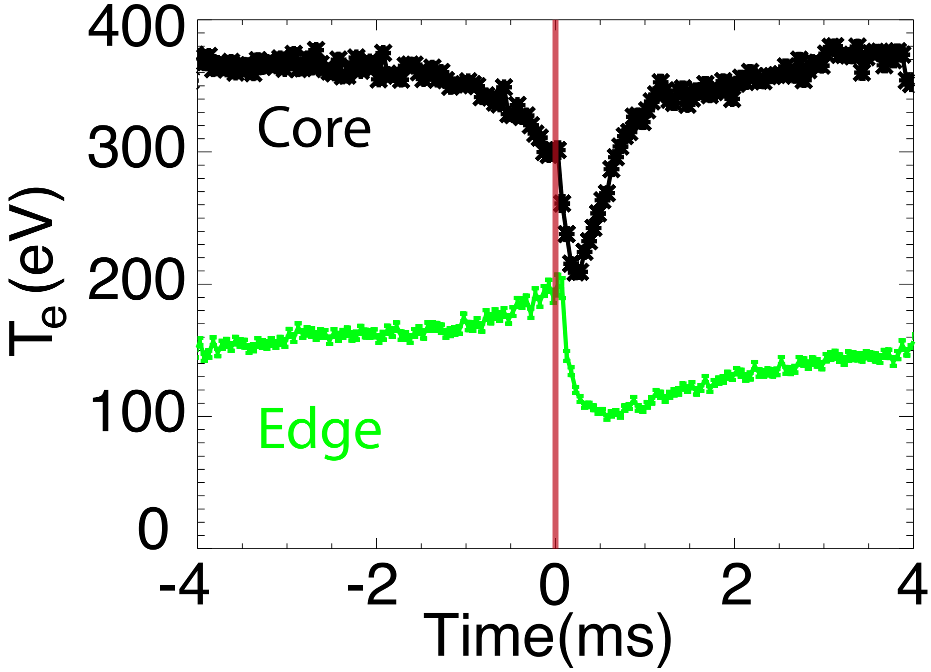

Figure 2.17: Electron temperature evolution for a core (black) and edge (green) point for a large ensemble of shots. The error bars shown here represent the standard error $\sigma/\sqrt{N}$ for the ensemble of data values at each time.

bars shown depict the standard error of the mean of the ensemble. It is this type of ensembled data that features the most prevalently in this thesis. The details of the ensembling process and a discussion of the profile evolution through a sawtooth event will appear in the next chapter.

REFERENCES

[1] Selden, A. C. Simple analytic form of the relativistic Thomson scattering spectrum. *Physics Letters A* **79**(5-6), 405 – 406 (1980).

[2] Matoba, T., Itagaki, T., Yamauchi, T., and Funahashi, A. *Japanese Journal of Applied Physics* **18**, 1127–1133 (1979).

[3] Selden, A. C. Simple analytic form of the relativistic Thomson scattering spectrum. *Culam Laboratory Report* (CLM-R220) (1982).

[4] Chapman, B. E., Chiang, C.-S., C., P. S., Sarff, J. S., and Stoneking, M. R. Strong E x B Flow Shear and Reduced Fluctuations in a Reversed-Field Pinch. *Phys. Rev. Lett.* **80**(10), 2137–2140 (1998).

[5] Reusch, J., Borchardt, M., Den Hartog, D., Falkowski, A., Holly, D., O'Connell, R., and Stephens, H. Multipoint Thomson scattering diagnostic for the Madison Symmetric Torus reversed-field pinch. *Review of Scientific Instruments* **79**(10), 10E733 (5 pp.) Oct. (2008).

[6] Stephens, H. D., Borchardt, M. T., Den Hartog, D. J., Falkowski, A. F., Holly, D. J., O'Connell, R., and Reusch, J. A. Calibration of a Thomson Scattering Di-

agnostic for Fluctuation Measurements. *Review of Scientific Instruments* **79**(10), 10E734 (5 pp.) Oct. (2008).

[7] O'Connell, R., Den Hartog, D., Borchardt, M., Holly, D., Reusch, J., and Stephens, H. Optimizing a Thomson scattering diagnostic for fast dynamics and high background. *Review of Scientific Instruments* **79**(10), 10E735 (5 pp.) Oct. (2008).

[8] SpectronLaser. User Manual for SL858g Nd:YAG Laser System.

[9] Den Hartog, D. J., Ambuel, J. R., Borchardt, M. T., Reusch, J. A., Robl, P. E., and Yang, Y. M. Pulse-burst operation of standard Nd:YAG lasers. *Journal of Physics: Conference Series* **227**(1), 012023 (2010).

[10] Den Hartog, D. J., Ambuel, J. R., Borchardt, M. T., Falkowski, A. F., Harris, W., Holly, D. J., Parke, E., Reusch, J. A., Robl, P. E., and Yang, Y. M. Pulse-burst Laser Systems for Fast Thomson Scattering. *Review of Scientific Instruments* **81**(10), 10D513 (2010).

[11] Dexter, R. N., Kerst, D. W., Lovell, T. W., Prager, S. C., and Sprott, J. C. The Madison Symmetric Torus. *Fusion Technol.* **19**(1), 131–139 (1991).

[12] Den Hartog, D. J. and Cekic, M. *Meas. Sci. Technol.* **5**, 1115–1123 (1994).

[13] Yang, Y. M. Stochastic Transport in PPCD Discharges. Masters of science, University of Wisconsin at Madison, 1150 University Ave., Madison, WI, 53706, (2010).

[14] Carlstrom et al., T. N. *Rev. Sci. Instrum.* **63**(10), 4901–4906 (1992).

[15] LeBlanc, B., Bell, R., Johnson, D. W., Hoffman, D. E., Long, D. C., and Palladino, R. W. *Rev. Sci. Instrum.* **74**(3), 1659 (2003).

[16] Carlstrom, T., DeBoo, J., Evanko, R., Greenfield, C., Hsieh, C.-L., Snider, R., and Trost, P. *Rev. Sci. Instrum.* **61**(10) (1990).

[17] Pieroni, L. and Segre, S. *Phys. Rev. Lett.* **34**(15), 928–930 (1975).

[18] Hsieh, C., Haskovec, J., Carlstrom, T., De Boo, J., Greenfield, C., Snider, R., and Trost, P. *Rev. Sci. Instrum.* **61**, 2855 (1990).

[19] Stephens, H. *Electron Temperature Structures Associated With Magnetic Tearing Modes in the Madison Symmetric Torus*. PhD thesis, University of Wisconsin at Madison, (2010).

[20] Parke, E. private conversation.

[21] Stephens, H. D., Den Hartog, D. J., Hegna, C. C., and Reusch, J. A. Electron thermal transport within magnetic islands in the reversed-field pinch. *Physics of Plasmas* **17**(5), 056115 (2010).

Chapter 3

The Sawtooth Evolution of the Magnetic Equilibrium in 400 kA Standard MST Discharges

The main goal of this work is to understand the dynamics and the nature of the heat transport in high current discharges in MST. New measurements of the electron temperature profile dynamics, made possible by the Thomson scattering system described in the last chapter, are critical to this understanding, but they tell us little about the heat source for the plasma. In this chapter, the radial profiles of the sources and sinks of heat are found by reconstruction of the magnetic equilibrium using a combination of data from many diagnostics, including the Thomson scattering diagnostic. As this process is involved, and the details of it are important for the final result, it will be described in some detail. This information is then used to determine the global and local heat transport throughout the canonical (i.e. ensemble averaged) sawtooth event in 400 kA standard MST discharges.

This chapter is divided into four sections. The first is a brief discussion of different models for the magnetic equilibrium of the RFP. In particular, the implementation of a two parameter model in the equilibrium reconstruction code MSTFit[1, 2] will be discussed. The second section discusses the sawtooth evolution of the reconstructed equilibrium. This section also includes a discussion of the sawtooth ensembling techniques used to gather all the data needed for the reconstructions and the evolution of the kinetic profiles. With the equilibrium evolution in hand, global confinement properties of the MST plasma as well as the local electron thermal diffusion as a function of time can be computed and are presented in the third section. Finally, a discussion of these results are presented in the last section.

3.1 Modeling the Magnetic Equilibrium in the RFP

The equilibrium magnetic fields can, in some plasmas, be measured directly using probes. In practice, however, direct measurements of high temperature plasmas with probes is impossible due to plasma probe interactions which destroy the probe and, in many cases, completely degrades the plasma as well. It is for this reason that non-invasive diagnostics, such as the Thomson scattering system described earlier, are so necessary for understanding the plasma behavior. Given that direct measurement is so often impossible and non-invasive measurements are generally limited, it is useful to have a model for the MHD equilibrium which synthesizes a diverse collection of measurements and fills in the information that is not measured. In the RFP, there are many models that describe the basic features of the experiment to varying degrees of success. These include several cylindrical models of varying complexity as well as the toroidal model implemented in MSTFit for fitting the equilibrium using all available data from the experiment.

3.1.1 Cylindrical Equilibrium Models

There are many models for the magnetic equilibrium in the RFP that describe the observed magnetic field and current density profiles in experiment. The first model that showed field reversal was the that of J.B. Taylor in which he posited that the global magnetic helicity should be conserved and that the MHD activity in the plasma would tend to drive it toward a minimum energy state, which has become known as the Taylor state[3, 4]. This equilibrium is described by $\nabla \times \mathbf{B} = \lambda \mathbf{B}$ (where λ is uniform in space) which, when evaluated in cylindrical coordinates, yields Bessel function solutions for the axial and poloidal magnetic field profiles. For this reason this model is generally referred to as the Bessel Function Model (BFM). The constant λ can be defined in terms of the reversal parameter (Θ) as $\lambda/B_0 = 2\Theta/a$ where a is the minor radius, Θ is the pinch parameter, and B_0 is an overall scale factor. One prediction of this model that is inconsistent with measurement is a nonzero current density at the plasma boundary. To capture this observation, several modifications to the Bessel Function Model were made assuming that the majority of the plasma maintained a minimum energy state, but that at some point in radius it deviated from this state in order to match the observed behavior at the boundary. These models include the Modified Bessel Function Model (MBFM), the Polynomial Function Model (PFM), and the Modified Polynomial Function Model (MPFM). These three models all have the property that they are fully specified by two easily measured global parameters, the reversal parameter $F = \frac{B_\phi(a)}{\langle B_\phi \rangle}$ and the pinch parameter $\Theta = \frac{B_\theta(a)}{\langle B_\phi \rangle}$. In the experiment, however, the magnetic equilibrium is not necessarily fully relaxed over the bulk of the plasma.

An alternative to this class of relaxed state models is the so called Alpha Model which allows the plasma to be in a state that is not relaxed across the bulk of the plasma. This model also takes into account pressure effects, but adds another required measurement in the process (see equation 3.1).

$$\nabla \times \mathbf{B} = \lambda\left(r/a\right)\mathbf{B} + \frac{\beta_0}{2B^2}\mathbf{B} \times \nabla P \tag{3.1}$$

Here, $\lambda(r/a) = \lambda_0\left(1 - (r/a)^{\alpha}\right)$ and, if a constant β_0 is assumed, then this again can be mapped directly to F and Θ. This model connects the measured variation in F and Θ throughout a discharge to a peaking and flattening of the current density through the sawtooth cycle. The understanding that develops is that the ohmic drive circuit causes the current density to peak at the magnetic axis and quasi-period sawtooth events flatten the current density back out, bringing the plasma closer to its minimum energy state.

3.1.2 Grad - Shafranov Equilibrium

The models discussed above go a long way to understanding and quantifying the equilibrium evolution of the RFP plasma, but are still limited by the fact that they are all cylindrical models and only dependent on edge measurements of $\mathbf{B}$. While this last point is generally considered a feature, it ignores the fact that a wide array of magnetic field profiles can yield the same edge measurements[2]. A better, though somewhat more complex solution is to use internal and external measurements to constrain a combination of Maxwell's equations and force balance $\mathbf{J} \times \mathbf{B} = \nabla P$ (assuming an axisymmetric toroidal plasma), to find the ideal magnetohydrodynamic equilibrium. The resulting equation that describes this equilibrium is called the Grad-Shafranov equation[5, 6]. This method reduces the problem to the specification of two radial flux functions, $F(\psi)$ and $P(\psi)$ (ψ is the poloidal flux), which cannot be mapped directly to edge or global measurements. Note that $F(\psi) = RB_\phi(\psi)$ and is not related to the reversal parameters F used in the cylindrical models. Note also that $F(\psi)$ is often written as $I(\psi)$ in the literature as $RB_\phi = \mu_0 I_\theta / 2\pi$, but for historical reasons the $F(\psi)$ notation is used here. Although these flux functions cannot be mapped directly to measurements, the most likely value for these functions can be found by simultaneously fitting many of the internal and external measurements made in MST. This fitting method has been implemented in the MSTFit code and is referred to as reconstructing the equilibrium[1]. Figure 3.1 shows the locations of the diagnostics used in MSTFit in a poloidal cross section. These diagnostics are spread around the machine toroidally.

This code finds the axisymmetric magnetic equilibrium by solving the Grad-Shafranov equation (equation 3.3) and then comparing all of the signals that can be predicted from the magnetic equilibrium to measurements made in MST. The free parameters in the fit are then varied and a non-linear least squares minimization using the Amoeba algorithm[7] is then performed to find the most likely magnetic equilibrium given the measurements. The free parameters in this case specify the flux functions F and p in the current density equation:

$$J_\phi = \frac{2\pi F F'}{\mu_0 R} + 2\pi R P' \tag{3.2}$$

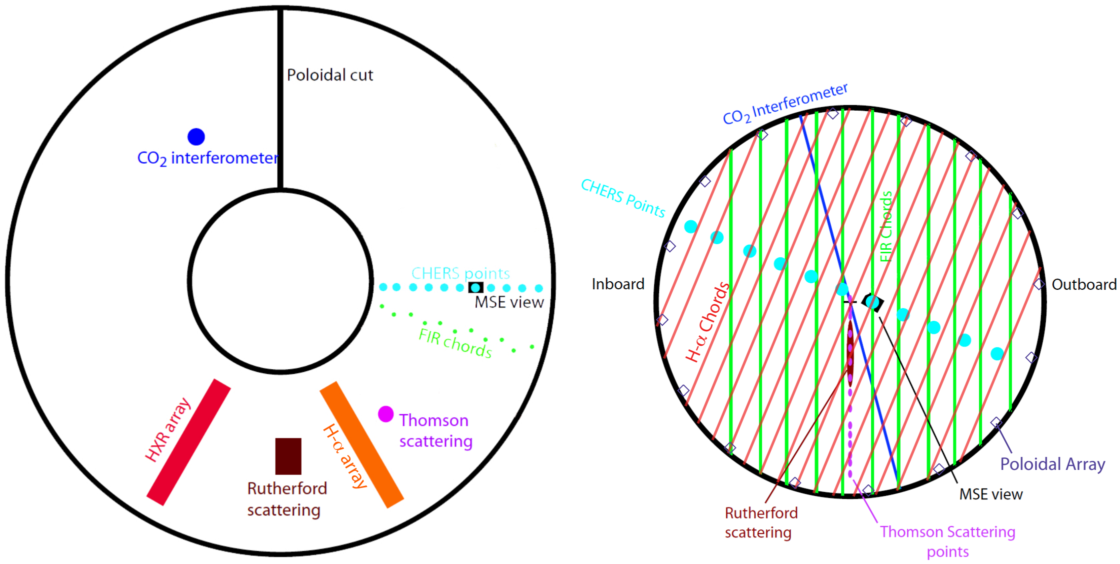

Figure 3.1: Toroidal (left) and poloidal (right) cross sections of the diagnostic coverage of MST courtesy of Max Wyman.

where the primes denote derivatives with respect to the poloidal flux, ψ. Once J is specified, ψ can be found using:

$$\Delta^*\psi = -\mu_0 R J_\phi \tag{3.3}$$

where $\Delta^* = R^2\nabla\cdot(\nabla/R^2)$. The inconsistency of requiring ψ in order to determine ψ is resolved by iterating over the J_ϕ and ψ calculation until the variation in ψ falls below a threshold value (i.e. until self consistency is reached). This leaves only the initial guess to be determined and, for historical reasons, this is supplied by the MPFM model.

The Δ^* operator is inverted on the non-uniform up-down symmetric triangular mesh grid shown in figure 3.2 using a Green's function. The Green's function is computed to find the poloidal flux at each grid point due to a unit current on every

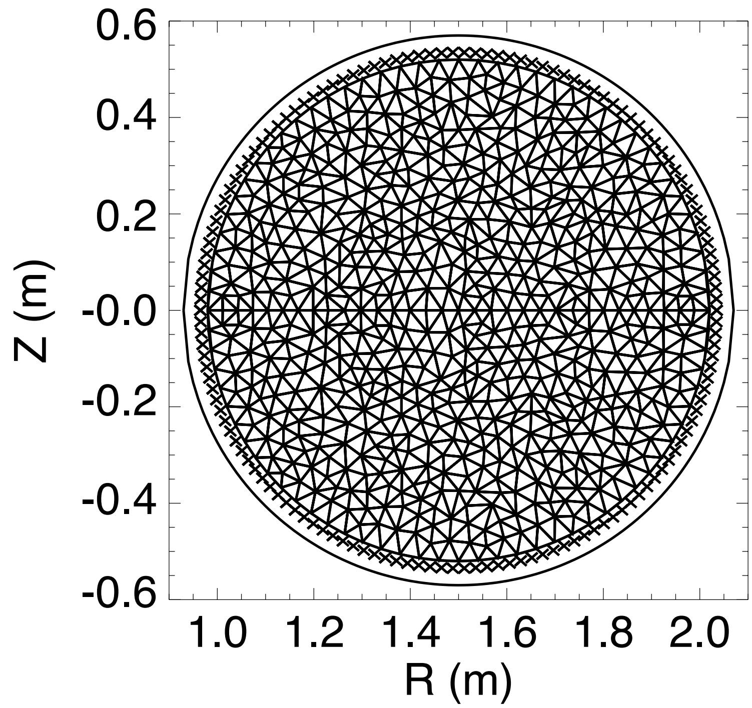

Figure 3.2: Up down symmetric non-uniform grid used in MSTFit.

other grid point assuming the boundary is an ideal conductor in the toroidal direction (in other words $\psi(a)$ is a constant). It should be noted that the assumption of an ideal conducting boundary is not a necessary condition, but given that the first wall of MST is 5 cm of aluminum, it is a good assumption to make and avoids the costly additional fitting parameters that would be need in order to define the mirror currents flowing in the shell. Computing the Green's function values is computationally expensive, but it only needs to be done once. Once the matrix of fluxes is defined, one need only specify a matrix of current density values and do a matrix multiplication to determine the poloidal flux in the machine. Contours of constant poloidal flux are often called flux surfaces and are surfaces upon which many quantities of interest are constant. Figure

3.3 show an example of the flux surfaces in MST. Note that while these surfaces appear to be concentric circles, they are actually somewhat distorted, on the inboard side in particular, from circles. Also, the conducting boundary defines a surface of constant flux which, for convenience, is defined to be $\psi = 0$. The last closed flux surface in the machine is the surface that contacts either the wall or the outboard limiter which is 1.5 cm from the wall. In practice it is always the latter condition that defines the last flux surface in standard plasmas.

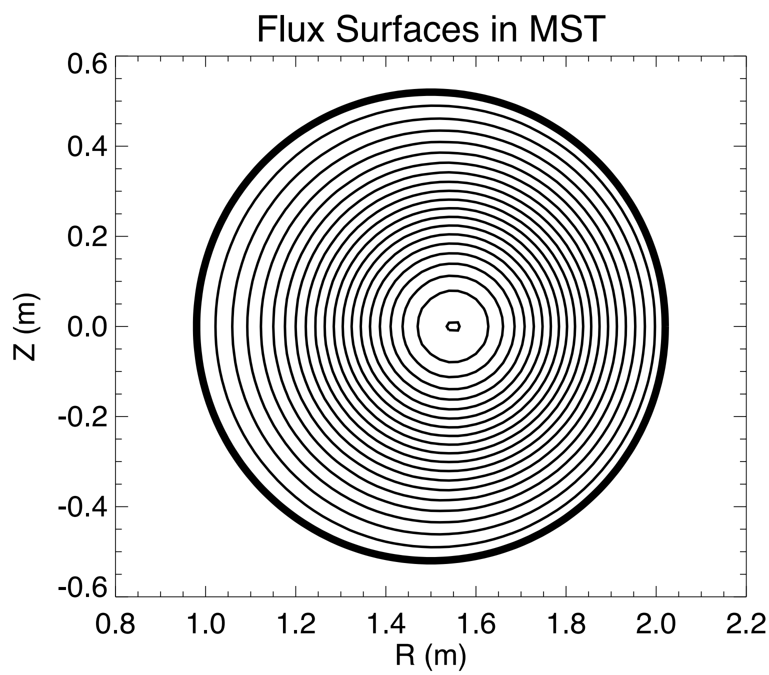

Figure 3.3: Example contours of constant poloidal flux, ψ, for a typical MSTFit equilibrium reconstruction.

There are two important points to make at this juncture. The first is that the pressure is generally not fit as part of the minimization procedure. Instead the electron and ion temperature and density profiles are fit independently and used to determine the pressure and $P'(\psi)$ profiles. In other words, for a given ψ profile, the pressure is a specified profile leaving only F as a free function to be determined. In practice it is actually the F' profile that is specified. This profile is then integrated in order to find F. For the work that appears here, a two parameter model was used unless otherwise stated. In this model $F' = A\left(1 - \hat{\psi}^B\right)\frac{\partial\hat{\psi}}{\partial\psi}$ where A and B are free parameters and $\hat{\psi}$ is the normalized poloidal flux, $\hat{\psi} = (\psi - \psi_{min})/(\psi_{lim} - \psi_{min})$. This model is often referred to as the 'alpha model' as it is analogous to the cylindrical alpha equilibrium model in the following way:

$$\lambda = \frac{\mu_0 a \mathbf{J}\cdot\mathbf{B}}{B^2} = 2\pi a F' + \frac{2\pi\mu_0 a F P'}{B^2} \tag{3.4}$$

$$\lambda_{cyl} = \lambda_0\left(1 - \left(\frac{r}{a}\right)^\alpha\right) \tag{3.5}$$

$$F' = A\left(1 - \hat{\psi}^B\right)\frac{\partial\hat{\psi}}{\partial\psi} \tag{3.6}$$

and thus we identify $\lambda_0 \approx 2\pi a A\frac{\partial\hat{\psi}}{\partial\psi}$ (where the lower case a is the minor radius), and the exponent $\alpha \approx B$. Note that B in this case is a free parameter and has no relation to the magnetic field $\mathbf{B}$ that appears in equation 3.4. In the force free case (i.e. when $P' = 0$ everywhere), this relation is exact. In practice, the effect of finite pressure is small in standard plasmas and the best fit values for A and B are both qualitatively and quantitatively similar to λ_0 and α. Figure 3.4 shows a comparison of α and λ_0 to B and A, respectively, for a time sequence of equilibria for a single shot. While the values are similar there is non trivial variation that is due to toroidicity and details of the pressure profile. This model greatly reduces fitting time and fit variability (i.e. χ^2 space is less flat) while maintaining reasonably small values of reduced χ^2 and capturing many of the features of the less constrained free knot spline fitting method

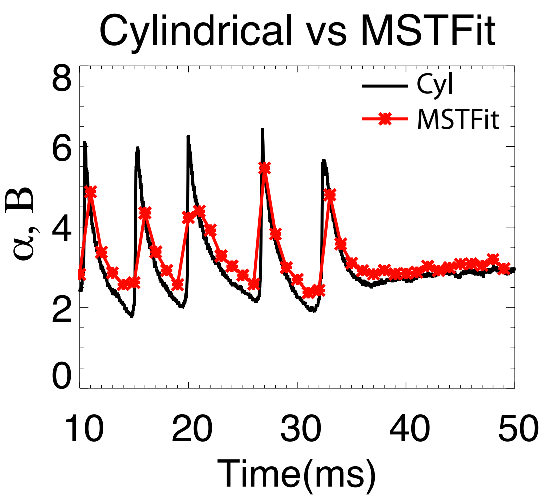

Figure 3.4: α and λ_0 for the cylindrical alpha model assuming 6% β compared to the B and A respectively from the two parameter fitting model from MSTFit. Notice that the decreasing α means the current density is slowly peaking leading up to the sawtooth. The sharp increase means the current density rapidly flattens at the sawtooth crash.

described in references [1, 2].

3.2 Sawtooth Evolution of the Magnetic Equilibrium in MST

The sawteeth in MST are not just core or edge localized events, rather, current is transported across the minor radius, significantly changing the entire magnetic equilibrium. In fact, the sawtooth event is seen on nearly every diagnostic signal in MST. As discussed in section 1.2 of chapter 1, this makes these events particularly good markers in time for ensemble averaging and, for the rest of the work presented in this chapter, the data from several thousand sawtooth events were averaged together. This averaged data was then used by MSTFit to determine the time evolution of the magnetic equilibrium in MST. In this section, the ensembling techniques used to generate the input for MSTFit are discussed and a subset of the averaged data are be presented. Two ensembling techniques are used. The first is for data taken continuously over the entire discharge at data rates at or above the rate for the operational diagnostics (200 kHz). The second is for discrete data. That is, data in which only a limited number of time points per discharge (in some case only one) are available for ensemble averaging. Particular attention is paid to the ensembling of the electron temperature data which is necessary for determining the P' profile and, more importantly, is of critical importance for the transport calculations presented in section 3.3. After presenting the ensembled data, the fit results for this data set are then presented and the evolution of the equilibrium is discussed.

3.2.1 Ensembling the Input Data

Using the sawtooth ensemble code developed for MST[8], the evolution of the equilibrium through a canonical sawtooth is determined. For this ensemble, the line integrated electron density, current, and reversal parameter were constrained. Due to technical difficulty with the CO_2 interferometer, which led to a relatively high measurement uncertainty for this data set, the density constraint was relatively weak with a range of 0.8×10^{19} m^{-3} to 1.2×10^{19} m^{-3}, or $\pm 20\%$. The reversal parameter was constrained to be from -0.22 to -0.18, or $\pm 10\%$. The plasma current constraint was somewhat tighter at 380 to 420 kA, or $\pm 5\%$. Figure 3.5 shows a histogram of the plasma current values used for this ensemble.

Once the sawteeth that are to be included in the ensemble have been selected, all of the signals needed for reconstructing the equilibrium can be ensemble averaged. Figure 3.6 shows the time evolution of several global quantities of interest. Notice the three distinct phases of the sawtooth. The first is the pre-sawtooth period in which

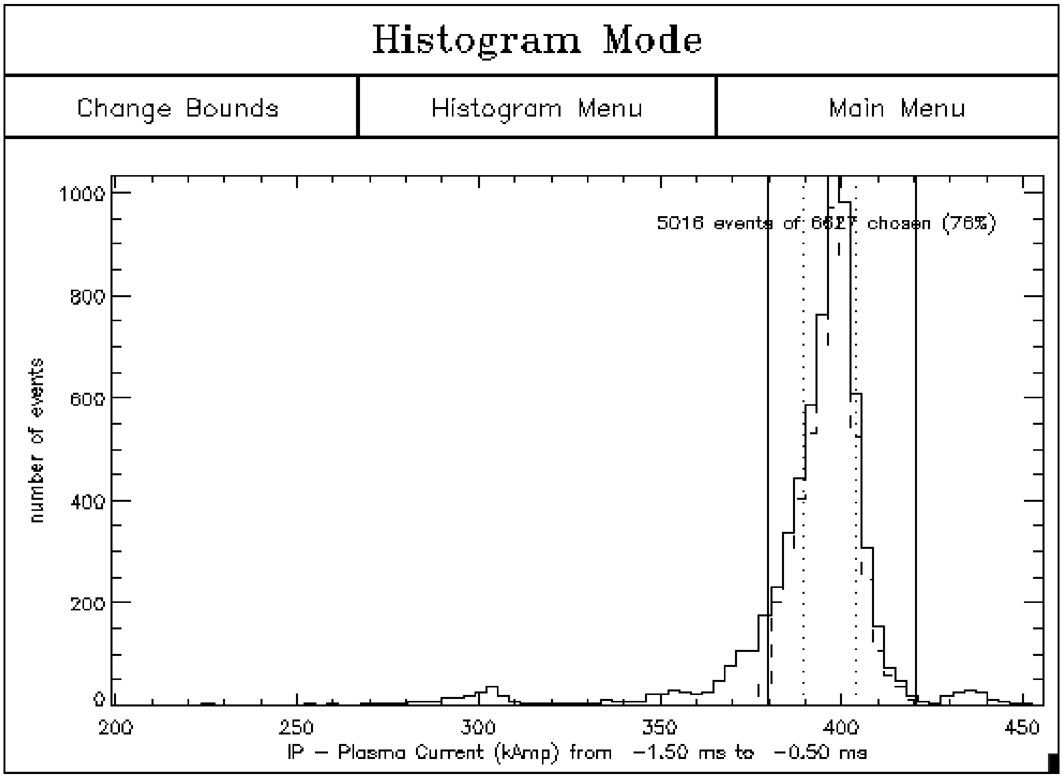

Figure 3.5: Histogram of the plasma current values for this ensemble. The value shown here is the average from 1.5 ms to 0.5 ms before the sawtooth crash.

the pinch and reversal parameters (top plots) are increasing slowly and the toroidal flux is decreasing slowly due to resistive decay in the external toroidal field circuit (if the shell were a perfect conductor in the poloidal direction there could be no change in the total toroidal flux inside). The second is the crash phase where F and Θ drop sharply. This drop is coupled with a sharp increase in the plasma current and toroidal flux (bottom plots). Finally, there is the post sawtooth phase where the toroidal flux is again decreasing and the reversal and pinch parameters are again slowly increasing.

There are many measured signals that can be used to constrain the equilibrium

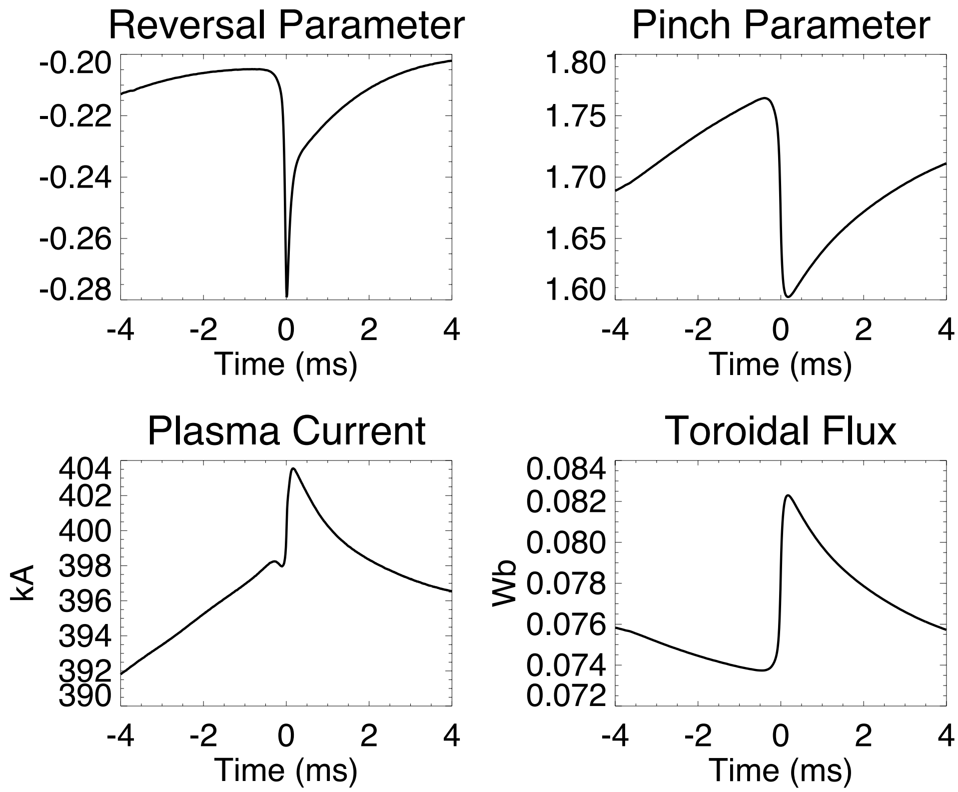

Figure 3.6: Sawtooth evolution of F, Θ, I_p, and toroidal flux.

reconstruction beyond the four shown here. The set that was used for the reconstructions presented here are F, Θ, I_p, toroidal flux, the set of 16 poloidal array coils, the on-axis MSE value of $|B|$, and the set of 11 polarimetery chords from the far infrared (FIR) interferometer/polarimeter system. A detailed description of how each of these signals are fit can be found in reference [2]. Additionally, the pressure profile was determined for the P' term using the set of 11 line integrated density measurements, the set of 21 thomson scattering measurements, and the Rutherford scattering measurement made near the axis. The ion density used for the pressure profile is assumed to have the same shape as the electron density profile and is scaled using an assumed scale factor. The determination of that scale factor is discussed in more detail later in this section.

Most of the data needed for the reconstructions was ensemble averaged with the standard sawtooth ensembling code used at MST, 'st_corr.pro'. This code provides both the average and the variance σ of the ensemble averaged data. The uncertainty used in the reconstruction process then is the uncertainty in the average $\sigma/\sqrt{N}$[9]. This ensembling code, however, is not well suited for data taken at a low data rate or for a short time window during each shot. The Thomson scattering, MSE, and Rutherford scattering data all had to be handled separately from the rest of the data for the reconstruction. Since the electron temperature is of primary importance for this work, the ensembling processes for it is described in some detail, but note that the same process was used for the MSE and Rutherford data. It should also be noted that the data from the operational signals and Thomson scattering come from over 3000 shots, the data from the FIR interferometer polarimeter system, MSE, and Rutherford come from a somewhat smaller subset of shots. This subset, however, still consists of several hundred shots and is expected to be a good representation of the typical sawtooth behavior.

3.2.2 Ensembling the Electron Temperature Data

Much of this analysis presented in this thesis is based around the idea that an ensemble average of many similar sawtooth events allows the determination of the canonical sawtooth event. When the signal in question is available on the same time base as the signal used to determine the exact time of the sawtooth event (generally this is the poloidal loop voltage, i.e. the voltage across the toroidal gap or, as it is commonly referred to in MST jargon, Vtg) then averaging together some time window around each sawtooth event is simply a matter of selecting the appropriate set of data samples corresponding to each event. Whenever the time resolution is different from that time base then some form of re-sampling must be done in order to get the ensemble averaged value of the signal. This is a simple process when the data rate is higher than that of the operational signals, but when the data rate is much lower, the accuracy of the ensemble average becomes questionable. In the case of Thomson scattering the data rate is not only much slower than that of the sawtooth time base, but it is also very sporadic. This makes interpolation unreasonable or even impossible. This was the case with data from before the 2009 upgrade where only one to four profiles per discharge could be obtained. For that reason, a set of bin averaging routines have been created using the Interactive Data Language (IDL). These routines have now been included with the MSTFit package and their usage is documented on the plasma wiki under the "Computation and Codes" heading. In this scheme, the time between each temperature profile and each sawtooth in a given shot is determined for the entire ensemble. Then the profiles are sorted into their appropriate bins. The fit quality as well as the fit uncertainty are automatically checked for each data point individually to ensure that only good data appears in the average.

3.2.2.1 Determining the Time Resolution

Once a scheme for determining the ensemble average is found, one is left to determine the optimal time resolution. The time resolution of the ensemble is functionally limited only by the amount of data available, however, practically speaking, the sawtooth events are not perfect carbon copies of each other and therefore it is advisable to reduce the data rate until there is a statistically significant number of data points in each bin. These criterion set a maximum possible and maximum advisable data rate for a given data set. The ensemble presented here consists of nearly 3000 shots taken over several years with about 900 of those shots taken with the system in its current form, which yields 30 profiles per discharge. This is, by most measures on MST, a very substantial data set. For the best performing radial points (i.e. the points with the lowest number of rejected data) the maximum resolution is about 200 kHz. However, this drops to about 100 kHz when the entire profile is considered and even then there are several points near the edge that have very few good data values near the sawtooth event. In order to get adequate data at all time and spatial points, the data rate was reduced to 20 kHz. At this data rate, most points were the average of over 100 measurements with the worst points consisting of 20 measurements. Figure 3.7 shows the bin averaged data at a 200 kHz data rate in black and a 20 kHz data rate in red. It is encouraging that the 20 kHz essentially smoothes out the hash in the 200 kHz data to produce a much cleaner time evolution. For this reason, it is expected that given sufficient data very high data rates could be realized using this method.

3.2.2.2 Uncertainty Estimates

The uncertainty estimate used for this data set was the uncertainty in the average, or the standard error, $\sigma/\sqrt{N}$. Figure 3.8 shows a histogram of electron temperature values in a bin with a relatively large number of good data values in it. For display purposes, a three parameter gaussian fit was done to this set of bins and bin heights and is shown here. In practice, a simple mean and standard deviation procedure are used on the data, but with sufficient data, these results are nearly identical to fitting

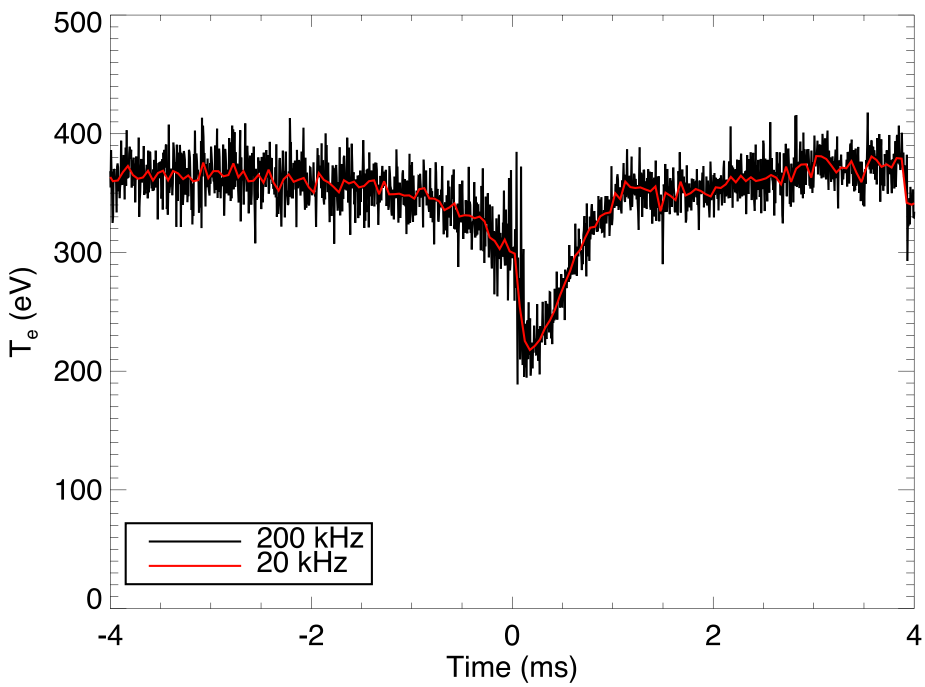

Figure 3.7: Bin averaged electron temperature at 200 kHz (black) and 20 kHz (red) data rates.

the distribution with a gaussian. The mean, standard deviation, and standard error are also shown.

A similar sort of analysis has been done for the MSE and Rutherford scattering data shown in figure 3.9. Notice that although the total toroidal flux increases dramatically at the sawtooth crash, the magnetic field near the magnetic axis actually decreases. The ion temperature, which is centered slightly off axis, increases sharply at the sawtooth crash and then cools slowly after the crash. This sharp spike in ion temperature will become important later when discussing the global confinement of the sawtooth event.

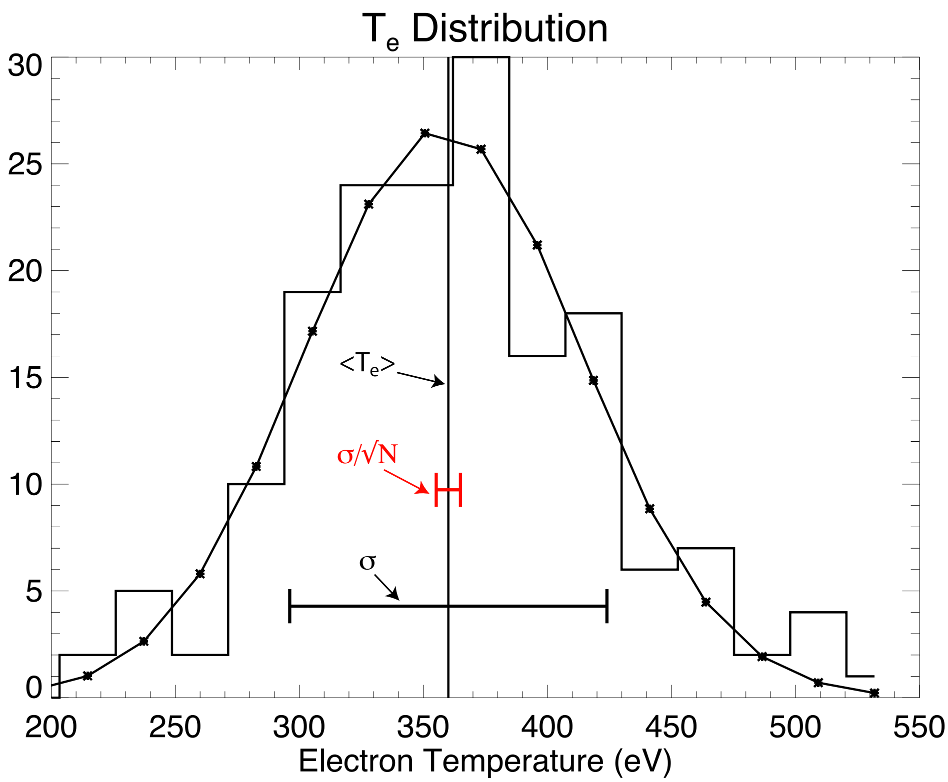

Figure 3.8: Distribution of electron temperatures in a bin. The solid black curve is a gaussian fit to the bin heights. The vertical black line is the average T_e, the red error bars show the uncertainty in the average, and the black shows the standard deviation of the distribution.

3.2.3 Pressure Evolution

Formally, the pressure profile is a flux function that needs to be determined to specify the equilibrium. This can be treated as a free function that is fit as part of the equilibrium reconstruction process, but for this work it is a specified profile supplied by measurements. While the P' contribution to the toroidal equilibrium is expected to be small for the RFP, the determination of the temperature and density on a consistent set of coordinates (i.e. as a function of poloidal flux) so they can be easily combined is critical for the transport calculations presented in section 3.3.

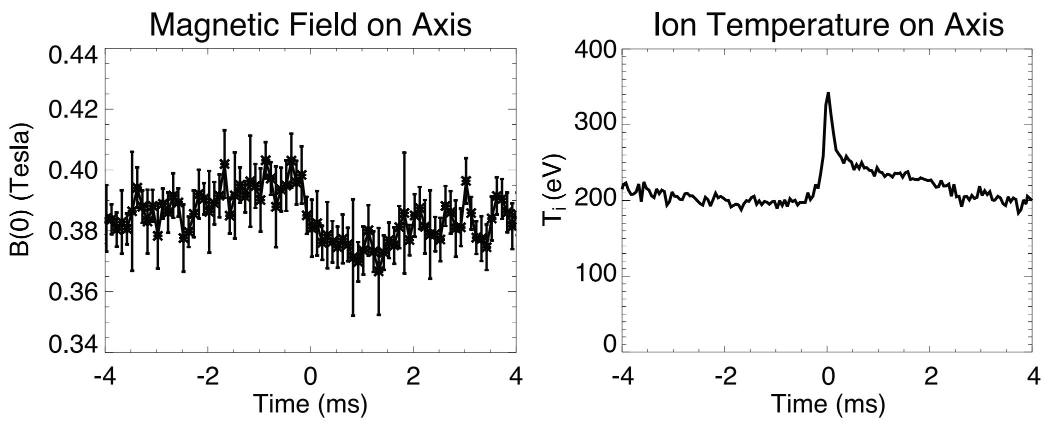

Figure 3.9: Bin averaged Motional Stark Effect $|B|$ (left) and Rutherford scattering majority ion temperature (right) measurements vs. time through the sawtooth cycle.

However, since they are first used to define the equilibrium, the temperature and density evolution will be presented here. The combination of the electron temperature profile from Thomson scattering measurements and the electron density profile from the FIR interferometer gives the electron pressure profile. The ion temperature is assumed to have the same shape as the electron temperature profile, but is scaled to match the core value measured by Rutherford scattering. The ion density profile is assumed to have the same shape as the electron density profile, but is scaled by Z_{eff}. These four quantities are assumed to be constant on a surface of constant flux so the data can be fit using relatively simple radial profiles.

In order to combine the data from these different diagnostics, the locations of the measurements are mapped into flux space. The value of the flux at each measurement location is determined exactly using the Green's function method described earlier except that here, the poloidal flux at the measurement points shown in figure 3.1 due to a unit current at each location on the triangular mesh is determined in advance so that the exact value of flux at the measurement point can be determined with a quick matrix multiplication during the reconstruction process. The poloidal flux then becomes the effective radial ordinate onto which fits to the radial profiles of all the measurements can be determined and combined in order to determine the total pressure. With the measurements in flux space, the data can be fit so that the pressure profile and the derivative of the pressure profile can be specified at each point on the triangular mesh. Once P' is determined, the Grad-Shafranov equilibrium can be computed. The locations of the data must then be recomputed on the resulting flux geometry and profiles refit. Again, this process is repeated until self consistency is reached.

For convenience, the fits are typically done in normalized flux space, $\hat{\psi}$, which was discussed earlier. The fit results presented here, however, will be show with respect to the effective radial coordinate,

$$\rho_v \equiv \sqrt{\frac{V_\psi}{2\pi^2 R}}, \tag{3.7}$$

where V_ψ is the volume of a flux tube and R is the major radius of the center of the flux tube, giving ρ_v units of meters. This is preferred to $\hat{\psi}$ as $\hat{\psi}$ is not a linear function of space, and it is preferred to minor radius as the magnetic axis is generally shifted four to six centimeters from the geometric axis and thus would obviously cause some confusion. What follows is a description of the measured T_e and n_e evolution followed by the evolution of the fits to that data. The ion temperature and density is then discussed and combined with the electron profiles to get the total pressure evolution.

3.2.3.1 Electron Temperature Evolution

The electron temperature profile changes dramatically through the sawtooth event. Figure 3.10 shows a surface plot of the ensemble averaged electron temperature data over the entire sawtooth cycle. There are several interesting features of this

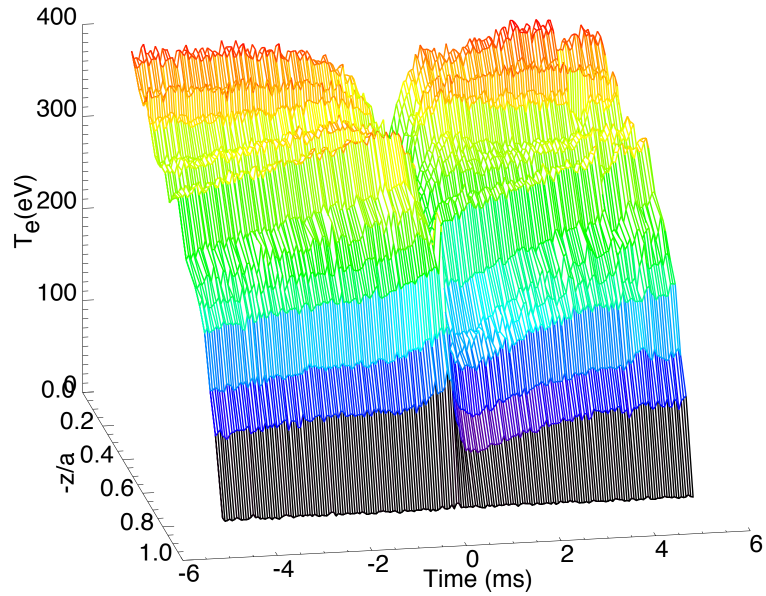

Figure 3.10: This figure shows a surface plot of the sawtooth evolution of the ensembled electron temperature data measured by the Thomson scattering system. Note that this is before any fitting has been done so the radial axis is -Z/a.

sawtooth evolution (see figure 3.11). In the core, about 1/3 of the heat is lost at the sawtooth event, but this loss actually starts well before the sawtooth crash and doesn't stop until about 0.25 ms after the sawtooth event. What is also striking about the core behavior is how quickly the electron temperature in this region recovers after the crash. Within about 1 ms the core T_e is nearly at the pre-sawtooth value. In contrast, the edge temperature actually increases leading up to the sawtooth as though the heat that is slowly lost from the core before the sawtooth crash accumulates in the

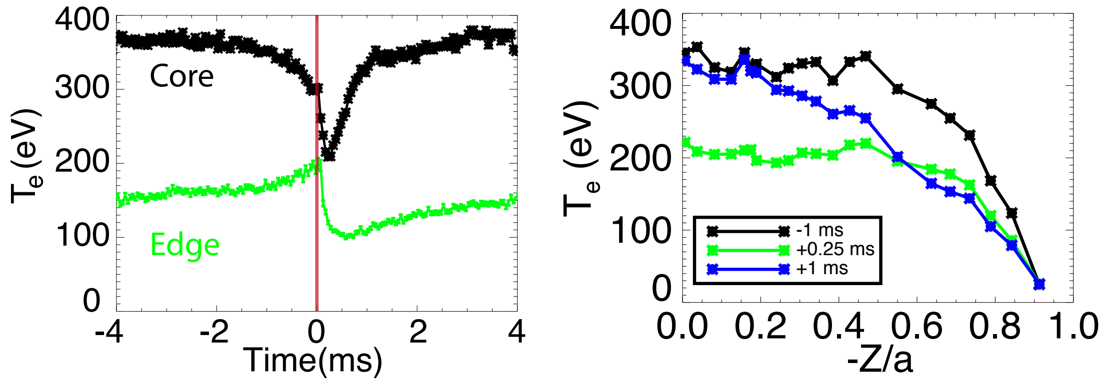

Figure 3.11: Electron temperature vs. time (left) and space (right). The red line on the left hand plot marks the time of the sawtooth crash for reference. The black line is from the -Z/a = 0.037 location while the green line is from the -Z/a = 0.788 location.

edge. This stored heat is then lost at the crash, reaching a minimum somewhat later than the core at just after +0.5 ms. The edge temperature then slowly recovers taking several milliseconds to get back to the pre-sawtooth level. Looking at the radial profile shape at three snapshots in time (figure 3.11 right) the variation in time is clearly seen. Before the sawtooth, the profile is relatively broad, it drops and flattens at the crash, then recovers in the core while continuing to drop in the edge.

This difference in core versus the edge behavior can also be seen in the RMS mode amplitudes (as measured by magnetic pick up coils located at the edge of MST) for the core resonant m=1 modes and the edge resonant m=0 modes (see figure 3.12). It can be seen that as the core modes increase in amplitude before the sawtooth event, the core temperature starts to decrease slowly. Conversely, after the sawtooth event, when the core is reheating rapidly, the m=1 modes are rapidly falling to a minimum value for the cycle. Meanwhile, the edge resonant m=0 modes stay very low right up until the sawtooth event where they spike and then take several milliseconds to fall

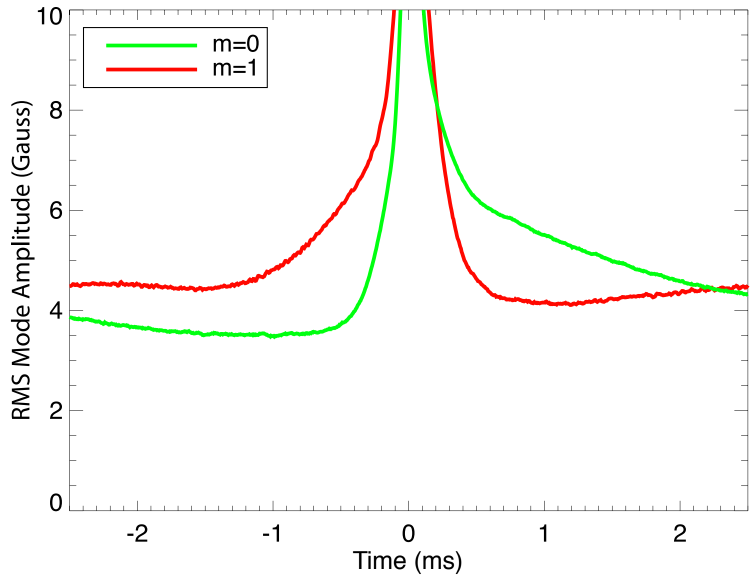

Figure 3.12: The RMS mode amplitudes for the core resonant m=1 modes (red) and the edge resonant m=0 modes (green). Notice that the core modes start to increase more than a millisecond before the sawtooth crash while the edge modes start to increase much later and stay high much longer after the sawtooth event.

to their pre-sawtooth levels. The relatively large tearing mode amplitudes in MST coupled with this qualitative agreement between the mode and temperature behavior suggests that the thermal transport is dominated by stochastic transport, which scales with $\tilde{B}_r^2$. It will be shown in Chapter 4, however, that while a significant portion of the heat transport is indeed due to stochasticity, near the sawtooth crash there are significant nonlinear effects that drive addition radial heat transport.

3.2.3.2 Electron Density Evolution

The electron density is measured in several ways on MST, but the diagnostic that is primarily used for the data presented in this work is the Far Infrared (FIR) interferometer[10]. The FIR system on MST gives the line integrated electron density simultaneously for the eleven different lines of sight shown in figure 3.1. The density is measured at a relatively high time resolution of 6 MHz allowing the density, its time derivative, and the fluctuations in the density to be measured. Since this work involved a large ensemble of data, the line integrated density for each chord was ensembled and then down sampled to the 20 kHz data rate used for equilibrium reconstructions. Some sense of the sawtooth evolution of the density can be gained immediately from the ensembled data simply by looking at the peaking factor. This is simply the ratio of the line integrated density for a line of sight that goes through the plasma core and one that only goes through the edge. If the two values are the same then (i.e. peaking factor=1) then all of the density is in the edge and the profile is hollow. If the density were constant throughout the entire plasma volume then this ratio would be equal to the ratio of the lengths of each line of sight. This, of course, is very unlikely to occur, but the relative change in this ratio does imply a change in how peaked the profile is. Figure 3.13 show the ratio of the P06 to the P43 chord (chord closest to the magnetic axis to the most outboard chord). Notice that the density profile peaks coming into the sawtooth, falls fairly rapidly at the sawtooth, and then begins to peak again over the course of several milliseconds.

3.2.3.3 Density and Temperature Profile Fitting

The local electron density and temperature are found in MSTFit using the free knot spline method described in ref. [1] and in more detail in ref. [2]. The density was fit with a four knot 'fixed' profile while the temperature was fit with a four knot 'free' profile where the radial positions of the two internal knot locations were adjusted in addition to the knot values in order to find a best fit. The boundary conditions on the

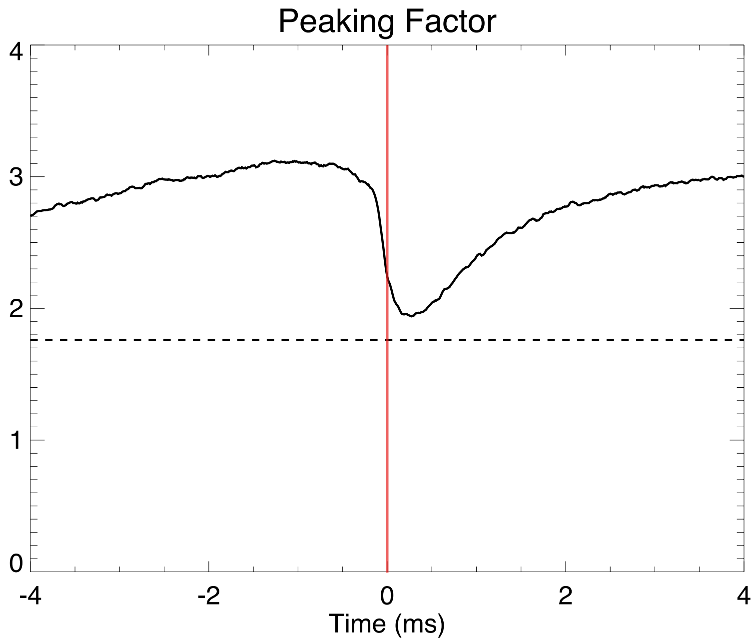

Figure 3.13: Peaking factor vs. time for the ensemble averaged FIR data. This is the ratio of the P06 to the P43 chord (6 and 43 cm outboard of the geometric axis respectively). The dashed line shows the ratio of the lengths of the two lines of sight.

density fit were that the density gradient on axis be equal to zero and that the edge density is equal to 2×10^{17} m^{-3}. This fixed edge density may be responsible for some amount of the hollowness of the fit profile at the sawtooth crash. The fitting routine simply does not allow for the edge density to increase as may well be happening at the peak of the sawtooth event. This is not a fundamental limitation of the fitting algorithm and may be changed in the future. The electron temperature fit also assumes that the temperature gradient goes to zero at the magnetic axis and that the edge temperature is fixed. In this case, the temperature is set to 30 eV, consistent with edge probe measurements made in MST.

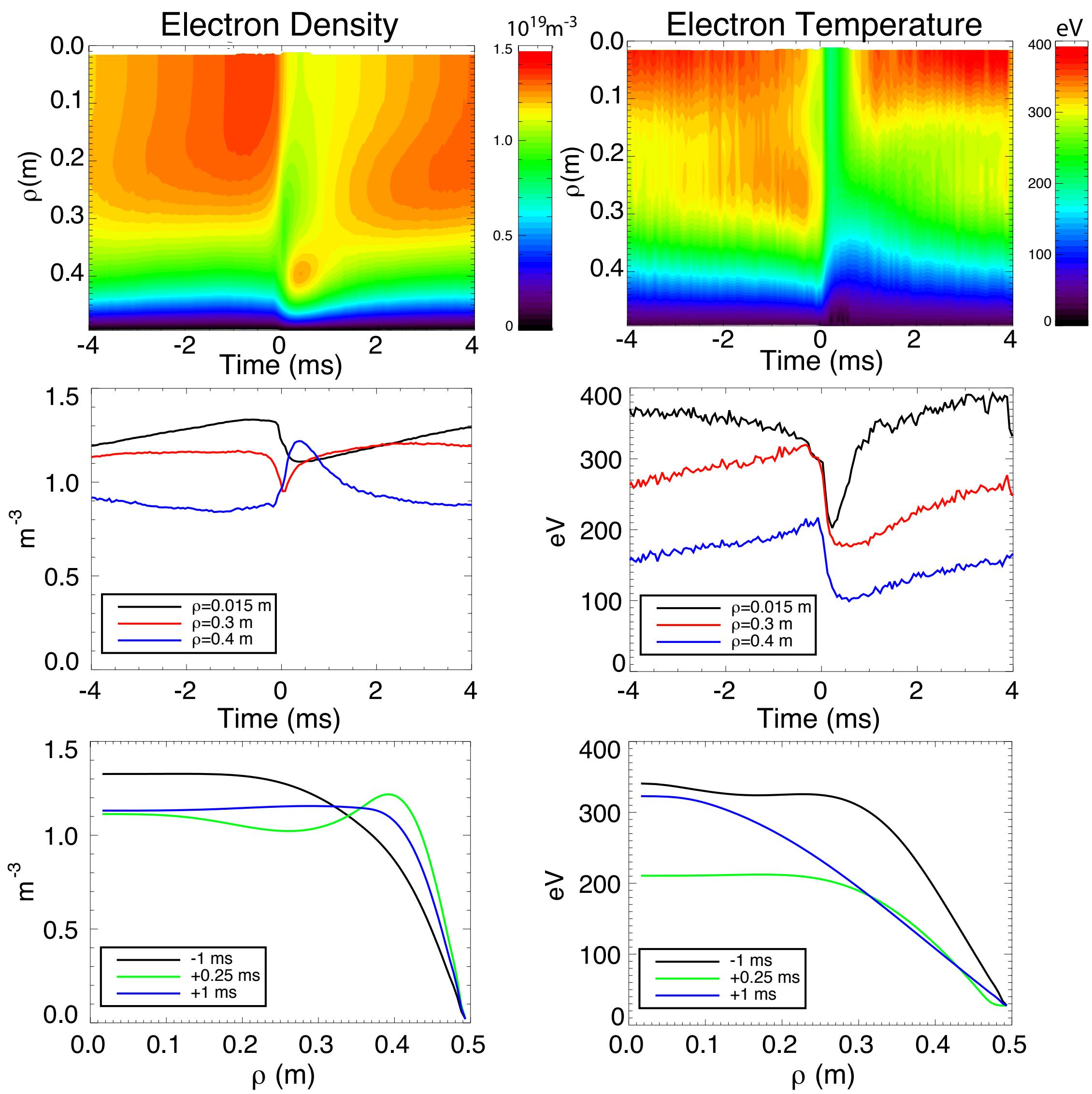

Figure 3.14: n_e and T_e profile fits. Notice that the density profile gets hollow just after the sawtooth crash while the temperature profile gets slightly hollow right at the sawtooth crash but quickly flattens as it drops to its minimum value.

3.2.3.4 Ion Density and Temperature Evolution

To get the total pressure profile, and thus P' for the Grad-Shafranov equation, the ion temperature and density profiles must either be measured or approximated in some way. For this analysis, the ion temperature profile is assumed to have the same shape as the electron temperature profile, however that profile is scaled to match the Rutherford scattering measurement in the core region of the plasma shown in figure 3.9. The ion density is assumed to match the electron density, but is scale by Z_{eff}. This is not as trivial as it seems because of the way Z_{eff} is calculated and so some time will be taken to discuss the ion density.

Since the electrical resistivity of a plasma comes from electron collisions with other particles in the plasma it is useful to define the effective electronic charge of the plasma through the collision frequency. The total collision frequency of electrons with all ions species is

$$\nu_{ei}(v) = \frac{n_e Z_{eff} e^4 ln(\lambda)}{(4\pi\epsilon_0)^2 m_e^2 v^3} \tag{3.8}$$

where

$$Z_{eff} = \frac{\Sigma_s n_s Z_s^2}{\Sigma_s n_s Z_s} = \frac{\Sigma_s n_s Z_s^2}{n_e}, \tag{3.9}$$

with the subscript 's' referring to the species of ion. Combining this definition of Z_{eff} with charge neutrality one can estimate the majority ion density for a simple two species plasma. The resulting values are as follows:

$$n_i = n_e \left(\frac{Z - Z_{eff}}{Z - 1} \right) \tag{3.10}$$

$$n_s = n_e \left(\frac{Z_{eff} - 1}{Z^2 - Z} \right) \tag{3.11}$$

where Z is the impurity ion charge so for a $Z_{eff} = 3$ due to fully stripped carbon with $Z = 6$ $n_i = \frac{3}{5}n_e$ and $n_s = \frac{2}{30}n_e$. This means that a 6.6% concentration of fully stripped carbon and 60% deuterium gives an effective charge of 3. The carbon impurity density, however, has been measured with the ChERS system and is less than 1% of the electron density. MST has an aluminum wall so it is informative to repeat this calculation with aluminum. The electron temperature in standard MST discharges is such that most of the aluminum in the core of the plasma should be ionized up to Z=7 (241.6 eV) and a significant number should make it to the helium like Z=11 charge state (441.98 eV). Assuming for the moment that we have all helium like aluminum in the plasma we get $n_i = 0.8n_e$ and $n_s = 0.018n_e$. In other words, for less than 2% helium like aluminum we see a $Z_{eff} = 3$ with the majority of the ions in the plasma being deuterium.

An effective charge of 3 was used in this example because global power balance estimates discussed later suggest that a $Z_{eff} = 3$ would be required to match the ohmic heating power to the average applied heating power. Therefore, the ion density used throughout the rest of this chapter is assumed to be $n_i = 0.8n_e$.

3.2.3.5 Pressure Profile Evolution

The total pressure in Pascals is defined as simply $P = n_e T_e + n_i T_i$ where the densities are in units of m^{-3} and the temperature is in Joules (i.e. $T = kT$) and all quantities are with respect to flux. The assumption that pressure is constant on a flux surface turns the gradient into a derivative with respect to normalized flux so the P' used for the equilibrium reconstruction is then simply $P' = \frac{\partial P}{\partial \hat{\psi}} \frac{\partial \hat{\psi}}{\partial \psi}$. Figure 3.15 shows the pressure and the derivative of pressure as a function of time and ρ. It is interesting

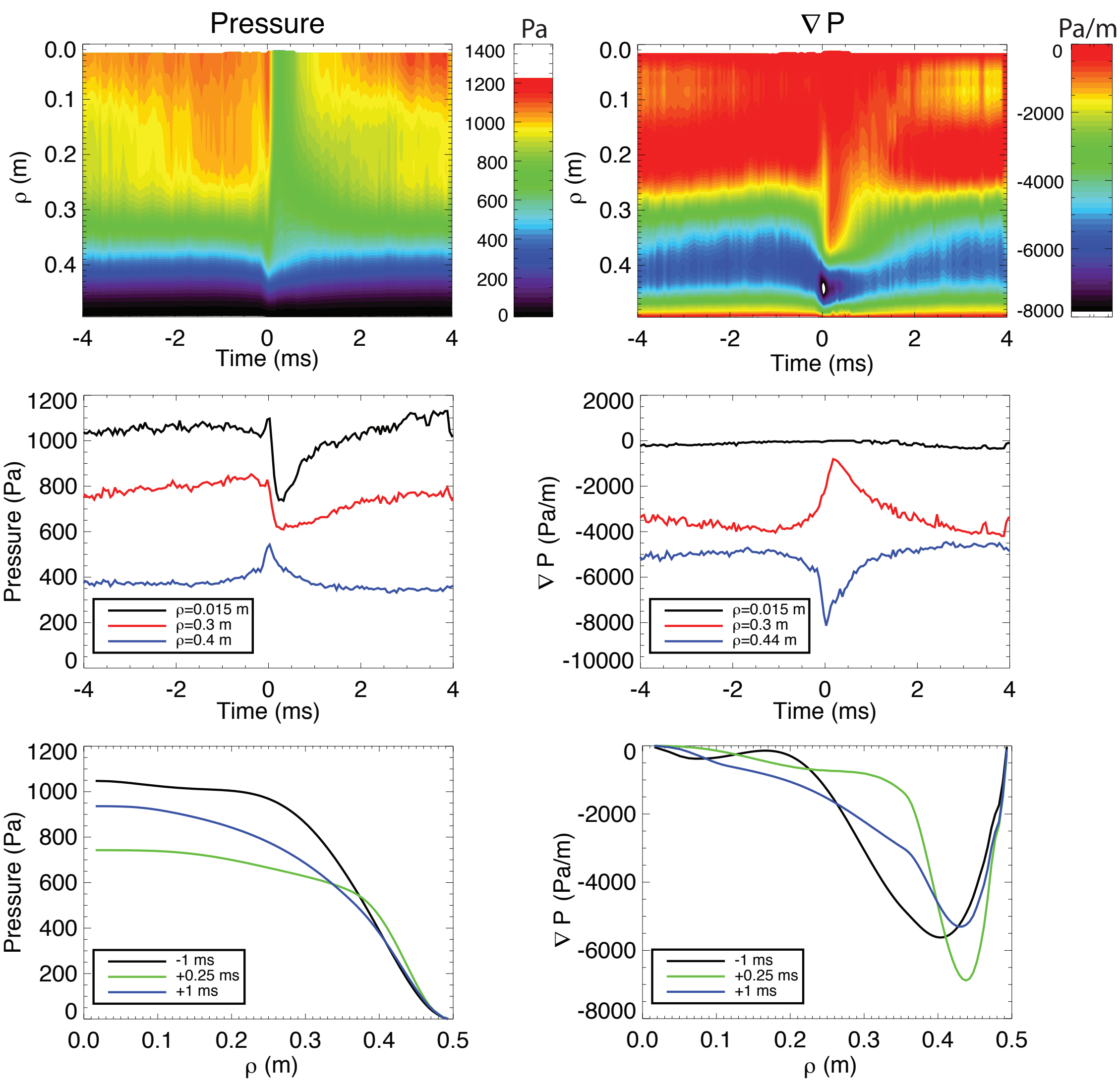

Figure 3.15: Total pressure (left) and P' (right) vs. time and space. The pressure gradient is always strongest in the edge and peaks at the crash.

to note that while the ion pressure increases at the crash, the electron pressure drops so much that the total pressure decreases. The effect of the pressure gradient on the toroidal current density is relatively weak inside the reversal surface, but is generally the dominant term out side the reversal surface.

3.2.4 Current Density Evolution

Finally, with the pressure profile in hand, we can compute the Grad-Shafranov equation and determine the magnetic equilibrium and the parallel current density that generates it. More importantly for this work, we can compute the evolution of that equilibrium through the sawtooth crash. This is important for this work as the Ohmic power dissipation is the largest heat source for the electrons. Figure 3.16 shows the evolution of the parallel current through the sawtooth crash. The current density

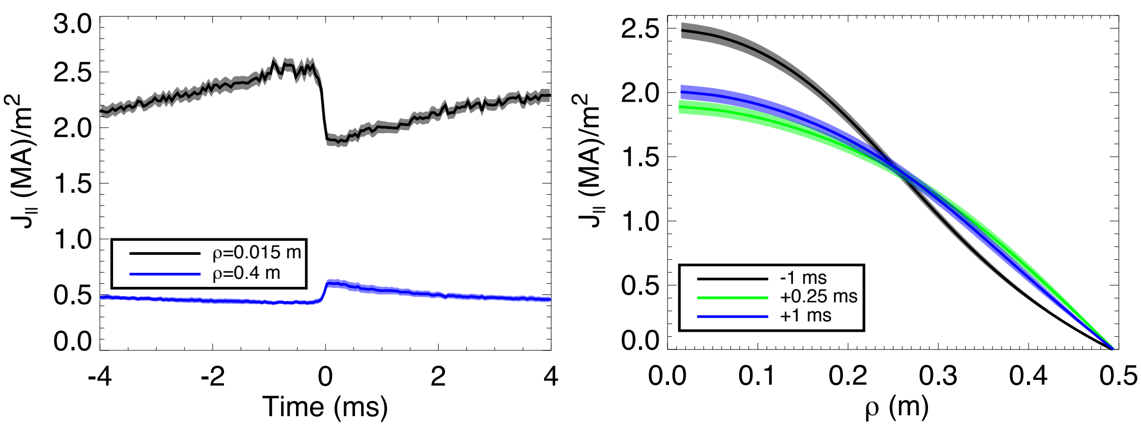

Figure 3.16: Evolution of the parallel current density in the core and edge (left) and the parallel current density profile before, during,and after the sawtooth (right).

varies by about 20% from the average value over the course of the sawtooth. At the sawtooth crash the current on axis drops significantly. This is most likely due to a strong $\mathbf{V} \times \mathbf{B}$ dynamo electric field that is expected to exist at the sawtooth and is clearly seen in the simulation results presented in the next chapter. Simulations show that this dynamo electric field gets very large at the crash, overcoming the inductive response of the plasma and pushing the current density down in the core and up at the edge as can be seen in the experimental measurements of the current density shown in figures 3.16 and 3.17.

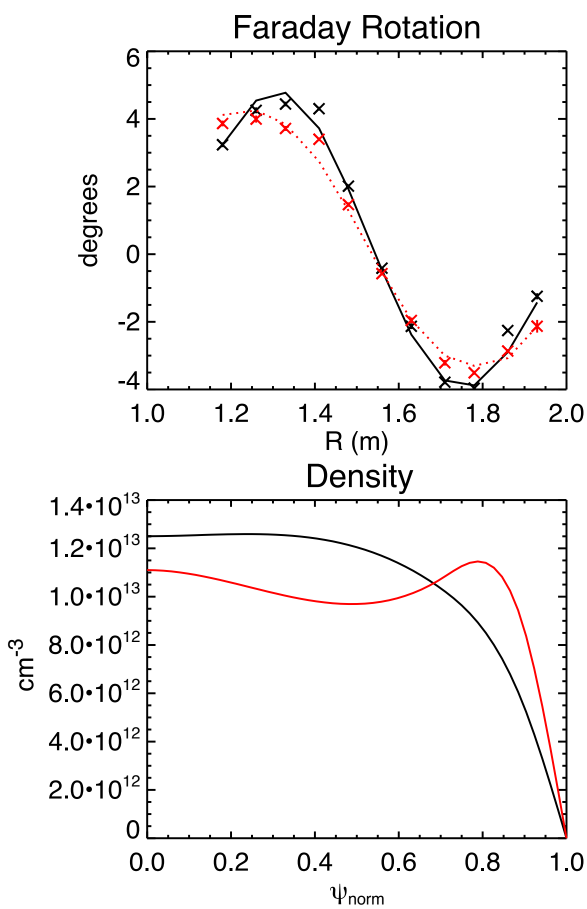

Figure 3.17: Faraday rotation and the line integrated density data as well as the electron density and the current density at two times, before (black) and at (red) the sawtooth crash. Notice that the current density drops on axis and increases near the edge at the sawtooth crash.

The magnetic fields are also modified substantially by the sawtooth. Figure

3.18 shows the sawtooth evolution of the toroidal (B_ϕ) and poloidal (B_θ) fields. At

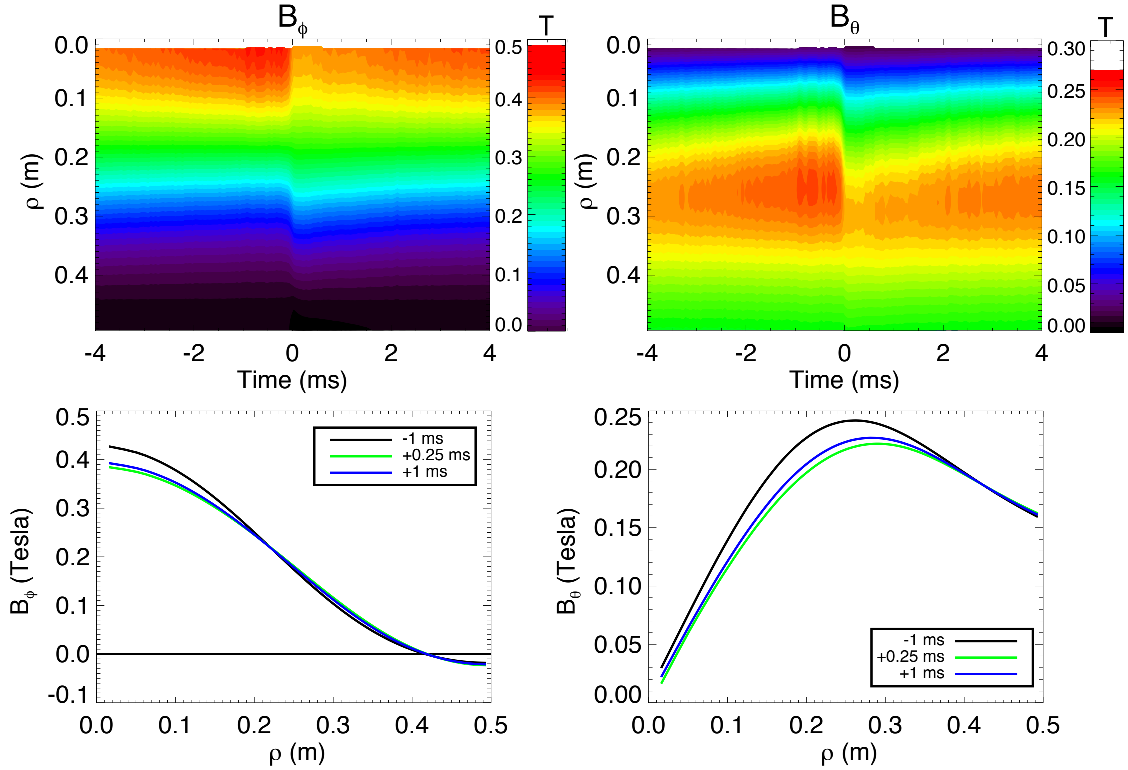

Figure 3.18: Toroidal (right) and poloidal (left) magnetic field surface plots (top) and radial profiles (bottom).

the sawtooth crash, the total toroidal flux in the plasma increases by more than ten percent. Interestingly, the toroidal field on axis actually decreases by about 10% at the sawtooth, but the field in the mid-radius and edge the magnetic field increases, more than making up for the lost flux in the core region. The poloidal magnetic field increases slightly at the edge at the sawtooth crash, consistent with the small increase in the plasma current, but decreases everywhere else. Even though the toroidal flux is increasing, the total stored magnetic energy, $W_{mag} = \int \frac{B_\theta^2 + B_\phi^2}{2\mu_0} dV$, actually decreases at the sawtooth event as can be seen in figure 3.19. This decrease is coincident with

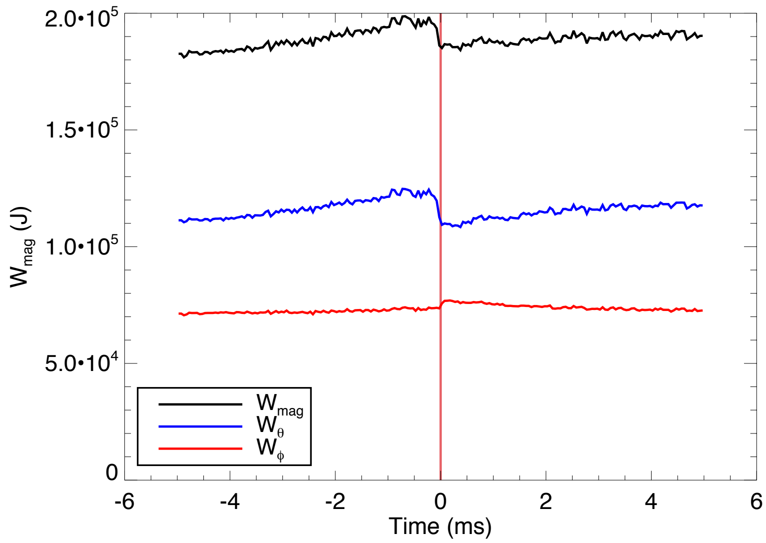

Figure 3.19: Energy stored in the toroidal (red), poloidal (blue) and total (black) magnetic field through the sawtooth cycle.

the increase in the ion temperature and is a likely source for the energy needed to explain the observed heating of the ions that occurs at the sawtooth crash[11]. The energy drop in the poloidal field seems to precede the energy increase in the toroidal field. Some amount of lag is likely due to the inductance of the plasma, though this difference may appear enhanced due to the choice of resolution for this sequence of equilibrium reconstructions.

The safety factor profile, $q(r) = rB_\phi/RB_\theta$, reflects these relative change in the magnetic field profiles. Figure 3.20 shows a contour plot of the safety factor evolution as well as the value on axis. Notice that the safety factor decreases slowly before the crash as the current density peaks. At the crash it jumps up substantially, crossing $q = 0.2$ and bringing the $m = 1$, $n = 5$ resonant surface into the plasma. Meanwhile, the edge q decreases and the reversal surface, where all the $m = 0$ modes are resonant, moves outward toward the boundary. This last point is consistent with insertable probe measurements of the magnetic fields made in lower current plasmas. After the crash, q decreases again as the ohmic drive circuit causes the current density to peak once again. It should be noted that this analysis is not sensitive to helical distortions of the magnetic axis of the type discussed in reference [12] that may occur just after the sawtooth.

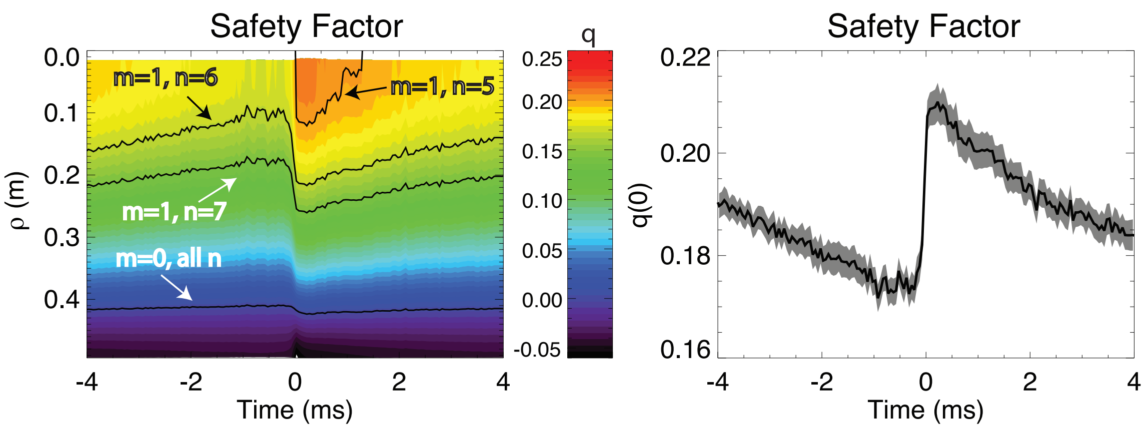

Figure 3.20: Contour plot showing the evolution of the safety factor profile is shown on the left. The $q = 1/5$, $1/6$, $1/7$, and 0 surfaces are shown in black. $q(0)$ is shown in the right.

This evolution of the q profile is also consistent with measurements of MHD activity made at the edge of MST. MST has a set of 64 coils arranged toroidally around the machine at 241° poloidal (lower inner region of the vessel) that measure the edge magnetic field in the poloidal and toroidal directions. This toroidal array data is then Fourier decomposed to determine the time evolution of various magnetic modes. Typically, the amplitude, phase, and velocity of the toroidal $n = 1 - 32$ modes and the poloidal $n = 1 - 15$ modes are recorded. These modes also show an interesting time evolution through the sawtooth. The B_θ, $n > 6$ are dominated by the $m = 1$

contribution. These modes, as will be discussed later, are resonant in the core region of the plasma and grow slowly before the sawtooth, then rapidly at the sawtooth crash. Shortly after the sawtooth event they fall to a minimum value and then begin to grow slowly once again. The low n toroidal fluctuations are dominated by the $m = 0$ contribution and are generally seen to grow rapidly at the sawtooth crash and then decay slowly for several milliseconds after the crash. While this behavior is generally true for all of the resonant $m = 0$ and $m = 1$ modes, the $n = 5$ mode is a special case. The mode grows at the sawtooth crash from a relatively low level and then stays relatively high while all the other $m = 1$ modes are reaching a minimum. Figure 3.21 shows the evolution of the $m = 1$, $n = 5$ and 6 modes through the sawtooth event. The $m = 1$, $n = 5$ mode amplitude starts to decrease about 1 ms after the crash, slightly before the rational surface is expected to leave the plasma.

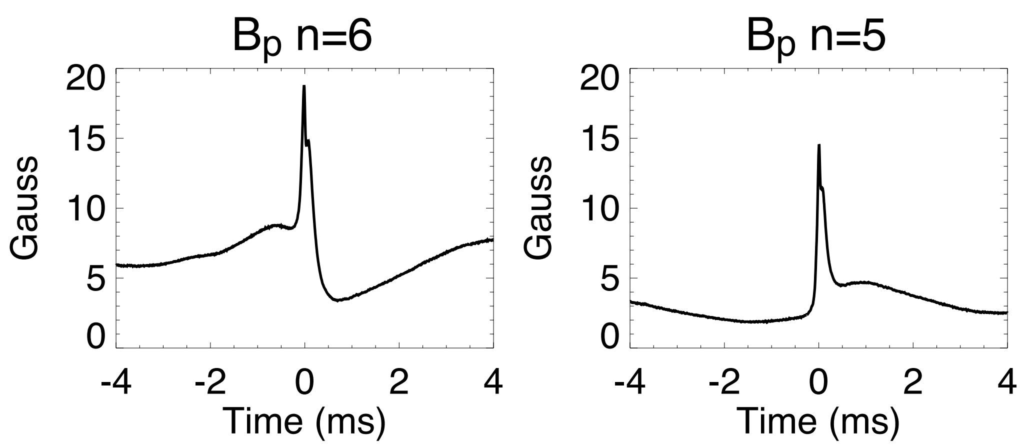

Figure 3.21: Sawtooth evolution of m=1, n=5 and 6 as measured at the edge

The measured magnetic fluctuations are likely dominated by tearing modes which are driven by the local current density gradient in the plasma. Figure 3.22

shows this evolution for the $m = 1$, $n = 6$, 7, and 28 mode rational surfaces as well as the $m = 0$ surface. Interestingly, the magnitude of the gradient in the core actually decreases slightly before the sawtooth while the $n = 7 - 28$ are increasing. In other words, this $m = 1$, $n = 6$ flattening may be causing the gradients at the mode rational surfaces of the higher n modes to increase until they reach large amplitude. The jump in the edge measured $m = 1$, $n = 6$ amplitude seen at the crash may simply be due to the rapid outward motion of its rational surface that occurs during the sawtooth crash (as the rational surface moves closer to the measurement location at the edge, the measured amplitude would be expected to increase). However, as will be shown later, measurements of radial component of the $m = 1$, $n = 6$ magnetic fluctuation in the core region of the plasma made with the FIR polarimetry system show a similar increase in the mode amplitude so it is not clear how much of the observed increase in the edge measurement is due to a geometric effect and how much is due to an actual increase in the total mode energy. The sawtooth flattens the current gradient across all these modes and causes the gradient at the edge to increase.

It has been suggested that the sawtooth crash is triggered by the current density gradient reaching a critical point and driving one or more of these modes unstable, resulting in the rapid increase in the measured mode amplitudes. Nonlinear coupling would then cause the rest of the modes to increase in amplitude. If this is type of phenomena is triggering the sawtooth crash, it is probably not the $m = 1$, $n = 6$ that is the primary player since the current density gradient doesn't change much leading up to the sawtooth. Rather it is more likely to be one of the modes resonant in the middle of the plasma. That said, it has been suggested that if the $m = 1$, $n = 6$ mode gets too close to the magnetic axis it will trigger a sawtooth. In this case, the current density gradient is not the correct parameter to look at. It should also be noted that the $m = 1$ mode amplitudes start to grow about 1 ms before the crash, consistent with the saturation in the current density gradient in the $m = 1$, $n = 7$ and higher modes.

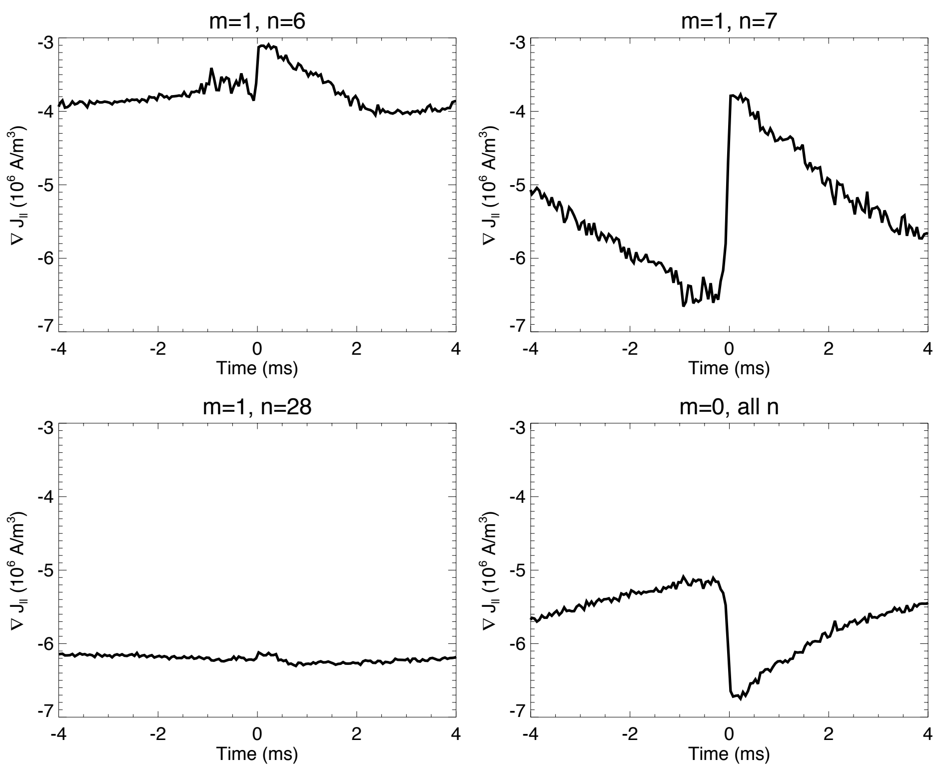

Figure 3.22: Sawtooth evolution of parallel current density gradient at the $m = 1$, $n = 6$, 7, and 28 surfaces as well as the $m = 0$ surface.

3.3 Global Confinement and the Electron Thermal Diffusion Through a Sawtooth

Determining the evolution of the magnetic equilibrium as well as the evolution of the kinetic profiles in the plasma allows global transport quantities, namely β_p and τ_E, as well as the local electron thermal diffusion χ_e to be computed. In order to compute these quantities, the heat source for the plasma is determined. Using global power balance arguments, the average effective charge in MST is found and then used to calculate the radial profile of the Ohmic heating. The local electron thermal diffusion is then found by inverting the energy balance equation to fit the electron temperature profile using a low resolution χ_e profile.

3.3.1 Global Confinement Characteristics

One relatively simple measure of confinement is the ratio of the total stored thermal pressure to the magnetic pressure supplied by the poloidal magnetic field at the edge

$$\beta_p = \frac{\langle P \rangle}{B_p(a)^2/2\mu_0}, \tag{3.12}$$

where the brackets denote a volume average. This is referred to as the poloidal beta. Figure 3.23 shows the time evolution of the poloidal beta through the sawtooth. The ion pressure increase is sufficient to cause β_p to increase slightly at the sawtooth crash despite the fact that the electron pressure is decreasing during this period. This drop in the electron pressure eventually overwhelms the increase from the ion pressure and causes β_p to decrease. The average β_p for this 400 kA standard case is $\sim$5.5% and the time evolution is qualitatively similar to the RMS $m = 0$ mode amplitude. This is consistent with past work in suggesting that it is the transport across the reversal surface which sets the global confinement characteristics of the standard MST plasma.

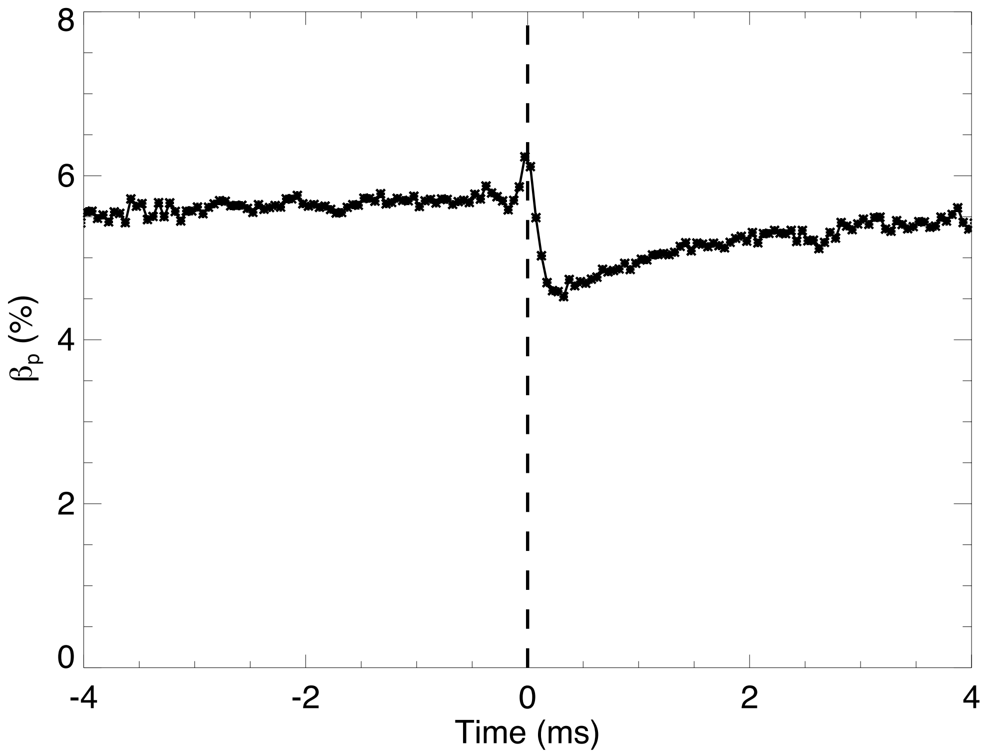

Figure 3.23: Sawtooth evolution of β_p.

Another important measure of confinement in the plasma is the energy confinement time. Perhaps the simplest statement of conservation of energy for a given volume of space is $\Delta W = E_{in} - E_{out}$ where W is the total energy stored in that volume of space. The instantaneous form of this equation is the power balance equation, $\dot{W} = P_{in} - P_{out}$ where $\dot{W}$ is the rate of change in the total energy stored in a volume, P_{in} is the energy per unit time going into a volume and P_{out} is the energy per unit time coming out. When only thermal energy is considered then:

$$\frac{dW_{th}}{dt} = P_h - P_{loss}, \tag{3.13}$$

$$W_{th} = \frac{3}{2}\int_0^a (n_eT_e + n_iT_i)dV, \tag{3.14}$$

where W_{th} is the stored thermal energy, P_h is the heating power, and P_{loss} is the heat lost through conduction, convection, and conversion to other forms of energy. If, as a thought experiment, we were to then turn off the heat source and assume that P_{loss} is constant in time, all of the stored thermal energy will be lost in some time, Δt. This, of course, is not what really happens, but it gives an intuitive sense of what these quantities mean. We can write this as:

$$-P_{loss} = \frac{0 - W_{th}}{\Delta t}. \tag{3.15}$$

We identify this Δt as the energy confinement time, τ_E, defined as,

$$\tau_E \equiv \frac{W_{th}}{P_{loss}} = \frac{W_{th}}{P_h - \frac{\partial W_{th}}{\partial t}}. \tag{3.16}$$

Measuring all the possible channels for power loss is generally significantly more challenging than measuring the heating power and the change in stored thermal energy so the latter form is generally the one used (note that the heating power is not the same as the input power as the input power also goes into other things such as changing the stored magnetic energy).

The dominant heat source at any given time in a standard MST plasma is Joule heating. In 1841 J.P. Joule reported that the heating power of a current carrying wire is $P_h = I^2R$ where I is the current and R is the resistance. More generally, power consumed by an electrical circuit is $P = VI = \int \mathbf{E}\cdot\mathbf{J}\, dV$. (Note that this doesn't mean that the power is dissipated in the circuit. Consider the case of an inductor which takes some amount of power to build up the stored magnetic field before the voltage drop across it goes to zero.) This is the total integrated rate of work done by the electromagnetic field on the circuit which is generally manifest as some combination of heat and mechanical motion.

Internal electric field profile measurements are relatively difficult to make in MST. A simpler method, especially for global measurements, is to apply the Poynting theorem (see appendix B):

$$\mathbf{E}\cdot\mathbf{J} = -\frac{d}{dt}\frac{1}{2}\left(\frac{1}{\mu}B^2 + \epsilon E^2\right) - \nabla\cdot\underbrace{(\mathbf{E}\times\mathbf{B})}_{\mathbf{S}}, \tag{3.17}$$

where $\mathbf{S}$ is generally called the Poynting vector. The volume integral of equation 3.17 is essentially another statement of energy conservation, this time for the electromagnetic field. The change in the total mechanical and magnetic energy in a give volume is equal to the electromagnetic power that goes into or out of that volume,

$$\begin{aligned} \dot{W}_{mech} &= \int_V \mathbf{E}\cdot\mathbf{J}\, dV & (3.18)\\ \dot{W}_{E-M} &= \frac{d}{dt}\frac{1}{2}\int_V \left(\frac{1}{\mu}B^2 + \epsilon E^2\right)\, dV & (3.19)\\ \dot{W}_{mech} + \dot{W}_{E-M} &= \underbrace{-\int_A \frac{1}{\mu_0}(\mathbf{E}\times\mathbf{B})\cdot dA}_{P_{Poynting}}, & (3.20) \end{aligned}$$

where $P_{Poynting}$ is the Poynting power through the surface A that encloses the volume V. Strictly speaking, this relation requires that the medium be linear in its electromagnetic properties, with negligible dispersion or losses, so that $\dot{W}_{E-M}$ represents the total electromagnetic energy density[13]. To good approximation μ and ϵ can be set to μ_0 and ϵ_0 for a plasma (if the plasma particles are considered free, though more sophisticated approximations are used in, for example, plasma wave analysis). For MST plasmas, the energy in the electric field is negligible compared to the energy in the magnetic field so $W_{E-M} \approx W_{mag}$. Assuming a toroidal surface at the plasma boundary, only the radial component of the cross product needs to be evaluated. The Poynting power then is expressed as:

$$\int_A \frac{1}{\mu_0} (\mathbf{E} \times \mathbf{B}) \cdot dA = \frac{1}{\mu_0} \left(\int_A (E_\theta B_\phi - E_\phi B_\theta) \, rR d\theta d\phi \right) = (V_\theta I_\theta - V_\phi I_\phi) \, . \tag{3.21}$$

Where V_ϕ and V_θ are the induced $\mathcal{EMF}$'s in the toroidal and poloidal directions respectively, I_ϕ is the measured plasma current, and $I_\theta \equiv \frac{2\pi R}{\mu_0} B_\phi(a)$. Putting all this together we can define P_h as:

$$P_h = (V_\phi I_\phi - V_\theta I_\theta) - \dot{W}_{mag}. \tag{3.22}$$

On a technical side note, the question of power flow in the toroidal circuit has recently come up. This contribution to the power, which is small at most times, changes sign and becomes large at the sawtooth crash. Unfortunately, the sign conventions of the operational diagnostics on MST are somewhat confusing and sometime contradictory. The plasma current, for example, is in the negative toroidal direction but is recorded as positive, presumably for convenience. The power flow from the poloidal circuit has to be into the plasma at all times so regardless of sign in the database, $I_\phi V_\phi$ is positive. For the toroidal circuit, the toroidal field at the edge is always negative in MST coordinates. This just leaves the induced poloidal voltage to be determined. Recall that the toroidal flux in MST increases at the sawtooth crash and that the integral form of Faraday's law is $\int \mathbf{E}\cdot d\mathbf{l} = -\frac{d\Phi_B}{dt}$. For a poloidal loop at r=a where a is the minor radius of MST, $2\pi a E_\theta$ must be negative at the crash to be consistent with the increase in toroidal magnetic flux. This means that $V_\theta I_\theta$ is positive at the sawtooth crash, meaning power is coming out of the plasma at the sawtooth crash and is being added to the plasma away from the sawtooth crash. This makes sense intuitively as one might expect the external circuits to be driving the plasma in the quiescent phase between sawteeth and that less obvious behavior may occur in the dynamic phase at the sawtooth crash. Finally, it should be noted that the combination of the shell and the eternal circuit make a good flux conserver, but the presence of the external circuit allows power to flow in and out of the plasma volume.

The energy confinement time can now be defined as:

$$\tau_E = \frac{W_{th}}{(V_\phi I_\phi - V_\theta I_\theta) - \dot{W}_{mag} - \dot{W}_{th}}. \tag{3.23}$$

It is important to note that this calculation assumes that all of the work done by the electromagnetic fields on the plasma goes into heating the plasma (in other words the electro-magnetic field is not doing any mechanical work on the plasma). In general this is a good assumption, but it may not be at the sawtooth crash when the motion of the plasma (the fluctuation amplitudes in particular) changes rapidly. Though this is likely to be a small effect, it may be important near the sawtooth crash, so the time right around the sawtooth crash has been left out of the following analysis.

The change in stored magnetic energy in equation 3.23 is found using the results of the time series of equilibrium reconstructions previously discussed and shown in figure 3.19. The time derivative can be found by performing a simple numerical derivative; however, this leads to a very noisy result that is primarily due to variation in the fields that are within the uncertainty in the fit result. The characteristic change in total stored magnetic energy clearly varies in a more uniform way than the sequence of reconstructions would suggest. For this reason, the magnetic energy was broken into two periods, before and after the sawtooth, and the values were fit with a line. The slope of this line is assigned as the characteristic $\dot{W}_{mag}$ and used for all of the time slices for which each of the two fits were performed. Again, the time points around the sawtooth event were left out of the fits. For the purpose of finding τ_E, the change in stored thermal energy in equation 3.23 is also found in this way. Figure 3.24 shows the fit results for these two quantities in the two regions of time. We

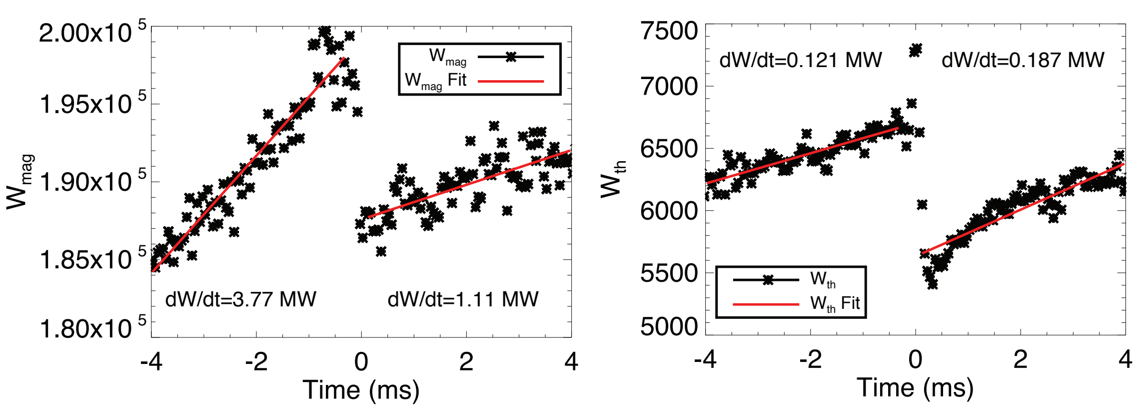

Figure 3.24: The stored magnetic and thermal energy and associated linear fits.

can combine this information with the evolution of the heating power to arrive at the energy confinement time. The Poynting flux and heating power as well as the resulting energy confinement time are shown in figure 3.25. The global energy confinement time

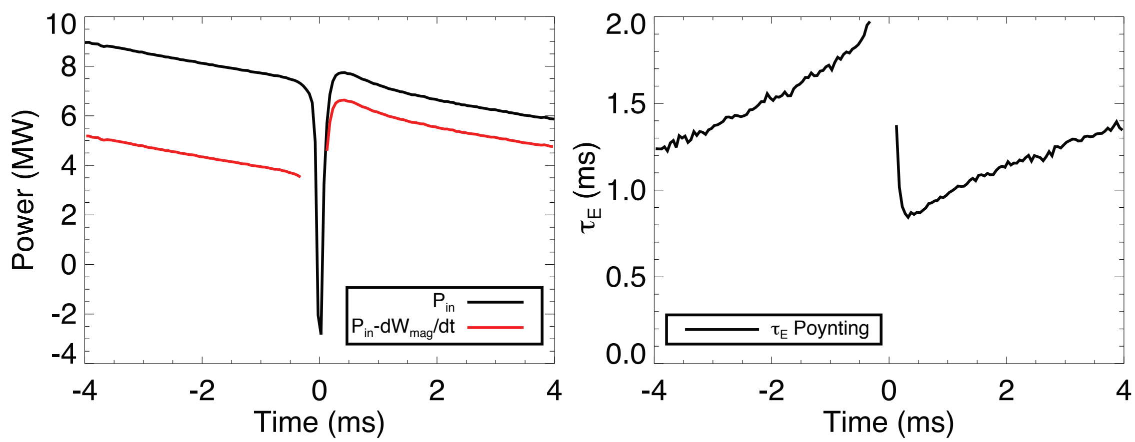

Figure 3.25: The Poynting power and heating power (left) and the resulting energy confinement time (right) for this set of data.

is about 1.31 ms on average.

The stored magnetic and thermal energies increase slowly between sawteeth and drop rapidly at the sawtooth crash. The external circuits are putting in about 7 MW of power over that period (~55 kJ total), a lot of which is either consumed or expelled at the crash. In terms of the magnetic field alone, about 10 kJ of energy are lost at the crash in about 100 μs, or 100 MW of power comes out of the magnetic field. A significant amount of this power can be accounted for due to measured ion heating and increased radiated power, but not all of it.

Assuming all of it went into heating the plasma and given the fact that about 10 MW of heat is still lost from the stored thermal energy, the implied energy confinement time is about 50 μs at the crash ($5000\ J/100\ MW \approx 50\ \mu s$). Of course, all the power does not go into heating, but again, it is difficult to account for all of it. Some is lost to radiation, some goes into heating the ions, and some probably goes into heating the electrons. This suggests that an alternate method for finding the input power may prove fruitful for looking at the energy confinement time near the sawtooth crash.

The use of the Poynting flux to find the input power is reasonable for a global analysis away from the crash, but it is less useful for the local analysis that is needed later for measuring the local thermal diffusion. This is due in part to the difficulty of determining the internal electric field profiles with a high degree of confidence. Furthermore, the difficulty in estimating the energy losses at the crash make using the Poynting flux during this phase of the sawtooth cycle unreasonable. A useful alternative is to apply Ohm's law instead of Poynting's theorem to find the heat source. The generalized Ohm's law is arrived at by combining the electron and ion equations of motion and can be expressed as :

$$\mathbf{E} = \eta\mathbf{J} - \mathbf{V}\times\mathbf{B} - \frac{1}{ne}\mathbf{J}\times\mathbf{B} - \frac{1}{ne}\nabla\cdot\mathbf{P} + \frac{m_e m_i}{\rho_M e^2}\frac{\partial\mathbf{J}}{\partial t}. \tag{3.24}$$

Assuming that equation 3.24 can be separated into components that are parallel and perpendicular to the magnetic field, and that it is the parallel component which is of primary interest, then the second and third terms on the right hand side are zero by definition, the parallel pressure gradient is assumed to be zero due to rapid conduction of heat along field lines, and the last term is always negligible. This analysis is only strictly true in the case in which the parallel direction actually means parallel to the full field. Typically, parallel and perpendicular are defined by the mean field only.

This means that second order terms such as $\left\langle \tilde{\mathbf{V}} \times \tilde{\mathbf{B}} \right\rangle$ can contribute to the mean electric field. It is not clear, however, that these fluctuations heat the plasma directly so we will consider only the zeroth order parallel Ohm's law,

$$E_{\|} = \eta J_{\|}. \tag{3.25}$$

The work done by the electromagnetic fields then is simply

$$\int \mathbf{E} \cdot \mathbf{J} dV \approx \int \eta J_{\|}^2 dV, \tag{3.26}$$

where $\int \eta J_{\|}^2 dV$ is referred to as the Ohmic power.

The parallel current density profile is computed using MSTFit and then combined with the resistivity profile to generate an estimate for the the Ohmic heating power delivered to the electrons in the plasma. The parallel electrical resistivity for a plasma in a magnetic field, called the Spitzer resistivity[14], is

$$\eta_{sp} = 1.04167 \times 10^{-4} \frac{Z_{eff} ln\left(\lambda\right)}{T_e^{3/2} f\left(Z_{eff}\right)} \tag{3.27}$$

where T_e is in eV and η_{sp} has units of Ωm. $ln(\lambda)$ is the Coulomb logarithm and f(Z) is the electron-electron collisional correction[15]. These are defined as

$$ln\left(\lambda\right) \approx 24 - ln\left(\frac{\sqrt{n_e}}{T_e}\right), \tag{3.28}$$

$$f\left(Z_{eff}\right) \approx \frac{1 + 2.96Z + 0.753Z^2}{1 + 1.198Z + 0.222Z^2}, \tag{3.29}$$

respectively, where T_e, once again, is in eV and n_e is in m^{-3}. For Z=1, f(Z)≈1.95 and is essentially the perpendicular to parallel scale factor shown in the NRL formulary. The fact that MST is a toroidal device requires the neoclassical correction, which adds two additional terms (and several quantities) of interest[16].

$$\eta_{neo} = \eta_{sp} \times \frac{1 + \xi(Z_{eff})\nu_{*\epsilon}}{1 + \xi(Z_{eff})\nu_{*\epsilon} - f_t} \times \frac{1 + \xi(Z_{eff})\nu_{*\epsilon}}{1 + \xi(Z_{eff})\nu_{*\epsilon} - C_R(Z_{eff})f_t} \tag{3.30}$$

where f_t is the trapped fraction, $\nu_{*\epsilon}$ is the ratio of the effective collision frequency to the bounce frequency, ξ is the effective electron collisionality, and C_R is a further enhancement of the resistivity due to electron-electron collisions.

The total Ohmic heating power within the plasma volume is defined as $P_\Omega \equiv \int_0^a \eta J_\parallel^2 \frac{\partial V}{\partial \rho_v} \partial \rho_v$ then the effective charge can be determined by adjusting Z_{eff} until $P_\Omega = -\dot{W}_{mag} - P_{Poynting}$. For this data set, a Z_{eff} of about 3, which occurs for moderate impurity ion concentrations as discussed earlier, satisfies this relation. Figure 3.26 show a comparison of the input power and energy confinement time for these two methods of determining the input power. The average τ_e found using the Ohmic input power is 1.34 ms, which is very close to the 1.31 ms found using Poynting's theorem.

For the rest of the work in this chapter, a flat Z_{eff} of 3 is assumed and the heat source is assumed to be simply ηJ^2. Note that there are several assumptions inherent here. In particular, it is assumed that the entirety of the work done by the electromagnetic field goes into heat with a negligible amount used to drive plasma motion, including the magnetic fluctuations that are so prevalent in the RFP. These fluctuation, however, are relatively small between sawteeth and it maybe that Z_{eff} is

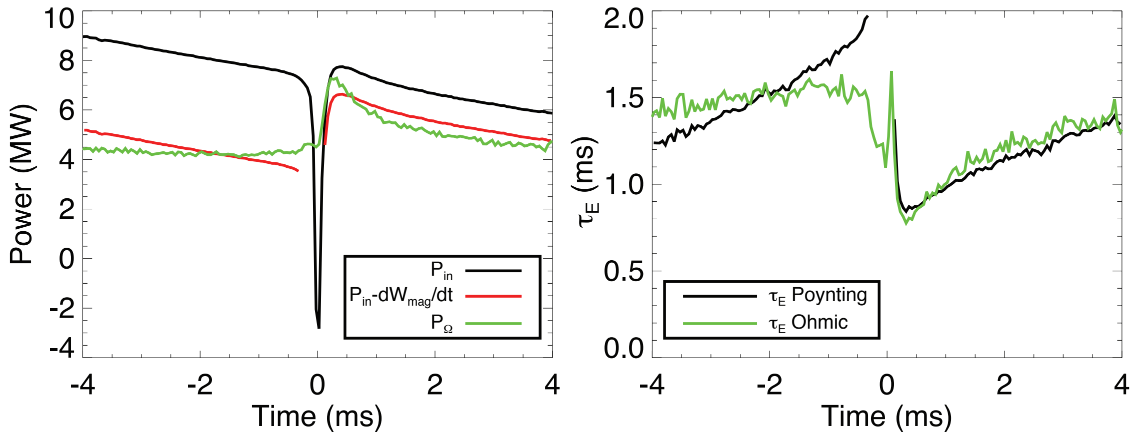

Figure 3.26: The Ohmic heating power and the heating power using Poynting's theorem (left) and the resulting energy confinement times (right) for this set of data.

really 3 on average. Furthermore, the Z_{eff} profile is assumed to be flat. It is not at all clear that this is the case as measurements of impurity ion density tend to show an off axis peak rather than a flat profile. That said, the global measurements presented here are relatively insensitive to the details of the profile of Z_{eff}.

3.3.2 Determining the Electron Thermal Diffusion

The energy confinement time was found by analyzing the global conservation of thermal energy. In this section, the conservation of total energy for a single species, namely the electrons, will be analyzed. The electrons are of particular interest and the statement of energy conservation is essentially $\dot{W}_{th,e} = E_{in} - E_{loss}$. Thermal energy can be added to the electrons by Ohmic heating (with power density $PD_\Omega = \eta J^2$) and by power transfer from the ions in the event that the ions are hotter than the electrons ($PD_{e\ to\ i}$). The main energy loss channels are conduction ($\mathbf{Q_{cond}}$), convection of particles ($\mathbf{Q_{conv}}$), radiation (PD_{rad}), and power transfer to ions when the ions are cooler than the electrons. Another way to think of this is that the change in stored thermal energy in a given region of space is due to the energy flux into or out of that region and the sources or sinks of energy contained within that region of space[17]:

$$\frac{\partial}{\partial t}\left(\frac{3}{2}n_e T_e\right) = S_E - \nabla \cdot \left(\mathbf{Q_{cond}} + \mathbf{Q_{conv}}\right). \tag{3.31}$$

The sources and sinks of energy are $S_E = PD_\Omega - PD_{e\ to\ i} - PD_{rad}$. The convective heat flux is $\mathbf{Q_{conv}} = \frac{5}{2}\mathbf{\Gamma}_e T_e$ (where $\mathbf{\Gamma}_e$ is the electron particle flux) and the conductive heat flux, as defined by Fourier's Law, is

$$\mathbf{Q_{cond}} = \mathbf{q_e} = -n_e \chi_e \nabla T_e, \tag{3.32}$$

where χ_e is the electron thermal diffusion. Taking the volume integral of this equation yields the power balance equation which, after solving for χ_e, has the form:

$$\chi_e = \frac{P_\Omega - \dot{W}_{th,e} - P_{rad} - P_{e\ to\ i}}{4\pi^2 R \rho_v n_e \frac{\partial}{\partial \rho_v} T_e} + \frac{5}{2}\frac{\Gamma_r T_e}{n_e \frac{\partial}{\partial \rho_v} T_e}. \tag{3.33}$$

where $\rho_v = \sqrt{\frac{V_\psi}{2\pi^2 R}}$, P_{rad} is the radiated power, $P_{e\ to\ i}$ is the electron to ion power transfer, and Γ_r is the radial component of the electron particle flux[2, 18].

The difficulty with finding χ_e by solving equation 3.33 is that when the temperature profile becomes moderately flat, the thermal diffusion can go to infinity or become negative depending on small differences in how the data is fit. Functionally, this leads to a strong dependence on choice of numerical model for the electron temperature profile. The value of the thermal diffusion can change by orders of magnitude depending on the shape chosen to describe the temperature profile data. If no shape is assumed and a free knot spline fit is used, the number of fit parameters chosen changes the local value of the thermal diffusion by orders of magnitude and often shifts the inflection points of the profile substantially. Since there is no strong physical basis for choosing one temperature model over another we are left with statistical methods such as an F-test which is likely to indicate a different best fit model for each individual case. This is not only unwieldy when processing a large amount of data, but also makes the resulting analysis somewhat suspect as the effect of changing the fitting model may be the biggest factor in any variation seen in the evolution of χ_e.

In this work, rather than fit the electron temperature profile and then determine the electron thermal diffusion, we guess the electron thermal diffusion and then, assuming $\dot{W}_{th,e}$ is known, solve equation 3.31 (which is now a second order ODE rather than a PDE) for T_e. The χ_e profile is then adjusted until a best fit to the temperature data is found. While this does not fundamentally change the "choice of model" problem, it does allow a somewhat easier interpretation of the physical effects of that choice of model. In particular the model can be chosen such that the radial resolution of the thermal diffusion profile is very low and only the characteristic value of the thermal diffusion in a given region of the plasma is considered. See Appendix C for more details on how this T_e profile is computed from χ_e.

The heat source term, S_E, is dominated by the ohmic power density, ηJ^2, but the electron to ion power loss and the power lost to radiation were also accounted for. The local change in thermal energy is also accounted for and is generally relatively small except in the core region near the sawtooth crash when it briefly reaches 60%

of the Ohmic power density. The convective transport was not considered for this work, though past work has shown that this term is generally small over most of the plasma[19, 18]. The amount of heat the electrons transfer to the ions through collisions was computed by Braginskii[20] as:

$$PD_{e\ to\ i} = 3\frac{m_e}{m_i}\frac{n_e\left(T_e - T_i\right)}{\tau_{ei}} \tag{3.34}$$

The majority ion species is deuterium and the collision time (again using $Z^2 n_i = Z_{eff} n_e$) is defined by as[21]:

$$\tau_{ei} = \frac{12\epsilon_0^2}{\sqrt{\frac{2e}{\pi^3 m_e T_e^3}} Z_{eff} n_e e^2 Ln\left(\Lambda\right)}. \tag{3.35}$$

Recall that the ion temperature is assumed to have the same profile shape as the electron temperature and is scaled such that the central temperature is equal to the Rutherford scattering measurement. This is likely a slight underestimate because the ion temperature is measured over an extended region near the axis (see figure 3.1), but not exactly on axis. This error, however, is expected to be small as the ion temperature profile is expected to be flat in the core region of the plasma.

The total radiated power is measured with a pyro bolometer and is assumed to be edge localized. The power density profile for the radiated power is assumed to be proportional to $P_\Omega * (r/a)^8$, and is scaled to match the pyro bolometer measurement made at the edge of MST[22]. Figure 3.27 shows the time evolution of the ensemble averaged pyro bolometer measurement as well as an example of the assumed radiated power profile away from a sawtooth.

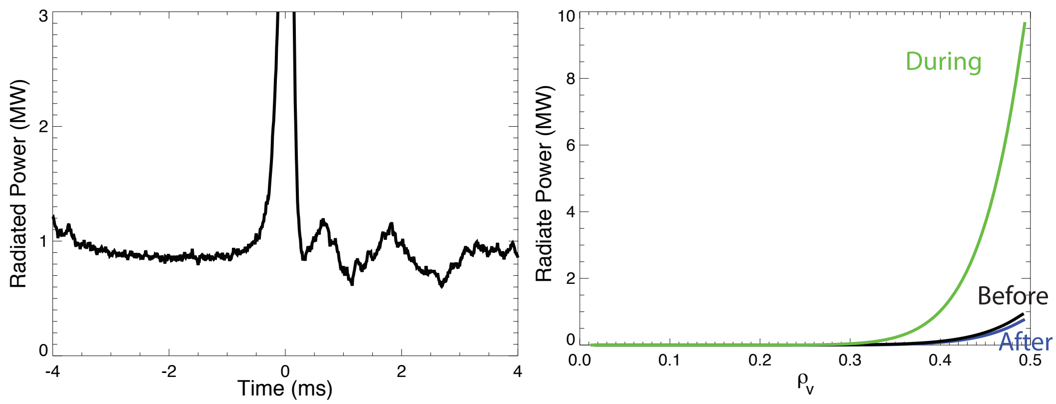

Figure 3.27: Radiated power measured by a bolometer at the edge of MST and the radiated power from before, during, and after a sawtooth.

Inside the reversal surface, the Ohmic power density is by far the largest heating source for the electrons except at the sawtooth crash when the change in stored thermal energy can briefly reach 60% of the Ohmic power. Figure 3.28 shows the value of each of the source terms at three different times.

The temperature profiles in standard plasmas in MST can generally be broken into four distinct regions. The designation of these regions is two fold. First, the temperature gradient tends to have boundaries or regions over which the temperature profile has a fairly linear slope to it. Second, the mode rational surfaces for the resonant magnetic perturbations fall roughly into four regions which correspond to these temperature gradient regions. The four regions are the 'core' where the low n, m=1 modes are resonant, the 'mid-radius' where the high n, m=1 modes are resonant, the 'reversal region' where all the m=0 modes are resonant, and the 'edge' region where the high n, m=-1 modes are resonant. Figure 3.29 shows three example temperature fits and fit χ_e profiles. The uncertainty in χ_e is shown by the shaded region which is

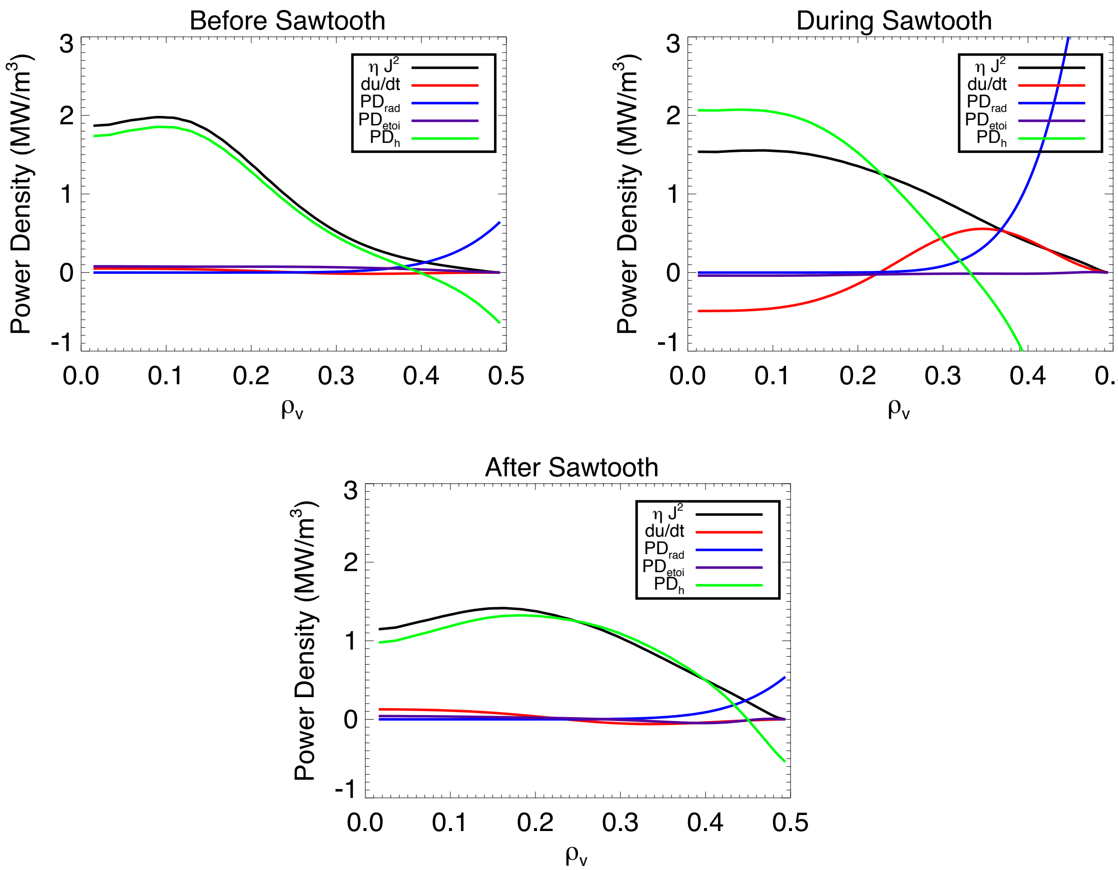

Figure 3.28: Power density profiles at three times, before (top left), at (top right), and after (bottom center) the sawtooth. The Ohmic power density is by far the largest term for most of the sawtooth cycle with the change in stored thermal energy and the radiated power becoming important near the sawtooth crash. The green line shows the total heat source $PD_h = \eta J^2 - \dot{u} - PD_{rad} - PD_{e\ to\ i}$. Note that $\dot{u} = \frac{3}{2}\frac{\partial n_e T_e}{\partial t}$. The typical relative uncertainty for ηJ^2 is less than 20%, for $\dot{u}$ about 300%, for PD_{rad} less than 3%, about 30% for $PD_{e\ to\ i}$.

found by Monte Carlo error analysis, varying all the dependent variables, including those found from the equilibrium reconstruction, within their uncertainties. Z_{eff} is assumed to be 3 ± 2.

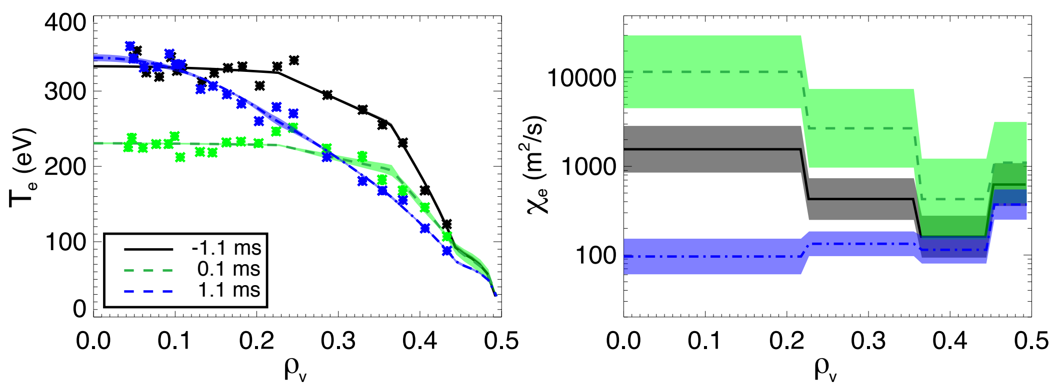

Figure 3.29: The fit electron temperature data (points) and profile fits (lines) at three time points, before, during, and after the sawtooth (left) and the χ_e values that generated those temperature profiles (right).

Finally, we can perform this same fit for the entire time sequence of equilibrium reconstruction and look at the time evolution of χ_e in the four different regions of the plasma (see figure 3.30). While all four regions have a similar time evolution in general, there are some differences. The core region varies over several orders of magnitude, reaching a maximum at the sawtooth crash and a minimum shortly after the sawtooth. The mid-radius and reversal region have a similar time history but less dramatically so. In these outer regions, the χ_e is relatively constant until about 1.5 ms before the sawtooth crash, while the core region increases more or less continuously from its minimum right after a crash. It is also interesting to note that shortly after the sawtooth crash (about +1 ms) the thermal transport in the mid radius and reversal region are higher than that of the core indicating that the electron confinement in

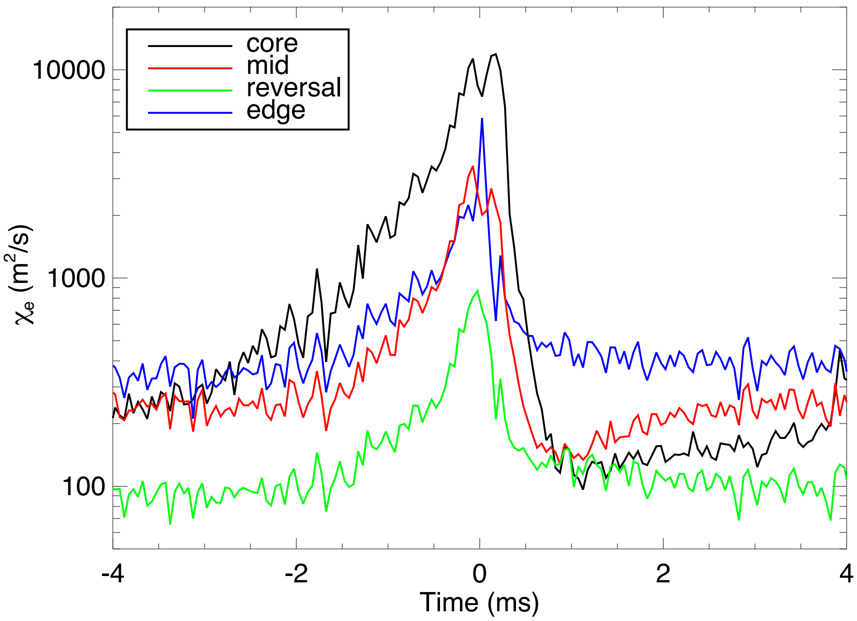

Figure 3.30: χ_e vs. time in four region of the plasma.

the core is quickly recovered and that the energy confinement further out in radius takes longer to recover. Finally, aside from the short period right after the sawtooth crash, the thermal diffusion in the reversal region is always the lowest with an average characteristic χ_e in this region of $\sim$80 m^2/s. Not surprisingly, this time behavior is consistent with the time history of the local mode amplitudes. The core mode amplitudes increase in time leading up to the sawtooth and reach a minimum after the sawtooth while the $m = 0$ modes increase rapidly right at the sawtooth event and decrease slowly afterwards. This all suggests that the thermal transport is MHD driven throughout the sawtooth cycle, consistent with previous work on MST. This is also consistent with work done on other machines in which the temperature profile evolution is estimated by assuming the χ_e is equal to the edge mode amplitudes for modes in a given region scaled by a fitting factor[23, 24].

The thermal transport in a stochastic magnetic field was described by Rechester and Rosenbluth as being proportional to $\tilde{b}^2/B^2$[25]. To estimate this with mode data from the edge of MST and from equilibrium reconstructions we can model the core region as:

$$\chi_e = C_{core} \sum_{6}^{8} \frac{\tilde{b}_{\theta,n}^2}{B_t(0)^2}. \tag{3.36}$$

Here the transport in the core region is assume to be due to the average of the $m = 1$, $n = 6 - 8$ mode amplitudes and the coefficient accounts for the difference between the edge measurement and the fluctuation amplitude at the rational surface as well as the average correlation length of the magnetic fluctuations. In the mid radius the time evolution of the mean field more closely resembles the average toroidal field so:

$$\chi_e = C_{mid} \sum_{9}^{15} \frac{\tilde{b}_{\theta,n}^2}{\langle B_t \rangle^2}. \tag{3.37}$$

In the edge the poloidal field dominates so the behavior at the thermal diffusion should go like:

$$\chi_e = C_{rev} \sum_{1}^{4} \frac{\tilde{b}_{\phi,n}^2}{B_p(a)^2}. \tag{3.38}$$

This implicitly assumes that $\tilde{b}_{r,n}$ is proportional to $\tilde{b}_{\theta,n}$ or $\tilde{b}_{\phi,n}$ for each mode, though this relationship has only been confirmed for the m=1, n=6 mode as was shown in [26]. The three coefficients are found by taking the average of the ratio of this χ_e to the fit χ_e. The time evolution of the resulting thermal diffusion is shown in figure 3.31. The edge region is not shown because there is no straight forward way to obtain data from MST for the modes resonant outside the reversal surface, but given the proximity of the conducting shell, the $\tilde{b}_r$ amplitude for the modes resonant in this region should

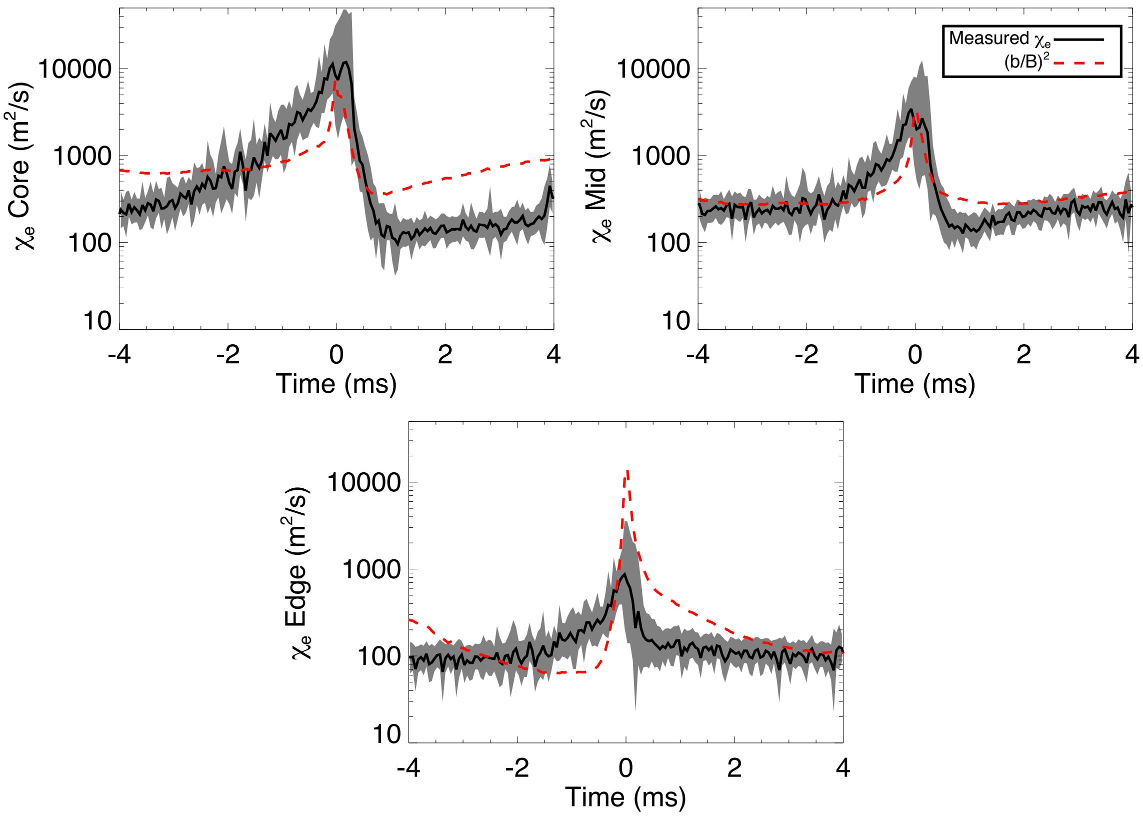

Figure 3.31: Time evolution of the χ_e from the T_e profile fit (black) compared to χ_e for a simple Rechester-Rosenbluth type transport (red dashed) in the three inner regions of the plasma. The edge region is not shown and is expected to be dominated by edge effects rather than stochastic transport.

be very small and the relatively large measured thermal diffusion is likely due to edge effects. While a high degree of quantitative agreement is not expected from this simple comparison, there is somewhat reasonable agreement in the core and striking agreement in the mid radius through most of the sawtooth cycle. The thermal diffusion near the reversal surface on the other hand does not appear to evolve in a way that is consistent with the m=0 mode amplitudes.

3.4 Discussion

In this chapter the reconstruction of the magnetic equilibrium for a sawtooth ensemble of data using a relatively simple two parameter fitting model was discussed. The magnetic equilibrium is an incredibly powerful tool for doing physics because it allows the accurate combination of many local measurements made in various locations around the machine. The implementation of a two parameter fitting model allows for rapid fitting of time sequences of data so that the time evolution of the plasma can be studied. The evolution of the equilibrium through a sawtooth was presented with particular attention paid to the evolution of the kinetic profiles, where the electron temperature and density were seen to drop sharply at the sawtooth crash and the ion temperature increased sharply. The global confinement characteristics of the plasma were then discussed where β_p was found to be about 5.5% and τ_E was found to be about 1.3 ms. The latter was found using Poynting's theorem, but the power through the shell is reasonably well matched by the Ohmic power if a flat $Z_{eff} = 3$ profile is assumed. The local electron thermal diffusion was then found (assuming the dominant heat source was Ohmic heating with the same $Z_{eff} = 3$ profile) by fitting a low resolution χ_e profile to the electron temperature profile measurements. The time sequence of these fits shows that the thermal diffusion changes by several orders of magnitude through the sawtooth cycle, particularly in the core. Furthermore, this evolution, at least in the core and mid-radius, is qualitatively similar to Rechester-Rosenbluth type stochastic thermal diffusion. A somewhat more involved quantitative comparison is discussed in the next chapter.

Arguably the most striking new result of this work is the determination of the χ_e

profile at high time resolution through a sawtooth event in high current MST plasmas with relatively low uncertainty. The critical quantities for this measurement are the electron temperature and the current density as the thermal diffusion is the most sensitive to these two profiles. The fact that the temperature profile is very flat in the inner half of the minor radius makes the power balance analysis very sensitive to the choice of model used to fit electron temperature profile. For this reason, the temperature profile was fit by specifying a thermal diffusion profile and computing the self consistent electron temperature that goes along with it. This has allowed some physical intuition to be used in choosing a fitting model to use. By dividing the plasma into four regions and assigning a characteristic value of thermal diffusion to each region we have obtained a time evolution for each region that makes physical sense and points to MHD driven transport throughout the sawtooth cycle. Furthermore, Poynting analysis of the global power balance away from the sawtooth has indicated that the effective charge is likely to be about 3. This value is slightly higher than the $Z_{eff} = 2$ that is typically used for MST, but is still physically reasonable and consistent with past results. Furthermore, direct measurements of Z_{eff} in PPCD using three different techniques, including recent measurements of the densities of many of the different impurity ion species using the ChERS system, suggest Z_{eff} is as high as 5. This is consistent with a value of 3 for standard plasmas as standard plasmas are cooler and are expected to have somewhat lower impurity ion confinement characteristics than the PPCD plasmas that were measured.

On a final note, it is worth commenting on the validity of a 1D model, which the standard method for transport analysis, for determining the heat transport in what is fundamentally a 3D problem. In the RFP, the equilibrium fields would decay rapidly where it not for some sort of dynamo action that converts the input poloidal flux to toroidal flux. This can occur through the MHD dynamo $\mathbf{E_{dynamo}} = -\mathbf{V} \times \mathbf{B}$, the Hall dynamo $\mathbf{E_{dynamo}} = \mathbf{J} \times \mathbf{B}$, or the kinetic dynamo where particles diffusing outward along stochastically wandering field lines carry significant current from the toroidal to the poloidal direction, or some combination of all three. The exact mechanism is not important here. The existence and sustainment of the RFP equilibrium speaks to the existence of some sort of dynamo mechanism and all of those mechanisms require a complex interaction between the equilibrium fields, the fluctuations, and the heat transport which modifies, and is modified by, both of these. Therefore, to fully understand the evolution of the heat transport in an RFP, the full 3D problem must be analyzed. That said, looking at the net effect of all that reaction and back reaction to see what the gross, observed behavior of the plasma is an important and useful first step in understanding the details of the transport in the RFP. Despite the fact that to be completely accurate one should consider the 3D system, the 1D analysis is still meaningful for identifying phenomenology. In fact, Frassinetti, *et al.*,[24] were able to go a step further and gain some degree of predictive capability for the equilibrium electron temperature profile by tying the evolution of the thermal diffusion to the measured evolution of the mode amplitudes (along some additional experimentally determined scaling factors) on the RFX device. As can be seen from figure 3.31, a method like this would likely work for the period between sawteeth, but is unlikely to work near the sawtooth as the evolution of the m=0 mode amplitudes in particular does not match the measured evolution of the thermal diffusion.

The simple comparison shown in figure 3.31 is in no way quantitative, but a more careful comparison in the next chapter in which significant effort has been put into obtaining an accurate quantitative comparison of the measured data to the Rechester-Rosenbluth model[25], will obtain a similar result to that shown in figure 3.31. The difficulty with making a quantitatively accurate comparison of the measured χ_e to that of a stochastic field is that one must accurately measure $\tilde{b}_r$ at the resonant surface for a given mode as well as the island width and the degree of island overlap (i.e. the stochasticity parameter). This means that one needs to know the radial profile of the mode amplitudes across the plasma minor radius. This is difficult to do experimentally so, as will be described in the next chapter, the MST plasma was simulated using a nonlinear, resistive, MHD code in order to obtain the fluctuation amplitudes at the mode rational surfaces. With this information, the electron thermal diffusion due to diffusion of the magnetic field lines can be calculated and compared to these measured values.

REFERENCES

[1] Anderson, J. K., Forest, C. B., Biewer, T. M., Sarff, J. S., and Wright, J. C. Equilibrium reconstruction in the Madison Symmetric Torus reversed field pinch. *Nuclear Fusion* **44**, 162–171 (2004).

[2] Anderson, J. K. *Measurement of the Electrical Resistivity Profile in the Madison Symmetric Torus*. PhD thesis, University of Wisconsin at Madison, (2001).

[3] Taylor, J. B. Relaxation of Toroidal Plasma and Generation of Reverse Magnetic Fields. *Physical Review Letters* **33**(19), 1139–1141 Nov (1974).

[4] Taylor, J. Relaxation and magnetic reconnection in plasmas. *Review of Modern Physics* **58**(3), 741–763 July (1986).

[5] Grad, H. Toroidal Containment of a Plasma. *Physics of Fluids* **10**(1), 137–154 (1967).

[6] Shafranov, V. Plasma equilibrium in a magnetic field. *Review of Plasma Physics* **2**, 103–151 (1966).

[7] Press, W., Teukolsky, S., Vetterling, W., and Flannery, B. *Numerical Recipes. The Art of Scientific Computing.* Cambridge University Press, New York, NY, 2nd edition, (1992).

[8] Chapman, J. T. *Spectroscopic Measurement of the MHD Dynamo in the MST Reversed Field Pinch.* Doctor of philosophy, University of Wisconsin at Madison, 1150 University Ave., Madison, WI, 53706, (1998).

[9] Bevington, P. R. and Robinson, D. K. *Data Reduction and Error Analysis for the Physical Science.* McGraw-Hill, 1221 Avenue of the Americas, New York, NY, 10020, third edition, (2003).

[10] Lanier, N. *Electron Density Fluctuations and Fluctuation-Induced Transport in the Reversed-Field Pinch.* PhD thesis, University of Wisconsin at Madison, 1150 University Ave., Madison, WI, 53706, (1999).

[11] Fiksel, G., Almagri, A. F., Chapman, B. E., Mirnov, V. V., Ren, Y., Sarff, J. S., and Terry, P. W. Mass-Dependent Ion Heating during Magnetic Reconnection in a Laboratory Plasma. *Phys. Rev. Lett.* **103**(14), 145002 Sep (2009).

[12] Stephens, H. *Electron Temperature Structures Associated With Magnetic Tearing Modes in the Madison Symmetric Torus.* PhD thesis, University of Wisconsin at Madison, (2010).

[13] Jackson, J. *Classical Electrodynamics.* John Wiley and Sons, Inc., 605 Third Avenue, New York, NY, third edition, (1999).

[14] Spitzer, L. and Härm, R. Transport Phenomena in a Completely Ionized Gas. *Phys. Rev.* **89**(5), 977–981 Mar (1953).

[15] Spitzer, L. *Physics of fully ionized gases.* Interscience tracts on physics and astronomy. Interscience Publishers, (1962).

[16] Hirshman, S. and Sigmar, D. Neoclassical Transport of Impurities in Tokamak Plasmas. *Nuclear Fusion* **21**(9), 1079 (1981).

[17] Hinton, F. L. and Hazeltine, R. D. Theory of plasma transport in toroidal confinement systems. *Rev. Mod. Phys.* **48**(2), 239–308 Apr (1976).

[18] Biewer, T. M. *Electron Thermal Transport in the Madison Symmetric Torus.* PhD thesis, University of Wisconsin at Madison, (2002).

[19] Biewer, T. M., Forest, C. B., Anderson, J. K., Fiksel, G., Hudson, B., Prager, S. C., Sarff, J. S., Wright, J. C., Brower, D. L., Ding, W. X., and Terry, S. D. Electron Heat Transport Measured in a Stochastic Magnetic Field. *Phys. Rev. Lett.* **91**(4), 045004 (2003).

[20] Braginskii, S. Transport processes in a plasma. *Reviews of Plasma Physics* **1**, 205 (1965).

[21] Goldston, R. and Rutherford, P. *Introduction to Plasma Physics.* Institute of Physics Publishing, Philadelphia, PA, (1995).

[22] Hokin, S. Particle and energy transport simulations of reversed field pinch plasmas. *Nuclear Fusion* **37**(11), 1615 (1997).

[23] Frassinetti, L., Alfier, A., Pasqualotto, R., Bonomo, F., and Innocente, P. Heat diffusivity model and temperature simulations in RFX-mod. *Nuclear Fusion* **48**(4), 045007 (13pp) (2008).

[24] Frassinetti, L., Brunsell, P., Cecconello, M., and Drake, J. Heat transport modelling in EXTRAP T2R. *Nuclear Fusion* **49**(2), 025002 (2009).

[25] Rechester, A. B. and Rosenbluth, M. N. Electron Heat Transport in a Tokamak with Destroyed Magnetic Surfaces. *Physical Review Letters* **40**(1), 38–41 (1978).

[26] Ding, W. X., Brower, D. L., Fiksel, G., Den Hartog, D. J., Prager, S. C., and Sarff, J. S. Magnetic-Fluctuation-Induced Particle Transport and Density Relaxation in a High-Temperature Plasma. *Phys. Rev. Lett.* **103**(2), 025001 Jul (2009).

Chapter 4

Numerical Simulations of MST at Experimental Values of Lundquist Number

4.1 Introduction

In the previous chapter the measured evolution of the magnetic equilibrium was found and used to determine the electron transport in MST. In this chapter, a set of first principles, force free, nonlinear, resistive MHD simulations performed with the DEBS code[1] are presented and used to determine the degree to which the electron transport in MST can be attributed to magnetic stochasticity. The low safety factor of MST allows for the possibility of a globally stochastic magnetic field, and this work was done to quantify the contribution of stochastic heat transport to the overall transport measured in MST. In order to achieve this goal, we performed several high spectral resolution runs at a Lundquist number that, for the first time in these nonlinear simulations, matches that of MST. Section 4.2 of this chapter gives a brief description of the DEBS code. Sections 4.3 and 4.4 show that at experimental values of Lundquist number, the simulation reproduces many of the features of a typical standard discharge in MST including the sawtooth period and the duration of the sawtooth crash. Section 4.5 show comparisons between the measured electron thermal diffusion, χ_e, from the previous chapter to the stochastic heat diffusion calculated in two different ways. The first method uses the Rechester-Rosenbluth model for stochastic heat diffusion[2] (χ_{RR}) and does not reproduce the experiment well. In contrast, the second method calculates the heat diffusion based on the calculated magnetic diffusion, referred to as χ_{MD}, and reproduce experimental results but only when trapped particles are taken into account[3].

4.2 Simulation Setup

All of the simulations presented here were performed with the DEBS code. DEBS computes the 3-D, nonlinear, resistive MHD equations in a periodic cylinder using a set of non-dimensional variables[1]. Table 4.1 presents these normalized variables used by DEBS in the first column as well as their dimensionalizing coefficients in the middle column. The dimensionalizing coefficients presented are necessary for physical interpretation of the simulation results and direct comparison to experiment. The associated numerical values from a typical 400 kA shot in MST are presented in the last column.

Normalized Quantity	Normalization Coefficient	MST 400kA Case
r, length	a (m) minor radius	0.52 m
T, temperature	T_0 (eV) temperature on axis	320 eV
Z, effective charge		2
ρ, mass density	$\rho_0 = \mu m_p n_i$ (kg/m^3)	4×10^{-8} kg/m^3
η, resistivity	$\eta_0 = 1.03 \times 10^{-4} \frac{ZLn(\Lambda)}{1.96 T_0^{1.5}}$ (Ω m)	$3\times10^{-7}\Omega$ m
$\mathbf{B}$, magnetic field	B_0 (Tesla) toroidal field on axis	0.4 T
$\mathbf{v}$, velocity	$v_{a0} = B_0/\sqrt{\mu_0\rho_0}$ (m/s) (Alfven vel.)	1.745×10^6 m/s
$\mathbf{J}$, current density	$J_0 = B_0/\mu_0 a$ (A/m^2)	6.14×10^5 A/m^2
$\mathbf{E}$, electric field	$E_0 = \eta_0 B_0/\mu_0 a$ (V/m)	0.184 V/m
V, voltage	$V_0 = E_0 a$ (V)	0.096 V
t, time	$\tau_r = \mu_0 a^2/\eta_0$ (s)	1.13 s
ν	$\nu_{\perp_0} = \eta_2^i/\rho_0$ (m^2/s) (perp. kin. visc.)	0.06 m^2/s
$S = \tau_r/\tau_a$	$\tau_r v_{a0}/a$ (Lundquist number)	3.8×10^6
$P_m = \mu_0\nu/\eta$	$\nu_{\perp_0}\tau_r/a^2$ (magnetic Prandtl number)	0.25
Θ, pinch parameter	$B_\theta(a)/\langle B_t\rangle$	1.7

Table 4.1: Normalization coefficients for DEBS fields.

DEBS solves the following equations to described the "force-free" plasma evolution:

$$\frac{\partial \mathbf{V}}{\partial t} = -S\mathbf{V}\cdot\nabla\mathbf{V} + S\mathbf{J}\times\mathbf{B} + \nu\nabla^2\mathbf{V} \tag{4.1}$$

$$\frac{\partial \mathbf{A}}{\partial t} = S\mathbf{V}\times\mathbf{B} - \eta\mathbf{J} \tag{4.2}$$

$$\mathbf{B} = \nabla\times\mathbf{A} \tag{4.3}$$

$$\mathbf{J} = \nabla\times\nabla\times\mathbf{A}. \tag{4.4}$$

Here, S is the Lundquist number, η is the resistivity, and ν is the viscosity. The Lundquist number on axis was set to match MST parameters as shown in Table 4.1. Since these were force free simulations in which the pressure was not self consistently evolved (i.e. zero β simulations), the resistivity profile can not be self consistently calculated. Resistivity, however, was included in the form of an ad-hoc profile that was fixed in time throughout the simulation. To try to match experimental data as closely as possible, a resistivity profile calculated from experimental data taken between sawteeth was used. Note that the slope of the neoclassical resistivity profile on axis is non-zero. While this was an oversight that could, in principle, cause problems with the code, none were seen. In fact, setting the derivative to zero and restarting the code and allowing it to run for several sawteeth did not result in any significant changes in the simulated plasma behavior. Two resistivity models were tried and the results of which will be shown here. The first was a Spitzer resistivity and the second a neoclassical resistivity profile calculated from experimental data from a few milliseconds before the sawtooth. Figure 4.1 shows the two normalized resistivity profiles used. Note that there is a slight mapping error here when going from the MST flux geometry to Debs. In MST the effective radius of the flux surfaces goes from zero on axis to about 50 cm at the limiter. This means that the comparable radius is actual 50 cm not 52 cm. In this work, the ρ_v ordinate was mapped to the r/a ordinate used in Debs by simply doing $\rho_v/max(\rho_v)$, but the minor radius was assumed to be 52 cm in Debs. In the future, it would be wise to make the minor radius 52 cm in Debs as this can be more accurately compared to the MSTFit results. The viscosity also can not be evolved self consistently, nor does it come from experimental measurements. Rather, the ν is dynamically adjusted in time and space to provide numerical stability. Specifically, it is adjusted such that $\nu = S_0 v_{max}/(k_{max} R_{cell})$ to damp sub-grid scale fluctuations. v_{max} and k_{max} refer to the maximum value of the magnitude of the fluid

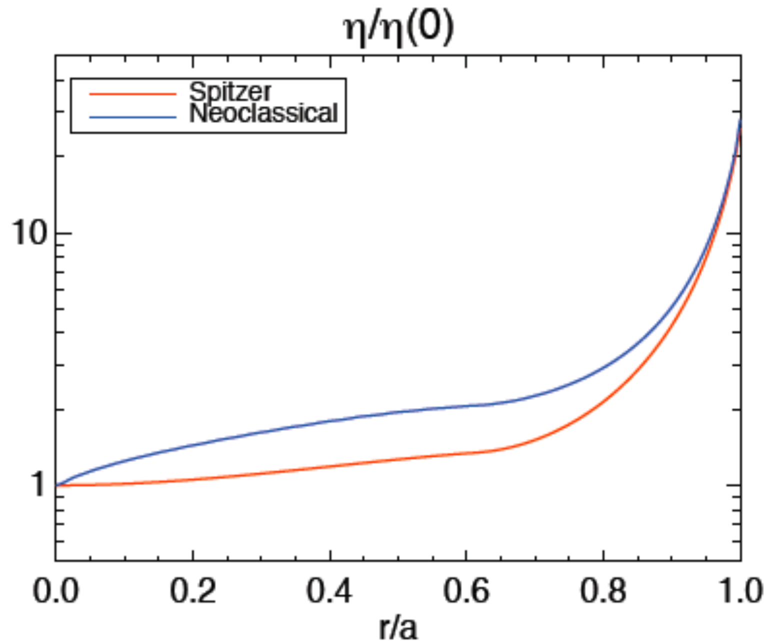

Figure 4.1: Normalized resistivity profiles used for the two simulations presented here. The red curve is the Spitzer resistivity and the blue curve is the neoclassical resistivity.

velocity and k-vector, respectively, on a cylindrical surface. ν, therefore, is just a function of radius rather than a 3D quantity, and R_{cell} is a user supplied input that is usually set to 0.1[4]. The degree of viscous dissipation relative to resistive dissipation is described by the Prandtl number $P_m = \mu_0\nu/\eta$ and is a useful scaling parameter to use along with the Lundquist number for characterizing a simulation. For the dimensionless case P_m is approximately ν. P_m for these MST discharges is typically about 0.25 (calculated using the perpendicular Braginskii viscosity) while the peak P_m for these simulations is typically about 250 between sawteeth (and several thousand at sawteeth) implying that the viscous dissipation is much higher in the simulation than in MST. It is also worth noting, however, that the effective anamalous radial (perpendicular to the mean field) viscosity, and thus the Prandtl number, has been estimated to be be about three orders of magnitude higher than the Braginskii form. Some attempt has been made to understand the effect of the large numerical viscosity on the simulated plasma and is discussed in section 4.3.1.

The final parameter of interest is the normalized current, $\Theta = B_p(a)/\langle B_t \rangle$ which is about 1.7 for the plasma conditions of interest here. The axial electric field at the edge is adjusted dynamically to keep Θ roughly constant using a proportional-integral-derivative (PID) feedback scheme. Table 4.1 shows a set of normalization factors for a simulation of a typical 400kA standard MST discharge.

The resolution for both simulations was 16 poloidal, 512 axial, and 160 radial points. Note that the radial resolution is somewhat low, but with the high viscosity, these simulations were still stable. That said, the Hartmann number is, at times, similar to that of previous work and the behavior suggests that higher radial resolution, lower Prandtl number runs should be performed. The calculations are performed in a double periodic cylinder and anti-aliasing is done to give an effective spectral resolution of 11 poloidal and 342 axial modes, all of which interact leading to significant nonlinear effects on the equilibrium. The simulations were run for a significant fraction of a resistive time, allowing many sawtooth events to occur. These sawteeth were then ensemble averaged for comparison to the ensemble averaged values from MST.

4.3 Sawtooth Evolution

One of the most noticeable features of the MST discharge, which was successfully reproduced by Debs in this work, is the sharp quasi-periodic MHD events known as sawteeth that occur every 6 - 8 ms in the experiment. As explained in chapter 3, sawteeth in the MST are global events where the entire spectrum of tearing modes grow exponentially and rapidly flatten the current density profile. It has long been observed in zero β simulations that as the Lundquist number is increased, intermittent bursts of MHD activity begin to occur[5]. At the experimental value of Lundquist number shown here, these bursts sharpen and the period between bursts lengthens to match that seen in the MST. What is somewhat surprising is that the duration of the simulated sawtooth crash ($\sim 100\ \mu$s), which can be thought of as a proxy for the reconnection time, is an order of magnitude faster than the value predicted by the Sweet-Parker model (~ 1 ms). A similar discrepancy is seen in tokamak sawteeth. In the tokamak case, two fluid effects have been shown to substantially reduce the predicted sawtooth duration, bringing it into closer agreement with the experimentally observed crash times[6]. For the RFP case, however, *single fluid* resistive MHD is sufficient to reproduce the experimentally observed crash durations if the simulations are run at high enough Lundquist number. It is not clear why this should be as the reconnection time for Sweet-Parker type reconnection scales like $\tau_A\sqrt{S}$ and thus should increase with Lundquist number. Presumably, the higher S allows stronger and smaller scale current sheets to form because of the decreased resistive dissipation. A similar effect has been seen in 2D reconnection studies where high S and high spectral resolution simulations of the current sheet showed the presence of the plasmoid instability[7]. When this instability is present, the reconnection time is much shorter than the Sweet-Parker prediction.

The simulations presented in this chapter were allowed to run for many sawteeth, and the results were ensemble averaged, as is typically done with experimental data. The upper plot in figure 4.2 shows the time evolution of the root mean squared (RMS) m=1 mode amplitude versus time for the entirety of a single simulation (in this case the simulation using the neoclassical resistivity profile). The lower plot in figure 4.2 shows the same data for a single MST discharge. While the typical MST discharge is much shorter than the simulation, the similarity in both character and periodicity of the sawteeth that occur during the current flattop is clear. In the experiment and in both of the simulations, a sawtooth cycle with the same three distinct phases as were seen in the experimental results are observed. This cycle, once again, consists of a rise phase, a crash phase, and a quiescent phase.

As in experiment, these events make good markers in time for ensemble averaging and much of the rest of the data presented in this chapter will be ensemble averaged. The ensemble for the simulations consists of 8 and 23 sawteeth for the Spitzer and neoclassical cases respectively. The reason for the factor of three difference in the number of sawteeth used is, as will be demonstrated later, that the neoclassical simulation did a better job of reproducing the data seen in experiment so it was considered unnecessary to continue the simulation using the Spitzer resistivity profile. It is worth noting that while the number of simulated sawteeth is well below the thousands of measured sawteeth in the ensemble of experimental data, the 23 for the neoclassical case required nearly a year of real time to generate. This means that generation of very large numbers of sawteeth, in order to have a comparable number of simulated sawteeth to that of the experimental data, is simply unmanageable at this time. None the less, an ensemble average of 23 sawteeth represents the most extensive data set used for this type of comparison to date.

A reasonable place to start directly comparing sawtooth ensembled simulated

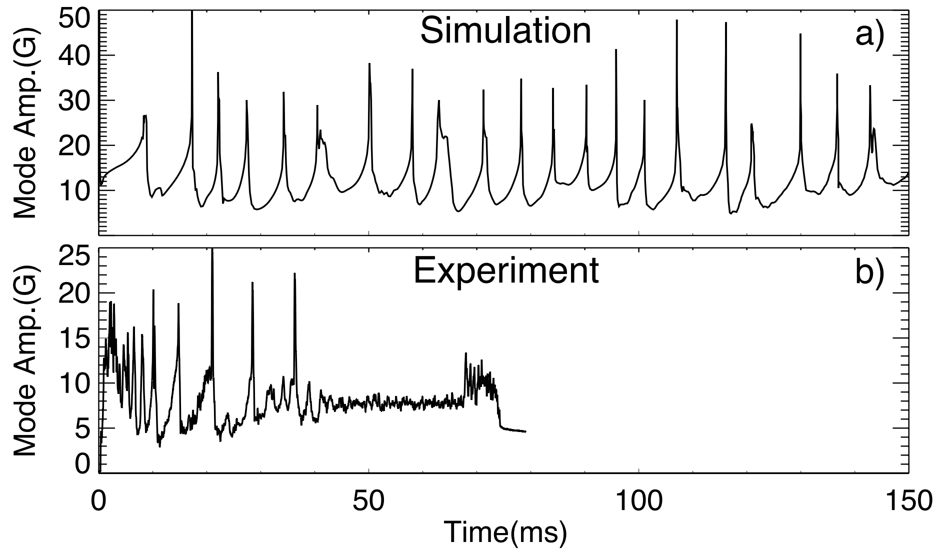

Figure 4.2: RMS m=1 mode amplitude from one of the simulations (a) and from measurements made in MST (b) by a toroidal array of edge magnetic pickup coils in MST and a synthetic diagnostic mimicking that array in the simulation.

and measured data is with the global equilibrium parameters, F and Θ. Figure 4.3 shows a comparison of the sawtooth ensembled reversal parameter, F, on the left and pinch parameter, Θ, on the right to the sawtooth ensemble of the simulated values of these parameters. What is important to note about this comparison is that the time averaged F and Θ for both simulations is very similar to the time average of the experimental values. The fact that the time history is different is primarily because the toroidal flux is explicitly conserved in the simulation where as it varies in time in the experiment. One of the features of the sawteeth in MST is the generation of substantial toroidal flux. In the simulation, the boundary is a perfect conductor so no toroidal flux can go into or out of the simulated plasma. Since $F = B_t(a)/\langle B_t\rangle$ and $\Theta = B_p(a)/\langle B_t\rangle$ and $\langle B_t\rangle$ is directly proportional to the total toroidal flux, it is not surprising that the time history is different.

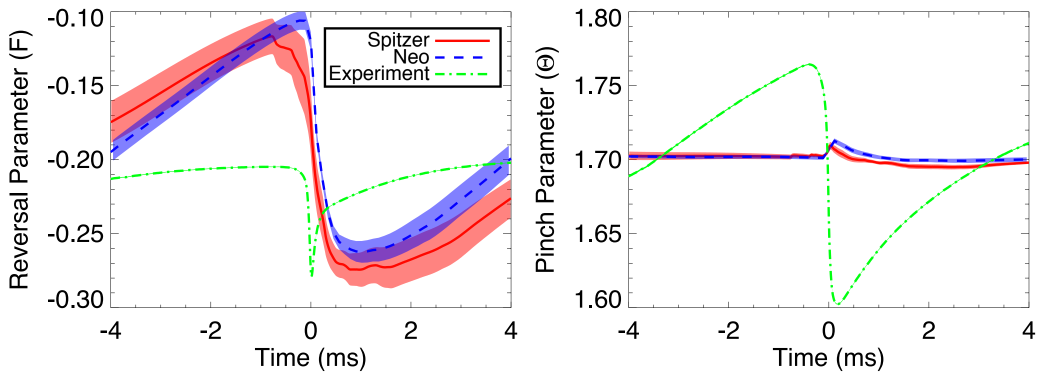

Figure 4.3: Reversal (left) and pinch (right) parameters vs time compared to the two simulations. The shaded regions show the uncertainty in the average value.

While the perfectly conducting boundary makes the evolution of F and Θ somewhat different than the experiment, the evolution of many of the internal profiles is actually quite similar to that of the experiment. There is striking agreement between the experiment and the simulation in the change in the safety factor profile $q(r) = rB_t/RB_p$ through the sawtooth. Figure 4.4 shows a set of three q profiles from MST equilibrium reconstructions[8] and from the two DEBS simulations and the plot on the left side of figure 4.5 shows a comparison of the time evolution of q on axis. Notice that the safety factor in MST is typically near 0.2 on axis and decreases monotonically, crossing zero at the reversal surface near the edge, to a minimum of approximately -0.05 at the boundary. In all three cases the safety factor on axis increases rapidly at the sawtooth crash and decreases rapidly at the edge. Note that the safety factor in both MST and the simulated plasma decrease as the current density is peaked by the Ohmic drive circuit. At the sawtooth crash, q on axis increases bringing the $m = 1$, $n = 5$ mode rational surface into the plasma. While the value of the

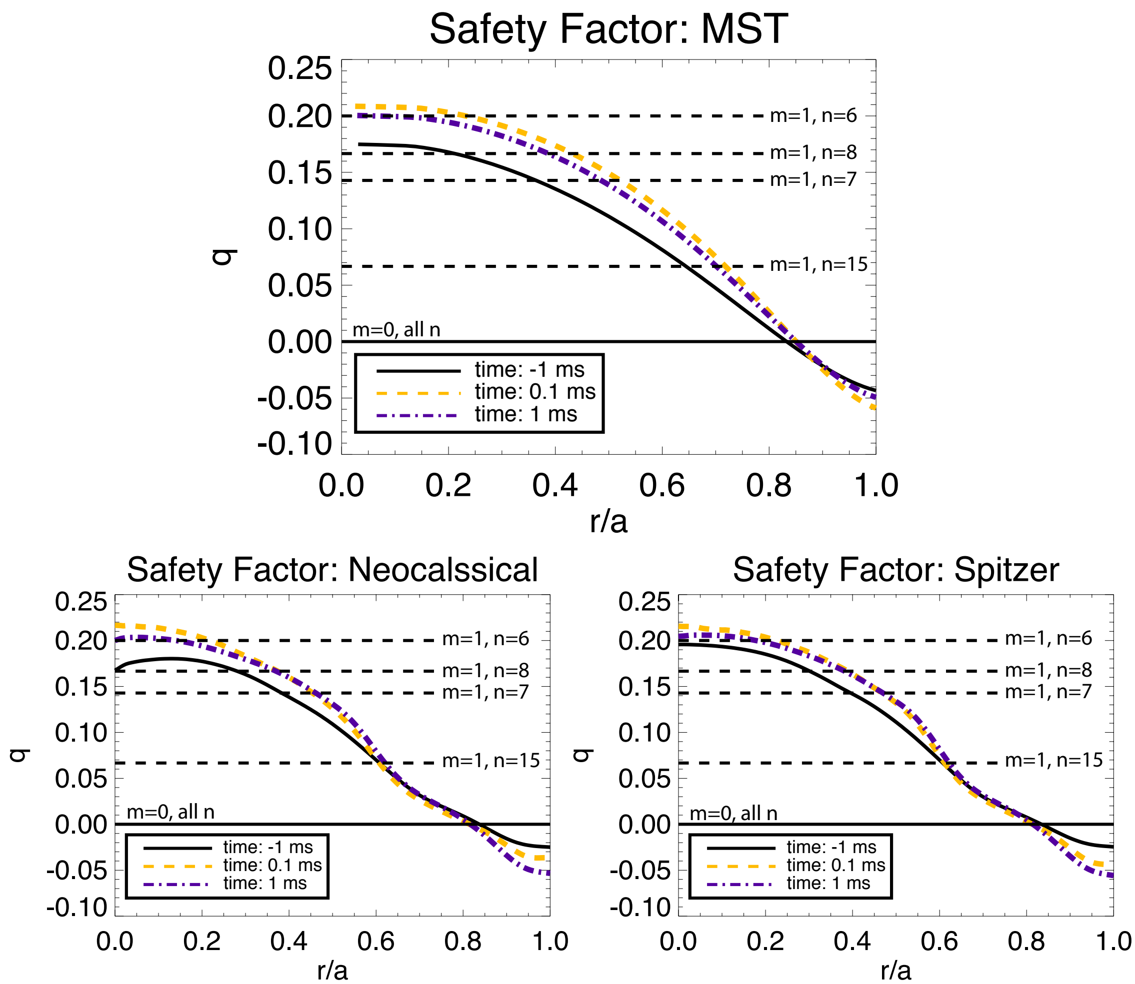

Figure 4.4: Safety factor profile at three times with respect to the sawtooth crash for the experiment as well as the neoclassical and Spitzer resistivity Debs runs.

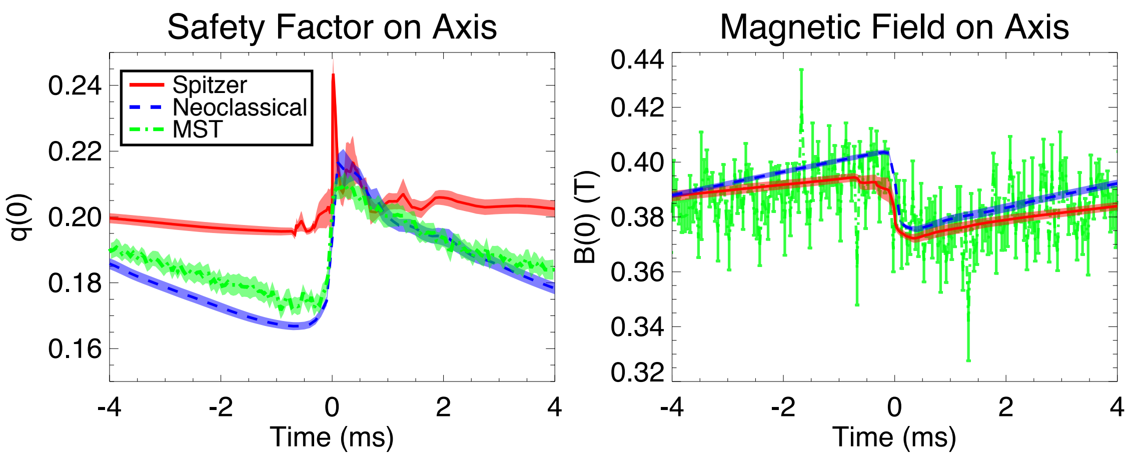

Figure 4.5: Safety factor (left) and magnetic field (right) on axis vs time through the sawtooth. Notice that the degree of variation in the simulation run with neoclassical resistivity is qualitatively more similar to the measured value.

safety factor on axis does not precisely match that of the experiment at all times, the degree of variation in time of the simulation using the neoclassical resistivity profile is consistent with the variation in the q profile seen in the reconstructions while the value from simulation using the Spitzer resistivity profile is much more muted than that in MST.

In figure 4.5, the sawtooth evolution of the toroidal magnetic field on axis compared to $|B|$ measured by the motional Stark effect (MSE) diagnostic in MST is also shown. Interestingly, even though the measured toroidal flux in MST increases at the sawtooth crash, the measured magnetic field on axis decreases. This behavior is very well reproduced by both simulations.

4.3.1 Effect of Numerical Viscosity on Equilibrium Evolution in Debs

As mentioned, the viscosity is adjusted dynamically to damp sub-grid scale fluctuations. At the sawtooth in particular, the viscosity can get very large. Figure 4.6

shows the viscosity profile from two time slices in the simulation using the neoclassical resistivity. The first is from before and the second from during a sawtooth event.

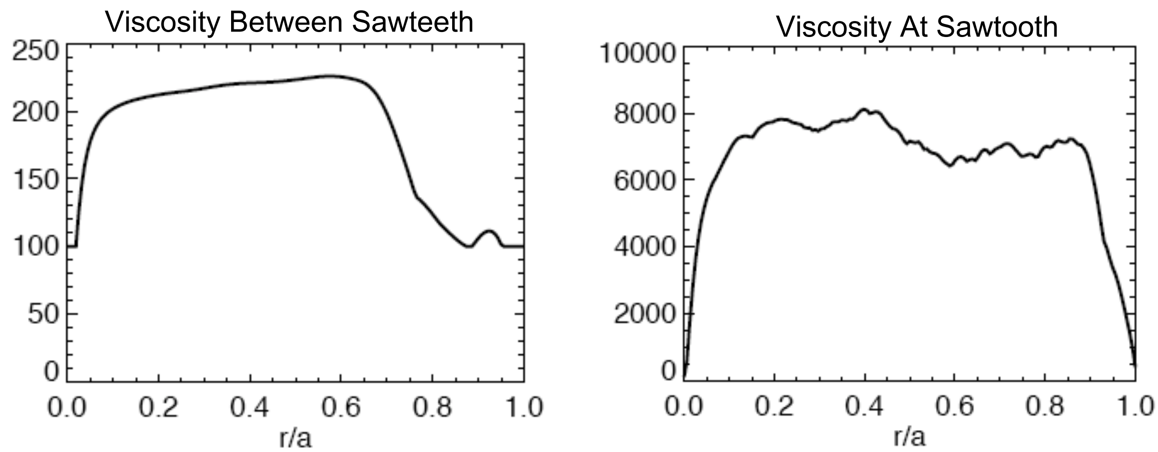

Figure 4.6: Dimensionless viscosity profile from before (left) and during (right) a sawtooth. Notice that the viscosity is adjusted at each radial point. The viscosity gets low in the core as k_{max} becomes large and low at the edge as the maximum fluid velocity, V_{max}, gets small.

Notice that the vertical scales are a factor of 40 different and that the profile shape as well as the maximum value change as the simulation evolves. Figure 4.7 shows the sawtooth ensembled time evolution of the maximum and minimum values of the viscosity profile for both simulations. The nominal minimum for the normalized viscosity was 100 for these runs, but as is clear from figures 4.6 and 4.7, the viscosity is generally higher than this across much of the minor radius throughout the sawtooth cycle. In order to get some sense of what the viscosity does to the global evolution of the plasma, the simulation was stopped and the minimum allowed viscosity was adjusted. The simulations were then restarted and allowed to evolve for several sawteeth. Table 4.2 shows a summary of global parameters for three different values of viscosity for

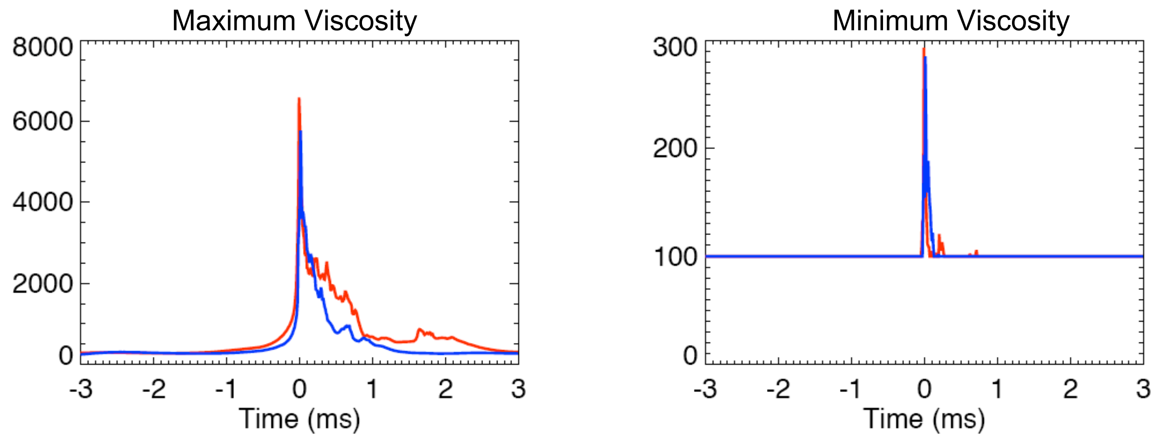

Figure 4.7: Maximum and minimum dimensionless viscosity versus time for the simulations using the Spitzer (red) and the neoclassical (blue) resistivity profile.

the two different resistivity profiles. Note that this is simply the minimum value of viscosity so it has the greatest effect on the ν near $r = 0$ and $r = 1$. The general effect of increasing the minimum viscosity is that the sawtooth period gets longer and reversal gets shallower. At high enough viscosity reversal is lost completely, presumably because of the loss of the MHD dynamo contribution to the parallel electric field. In contrast, with lower viscosity the reversal gets deeper but the sawtooth evolution becomes less reproducible and the sawtooth period gets shorter. At low enough viscosity the periodic nature of the sawtooth events is lost completely and the discrete sawteeth are replaced by random small bursts of MHD activity. Insufficient resolution in these simulations may be the cause of this behavior, so the limiting behavior has not been fully explored. This is not to mention the fact that in all cases, the algorithm automatically increased the viscosity during the sawtooth crash, suggesting that a significant increase in resolution is needed to fully resolve the dynamics at the sawtooth. That said, the effective radial viscosity in MST may also increase at the sawtooth crash, so it is not clear that the time behavior that came out of this simulation is entirely wrong. What should really be done is a correct solution to the stress tensor, but that will be the subject of another thesis.

Resistivity Type	**Min $\mathbf{Pr_m}$**	**Max $\mathbf{Pr_m}$**	**ST Period (ms)**	**F**
Spitzer	1000	1000	12.5	-0.05
Spitzer	100	250	8.8	-0.14
Spitzer	10	300	8.0	-0.16
neoclassical	1000	1000	8.5	-0.06
neoclassical	100	250	6.4	-0.15
neoclassical	15	275	6.2	-0.16
experiment	0.13	0.25	6-10	-0.2

Table 4.2: Table of global values from several runs for both the Spitzer and neoclassical resistivity profiles in which the minimum allowed value of dimensionless viscosity was varied. Minimum and maximum values of viscosity and the reversal parameter listed here are the average from before sawteeth.

Interpretation of the dimensionless viscosity is somewhat difficult as there is no physics model used to determine the radial profile of the viscosity. Furthermore, the plasma viscosity is expected to be highly anisotropic while a viscosity that was constant in the poloidal and axial directions was used in the simulation. The classical collisional kinematic ion viscosity for the MST case can be expressed as[9] (though it appears here in the notation of the NRL plasma formulary[10]):

$$\eta_0^i = 0.96nT\tau_i/\rho_m \approx 1.2 \times 10^7 \ m^2/s, \tag{4.5}$$

$$\eta_2^i = \frac{6nT}{5\omega_{ci}^2\tau_i\rho_m} \approx 0.06 \ m^2/s, \tag{4.6}$$

where ω_{ci} is the ion cyclotron frequency, τ_i is the ion collision time, and ρ_m is the mass density. The parallel viscosity is approximately η_0^i and the perpendicular is approximately η_2^i. In low current plasmas in MST, the radial viscosity has been estimated to be $\sim$ 50 m^2/s which is anomalously high[11], most likely due to stochastic magnetic field lines mixing the parallel and perpendicular viscosities. It is not clear that any of these should be used to dimensionalize the viscosity as the code dynamically adjusts the viscosity using the fluid velocity and the somewhat arbitrarily set cell Reynolds number. The equation that is solved is in effect $\rho dv/dt = \mu\nabla^2 v$ which goes to $v_a/\tau_r = \nu_0 v_a/a^2$ where $\nu = \mu/\rho$ is the kinetic viscosity, μ is the dynamic viscosity, and ρ is the mass density. So, $\nu_0 = a^2/\tau_r$ which is 0.24 m^2/s which leads to a typical value from between sawteeth for the simulation of about 60 m^s/s which is similar to the value measured in MST in lower current discharges. It is unclear if this is just serendipitous or if it is actually important to run with anomalous viscosity to get MST like behavior, but going to higher viscosity causes clearly different behavior and it seems like lower viscosity would as well, though it is possible that going to much lower viscosity would yield characteristically different results. The right way to address this question, of course, is to compute the anisotropic viscosity, but this would be a non-trivial change to the code and would likely require very high radial resolution to get convergence due to the high anisotropy factors. From this brief scan of viscosity discussed in the table earlier, it appears that the simulated plasma is not terribly sensitive to the exact value of viscosity selected and that the value used for this work (a minimum of 100 with a typical maximum value between sawteeth of 250) is about right to get MST like dynamics, though a more complete set of measurements in MST and simulations would be needed to determine if this was indeed causal.

One thing that can be tested is the behavior of the viscosity with changing resolution. Ideally, this would be done as part of a careful convergence study, however this was not done. What we have done is a brief study of a few sawteeth with increasing radial resolution. In general what seems to happen is that the magnetic fluctuations increase and the viscosity decreases with increased resolution. The equilibrium behavior stays more or less the same. With much higher resolution, one might expect to start seeing a significant change in the equilibrium behavior as the viscosity actually starts to change by a significant amount, but the resolution would have to be substantially improved for this to occur. In the future, if this code is parallelized, then it may become possible to run at constant viscosity throughout the sawtooth cycle. For now, the small variation in the long time scale behavior with a 50% increase in radial resolution suggests that the run has converged, it just has high dissipation, but a more careful study is needed.

4.4 Magnetic Fluctuations

As previously mentioned, the magnetic fluctuations in the RFP play a critical role in governing the evolution of the magnetic equilibrium. In these simulations the mode amplitudes are about a factor of two higher than those measured in MST. This discrepancy has been seen in the past and persists in simulations run at experimental values of Lundquist number. While this may be due to boundary effects, finite β effects, or the high viscosity in these simulations, work done with the extended MHD code NIMROD suggests that this discrepancy is more likely due to the lack of two fluid effects, in particular ion-gyroviscosity[12], in the physics model DEBS uses. Despite the fact that the mode amplitudes are not quite right, a comparison between the simulated and measured mode spectral shapes show good agreement. Figure 4.8 shows

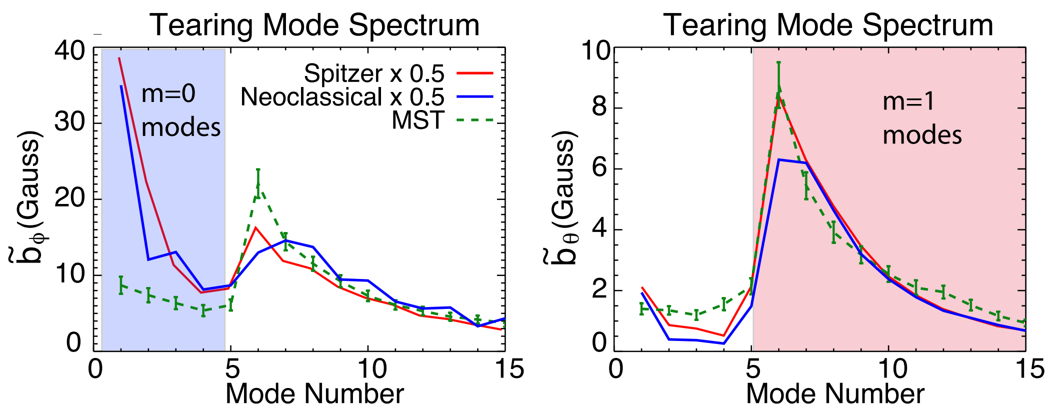

Figure 4.8: Comparison of the simulated and measured toroidal (left) and poloidal (right) magnetic fluctuation amplitudes measured at the boundary. The simulated mode amplitudes are scaled by a factor of two so the spectral shapes can be more easily compared. The m=1 values from the simulations are generally within a factor of 2 of measurement while the m=0 values are a factor of 3 to 10 higher than the measured values.

the poloidal and toroidal mode spectra measured by a toroidal array of edge magnetic pickup coils in MST and by a synthetic diagnostic mimicking that coil array in the Debs code. The spectral shape of the mode amplitudes measured in MST is generally well reproduced by both simulations with the exception of the low n toroidal modes associated with the $m = 0$ fluctuations. The $m = 0$, $n = 1$ mode in particular is generally 8 to 10 time higher than the measured value while the higher n, $m = 0$ modes are generally 3 to 4 times higher than the measured values (blue box in the left plot of figure 4.8). The core resonant $m = 1$ fluctuations, which are the primary contributors to the high n poloidal mode amplitude measurement, are typically 1.5 to 2 times larger than those of MST (red box on the right plot of figure 4.8). The $n \geq 12$ modes have some contribution from the $m = 2$ modes, but this is generally expected to be negligible compared to the $m = 1$ contribution, and certainly is in the simulations (not shown). The simulated mode spectrum is scaled by a factor of two so that the spectral shape can be more easily compared. The low n values of the toroidal mode spectrum are dominated by the $m = 0$ modes resonant at the reversal surface while the $n > 5$ values of the poloidal mode amplitudes are dominated by the core and mid-radius resonant $m = 1$ modes. The remaining modes shown in each plot contain a mixture of the $m = 0$ and $m = 1$ mode amplitudes. The time evolution of the $m = 1$ mode spectrum is generally well reproduced by the simulation however, the low n toroidal fluctuations which, again are associated with the edge resonant $m = 0$ modes, are not as well reproduced. This discrepancy is likely due to a combination of the lack of a circuit model for the applied poloidal loop voltage at the boundary and physics effects that have been left out of these simulations such as toroidicity and finite pressure effects.

The FIR polarimetry system on MST can measure the average $\tilde{B}_r$ in the core region of the plasma for the $m = 1$, $n = 6$ mode[13]. This measurement shows the time evolution $\tilde{B}_r$ in the core matches $\tilde{B}_\theta$ in the edge for the $m = 1$, $n = 6$ mode and is scaled by a factor of about 2.5. Since the simulations give us detailed information about the radial shape of the magnetic perturbation amplitude, we can easily compare this data to the simulation results. In figure 4.9 the time evolution of $\tilde{B}_\theta$ at the edge and the average $\tilde{B}_r$ over the inner half of the simulated plasma are shown along with a reproduction of the measured value from ref.[13]. The behavior in both simulations is similar to the measured value with the neoclassical value again qualitatively reproducing the experimental observations more closely.

4.4.1 The MHD Dynamo

DEBS computes the dimensionless electric field as $\mathbf{E} = \eta\mathbf{J} - S\mathbf{V} \times \mathbf{B}$. Away from

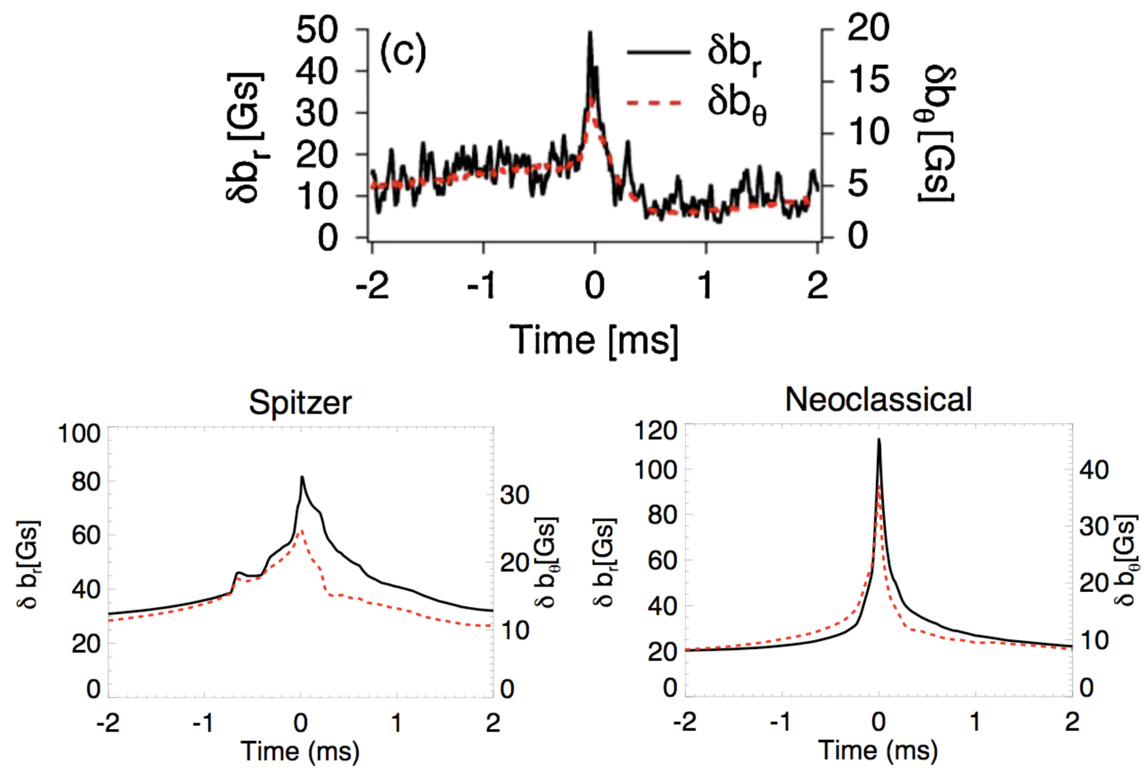

Figure 4.9: Core averaged $\tilde{B}_r$ for the $m = 1$, $n = 6$ mode (black solid line) compared to $\tilde{B}_\theta$ in the edge (red dashed line) for MST (top) and the two simulations (bottom). The scale for $\tilde{B}_\theta$ is on the right hand side of the three plots and is a factor of 2.5 smaller than the $\tilde{B}_r$ scale that appears on the left hand side of the three plots. While in both simulations the edge measurement tracks the core measurement, as in the experimental result, neoclassical case (bottom right) is in better qualitative agreement with the measurements than the Spitzer case.

the sawtooth the electric field from the MHD dynamo is small compared to the Ohmic field. In contrast, at the sawtooth crash the dynamo becomes the dominant source of electric field. This is consistent with previous measurements made in MST[14]. Figure 4.10 show the contribution of the $m = 1$, $n =$ 5-8 modes to the total dynamo electric field (upper left) and the $m = 0$, $n =$ 1-4 modes (upper right). On the lower left the total $\mathbf{E}_{\|}$ as well as the relative contributions to $\mathbf{E}_{\|}$ from $\eta\mathbf{J}$ and the total $\mathbf{V} \times \mathbf{B}$ dynamo term are shown. The safety factor profile for this time slice is shown on the lower right. Notice that the total dynamo contribution to the mean field is small and peaks at the mid radius where it is actually the $m = 1$, $n = 7$ mode that provides the dominant contribution.

At the sawtooth crash, the picture is entirely different. Figure 4.11 shows the same four plots, but here we can see that the MHD dynamo is now the dominant contributor to the parallel electric field. The dynamo field comes primarily from the $m = 1$, $n = 5$ and 6 modes at this time, though the higher n modes also provide a significant contribution to the overall electric field. It should be noted that this large dynamo field is only seen in the simulations for a very brief period of time right around the sawtooth crash. It begins to increase a few hundred milliseconds before the sawtooth and decreases rapidly after the sawtooth. It is also interesting to note that during the rise and crash phases, there is no single mode that is the dominant source of the dynamo field. It is the combined effect of many modes that generates the large electric fields seen at the crash. After the crash however, there is a brief period as the dynamo field is decaying where the $m = 1$, $n = 5$ mode becomes the largest single contributor to the electric field and the $m = 1$, $n = 6$ mode actually

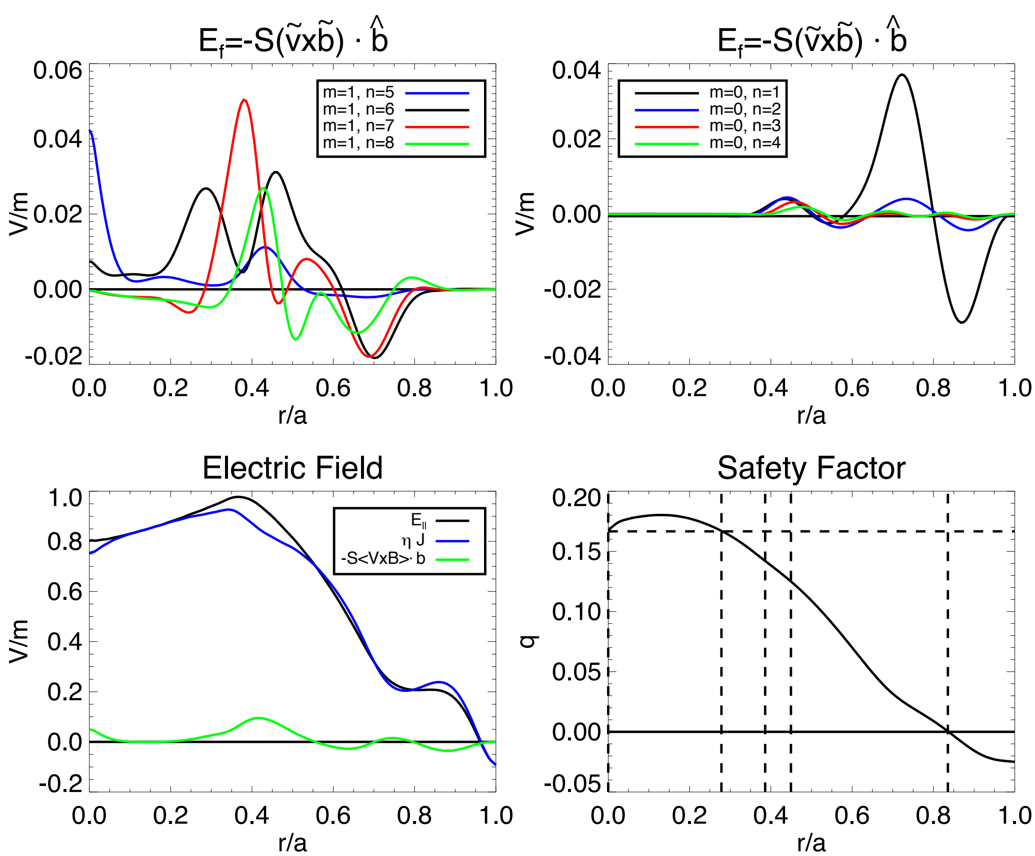

Figure 4.10: $\langle \mathbf{V} \times \mathbf{B} \rangle$ vs $\eta \mathbf{J}$ away from the sawtooth. Note that the parallel electric field is almost completely accounted for by $\eta \mathbf{J}$.

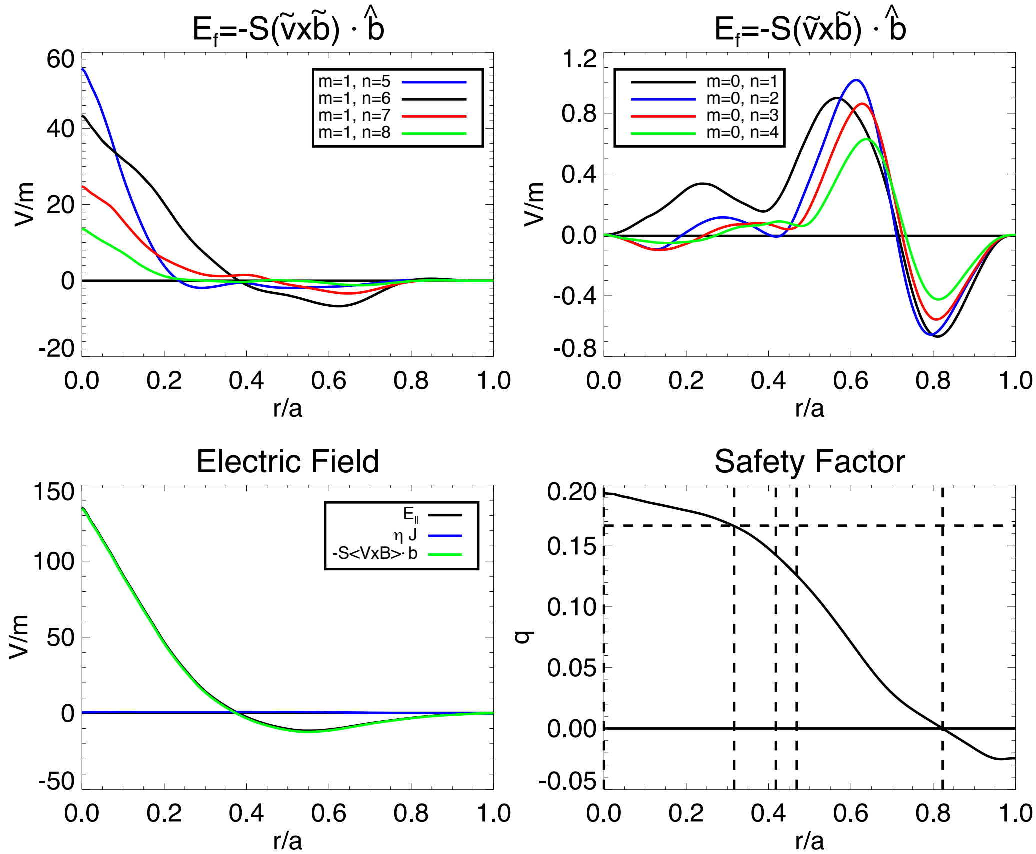

Figure 4.11: $\mathbf{V} \times \mathbf{B}$ vs $\eta\mathbf{J}$ at the sawtooth.

generates a dynamo field that opposes that of the $m = 1$, $n = 5$ mode. While the $m = 1$ modes generate a large electric field in the core, the $m = 0$ modes generate a more modest electric field at the edge, providing the primary contribution to the total parallel electric field near the reversal surface.

4.5 Electron Thermal Diffusion

One of the primary motivations for performing these simulations was to try to better understand the electron thermal transport in MST. Since these are zero β simulations, transport quantities can not be computed directly for comparison to measurement. However, these simulations do provide enough information to allow the stochastic transport to be computed. In particular, one unique piece of information that the simulations can provide is the detailed radial shape of the B_r perturbation amplitude and the evolution of that radial shape. Figure 4.12 shows the $m = 1$, $n = 6$ (left) and $n = 5$ (right) before during and after the sawtooth crash. While both modes grow significantly at the sawtooth crash, notice that the $m = 1$, $n = 6$ mode, which is resonant around $r/a = 0.35$, falls to a relatively small value after the crash while the $m = 1$, $n = 5$ mode, which is resonant near the magnetic axis at $r/a = 0$, stays relatively large for a few milliseconds after the crash. The large mode amplitudes and closely spaced mode rational surfaces in MST suggest that the magnetic field may be stochastic across the volume and that parallel losses along stochastically wandering magnetic field lines dominate the heat diffusion in the plasma. Coupling the high time resolution measurements of χ_e discussed in the previous chapter with the wealth of new simulation data allows the contribution of the stochasticity to the overall thermal diffusion in MST to be determined. A relatively simple way to compute the stochastic

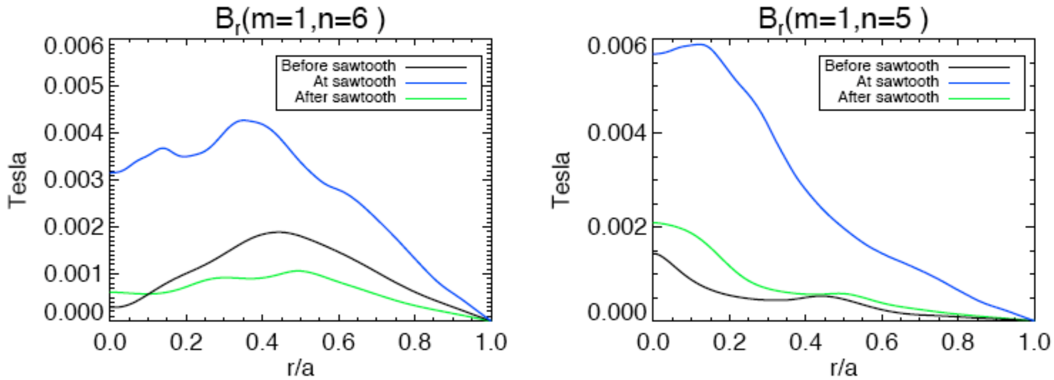

Figure 4.12: Ensemble averaged amplitude of the $m = 1$, $n = 6$ (left) and $n = 5$ (right) from before, during, and after the sawtooth. While both modes grow at the sawtooth, the (1,6) is relatively small after the sawtooth while the (1,5) is relatively large, consistent with measurements made in MST.

thermal diffusion is through the Rechester-Rosenbluth model[2], namely

$$\chi_{RR} = v_{\parallel} D_{mag} \approx v_{th,e} L_c \sum_{m,n} \frac{|\tilde{b}_{mnr}(r)|^2}{B^2} \delta\left(\frac{m}{q(r)} - n\right), \tag{4.7}$$

with L_c replacing πR as the correlation length to account for the variation in stochasticity with radius. L_c is defined in ref. [2] as $L_c = \pi R / ln\left(\pi s/2\right)$ (although it is defined in a myriad of other ways in other works[15, 16, 17, 18]). The parameter s that appears in the L_c equation is the stochasticity parameter which is defined as

$$s = \frac{\Delta_{mn} + \Delta_{m'n'}}{2|r_{mn} - r_{m'n'}|}, \tag{4.8}$$

where Δ is the width of the magnetic island and is defined for the RFP as[19]

$$\Delta_{mn} = 4\sqrt{r_{mn}|\tilde{b}_{rmn}| / \left(nB_\theta |q'_{mn}|\right)}. \tag{4.9}$$

The delta function in equation 4.7 should be interpreted as excluding all modes that are not resonant at the same rational surface from the sum. In other words, this formula only provides the thermal diffusion at rational surfaces. Furthermore, since we only have $m = 0$ and $m = 1$ amplitude information, the sum was never actually carried out. It only appears here as this is the formally correct form of the equation. Note that this interpretation is different than the intuitively reasonable interpretation that the amplitudes of any modes with overlapping islands should be summed. This makes sense as it is the overlap of modes resonant at different radial locations that leads to magnetic stochasticity. Using this interpretation, the value of the thermal diffusion can be determined in any part of the radius in which islands are found to overlap. To be clear, it was the former, more mathematically correct interpretation that was used in this work. The experimental measurement, in contrast, provides the characteristic value of thermal diffusion over a given region of the plasma. The core region, once again, is where the $m = 1$, $n =$ 6-8 modes are generally resonant so for the purposes of comparison and discussion the value of thermal diffusion from the core region will be the average of χ_{RR} for the $n =$ 6-8 modes. The mid-radius region of the MST results included the $m = 1$, $n =$ 9-32 modes and so χ_{RR} for the mid-radius will be the average value from that same set of modes. To accurately determine χ_{RR} for MST using the profile information from DEBS, the ensemble averaged mode amplitudes from DEBS must be scaled to match the ensemble averaged mode amplitudes measured at the edge of the experiment. In order to perform this scaling, each ensemble averaged mode amplitude from DEBS was scaled at each time point to match the ensemble averaged value for the corresponding mode measured at the edge of MST. This scale factor was then applied to the $\tilde{b}_r$ profile and the value of χ_{RR} is calculated. Note that because the neoclassical resistivity model consistently performed better than the Spitzer model, the rest of the analysis presented in this chapter was only carried out on the neoclassical simulation results.

The island widths can become very large in MST and, especially in the mid radius region, can overlap completely. Equation 4.7 is formally valid if the stochasticity parameter is greater than 1. Figure 4.13 shows the magnetic islands and the stochasticity parameter expected for MST away from a sawtooth. As can be seen in figure 4.13, s is nearly always greater than 1 in MST, yet it turns out that the Rechester-Rosenbluth model does not, in general, do a very good job of reproducing the measured value of χ_e. The average stochasticity parameter in the core and mid-

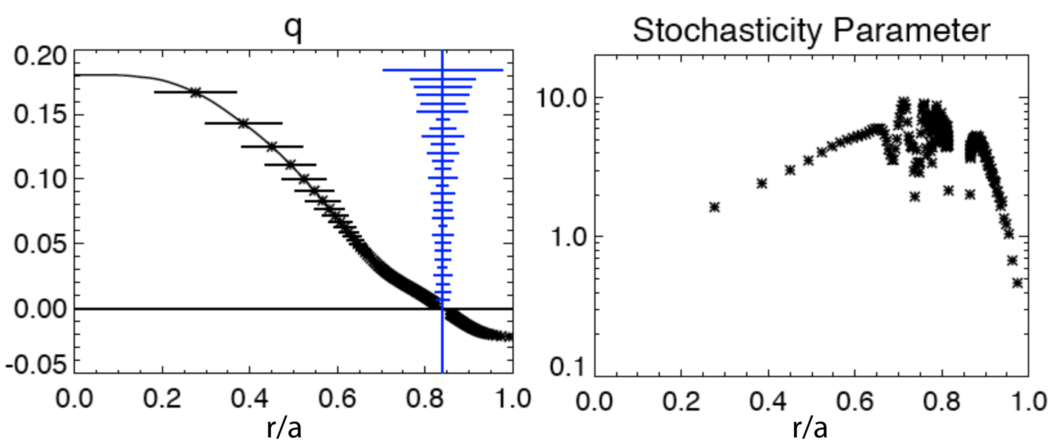

Figure 4.13: Safety factor profile with many of the $m = 1$ and $m = 0$ island widths overplotted (left) and the stochasticity parameter for the $m = 1$ modes (right).

radius of the plasma is shown in figure 4.14. The average stochasticity parameter in the core region is always above 1 and it increases at the sawtooth crash. The average in the mid-radius is always much greater than 1 so this region is expected to be very stochastic at all times. Interestingly, when magnetic field lines are traced, remnant

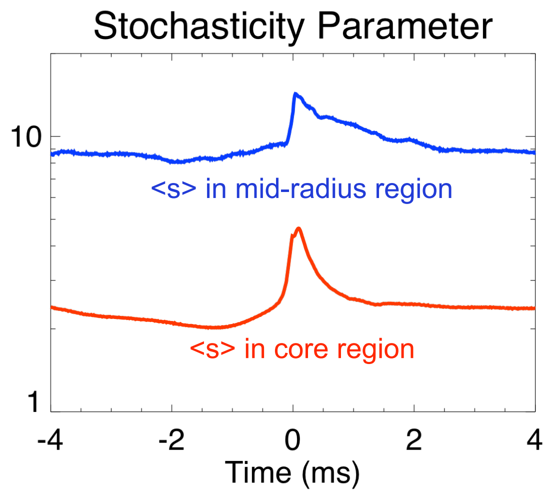

Figure 4.14: Average stochasticity parameter in the core and mid-radius of the plasma vs time through the sawtooth crash.

island structures can be seen when the stochasticity parameter is less than 2.5. Recalling equation 4.8 and the definition of s, this makes sense; a stochasticity parameter of 1 simply means the edges of the islands are overlapping. If the islands are of equal size, then a stochasticity parameter of 2 means the islands are completely overlapping. In the more realistic case of islands that are not equal, the stochasticity parameter has to be larger than 2 for islands to completely overlap and the stochasticity to become fully developed. Figure 4.15 shows puncture plots of the magnetic field at three times. Remnant island structures are seen both before and after the sawtooth. These island structures are similar in character to electron temperature structures that have recently been measured on MST[20] with a $m = 1$, $n = 6$ island appearing before the sawtooth, fully developed stochasticity across the entire minor radius at the sawtooth crash, and a relatively large $m = 1$, $n = 5$ island appearing after the sawtooth.

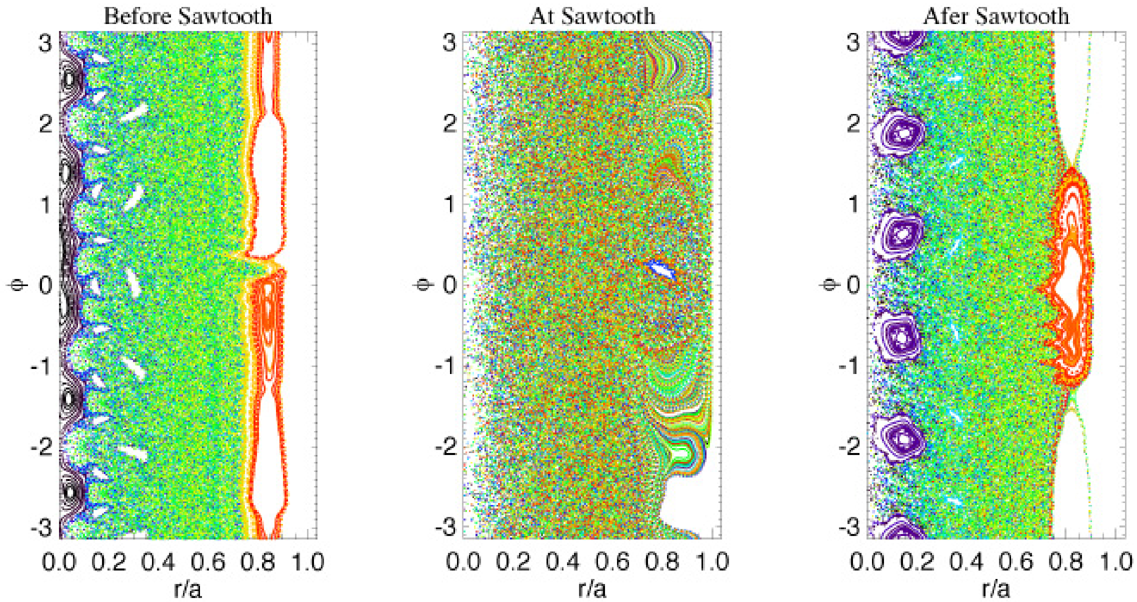

Figure 4.15: Puncture plots of the magnetic field from before (left), during (center), and after (left) the sawtooth crash.

Figure 4.16 shows a comparison of the thermal diffusion in the two regions. While the mid-radius is reasonably well reproduced except at the sawtooth crash, the core region is over predicted before the crash and under predicted at the crash. The Rechester-Rosenbluth thermal diffusion should represent the minimum possible thermal diffusion and so the fact that it over predicts the measured value in the core suggests that the remnant island structures seen in MST are sufficiently large that this analytic model may not be valid in this region. The fact that it under predicts the thermal diffusion in both the core and the mid radius at the sawtooth crash suggests that there is significant thermal transport in addition to simple stochastic diffusion that is occurring at these times. It has also been suggested that the simple definition of L_c used in this analysis should be modified to take into account collisional effects[15] and others saying that it should never be used as correlation length [16] while still

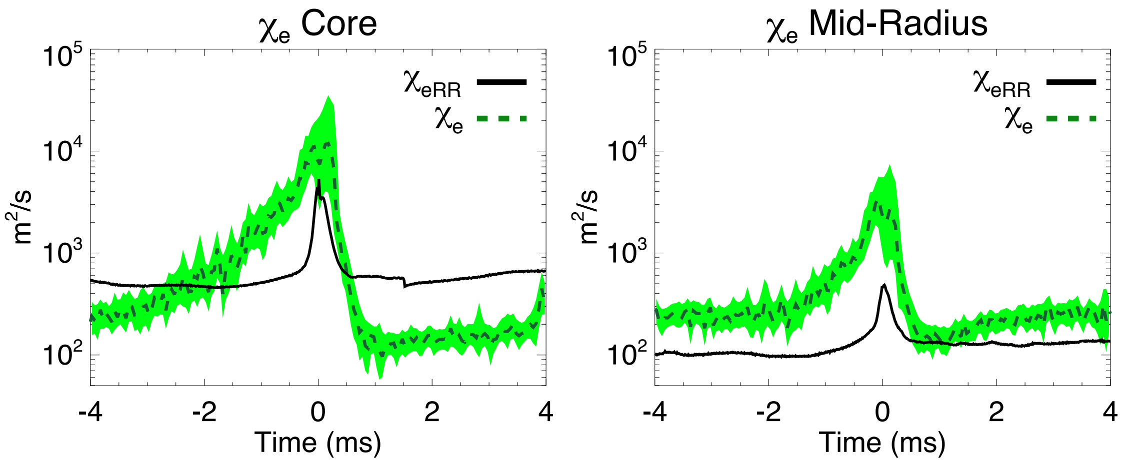

Figure 4.16: Time evolution of χ_{RR} compared to the measured value from MST.

others have shown that it is the right length scale to use for the RFP case[17, 18].

We can simultaneously account for the effect of magnetic islands and avoid any confusion about L_c by directly tracing the magnetic field lines and computing the magnetic diffusion from this information. To do this, the set of scale factors discussed earlier is used to scale the modes at each time step of the simulation by determining its time relative to the closest sawtooth. The magnetic field is then traced with the Magnetic Lines (MAL) code and χ_{MD} is then calculated[21]. χ_{MD} is defined as

$$\chi_{MD} = v_{th,e} D_{mag} = v_{th,e} \frac{\left\langle (r - r_0)^2 \right\rangle}{2L}, \tag{4.10}$$

where $V_{th,e}$ is the electron thermal velocity, r is the minor radial position, and L is the distance along the field line (which was set at a value of 32 m, which is close to the electron mean free path). The χ_{MD} profile is ensemble averaged and compared to the measured χ_e from MST.

An initial comparison of χ_{MD} to the measured χ_e (left side of figure 4.17) found that χ_{MD} significantly over predicted the thermal diffusion in general (with the notable exception of the relatively good agreement found at the crash), but was particularly bad in the mid-radius where the analytic model found modest agreement. This was unexpected as χ_{MD}, once again, should be the minimum possible value for the measured χ_e. However, as is pointed out in ref. [3], trapped particles will not conduct heat along magnetic field lines and thus, χ_{MD} should be defined as,

$$\chi_{MD} = f_c v_{th,e} D_{mag} \tag{4.11}$$

where f_c is the circulating fraction of the electron population. Note that the f_c used here was simply the average value of the circulating fraction for each region of the plasma where the regions are defined as having the same radial extent as the four regions used in the χ_e analysis in the previous chapter. The particle trapping is simply from variation in the magnitude of $\mathbf{B}$ as a particle travels poloidally around a flux surface. This work does not make any attempt to quantify the additional effect of particle trapping due to the radial motion of the stochastically wandering field lines, which could in principle be a much larger effect than the one used in this work. The right column of figure 4.17 shows the time evolution of the measured electron thermal diffusion compared to that from equation 4.11. With the trapped particle effects accounted for it becomes clear that the thermal conduction in the mid-radius is dominated by magnetic diffusion throughout most of the sawtooth cycle. In the core, the magnetic diffusion likely accounts for all of the measured χ_e after the crash, but there are obviously still other mechanisms that become important leading up to

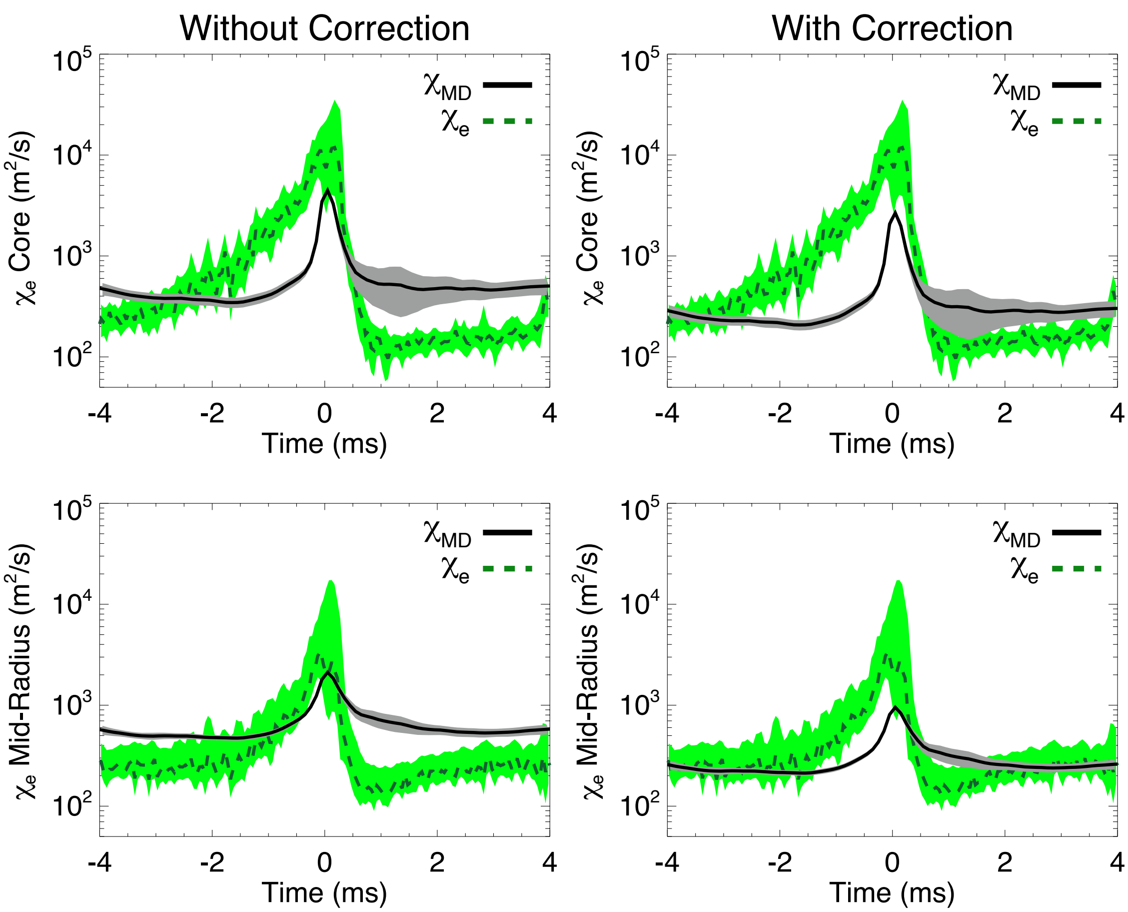

Figure 4.17: A comparison of the measured vs predicted values of the electron thermal diffusion without (left) and with (right) the reduction in thermal diffusion due to trapped particles taken into account. Average electron thermal diffusivity for the core region ($0 \leq r/a \leq 0.45$) from MAL (equation 4.11) from MAL is shown with the black solid line and from the fit to experimental data shown with the green dashed line. Note that the value of χ_{MD} decreases between -4 and -1 ms because the thermal velocity is decreasing.

and including the crash time. These mechanisms may include presence of magnetic islands[22] (which Eq. 4.11 will not account for correctly due to the bounded nature of the field lines around the island[21]), as well as non-linear mechanisms like those described in ref. [23].

4.6 Discussion

In this chapter a quantitative comparison of high spectral resolution resistive MHD simulations to MST data was presented. The main results of these simulations are that at high Lundquist number and high spectral resolution many of the features of the MST plasma are reproduced including the sawtooth period and the duration of the sawtooth crash. The use of resistivity profiles that match those of MST, in particular the neoclassical resistivity profile, further improves the ability of the simulation to reproduce MST plasmas. These simulations also allow the evaluation of the role of the MHD dynamo through the sawtooth crash and it is found to be small except at the crash, consistent with measurements of the dynamo made MST[14]. Finally, the radial profiles of the magnetic perturbation amplitudes produced by the code were used to calculate the stochastic transport for the MST case using the Rechester-Rosenbluth analytic model and a more exact version of the same transport mechanism using the diffusion of the magnetic field. In general, the two methods did not agree and neither method was in good agreement with measurement. However, by accounting for the reduction in heat transport due to trapped particle effects, the thermal diffusion predicted by field line tracing was found to be consistent with measurement. This analysis suggests that away from the sawtooth the heat transport is dominated by magnetic diffusion, however, near the sawtooth and at the sawtooth crash there are substantial additional nonlinear mechanisms of heat transport across the plasma.

There are many other physical effects that my be important for capturing the full dynamics of the sawtooth accurately, so it is very possible that the observed discrepancies are simply due to the simulation not reproducing the behavior of MST with sufficient accuracy. For example, even with corrections to χ_{MD} due to trapped particles, the χ_{MD} is still higher than χ_e just after the sawtooth. This may be due to the dynamics of the slow particles in the distribution function which are expected to substantially modify the energy flux in some cases[24]. Another possible reason for this discrepancy is the higher viscosity in the simulation at and just after the sawtooth which likely effects the equilibrium evolution. A lower ν would allow $\tilde{b}_r$ to be temporarily higher and thus it would flatten $J_{\|}$ faster. This would shut down the drive for tearing modes more quickly and could cause a faster, and possible stronger, suppression of the mode amplitudes, thus reducing the magnetic diffusion after the crash.

Despite the limitations in the model, the overall ability of these cylindrical, zero β simulations to accurately model MST is impressive. Using these simulations to determine the electron thermal diffusion, however, is unwieldy in the sense that so many complicated steps have to be taken to obtain a value that can be compared to the measurements. A more ideal way to make this comparison is to simulate the heat transport directly and then compare the measured temperature evolution to the simulated evolution. One such attempt is presented in the next chapter where the heat transport is modeled as anisotropic classical collisional transport[9]. This model not only allows the equilibrium profile to be determined, but also the temperature fluctuations, which will be compared directly to fluctuation measurements made with the Thomson scattering system on MST.

REFERENCES

[1] Schnack, D. D., Barnes, D. C., Mikic, Z., Harned, D. S., and Caramana, E. J. Semi-implicit magnetohydrodynamic calculations. *Journal of Computational Physics* **70**(2), 330 – 354 (1987).

[2] Rechester, A. B. and Rosenbluth, M. N. Electron Heat Transport in a Tokamak with Destroyed Magnetic Surfaces. *Physical Review Letters* **40**(1), 38–41 (1978).

[3] Chandran, B. D. G. and Cowley, S. C. Thermal Conduction in a Tangled Magnetic Field. *Phys. Rev. Lett.* **80**(14), 3077–3080 Apr (1998).

[4] Scheffel, J. and Schnack, D. Numerical studies of confinement scaling in the conventional reversed field pinch. *Nuclear Fusion* **40**(11), 1885–1896 (2000).

[5] Cappello, S. and Biskamp, D. Reconnection processes and scaling laws in reversed field pinch magnetohydrodynamics. *Nuclear Fusion* **36**(5), 571 (1996).

[6] Bhattacharjee, A. private communication.

[7] Samtaney, R., Loureiro, N. F., Uzdensky, D. A., Schekochihin, A. A., and Cowley, S. C. Formation of Plasmoid Chains in Magnetic Reconnection. *Phys. Rev. Lett.* **103**(10), 105004 Sep (2009).

[8] Anderson, J. K., Forest, C. B., Biewer, T. M., Sarff, J. S., and Wright, J. C. Equilibrium reconstruction in the Madison Symmetric Torus reversed field pinch. *Nuclear Fusion* **44**, 162–171 (2004).

[9] Braginskii, S. Transport processes in a plasma. *Reviews of Plasma Physics* **1**, 205 (1965).

[10] Huba, J. NRL Plasma Formulary. Naval Research Laboratory, Washington, D.C. 20375, (2009).

[11] Almagri, A. F., Chapman, J. T., Chiang, C. S., Craig, D., Den Hartog, D. J., Hegna, C. C., and Prager, S. C. Momentum transport and flow damping in the reversed-field pinch plasma. *Physics of Plasmas* **5**(11), 3982–3985 (1998).

[12] King, J. R., Sovinec, C. R., and Mirnov, V. V. First-order finite-Larmor-radius effects on magnetic tearing in pinch configurations. *Physics of Plasmas* **18**(4), 042303 (2011).

[13] Ding, W. X., Brower, D. L., Fiksel, G., Den Hartog, D. J., Prager, S. C., and Sarff, J. S. Magnetic-Fluctuation-Induced Particle Transport and Density Relaxation in a High-Temperature Plasma. *Phys. Rev. Lett.* **103**(2), 025001 Jul (2009).

[14] Ennis, D. *Local Measurements of Tearing Mode Flows and the MHD Dynamo in the MST Reversed-Field Pinch*. PhD thesis, University of Wisconsin at Madison, (2008).

[15] Harvey, R. W., McCoy, M. G., Hsu, J. Y., and Mirin, A. A. Electron Dynamics Associated with Stochastic Magnetic and Ambipolar Electric Fields. *Phys. Rev. Lett.* **47**(2), 102–105 Jul (1981).

[16] Kromes, J., Oberman, C., and Kleva, R. Plasma transport in stochastic magnetic fields. Part3. Kinetics of test particle diffusion. *Journal of Plasma Physics* **30**(1), 11–56 (1983).

[17] D'Angelo, F. and Paccagnella, R. The stochastic diffusion process in reversed-field pinch. *Physics of Plasmas* **3**(6), 2353–2364 (1996).

[18] D'Angelo, F. and Paccagnella, R. Stochastic diffusivity and heat transport in the presence of a radial dependence of the perturbed magnetic field in the reversed field pinch. *Plasma Physics and Controlled Fusion* **41**(8), 941 (1999).

[19] Almagri, A. F. *The Effects of Magnetic Field errors on Reversed Field Pinch Plasma*. PhD thesis, University of Wisconsin at Madisonn, 1150 University Ave., Madison, WI, 537065, (1990).

[20] Stephens, H. D., Den Hartog, D. J., Hegna, C. C., and Reusch, J. A. Electron thermal transport within magnetic islands in the reversed-field pinch. *Physics of Plasmas* **17**(5), 056115 (2010).

[21] Hudson II, B. *Fast Ion Confinement in The Reversed-Field Pinch*. PhD thesis, University of Wisconsin at Madison, (2006).

[22] Fitzpatrick, R. Helical temperature perturbations associated with tearing modes in tokamak plasmas. *Physics of Plasmas* **2**(3), 825–838 (1995).

[23] Prager, S. C. Transport and fluctuations in reversed field pinches. *Plasma Physics and Controlled Fusion* **32**(11), 903 (1990).

[24] Predebon, I. and Paccagnella, R. Influence of slow particle dynamics on transport in stochastic plasmas. *Physics of Plasmas* **14**(8), 082310 (2007).

Chapter 5

Simulating the Pressure Evolution in MST

Performing simulations with DEBS in zero β mode, as was shown in the previous chapter, can tell us a great deal about the tearing mode activity in the RFP and how it affects the equilibrium, but it cannot tell us anything about the thermal transport directly. Also, the effect of pressure driven modes is neglected. Preliminary results from DEBS with finite β are presented in this chapter. ***Caveat: this work has not been verified and past work indicates that it will not have converged at the resolution used. This may cause qualitative changes in the result.*** Given that caveat, the results turn out to be very similar to those measured in MST so it is worth taking a look at.

In addition to self consistently modeling the single fluid MHD equations, DEBS has the ability to self consistently model the pressure evolution equation[1, 2, 3]. The pressure force is added to the momentum equation as well, but viscous heating is left out due to the lack of a physical viscosity model. The dimensionless set of equations that are solved in this mode are:

$$
\begin{aligned}
\frac{\partial P}{\partial t} &= -S\nabla\cdot(P\mathbf{V}) - S(\gamma-1)P\nabla\cdot\mathbf{V} + \frac{2(\gamma-1)}{\beta_0}\eta\mathbf{J}^2 + \nabla\cdot\left(\kappa_\perp^i\nabla_\perp T + \kappa_\parallel^e\nabla_\parallel T\right),\\
\frac{\partial \mathbf{V}}{\partial t} &= -S\mathbf{V}\cdot\nabla\mathbf{V} + S\mathbf{J}\times\mathbf{B} + \nu\nabla^2\mathbf{V} - S\frac{\beta_0}{2}\nabla P,\\
\frac{\partial \mathbf{A}}{\partial t} &= S\mathbf{V}\times\mathbf{B} - \eta\mathbf{J},\\
\mathbf{B} &= \nabla\times\mathbf{A},\\
\mathbf{J} &= \nabla\times\nabla\times\mathbf{A}.
\end{aligned}
$$

The continuity equation was not used for this work and the mass density was held fixed in time and space throughout the simulation. The first equation is the pressure evolution equation which includes Ohmic heating and anisotropic thermal conduction. The components of the thermal conduction, $\kappa_\perp^i$ and $\kappa_\parallel^e$, are defined (again in the dimensionless form) as:

$$
\begin{aligned}
\kappa_\perp^i &= 4.97\beta_0\frac{\rho^2}{B^2T^{1/2}},\\
\kappa_\parallel^e &= 4.97\beta_0 T^{5/2}\frac{\kappa_{\parallel 0}}{\kappa_{\perp 0}}.
\end{aligned}
$$

There are several important parameters that need to be set for the pressure evolution to be modeled. The Lundquist number (S) and the target Θ are inputs, as before, but additionally the ratio of the stored thermal to magnetic energy ($\beta = 2\mu_0 P/B^2$), and the ratio of the parallel to perpendicular heat conduction, $C_{\kappa_\parallel} = \kappa_{\parallel 0}/\kappa_{\perp 0}$, also need to be set. A derivation of the dimensionless form of $\kappa_\parallel$ and $\kappa_\perp$ is shown in appendix A. The γ in this case is the thermodynamical $\gamma = C_p/C_v = 5/3$.

A boundary condition for the pressure is also needed. This can either be to set the pressure gradient at the edge to zero or to set the edge pressure to a given value, β_{wall}, that is fixed in time throughout the simulation. When the pressure gradient at the edge is set to zero it tends to flatten the profile from the core to the edge. In the experiment the edge pressure tends to be low so setting the edge pressure to a fixed value yields more realistic behavior. The value of β_{wall} is some fraction of the initial pressure and is fixed in time. It is important to note that while it is the pressure that is evolved, the continuity equation, at least for the simulations discussed here, is not. In other words, the normalized mass density is held fixed in time and space at 1. This means that the pressure evolution is effectively a temperature evolution.

The simulations involving pressure evolution can be initialized in one of several ways. The most common cases are the so called 'Serg' case and the 'Para' case. In the 'Serg' case, the initial condition is a cold plasma with a uniform toroidal field and then a toroidal loop voltage is applied and the normalized current is ramped up to a target value over a specified number of resistive times (usually 1 to 2). In the 'Para' case, the initial condition is the paramagnetic equilibrium. The 'Serg' method takes a little longer to get to a reversed state than starting from the paramagnetic equilibrium, but has the advantage that it is more straight forward to interpret. Table 5.1 contains a list of run parameters used to generate the simulation results presented in this chapter.

The rest of this chapter will be concerned with the detailed study of a single DEBS simulation initialized with the 'Serg' method. This run has several interesting features that will be explored and compared directly to measurements made in MST.

Value	Z=2.5, μ=2
Minor radius, a	0.52 m
Major radius, R_0	1.5 m
Temperature, $T_0 = (T_i + T_e)/2$	13.6 eV
Density, n_0	$1 \times 10^{19} m^{-3}$
Toroidal Field, B_0	0.09 T
$Ln\left(\Lambda\right) = Ln\left(1.5476 \times 10^{10}\sqrt{\frac{10^6 T_0^3}{n_0}}\right)$	12.41
Pressure, $P_0 = 2n_0T_0$	43.57 Pa
$\beta_0 = 2\mu_0 P_0/B_0^2$	0.0135%
$\beta_{wall} = P_{wall}/P_0$	0.01
$\nu_{\|0} = 8.5 \times 10^4 T_0^{\frac{5}{2}} / \left(aB_0\sqrt{n_0}Ln\left(\Lambda\right)\right)$	0.0315
S_0	8,610.24
$\kappa_{\|} = 32.5\nu_{\|0}\sqrt{\mu}$	1.45
$\kappa_{\perp} = 10\beta_0\sqrt{\mu}/S_0$	2.22×10^{-5}
$C_{\kappa_{\|}} = \kappa_{\|}/\kappa_{\perp}$	65,315
$\eta_0 = 1.03 \times 10^{-4} Z Ln(\Lambda)/1.96 T_0^{1.5}$	$3.2\times10^{-5}\Omega$ m
$\tau_r = \mu_0 a^2/\eta_0$	10.5 ms
κ multiplier	0.2

Table 5.1: Parameters of interest for DEBS with pressure evolution as defined in ref. [3].

This is still a cylindrical calculation and uses the Spitzer resistivity as a resistivity model. This resistivity is calculated at each grid point based on the local temperature and density. The Z_{eff} used for this calculation was 2.5. The ions were assumed to be deuterium, so $\mu = 2$. Making Z_{eff} and μ different from one has a substantial effect on both S and $C_{\kappa_{\|}}$. A slight inconsistency is also introduced in the fact that $n_e = n_i = n$ is still assumed even though Z has changed. Anisotropic thermal conduction was also used in this run. The primary heat source is from resistive dissipation, ηJ^2. The primary heat loss for this run is thermal conduction to the wall. The resolution was 16 poloidal and 64 axial modes with 252 radial points. After de-aliasing this yields a resolution of 11 poloidal and 43 axial nonlinearly interacting modes that are evolved. The ratio of parallel to perpendicular conductivity, as mentioned above, is a relatively low 65,000. This ratio increases to over 10^7 as the simulation evolves because the scaling of the two conductivities with temperature, density, and magnetic field is maintained. As previously mentioned, this resolution is likely no where near high enough to get convergence. The radial resolution in particular needs to be significantly larger, perhaps several orders of magnitude, because the finite difference operator is only second order accurate. The density for this simulation was held constant. This is not a fundamental limitation of DEBS, as it can self consistently evolve the continuity equation as well, rather, it is a functional limitation. It seems that the continuity equation alone is not sufficient to model the density evolution observed in experiment. While the implementation of the density evolution should be numerically stable, large waves of density that propagate back and forth across the minor radius rapidly develop during the initial phase of the simulation whenever the density evolution is used. This eventually either causes negative densities or other non-physical results that cause the code to stop, so the density could not be evolved during the formation phase. If the density evolution is turned on after the plasma is well established, a large $m = 0$, $n = 1$ density perturbation that spans the minor radius of the plasma grows until the density begins to go negative. This $m = 0$, $n = 1$ density perturbation is mirrored by an $m = 0$, $n = 1$ temperature perturbation such that the pressure is largely unaffected until the density becomes negative. In the end, the density evolution was left off making the pressure evolution an effective temperature evolution.

There were a few other interesting general notes that should be made about this run. First, the dimensionless viscosity had to be relatively low in order to maintain reversal in these simulations. Remember that the dimensionless viscosity, which in the zero β case is approximately the Prandtl number, had to be 100 or more to keep the code stable, but here we see that the with a viscosity much above one we get no reversal at all. The minimum viscosity used here was 0.03. This difference in the scale of the viscosity is due simply to the fact that the resistivity in the simulation is less than one so the Prandtl number is still large even though the dimensionless viscosity is small. Also, the flat resistivity profiles that come from the Spitzer calculation help to stabilize the high n modes somewhat, necessitating even lower viscosities to get MST like behavior. Finally, the low n, $m = 1$ modes are still significantly higher than in MST. This may simply be a matter of resolution as the amplitudes of the higher n modes are similar to those measured in the experiment. There is some evidence that going to higher mode resolution, particularly in the poloidal direction, spreads out the energy in frequency space to some degree. However, recent work by the NIMROD group suggests that including additional physics will cause the mode amplitudes to saturate at the lower values seen in the experiment. The addition of ion gyro-viscosity in particular has has been shown to cause this saturation in cylindrical RFP simulations performed with the NIMROD code[4], but such two-fluid effects have not yet been successfully implemented in DEBS.

Simulating these plasmas with realistic β at MST parameters has proven to be a challenge, but has now been done with DEBS. Figure 5.1 shows the time evolution of several equilibrium quantities of interest. There are several interesting features of each of these plots that are worth discussing. The specified current drive can be seen in the plot of the pinch parameter where the current is ramped in about 10 ms from zero to 1.7 and then held fixed at that value for the rest of the simulation. The current is again controlled through a PID feedback scheme that, given the relatively low viscosity of these plasmas, essentially just keeps Θ constant in time. The reversal parameter crosses zero as the simulation reaches the current flattop and begins sawtoothing, as expected, but the sawtooth period is initially between 13 and 19 ms. This is much longer than we would typically expect on MST. Also, the maximum in the reversal parameter between sawteeth is closer to zero, or relatively shallow reversal, compared to both the MST case and the zero β case (though the sawteeth are huge, reaching a minimum of almost -0.4). This may well be due to the relatively low mode resolution as higher resolution allows for a lower overall viscosity and a stronger MHD dynamo, which is what drives the reversal in these simulations. Another point of interest is that the safety factor profile is sawtoothing in the way we expect from the experimental results. The safety factor on axis decreases slowly as the ohmic drive peaks the current density profile. At the sawtooth crash, the safety factor jumps up above 0.2 bringing the $m = 1$, $n = 5$ surface into the plasma before decaying, much like the evolution of q in MST. Finally, the volume averaged radial magnetic field is shown. Here again we see the three phases of the sawtooth described earlier.

While there are a lot of interesting dynamics to look at in these plasmas, there are four time points in particular that will be examined more closely. These are a time before, during and after the sawtooth at 84.6 ms and a time at 45 ms, where the decay of the safety factor on axis has hesitated, keeping the $m = 1$, $n = 5$ mode resonant for longer than is typical.

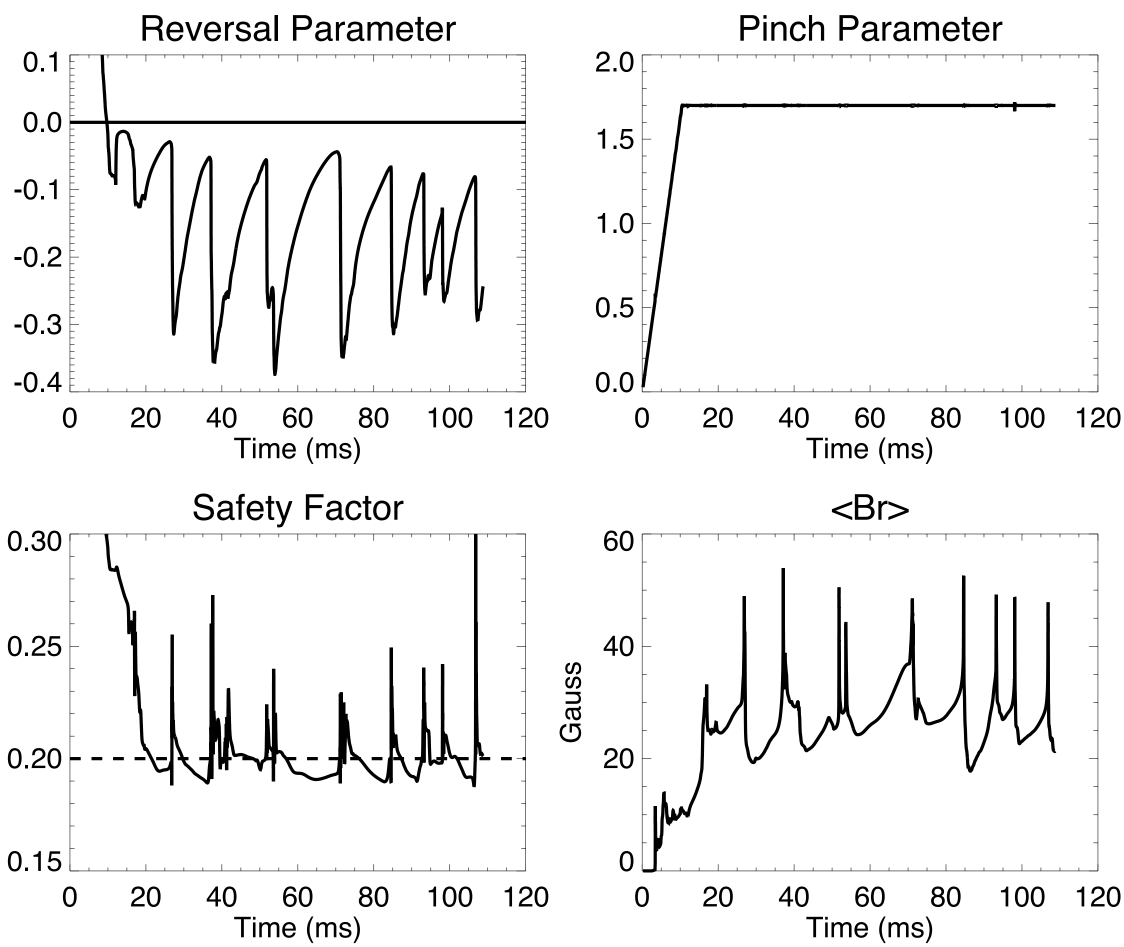

Figure 5.1: The equilibrium evolution is well behaved and shows several features expected from the MST plasma. These features include field reversal, sharp periodic sawteeth driven by spikes in the magnetic mode activity, and a safety factor that transitions across 0.2 at the sawtooth crash.

Figure 5.2 shows the time evolution of several of the pressure dependent quantities of interest. The primary goal of this run was to attain a Lundquist number of about 4×10^6 to look at dynamics that are similar to those seen in MST at a current that is comparable to that of MST. This was accomplished in this run as the Lundquist number, which goes through significant variation over the course of the sawtooth cycle, is about or a little higher than the target value on average. The Lundquist number scales strongly with temperature so it is not surprising that a temperature of 300 to 400 eV on axis is also seen. The poloidal β, which is defined as $\beta_p = \frac{\int P \partial V}{B^2_{\theta_{wall}}}$, is a little higher than the 5 to 6% typically seen in MST. This is because of profile effects that will be discussed shortly. The energy confinement time is also somewhat higher than that typically seen in MST, though it is generally within a factor of 2 of what is expected. The sawtooth evolution of τ_e is also similar to the evolution of the confinement time in MST.

Figure 5.3 shows the integrated B_r^2 for several modes of interest. This value is typically a good proxy for the qualitative behavior of the mode amplitudes measured at the edge of the plasma. It should be noted that quantitatively, the scaling of these profiles to the edge measurements varies significantly from mode to mode. There are several features of the mode evolution that are interesting. First, the energy in the $m = 1$, $n = 7$ mode rises slowly then spikes at the sawtooth crash as we would expect from the experimental data. However, the $m = 1$, $n = 6$ mode, which exhibits a similar behavior in MST, does not always have this type of time history in this simulation. Instead, it often saturates or even decreases in energy just before the sawtooth crash. (Note that the jump in the edge measured value in MST may be simply from the mode

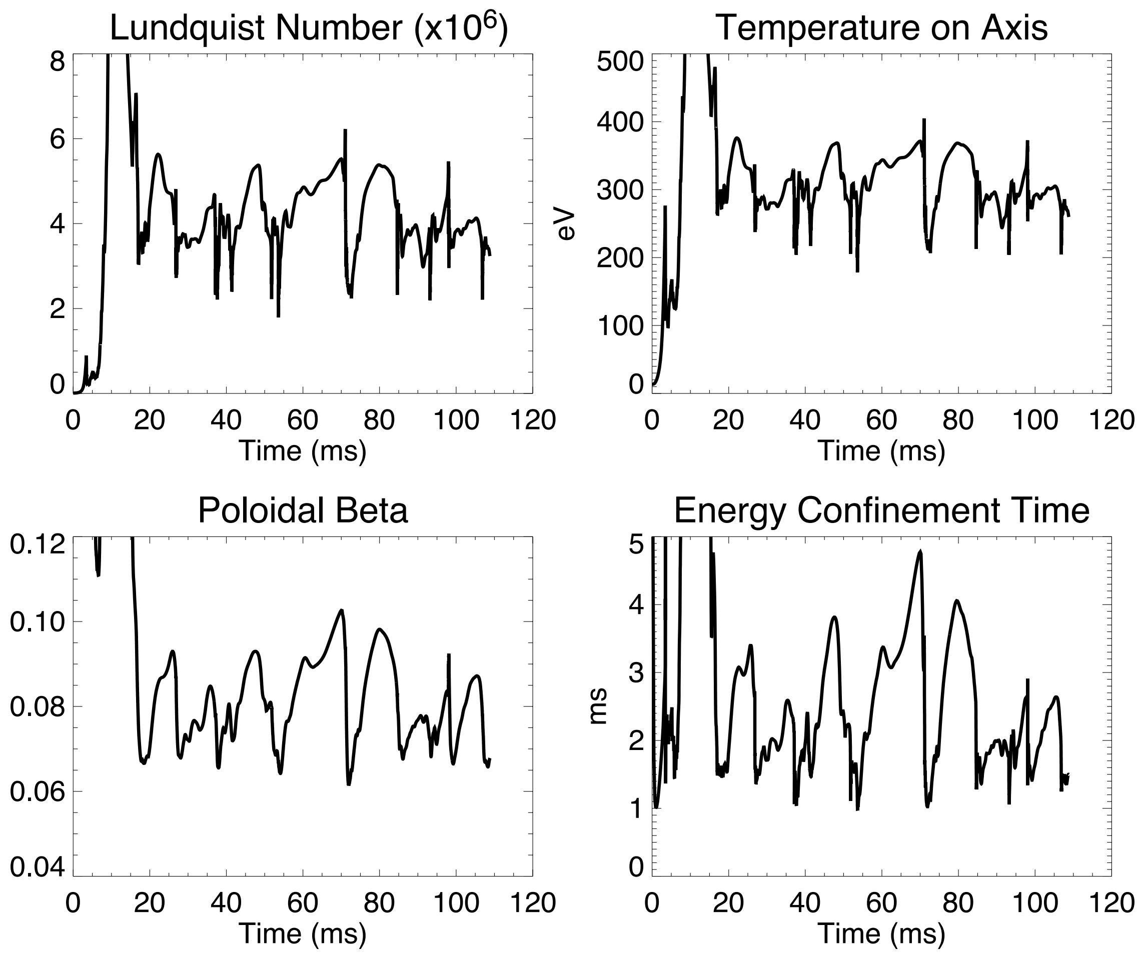

Figure 5.2: The equilibrium evolution of several global parameters of interest are shown in this figure. The Lundquist number on axis is about 4×10^6 as expected from MST. The temperature is about 300 eV with β_p of about 8% and τ_e of about 2.5 ms

jumping outward at the sawtooth crash, though measurements with the FIR system suggest that the mode may actually be growing rapidly as well.) Second, we see that the $m = 0$ mode evolution is quite different from the zero β simulations in the early part of the run where the sawtooth period is very long. As previously discussed, the $m = 0$ mode behavior is usually very different in the DEBS simulations than what we see in MST. In the zero β simulations the $m = 0$, $n = 1$ amplitude in particular would spike up at the sawtooth, then decrease almost linearly until the next sawtooth. In MST, they typically spike up then have a two phase decay to some nominal between sawtooth value. The first is a decay rapidly phase followed by a slower more resistive like decay phase. It is interesting that while we never see quite the same behavior, in the early phase of this simulation the sawtooth period is actually long enough to see the $m = 0$ modes decay to a relatively constant value before the next sawtooth. While this value is relatively low for these simulations, it's still somewhat higher than we would expect from experiment. Interestingly, it is more in line with the factor of 1.5 to 3 discrepancy that has long been observed in the $m = 1$ mode amplitudes rather than the factor of 4 to 10 seen in the zero β simulations. Later in the simulation, when the sawtooth cycle gets shorter, the behavior seen in the zero β simulations is recovered. This implies that there is some physical effect that is still not being accounted for in the simulation that enhances the decay rate of these $m = 0$ modes shortly after the sawtooth crash leading to the two phased decrease in the mode amplitude seen in MST. The implication is that the $m = 0$ modes are driven to high amplitude by the MHD physics captured by the simulation and, according to MHD, they should decay on a resistive dissipation type time scale, as is shown by the simulation. This time scale is also consistent with the time scale of the slower decay phase of the mode amplitudes in the experimental measurements. In the experiment, however, there is some additional effect that acts in the brief period after the crash to cause the mode amplitude to decrease rapidly before it starts the slower resistive decay.

5.1 Sawtooth Evolution of the Simulated Temperature

5.1.1 Equilibrium Evolution

Figure 5.4 shows the ensemble averaged electron temperature at two radial locations from MST and the temperature at the same two radial locations from DEBS for a single sawtooth. The temperature decreases in the core and increases in the edge at the sawtooth crash however, the temperature profile change is much faster in the simulation than is typically seen in MST. Figure 5.5 shows the ensemble averaged electron temperature profile from MST at three times relative to the sawtooth (left) compared to the same for a single sawtooth from DEBS (right). While this is not a perfect comparison by any means, it does illustrate that the temperature profiles in DEBS are generally much flatter than those of MST. While the on axis value, and even the value of the temperature near the reversal surface (r/a=0.8) show similar degrees of variation over the sawtooth, the temperature outside the reversal surface is much higher than we would expect from MST. Also, MST shows a strong gradient over the reversal region where as the DEBS simulation is essentially wall confined with the reversal surface flattening the profile if anything. From puncture plots of the simulated magnetic field it is expected that the magnetic stochasticity is reduced around the reversal surface and an $m = 0$ island with healed flux surfaces appears, leading

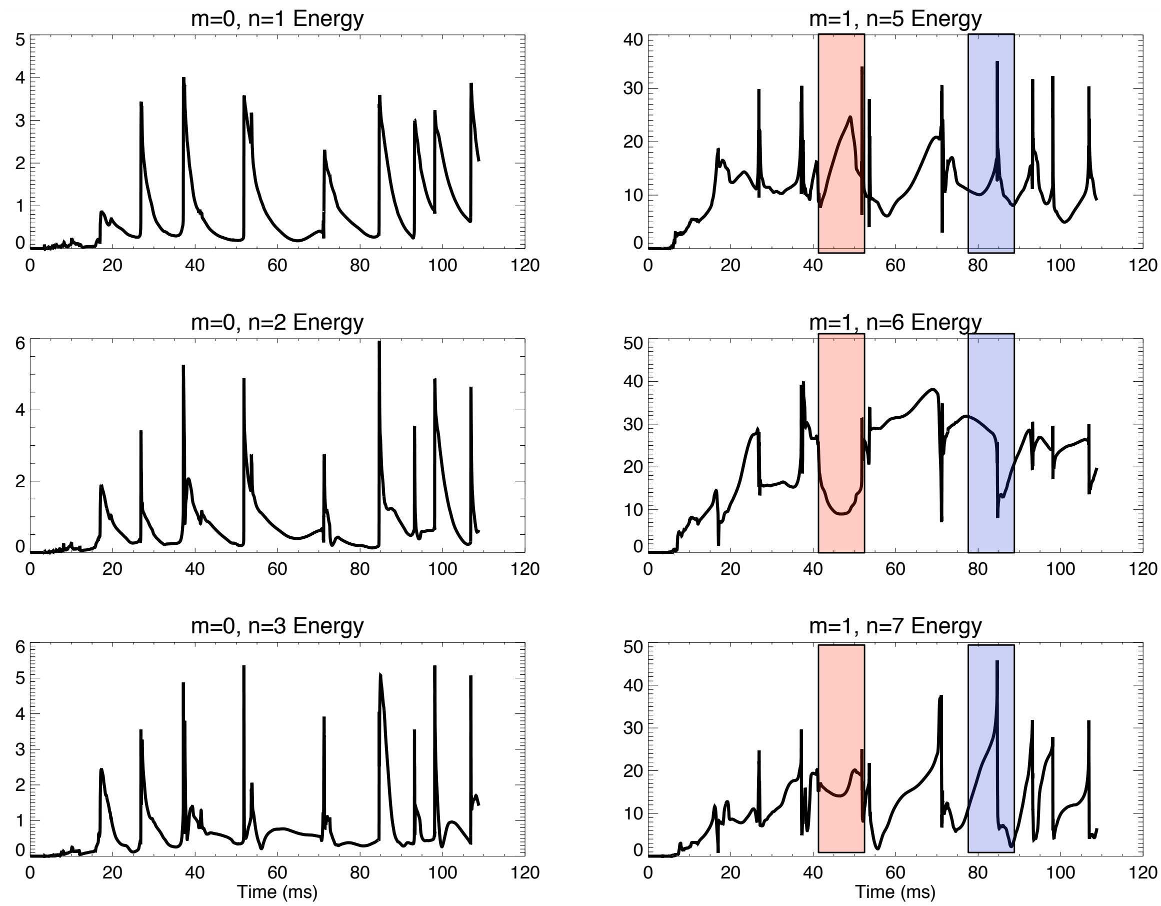

Figure 5.3: This figure shows the integrated B_r^2 for different mode numbers. The qualitative behavior of this quantity is generally a good proxy for the mode amplitudes measured at the edge of the plasma.The pink region indicates a region of QSH like behavior while the blue region indicates the sawtooth event that will be looked at in more detail.

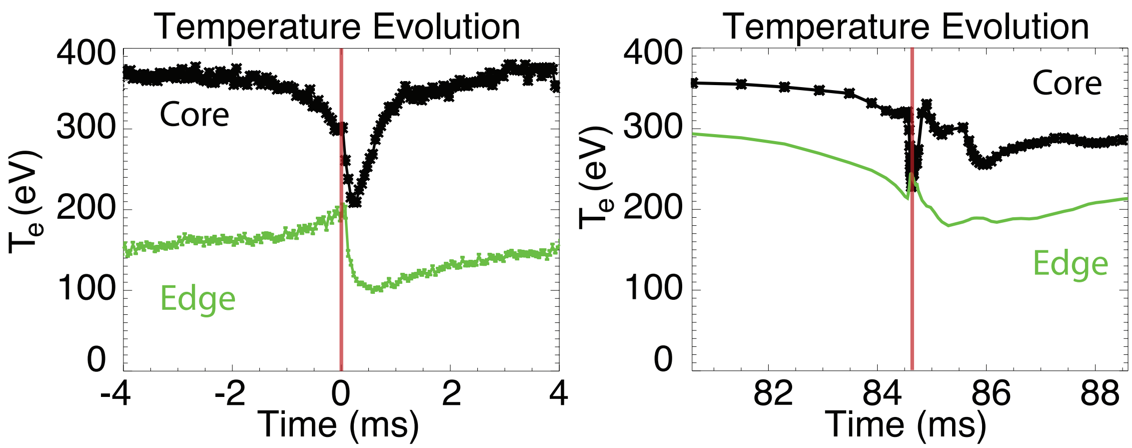

Figure 5.4: The ensemble averaged electron temperature from MST (left) compared to the temperature evolution from a single sawtooth in this pressure run (right).

to temperature profile flattening due to the high parallel heat transport. Because the $m = 0$ amplitudes are always relatively large in DEBS compared to the experiment, the heat transport across this island is relatively high for most of the sawtooth period. Furthermore, it has been suggested that ambipolarity constraints, which are not accounted for in the simulation, may reduce the heat transport in this region of the MST plasma[5]. Of course, numerical convergence may also be an important factor as the parallel heat flux will tend to leak across field lines if the simulation has not fully converged.

5.1.2 Evolution of Temperature Structures in the Simulation

These simulations also allow the examination of the behavior of temperature fluctuations which, for the first time, can be compared directly to measurements of electron temperature fluctuations made in MST. In the past, the measured temperature structures were compared to magnetic structures that were seen in the zero β

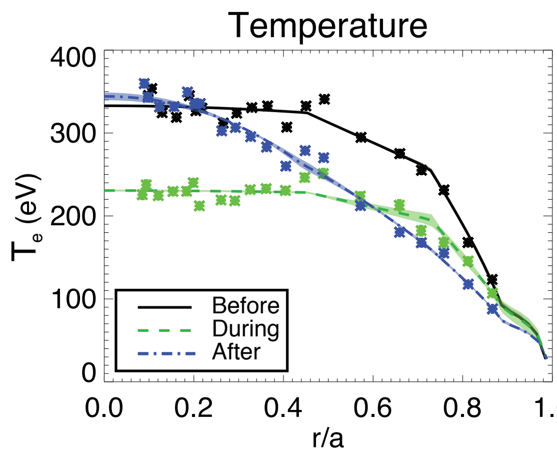

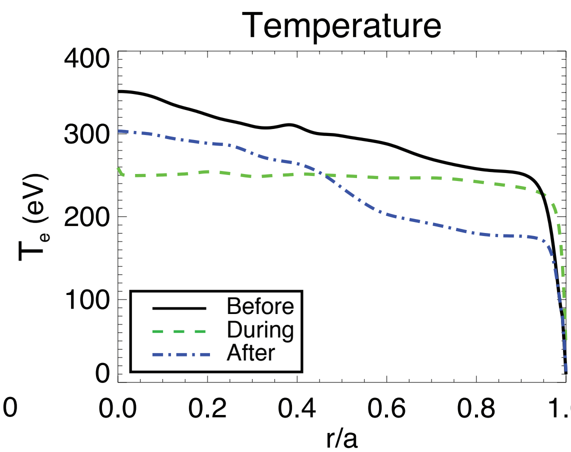

Figure 5.5: The ensemble electron temperature profile from MST (left) compared to the temperature profile from a single sawtooth in this pressure run (right) at three time points, before (black), during (green), and after (blue) the sawtooth.

simulations. With these simulations a much more direct comparison of the predicted temperature fluctuations to the measured electron temperature fluctuations[6] can be made. These fluctuations turn out to show a remarkable degree of agreement, even for the $m = 1$, $n = 6$ mode which has a time history that is somewhat different than expected for MST. Figure 5.6 shows a contour plot of the equilibrium temperature plus the $m = 1$, $n = 6$ fluctuation versus minor radius and toroidal angle from the DEBS simulation compared to a contour plot of the same data for the MST case from before a sawtooth. In both contour plots a clear flattening of the temperature profile is seen. In the simulation, this flattening is centered around the mode rational surface. In the MST case, it was originally reported that the temperature perturbation was centered around a point radially inward from the mode rational surface predicted by the MSTFit equilibrium reconstructions[7]. However, a comparison of the center of the temperature perturbation from that work to the mode rational surface predicted

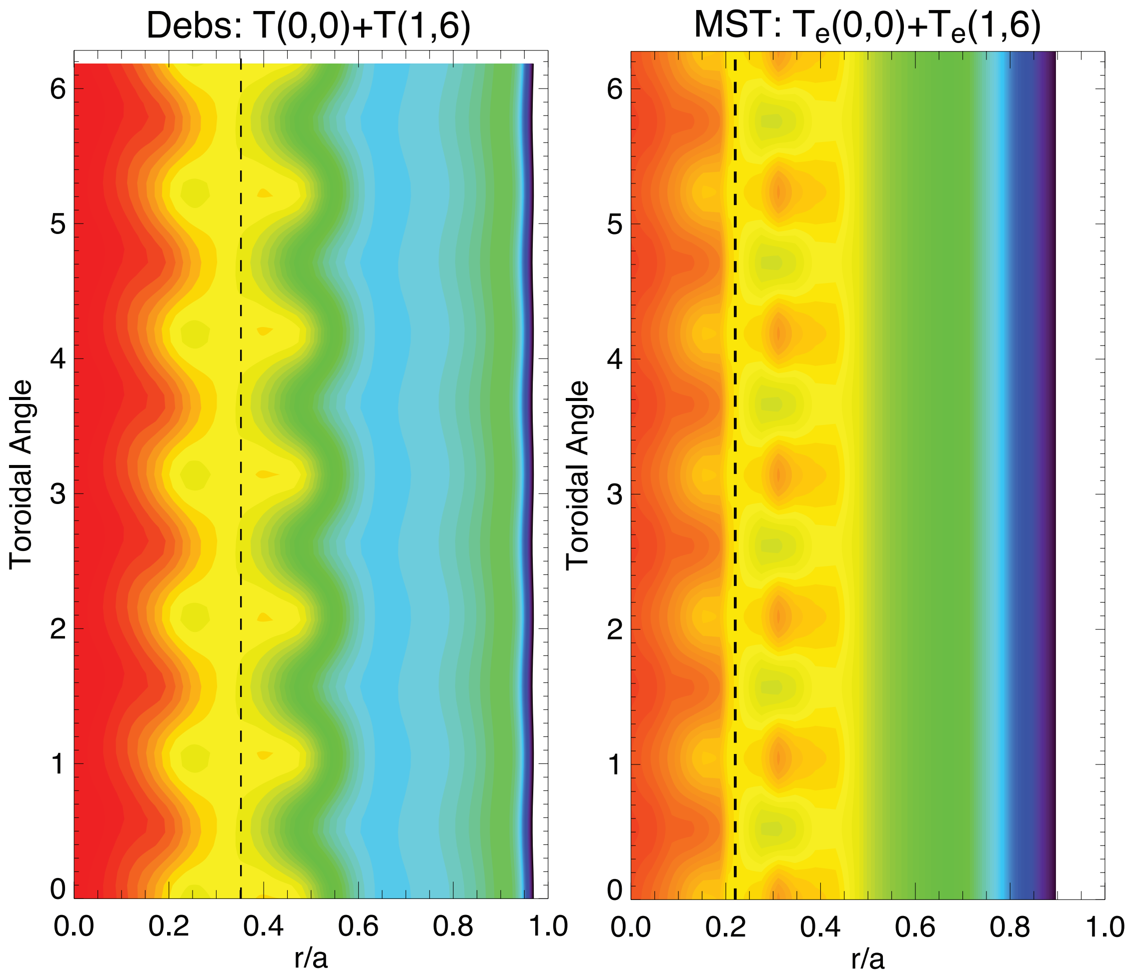

Figure 5.6: Contour plot of the equilibrium temperature plus the $m = 1$, $n = 6$ perturbation from simulation (left) and experiment (right). The dashed line indicates the location of the zero crossing of the pressure perturbation which in roughly co-located with the mode rational surface in the simulation.

by the safety factor profile evolution shown in chapter 3 is actually in fairly good agreement. The difference in the radial location of the predicted rational surface is likely due to the fact that equilibrium reconstructions presented in chapter 3 were constrained with a more complete data set than those in ref. [7]. This behavior is more clearly shown in figure 5.7 where the amplitude and temperature profile versus minor diameter (i.e. temperature profile across the X and O points of the perturbation) are shown for the simulation and the experimental data. The experimental data in both of these figures is from reference [6].

The $m = 1$, $n = 6$ temperature fluctuation shows a clear phase flip about the rational surface of the magnetic mode. The effect of the fluctuation is to reduce the temperature on the core side and increase the temperature on the wall side, flattening the equilibrium temperature across the rational surface of the magnetic mode, as was seen in the experiment. Also, this particular time slice has a perturbation of 10 to 20 eV which is also consistent with the fluctuation levels seen in MST. It is important to note that the data from the simulation is a single representative time slice that is compared to the ensemble averaged fluctuations measured in MST. Note also that the fluctuation in both cases is defined as $T_e = T_{e,0} + \tilde{T}_e cos(\theta)$ where θ is the phase of the magnetic perturbation measured at the edge. In other word, the phase relative to the magnetic perturbation folded into it, and thus the sign of the amplitude flips across the rational surface of the magnetic mode as the phase of the temperature perturbation relative to the phase of the magnetic perturbation changes by 90 degrees at the rational surface. In the simulation, the phase of the $m = 1$, $n = 6$ fluctuation in the poloidal magnetic field is approximately $-\pi/2$, which is in phase with the pressure

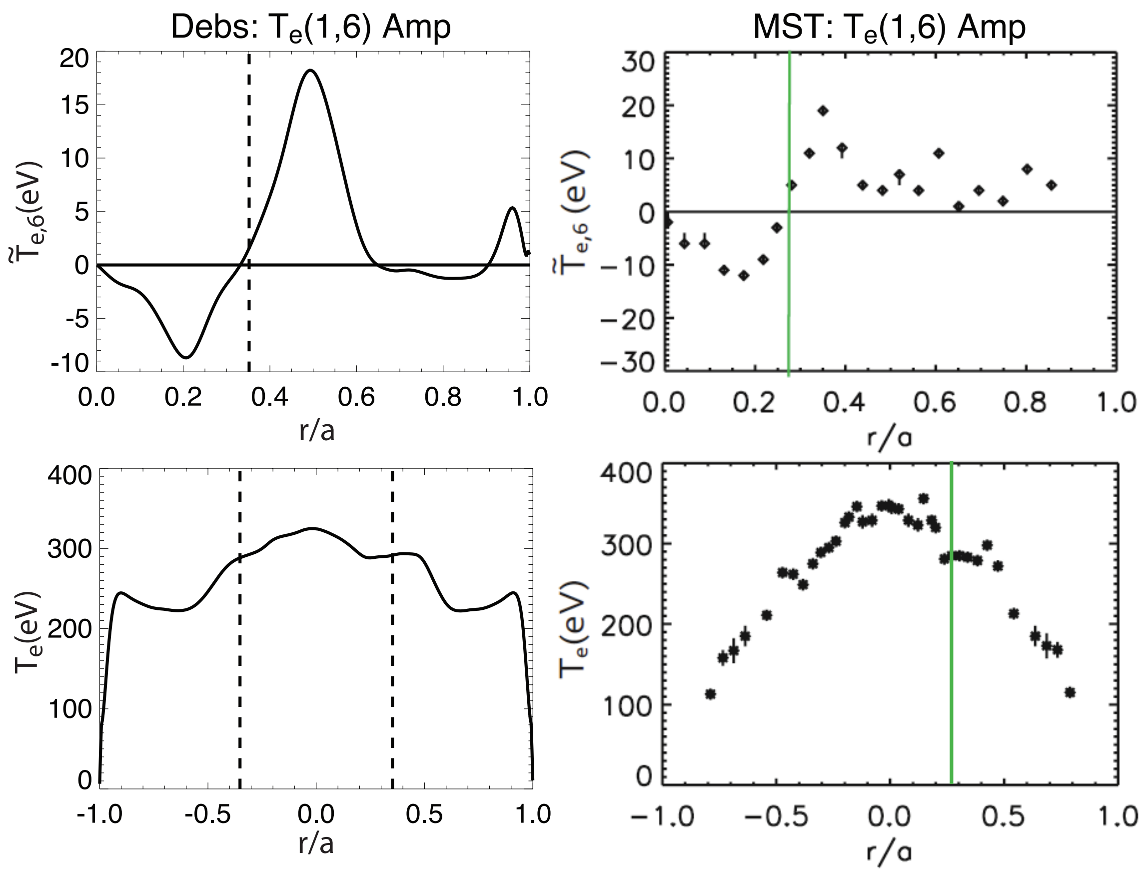

Figure 5.7: Temperature fluctuation amplitude and the resulting temperature profile from Debs (left) and a reproduction of the same data from reference [6]. In both cases the data is from a time before a sawtooth event and only takes the $m = 1$, $n = 6$ fluctuation into account. The bottom plots, therefore, are just the equilibrium plus the perturbation across the X and 0 points of the temperature structure.

perturbation in the mid-radius and π out of phase in the core region. This sign flip in the phase of the temperature fluctuation generates a temperature fluctuation profile very similar to what is observed in MST. While the phase change in this case is fairly abrupt and the phase across each side of the perturbation reasonably constant, they are not perfectly so. Thus, this analysis method slightly underestimates the temperature perturbation. In some cases, the relative phase does not stay constant with radius suggesting that a measurement of the perturbation would significantly underestimate the fluctuation amplitude as compared to an uncorrelated measurement.

At the sawtooth crash, all the correlated $m = 1$ temperature fluctuations in MST disappear, with the fluctuation amplitudes falling to within uncertainty of 0. However, there are correlated $m = 0$ fluctuations that appear briefly around the sawtooth event. In the simulation, the $m = 1$ temperature perturbation amplitudes decrease, but significant $m = 1$ temperature fluctuations persist throughout the sawtooth event. These fluctuations tend to be out of phase with the magnetic perturbations and do not change sharply at the mode rational surface as was seen before the sawtooth. Furthermore, the time evolution of the phase near the sawtooth crash does not track the time evolution of the phase of the magnetic perturbation. In other words, the relative phase of the temperature fluctuation with respect to the magnetic fluctuation becomes random and would average to zero in an ensemble. It is possible that this same behavior is going on in MST and that by assuming correlation to the magnetic perturbation, the experimental measurement is not able to detect these fluctuations. Future upgrades to the Thomson scattering system on MST will enable uncorrelated temperature fluctuation measurements which will definitively answer this question.

For now, we can look at the temperature fluctuations that are correlated to the $m = 0$ fluctuations in both the simulation and measurement. Figure 5.8 shows contour plots of the temperature fluctuation from DEBS and MST for the $m = 0$, $n = 1$ mode at the sawtooth crash. This perturbation is strongly edge peaked, as expected, however it extends across the entire minor radius. This is consistent with recent measurements from MST that show the $m = 0$, $n = 1$ temperature fluctuation extending all the way into the core[8, 9]. Interestingly, in MST this perturbation, as can be seen in figure 5.9, is phase locked, decreasing the temperature uniformly across the profile, and it is simply the amplitude that changes. In the simulation the perturbation amplitude gets very small and slightly positive in the mid radius while the core and the edge see substantial reduction in the temperature at the 0-point of the mode.

Perhaps the most striking thing that the electron temperature fluctuation measurements in MST revealed was the presence of a large temperature fluctuation that forms in the core region of plasma just after the sawtooth crash. This fluctuation has an $m = 1$, $n = 5$ character and grows to over 10% of the equilibrium temperature and encompasses over 20% of the minor radius. A similar structure can also be seen with the DEBS code. Figure 5.10 shows the electron temperature versus radius and toroidal angle for both simulation and experiment. While the simulated temperature perturbations tend to be about a factor of two smaller than those seen in MST after the sawtooth, the structure and time history is very similar. These perturbations form and grow in the few milliseconds after the sawtooth event and then slowly decay away after the rational surface leaves the plasma. The $q = 0.2$ surface for this time point is $r/a \approx 0.19$ (dashed line in the left plots of figure 5.11) which is slightly radially

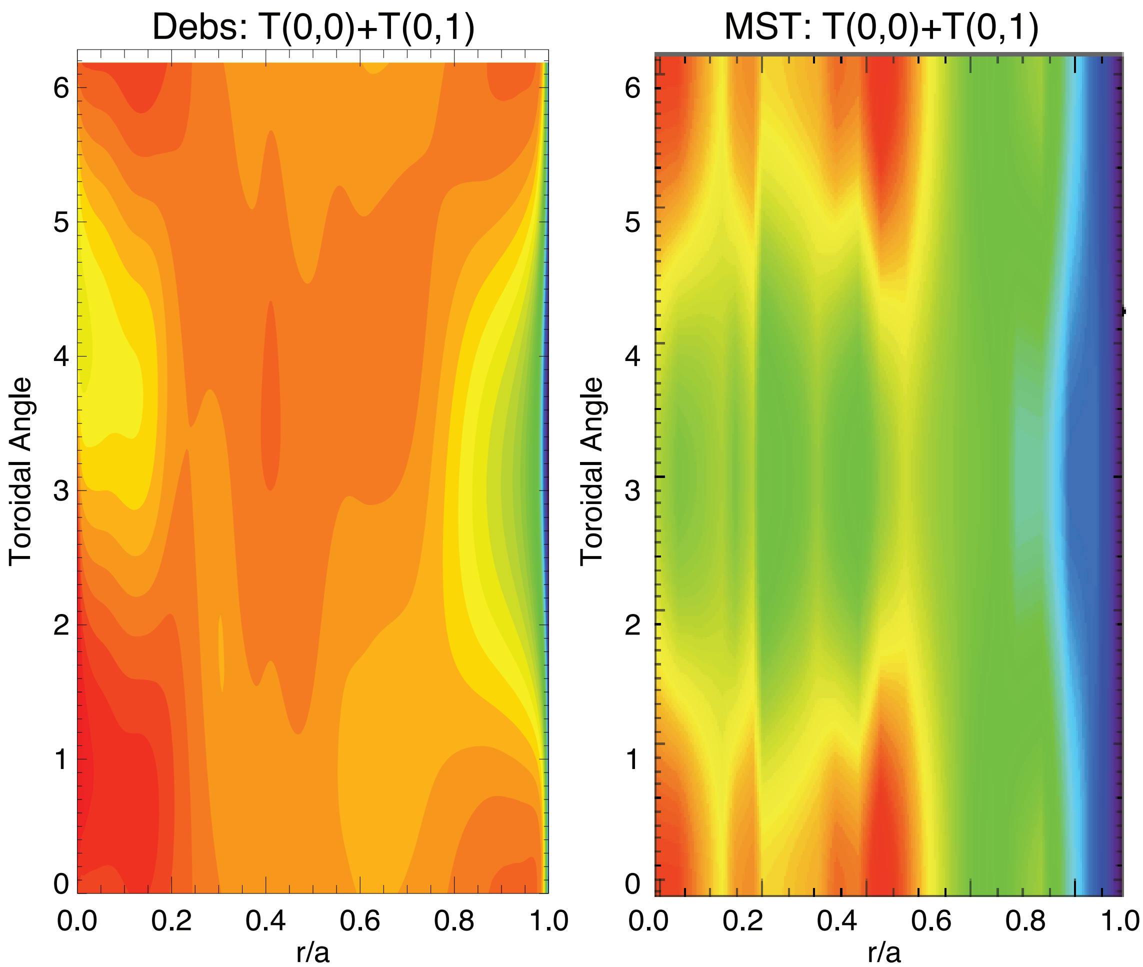

Figure 5.8: Contour plot of the equilibrium temperature plus the $m = 0$, $n = 1$ perturbation from the DEBS simulation (left) and the equilibrium plus $m = 0$, $n = 1$ perturbation measured in MST (right). Note that the rational surface from the typical cylindrical q calculation is about $r/a = 0.8$. Note that the color scales for the two plots are different.

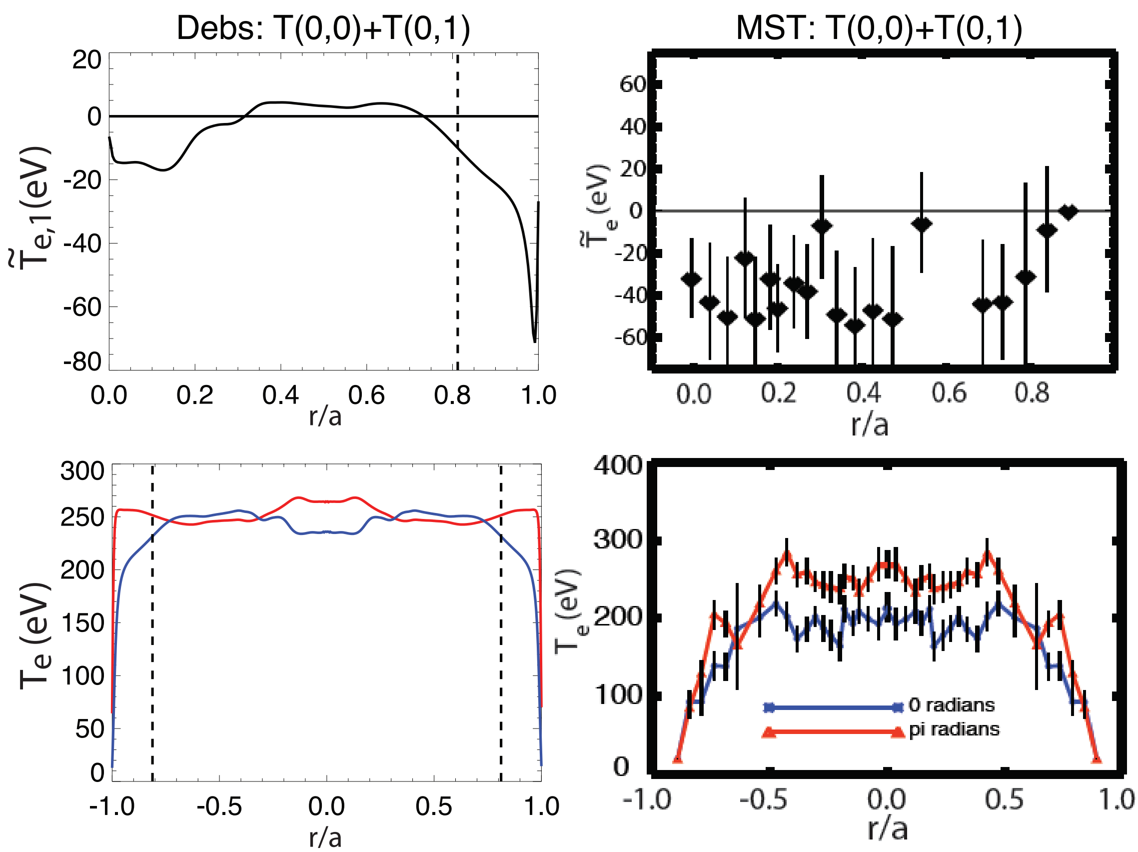

Figure 5.9: Left: radial profile of the $m = 0$, $n = 1$ temperature fluctuation amplitude and equilibrium plus $m = 0$, $n = 1$ fluctuation at 0 (blue) and π (red) radians. Right: Reproduction of the $m = 0$, $n = 1$ fluctuation from reference [8]. The profiles of the temperature fluctuation amplitude and equilibrium temperature plus the $m = 0$, $n = 1$ perturbation are shown.

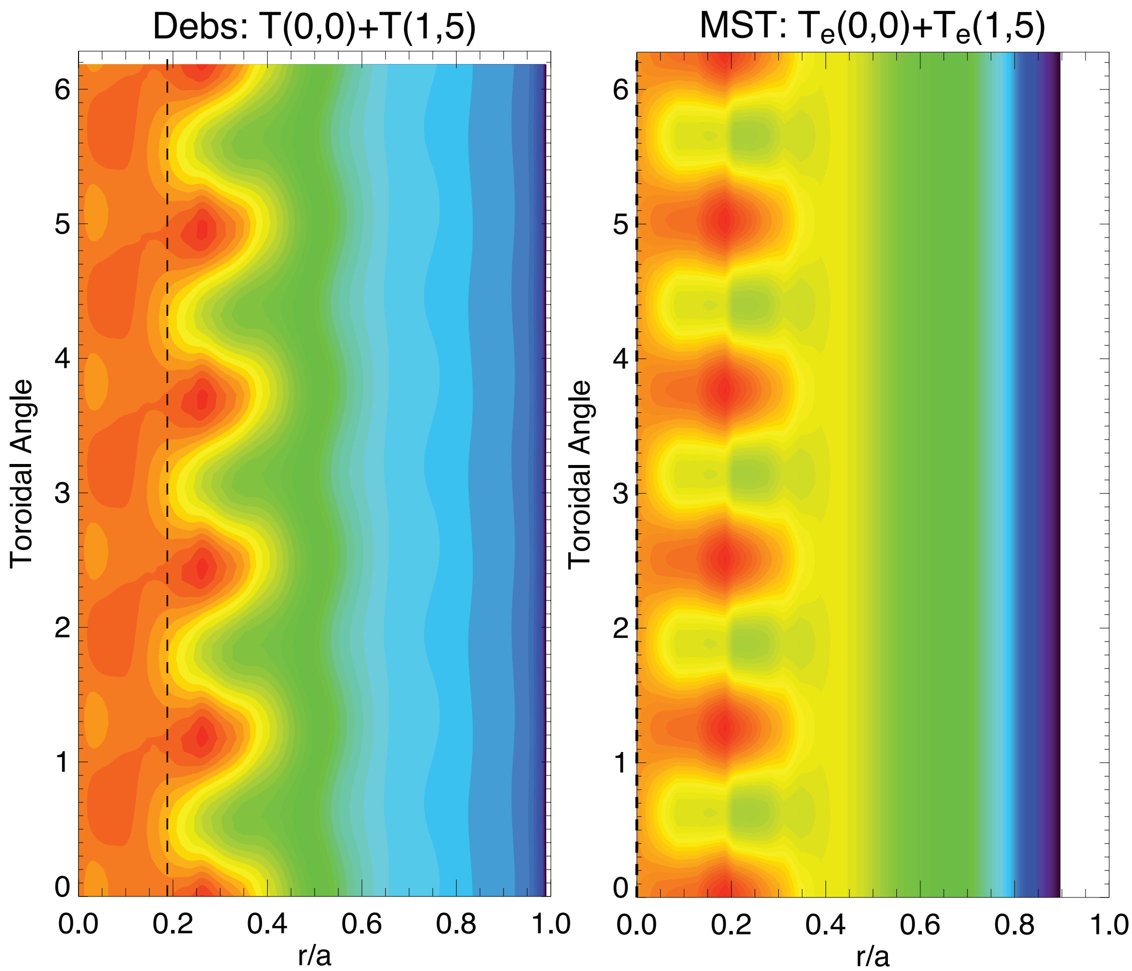

Figure 5.10: Contour plot of the equilibrium temperature plus the $m = 1$, $n = 5$ perturbation. The dashed line on the left plot shows the rational surface for the $m = 1$, $n = 5$ mode from the typical cylindrical q calculation at $r/a = 0.18$ while the $q = 0.2$ location for the MST case is expected to be about $r/a = 0.1$ (not shown). In both cases, the hot structure is far from the rational surface and a clear phase flip around the rational surface is not seen.

outward from where the π phase change is seen. What is really interesting about this is that there appears to be a small amount of cooling in the inner 10% of the minor radius. Due to the viewing geometry of the Thomson scattering system on MST, there is poor resolution in this region so it is hard to say for sure if a similar structure exists in the experiment. That said, in the region where we have good coverage with the Thomson diagnostic, we do see a clear hot structure that consistently appears after sawteeth in both the experiment and in this simulation. Much like the experiment this structure takes up over 20% of the minor radius and the phase of the perturbation is nearly constant across that whole hot region and is nearly in phase with the edge poloidal magnetic perturbation. This last point indicates that this perturbation is essentially the hot part of the temperature flattening seen with the $m = 1$, $n = 6$ perturbation.

5.2 QSH Like Temperature Structure in the Simulation

The first shaded region in figure 5.3 (from 40 to 50 ms) shows a quasi-single helicity (QSH) like event. This is not a QSH event by the typical N_s definition as the secondary modes are still very large, but it has the same character as events seen in experimental data in that the primary mode grows in time while the secondary modes decrease in time. This event persists until the $m = 1$, $n = 5$ resonant surface leaves the plasma. Interestingly, the mode amplitude does not fall dramatically at this time. Instead, the mode amplitude decrease over several milliseconds.

This mode has an associate temperature structure that, much like the case of the $m = 1$, $n = 5$ after the sawtooth, appears radially outward from the rational surface (see figure 5.12). The rational surface approaches the magnetic axis as the

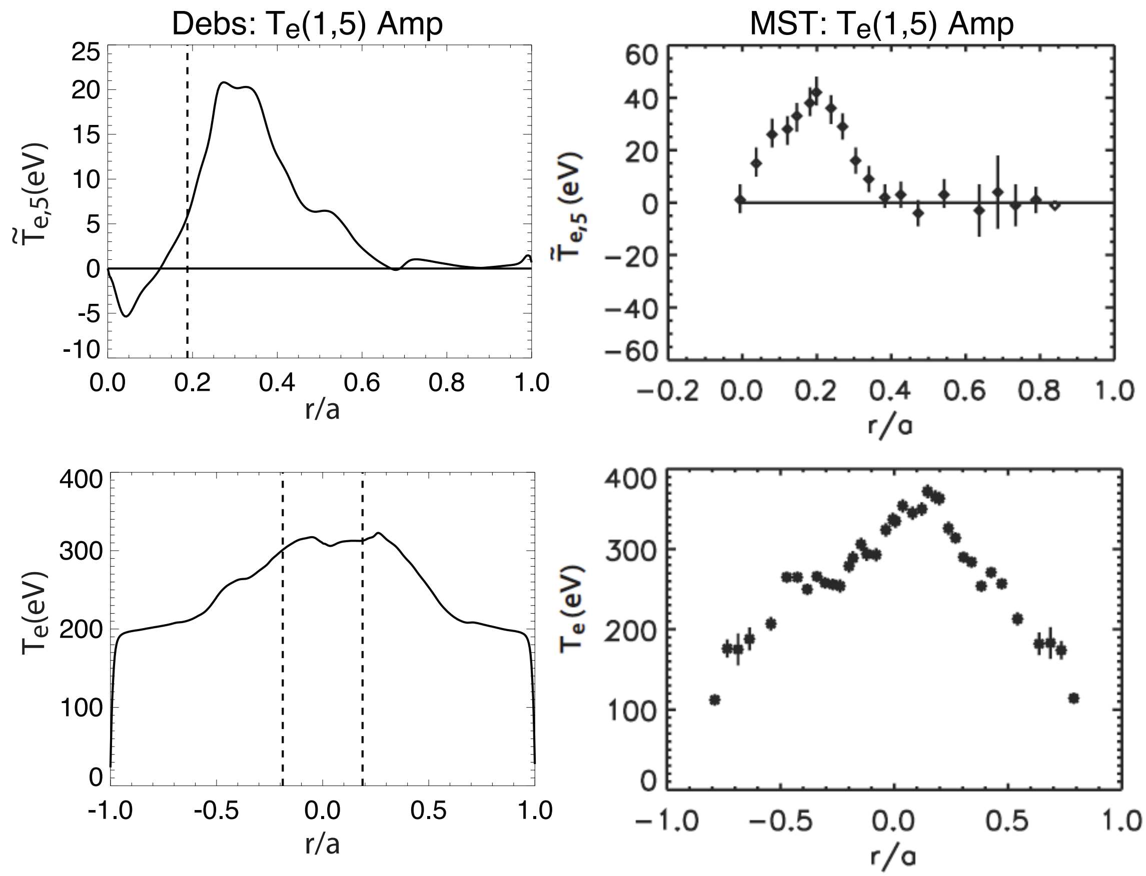

Figure 5.11: The amplitude and the profile of the equilibrium plus $m = 1$, $n = 5$ perturbation across the X and O points of the perturbation. Notice that the phase changes by π radially inward from the rational surface and the dominant structure is that of a hot island. There is a small amount of cooling towards the core, but this is only about a quarter of the amplitude of the hot part of the fluctuation.

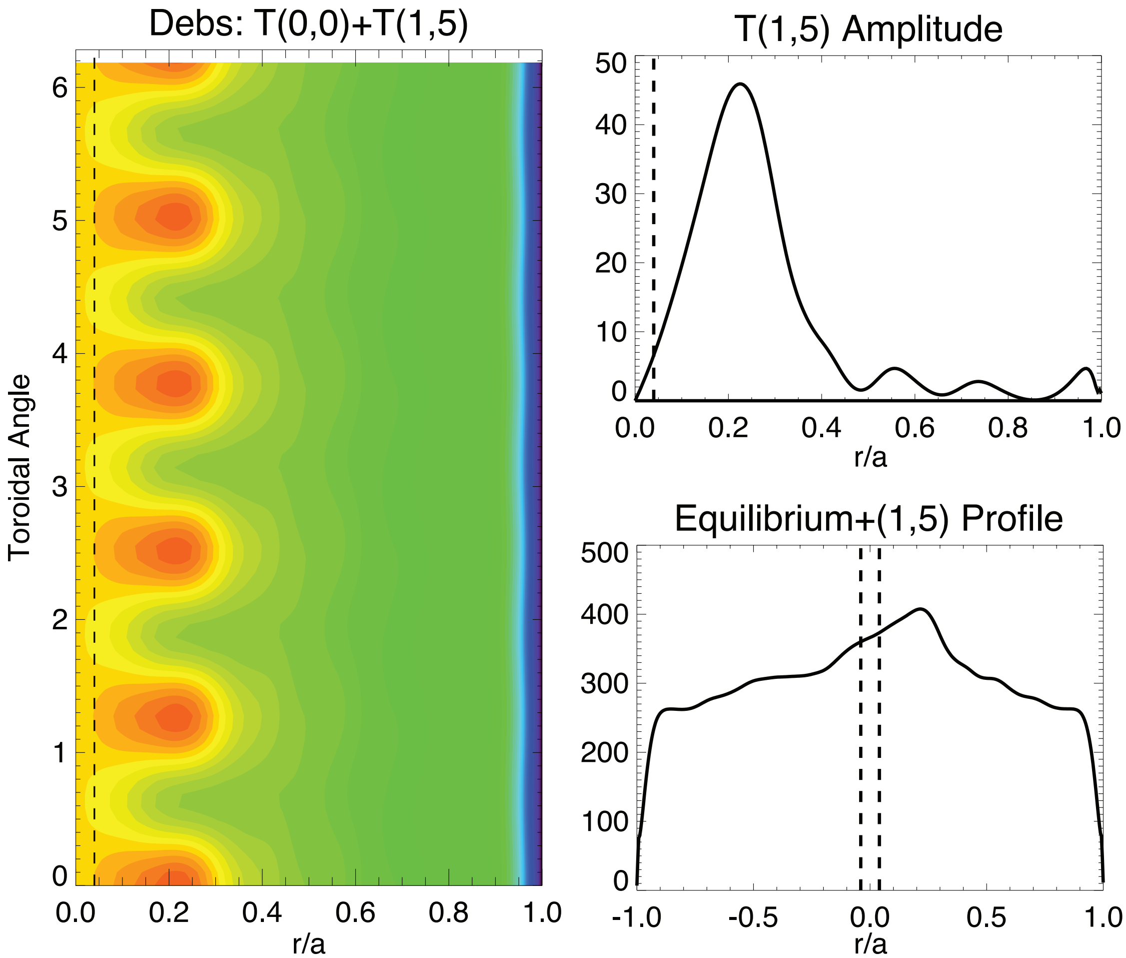

Figure 5.12: Contour plot of the equilibrium temperature plus the $m = 1$, $n = 5$ perturbation. Note that the rational surface from the typical cylindrical q calculation is nearly at the magnetic axis. The 1D plots are of amplitude of the $m = 1$, $n = 5$ perturbation and the profile for the equilibrium plus the $m = 1$, $n = 5$ perturbation.

current is peaked from the ohmic drive. However, in this case, the safety factor on axis stays above 0.2 for almost 10 ms. This allows the $m = 1$, $n = 5$ mode to grow to a relatively high amplitude. The temperature perturbation grows to an amplitude of over 46 eV before the $q = 1/5$ surface moves out of the plasma. By looking at the evolution of this mode, it appears that a large $m = 1$, $n = 5$ tearing mode resonant near the core slowly moves out of the plasma. However, as the mode rational surface moves near the axis, the amplitude does not decay significantly, remaining relatively large even after the resonant location of the mode appears to be outside the plasma. One can think of this as an internally non-resonant mode. It has been suggested that the magnetic axis may be significantly distorted by this perturbation, moving around significantly due to the large magnetic perturbation near it. However, even though this perturbation is large compared to other perturbations, it is still less than 2% of the mean field. If we define the magnetic axis as the location where the poloidal field crosses zero then the magnetic axis only moves by about 1 cm (or 2% of the minor radius). This suggests that, at least in the simulation, this hot island is not due to a significant helical distortion of the magnetic axis. Interestingly, though perhaps not unexpectedly, puncture plots of the magnetic field also show that a relatively large $m = 1$, $n = 5$ island structure that persists after the mode rational surface leaves the plasma. This structure in the magnetic field is consistent with the structures seen shortly after sawteeth in the zero β simulations.

5.3 Discussion

The primary goal of the simulation presented in this chapter was to obtain a peak temperature similar to that measured in MST as well as a profile that varied significantly through the sawtooth cycle. This was accomplished by adjusting the majority ion mass and the effective charge assumed for the plasma and thus adjusting the value of the ratio of parallel to perpendicular thermal conduction. The values of 'κ multiplier' and 'betawl' were also adjusted until the temperatures we wanted were achieved. Using the values of $\mu = 2$ and $Z_{eff} = 2.5$ yielded the MST like results seen here. The value of β_{wall} was somewhat arbitrarily set to the relatively low value of 0.01 due to the faulty assumption that it was a fraction of the core value which changes in time, whereas it is actually constant in time for these computations. This set of assumptions reduced the thermal conductivity sufficiently that the peak value of the temperature and the profile shape more closely matched what is seen in MST.

Using a higher β_{wall} and a different Z_{eff} would produce results that are more consistent with the relatively flat temperature profiles expected for the large magnetic modes in this simulation. Furthermore, it is likely that a higher parallel thermal conduction (if resovled) would cause the pressure fluctuations to stay relatively small except when a coherent magnetic island appears. While ideally one would model all the physics such that the self consistent solution yields the experimental measurement, this work suggests that one can take a short cut by countering the relatively high magnetic diffusion with relatively low thermal conductivity to get temperature behavior that matches the experiment. What is intriguing is that the thermal conductivity needs to be reduced to get MST like behavior. This ties into the result from the previous chapter as it suggests that the effect of trapped particles on both the resistivity and the thermal conductivity may need to be applied in the simulation to model the transport correctly. While this cannot be done self consistently because of the cylindrical geometry Debs uses, it may be possible to include it as an ad-hoc radial dependence. Hopefully, this is something that will be explored in the future as there is clearly much more to examine with these simulations.

In conclusion, this chapter presented a direct comparison between data from a simulation in which the pressure was self consistently evolved and experimental data from MST. The simulated plasma dynamics are generally found to be in good agreement with measurements despite the fact that the simulation results have likely not converged. In particular, fluctuations in the simulated temperature are very similar to temperature fluctuations measured in MST. This encouraging results will hopefully prompt future exploration of this type of simulation. There is a great deal of physics to be learned about the mechanisms of the formation of these temperature structures, in particular the hot island structures, that seem to appear far from the rational surface of the magnetic modes. Understanding how this code has produced those structures may give real insight into the physics that is happening in the RFP device. With more work in this regard, there is hope that a code like DEBS could be used to do predictive modeling of the transport in the RFP.

REFERENCES

[1] Sovinec, C. R. *Magnetohydrodynamic Simulations of Noninductive Helicity Injection in the Reversed-Field Pinch and Tokamak*. PhD thesis, University of Wisconsin at Madison, 1150 University Ave., Madison, WI, 53706, (1995).

[2] Scheffel, J. and Schnack, D. D. Confinement Scaling Laws for the Conventional Reversed-Field Pinch. *Phys. Rev. Lett.* **85**(2), 322–325 Jul (2000).

[3] Scheffel, J. and Schnack, D. Numerical studies of confinement scaling in the conventional reversed field pinch. *Nuclear Fusion* **40**(11), 1885–1896 (2000).

[4] King, J. R., Sovinec, C. R., and Mirnov, V. V. First-order finite-Larmor-radius effects on magnetic tearing in pinch configurations. *Physics of Plasmas* **18**(4), 042303 (2011).

[5] Terry, P. W., Fiksel, G., Ji, H., Almagri, A. F., Cekic, M., Den Hartog, D. J., Diamond, P. H., Prager, S. C., Sarff, J. S., Shen, W., Stoneking, M., and Ware, A. S. Ambipolar magnetic fluctuation-induced heat transport in toroidal devices. *Physics of Plasmas* **3**(5), 1999–2005 (1996).

[6] Stephens, H. D., Den Hartog, D. J., Hegna, C. C., and Reusch, J. A. Electron thermal transport within magnetic islands in the reversed-field pinch. *Physics of Plasmas* **17**(5), 056115 (2010).

[7] Stephens, H. *Electron Temperature Structures Associated With Magnetic Tearing Modes in the Madison Symmetric Torus*. PhD thesis, University of Wisconsin at Madison, (2010).

[8] Kasten, C. *Electron Temperature Fluctuations Correlated to Tearing Mode Activity in the Reversed-Field Pinch*. Undergraduate senior thesis, University of Wisconsin at Madison, (2011).

[9] Kasten, C., Den Hartog, D., Stephens, H., Hegna, C., and Reusch, J. Electron temperature fluctuations during sawtooth events in a reversed-fi eld pinch. *Physics of Plasmas* (submitted for publication).

Chapter 6

Conclusions and Future Work

This thesis contains results from two major projects. These results are:

- New Thomson scattering capabilities facilitated the determination of the sawtooth evolution of the T_e profile, the magnetic equilibrium, and χ_e at a 20 kHz time resolution in 400 kA standard MST plasmas.
- χ_e varies by two orders of magnitude in the core region of the plasma and an order of magnitude in the mid radius throughout the sawtooth cycle.
- Nonlinear single fluid MHD simulations reproduce the equilibrium evolution well including the duration of the sawtooth crash.
- Trapped particles do not carry heat along diffusing magnetic field lines and must be taken into account for the predicted χ_e to match the measured χ_e.
- χ_e in the mid-radius is stochastic, other transport mechanisms are important in the core at some times.
- Simulations with self consistent pressure evolution show temperature fluctuations that are remarkably similar to $\tilde{T}_e$ measurements made in MST.

6.1 Discussion

The primary motivation for this work has been to understand and document, in a quantitative way, the role of magnetic stochasticity in the overall thermal transport throughout a sawtooth event. In this thesis, understanding the effect of stochastic transport was approached in two ways. The first was to compare the measured thermal diffusion to the value of stochastic diffusion predicted using zero β simulations run at parameters matching those of 400 kA discharges in MST as closely as possible. One critical point that emerged from this analysis is that trapped particles cannot carry heat along stochastically wandering field lines. In MST, the trapped fraction is $\sim 50\%$ across much of the plasma leading to about a factor of two reduction in thermal transport. With this reduction there are two key insights that are gained into the thermal diffusion in MST. The first is that the transport in the mid radius of the plasma is indeed dominated by stochastic diffusion at nearly all times through the sawtooth cycle. The second point is that while the heat transport in the core is generally dominated by stochastic thermal diffusion between sawteeth, near the sawtooth crash is not. Rather, the transport is likely dominated by a combination of the 3D effects of magnetic islands in the core region of the plasma[1] and additional, possibly electrostatic fluctuation driven[2], transport mechanisms.

The second way stochastic transport was evaluated was to self consistently model the pressure evolution using classical anisotropic thermal conduction so that the computed temperature profiles could be compared directly to measurements. By allowing the full 3D evolution of the temperature, a direct comparison of the temperature fluctuation evolution could also be made. One clear, though not unexpected, feature seen using this method is that the temperature profile behavior in the reversal region does not agree with experimental measurements. What is somewhat surprising is the striking agreement between the temperature fluctuations measured in the core of MST and those in the simulation. This suggests that the fluctuations are not sensitive to any physics left out of the model, and that the necessary physics to generate the observed temperature structures is largely captured by the code. This is important as the exploration of quasi-single helicity and single helical axis states[3] is an increasingly important part of the experimental programs at both the MST and other RFP devices.

The knowledge gained by this work represents an advancement in the understanding of the dominant mechanisms of thermal transport in MST, information necessary for mitigating losses and enhancing energy confinement in RFP devices. These results also have further reaching consequences. For example, the reduction in transport due to trapped particles was originally made when considering heat transport in the inter-cluster medium of galaxy clusters[4, 5] where turbulent mixing can create stochastic magnetic fields, but the potential for large mirror ratios in this case, could substantially reduce the thermal transport in these plasmas. In tokamak plasmas, stochastic magnetic fields are generated when resonant magnetic perturbations (RMPs) are applied in order to reduce the occurrence of edge localized modes (ELMs)[6]. In the tokamak case, the trapped particle fraction can be over 70%, possibly leading to the smaller than expected thermal transport observed. The excellent agreement between equilibrium reconstructions of MST discharges and force free simulations shows that single fluid resistive MHD captures much of the important physics for the RFP. However, the fact that the magnetic mode amplitudes are still larger than those observed in experiment may be an important consideration in future high Lundquist number simulations. Finally, further analysis of the finite β DEBS simulations could lend real insight into how temperature structures observed in the experiment form and how they might scale with such parameters as Lundquist number and aspect ratio.

6.2 Future Work

There is a great deal more that should be done with this analysis. For the work presented in chapter 3 the convective transport should be properly computed and included in the calculation. While this is unlikely to make any significant contribution to the behavior in the core, the lack of convective transport numbers likely has a noticeable effect on the thermal diffusion near the reversal surface. The convective transport can now be computed using the Monte Carlo code NENE for any given equilibrium reconstruction. While it would not be trivial, it would not be overly difficult to use this code to get the convective transport numbers for the data set used in this thesis. This would allow a comparison to past results that found that the electron transport near the reversal surface was Rechester-Rosenbluth like if the electron thermal velocity was replaced by the ion thermal velocity, suggesting an ambipolarity constraint[7]. Furthermore, continued improvements in the diagnostics on MST make it possible to gather the data presented here with a similar degree of confidence in a matter of days rather than weeks of run time. This means that it is entirely feasible to perform a similar analysis for different run conditions on MST in order to determine a scaling of quantities like the thermal diffusion with current and density. Other plasma types could also be investigated, such as $F = 0$, enhanced confinement, and PPCD plasmas.

In terms of the zero β simulations, performing the same sort of analysis at different Lundquist numbers would provide a sense of how the stochastic transport scales. It may be that as Lundquist number is increased, the magnetic fluctuation induced energy transport decreases and other mechanisms become increasingly important. Ideally, this code would be parallelized so that these simulations could be run at much higher resolution. It has been suggested that at higher resolution, the amplitudes of the core resonant modes decrease, becoming more MST like. Even without parallelization, as computers become ever faster, this sort of analysis will be come more and more tractable. That said, reproducing the whole set of analysis at the lowest possible Lundquist number that the diagnostic set on MST allows would help to make this comparison with a large number of sawtooth events possible and higher resolution more attainable. When this project was started, the 400 kA, density of 1×10^{19} m^{-3} case was selected because all of the internal diagnostics work well in these conditions. Since then, the operational range of many of the diagnostics have improved, so the 200 kA case, for example, can now be measured with a full diagnostic set. In addition, adding a toroidal circuit model so that the reversal parameter can be controlled and the toroidal flux can be allowed to change in time would also be interesting to look at. This would likely improve the agreement between edge measurements and the simulation result and may improve the comparison of the time evolution of the $m = 0$ modes in particular. Understanding the transport around the reversal surface is very important for understanding the global confinement of the RFP as the temperature gradient tends to be steepest in this region.

Finally, running DEBS with finite β has proven to reproduce many interesting features seen in MST. The results presented were preliminary and should be more thoroughly explored. In particular, the addition of an ad-hoc trapped particle fraction to the resistivity and the parallel heat transport may generate MST like equilibrium temperature profiles. With some luck (and significantly higher numerical resolution), use of a code like DEBS may someday allow predictive modeling for the temperature behavior in the RFP.

REFERENCES

[1] Fitzpatrick, R. Helical temperature perturbations associated with tearing modes in tokamak plasmas. *Physics of Plasmas* **2**(3), 825–838 (1995).

[2] Prager, S. C. Transport and fluctuations in reversed field pinches. *Plasma Physics and Controlled Fusion* **32**(11), 903 (1990).

[3] Lorenzini, R., Terranova, D., Alfier, A., Innocente, P., Martines, E., Pasqualotto, R., and Zanca, P. Single-Helical-Axis States in Reversed-Field-Pinch Plasmas. *Phys. Rev. Lett.* **101**(2), 025005 Jul (2008).

[4] Chandran, B. D. G. and Cowley, S. C. Thermal Conduction in a Tangled Magnetic Field. *Phys. Rev. Lett.* **80**(14), 3077–3080 Apr (1998).

[5] Chandran, B. D. G., Cowley, S. C., Ivanushkina, M., and Sydora, R. Heat Transport Along an Inhomogeneous Magnetic Field. I. Periodic Magnetic Mirrors. *The Astrophysical Journal* **525**(2), 638 (1999).

[6] Park, G., Chang, C. S., Joseph, I., and Moyer, R. A. Plasma transport in stochastic magnetic field caused by vacuum resonant magnetic perturbations at diverted tokamak edge. *Physics of Plasmas* **17**(10), 102503 (2010).

[7] Fiksel, G., Bengtson, R. D., Cekic, M., Den Hartog, D. J., Prager, S. C., Pribyl, P., Sarff, J., Sovinec, C., Stoneking, M. R., Taylor, R. J., Terry, P. W., Tynan, G. R., and Wootton, A. J. Measurement of magnetic fluctuation-induced heat transport in tokamaks and RFP. *Plasma Physics and Controlled Fusion* **38**(12A), A213 (1996).

Appendix A

Anisotropic Conduction Formulation

A.0.1 Derivation from Dalton Schnack

The units for this derivation, where it matters, are cgs with the exception of the temperature which is generally in eV. The electron charge is 4.8032×10^{-10} stat-coulombs and the energy associated with 1 eV is 1.602×10^{-12} ergs.

$$\frac{3}{2} n_e k \frac{dT_e}{dt} + p_e \nabla \cdot \overrightarrow{v_e} = -\nabla \cdot \overrightarrow{q_e} - \overrightarrow{\overrightarrow{P}}_e : \nabla \overrightarrow{v_e} + Q_e \tag{A.1}$$

$$\frac{3}{2} n_i k \frac{dT_i}{dt} + p_i \nabla \cdot \overrightarrow{v_i} = -\nabla \cdot \overrightarrow{q_i} - \overrightarrow{\overrightarrow{P}}_i : \nabla \overrightarrow{v_i} + Q_i \tag{A.2}$$

Together these make:

$$\frac{3}{2} k \left(n_e \frac{dT_e}{dt} + n_i \frac{dT_i}{dt} \right) + p_e \nabla \cdot \overrightarrow{v_e} + p_i \nabla \cdot \overrightarrow{v_i} = -\nabla \cdot (\overrightarrow{q_e} + \overrightarrow{q_i}) - \overrightarrow{\overrightarrow{P}}_e : \nabla \overrightarrow{v_e} - \overrightarrow{\overrightarrow{P}}_i : \nabla \overrightarrow{v_i} + Q_e + Q_i \tag{A.3}$$

Now, $n_e = n_i$ and $T = T_e + T_i$ so:

$$\frac{3}{2}nk\frac{d}{dt}\left(T_e + T_i\right) = \frac{3}{2}nk\frac{dT}{dt} \tag{A.4}$$

$$\overrightarrow{v_e} = \frac{m_e\overrightarrow{v_e} + m_i\overrightarrow{v_i}}{m_e + m_i} = \frac{\overrightarrow{v_i} + \frac{m_e}{m_i}\overrightarrow{v_e}}{1 + \frac{m_e}{m_i}} \approx \overrightarrow{v_i} \tag{A.5}$$

also $p_e = nkT_e$ and $p_i = nkT_i$ so:

$$p_e\nabla\cdot\overrightarrow{v_e} + p_i\nabla\cdot\overrightarrow{v_i} = nkT_e\nabla\cdot\overrightarrow{v_e} + nkT_i\nabla\cdot\overrightarrow{v_i} \tag{A.6}$$

let $T_e = T_i = \frac{1}{2}T$. We then have:

$$p_e\nabla\cdot\overrightarrow{v_e} + p_i\nabla\cdot\overrightarrow{v_i} = \frac{nkT}{2}\nabla\cdot\left(\overrightarrow{v_e} + \overrightarrow{v_i}\right) \tag{A.7}$$

Now the heat flux is:

$$\overrightarrow{q} = \overrightarrow{q_e} + \overrightarrow{q_i} = -\left(\kappa_{ll}^e + \kappa_{ll}^i\right)\nabla_{ll}\frac{kT}{2} - \left(\kappa_\perp^e + \kappa_\perp^i\right)\nabla_\perp\frac{kT}{2} - \left(\kappa_T^e + \kappa_T^i\right)\hat{(b)}\times\nabla_\perp\frac{nkT}{2} \tag{A.8}$$

Now then, if we look on page 37 of the 2007 NRL formulary we can plug in a few things here. For the parallel component we have:

$$\frac{\kappa_{ll}^i}{\kappa_{ll}^e} = 3.9\frac{nkT_i\tau_i}{m_i}\frac{1}{3.2}\frac{m_e}{nkT_e\tau_e} = \frac{3.9}{3.2}\frac{m_e\tau_i}{m_i\tau_e} \tag{A.9}$$

$$\frac{\tau_i}{\tau_e} = \frac{2.09\times10^7}{3.44\times10^5} \approx \sqrt{\frac{m_i}{m_e}} \tag{A.10}$$

$$\frac{\kappa_{ll}^i}{\kappa_{ll}^e} \approx \frac{m_e}{m_i}\sqrt{\frac{m_i}{m_e}} \approx \sqrt{\frac{m_e}{m_i}} \approx \frac{1}{\sqrt{1836}} \approx 2\times10^{-2} \ll 1 \tag{A.11}$$

For the perpendicular component:

$$\kappa_{\perp}^{\alpha} \approx \frac{\kappa_{ll}^{\alpha}}{\left(\omega_{c_\alpha}\tau_\alpha\right)^2} \quad \text{(A.12)}$$

$$\omega_{c_i} = \frac{m_e}{m_i}\omega_{c_e} \quad \text{(A.13)}$$

$$\frac{\kappa_{\perp}^{i}}{\kappa_{\perp}^{e}} = \frac{\kappa_{ll}^{i}}{\kappa_{ll}^{e}}\frac{\left(\omega_{c_e}\tau_e\right)^2}{\left(\omega_{c_i}\tau_i\right)^2} = \sqrt{\frac{m_e}{m_i}}\left(\frac{m_i}{m_e}\right) = \left(\frac{m_e}{m_i}\right)^{\frac{3}{2}}\left(\frac{m_e}{m_i}\right)^{-2} = \sqrt{\frac{m_i}{m_e}} \approx 43 \gg 1 \quad \text{(A.14)}$$

For the transverse (or off diagonal) components we have:

$$\kappa_{T}^{\alpha} \approx \frac{\kappa_{ll}^{\alpha}}{\left(\omega_{c_\alpha}\tau_\alpha\right)} \quad \text{(A.15)}$$

$$\frac{\kappa_{T}^{i}}{\kappa_{T}^{e}} = \frac{\kappa_{ll}^{i}}{\kappa_{ll}^{e}}\frac{\left(\omega_{c_e}\tau_e\right)}{\left(\omega_{c_i}\tau_i\right)} = \sqrt{\frac{m_e}{m_i}}\left(\frac{m_i}{m_e}\right)\sqrt{\frac{m_e}{m_i}} = 1 \quad \text{(A.16)}$$

Therefor,

$$\overrightarrow{q} \approx -\kappa_{ll}^{e}\nabla_{ll}\frac{kT}{2} - \kappa_{\perp}^{i}\nabla_{\perp}\frac{kT}{2} - \left(\kappa_{T}^{e} + \kappa_{T}^{i}\right)\hat{b}\times\nabla_{\perp}\frac{kT}{2} \quad \text{(A.17)}$$

$$= -\kappa_{ll}\nabla_{ll}kT - \kappa_{\perp}\nabla_{\perp}kT - \kappa_{T}\hat{b}\times\nabla_{\perp}kT \quad \text{(A.18)}$$

where,

$$\kappa_{ll} = \frac{\kappa_{ll}^{e}}{2} = \frac{3.2}{2\times 2}\frac{nkT\tau_e}{m_e} = \frac{3.2k_B}{m_e}nT\frac{\left(3.44\times 10^5\right)}{2\times 2\times 10}\frac{T^{\frac{3}{2}}}{n} \quad \text{(A.19)}$$

$$= \frac{1.1\times 10^5}{2\times 2}\frac{k_B}{m_e}T^{\frac{5}{2}} = \frac{5.5\times 10^4}{2}\frac{k_B}{m_e}T^{\frac{5}{2}} = 2.75\times 10^4\frac{k_B}{m_e}T^{\frac{5}{2}} \quad \text{(A.20)}$$

$$= 2.75\times 10^4\frac{1.6\times 10^{-12}}{9.1\times 10^{-28}}T^{\frac{5}{2}} = 4.8\times 10^{19}T^{\frac{5}{2}} \quad \text{(A.21)}$$

so finally we have:

$$\kappa_{ll} \approx 5 \times 10^{19} T^{\frac{5}{2}} \qquad = C_{ll}\widetilde{\kappa}_{ll} \tag{A.22}$$

$$C_{ll} = 5 \times 10^{19} T_0^{\frac{5}{2}} \tag{A.23}$$

For $\kappa_\perp$ we have:

$$\kappa_\perp = \frac{1}{2}\kappa_\perp^i = \frac{1}{2}\frac{2nk_BT/2}{m_i\omega_{c_i}^2\tau_i} \qquad \omega_{c_i} = \frac{eB}{m_ic} = 9.58 \times 10^3 B \tag{A.24}$$

$$= \frac{1}{2}\frac{nk_BT}{m_i\omega_{c_i}\tau_i} \qquad \tau_i = 2.09 \times 10^6 \frac{T^{\frac{3}{2}}}{n} \tag{A.25}$$

$$= \frac{1}{2}\frac{1.6 \times 10^{-12}}{1.67 \times 10^{-24}}\frac{nT}{\left(9.58 \times 10^3\right)^2 B^2}\frac{n}{\left(2.09 \times 10^6\right) T^{\frac{3}{2}}} \tag{A.26}$$

$$= 2.5 \times 10^{-3}\frac{n^2}{B^2T^{\frac{1}{2}}} \tag{A.27}$$

Now if we say, once again, that $\kappa_\perp = C_\perp\tilde{\kappa}_\perp$ then,

$$C_\perp = 2.5 \times 10^{-3}\frac{n_0^2}{B_0^2T_0^{\frac{1}{2}}} \tag{A.28}$$

Now for the transverse conduction.

$$\kappa_T = \frac{1}{2}\left(\kappa_T^e + \kappa_T^i\right) \tag{A.29}$$

$$\kappa_T^e = \frac{5}{2}\frac{nkT/2}{m_e\omega_{c_e}} = \frac{5}{4}\frac{nk_BT}{m_e\omega_{c_e}} \tag{A.30}$$

$$\kappa_T^i = \frac{5}{2}\frac{nkT/2}{m_i\omega_{c_i}} = \frac{5}{4}\frac{nk_BT}{m_i\omega_{c_i}} \tag{A.31}$$

$$\tag{A.32}$$

letting $m_i\omega_{c_i} = m_e\omega_{c_e}$

$$\begin{aligned}
\kappa_T &= \frac{5}{8}nk_BT\left(\frac{1}{m_e\omega_{c_e}} + \frac{1}{m_i\omega_{c_i}}\right) && \text{(A.33)}\\
&= \frac{5}{8}\frac{nk_BT}{m_i\omega_{c_i}}\left(1 + \frac{m_i\omega_{c_i}}{m_e\omega_{c_e}}\right) && \text{(A.34)}\\
&= \frac{5}{8}\frac{nk_BT}{m_i\omega_{c_i}}\left(1 + \frac{m_i m_e}{m_e m_i}\right) && \text{(A.35)}\\
&= \frac{5}{4}\frac{nk_BT}{m_i\omega_{c_i}} && \text{(A.36)}\\
&= \frac{5}{4}\frac{1.6\times10^{-12}nT}{(1.67\times10^{-24})(9.58\times10^{3}B)} && \text{(A.37)}\\
&= 1.25\times10^{8}\frac{nT}{B} && \text{(A.38)}
\end{aligned}$$

Now if we say, once again, that $\kappa_T = C_T\tilde{\kappa}_T$ then,

$$C_T = 1.25\times10^{8}\frac{n_0T_0}{B_0} \tag{A.39}$$

Ok, now that we have those taken care of,

$$\begin{aligned}
\frac{3}{2}nk_B\frac{dT}{dt} &= -\nabla\cdot\vec{q} && \text{(A.40)}\\
&= \nabla\cdot\left[\kappa_{ll}\nabla_{ll}k_BT + \kappa_\perp\nabla_\perp k_BT + \kappa_T\hat{b}\times\nabla_\perp k_BT\right] && \text{(A.41)}\\
\frac{3}{2}n_0\tilde{n}\frac{T_0}{\tau_r}\frac{d\tilde{T}}{d\tilde{t}} &= \frac{T_0}{a^2}\tilde{\nabla}\cdot\left[C_{ll}\tilde{\kappa}_{ll}\tilde{\nabla}_{ll}\tilde{T} + C_\perp\tilde{\kappa}_\perp\tilde{\nabla}_\perp\tilde{T} + C_T\tilde{\kappa}_T\tilde{\hat{b}}\times\tilde{\nabla}_\perp\tilde{T}\right] && \text{(A.42)}\\
\frac{1}{\tau_r}\frac{d\tilde{T}}{d\tilde{t}} &= \frac{2}{3}\frac{C_\perp}{n_0a^2}\frac{1}{\tilde{n}}\tilde{\nabla}\cdot\left[\frac{C_{ll}}{C_\perp}\tilde{\kappa}_{ll}\tilde{\nabla}_{ll}\tilde{T} + \tilde{\kappa}_\perp\tilde{\nabla}_\perp\tilde{T} + \frac{C_T}{C_\perp}\tilde{\kappa}_T\tilde{\hat{b}}\times\tilde{\nabla}_\perp\tilde{T}\right] && \text{(A.43)}
\end{aligned}$$

From this we can pull out a time scale for the conduction $\frac{1}{\tau_\kappa} = \frac{2}{3}\frac{C_\perp}{n_0a^2}$ or:

$$
\begin{aligned}
\tau_\kappa &= \frac{3}{2}\frac{n_0 a^2}{C_\perp} = \frac{3}{2}\frac{n_0 a^2 B_0^2 T_0^{\frac{1}{2}}}{2.5\times 10^{-3} n_0^2} = 6\times 10^2 \frac{B_0^2 a^2 T_0^{\frac{1}{2}}}{n_0} && \text{(A.44)}\\
\tau_r &= 1.2\times 10^{-7} a^2 T_0^{\frac{3}{2}} && \text{(A.45)}
\end{aligned}
$$

Now if we compare these time scales we get:

$$
\begin{aligned}
\frac{\tau_r}{\tau_\kappa} &= \frac{1.2\times 10^{-7} a^2 T_0^{\frac{3}{2}} n_0}{6\times 10^2 B_0^2 a^2 T_0^{\frac{1}{2}}} && \text{(A.46)}\\
&= 2\times 10^{-10}\frac{n_0 T_0}{B_0^2} = \frac{2\times 10^{-10}}{8\pi k_B}\frac{8\pi n_0 k_B T_0}{B_0^2} && \text{(A.47)}\\
&= \frac{2\times 10^{-10}}{8\pi\left(1.6\times 10^{-12}\right)}\beta_0 && \text{(A.48)}\\
&= 4.97\beta_0 && \text{(A.49)}
\end{aligned}
$$

ok so that's it, that is where the magic factor comes from. So it looks like in normalizing the time derivative you get a $1/\tau_r$ and the rest is just pulling the normalization factors out the equation.

$$
\begin{aligned}
\tilde{C}_{ll} &= \frac{C_{ll}}{C_\perp} = \frac{5.9\times 10^{19} T_0^{\frac{5}{2}} B_0^2 T_0^{\frac{1}{2}}}{2.5\times 10^{-3} n_0^2} && \text{(A.50)}\\
\tilde{C}_{ll} &= 2.36\times 10^{22}\frac{B_0^2 T_0^3}{n_0^2} && \text{(A.51)}
\end{aligned}
$$

For the case of $B_0 = 10^3$, $T_0 = 5 \times 10^2$, and $n_0 = 10^{14}$, $\tilde{C}_{ll} = 5.9 \times 10^5$.

$$\begin{aligned}
\frac{B^2 T^3}{n^2} &= \frac{B^2}{nT}\frac{T^4}{n} && \text{(A.52)}\\
&= 8\pi k_B \frac{B^2}{8\pi n k_B T}\frac{T^4}{n} && \text{(A.53)}\\
&= \frac{4 \times 10^{-11}}{\beta_0}\frac{T_0^4}{n_0} && \text{(A.54)}
\end{aligned}$$

$$\begin{aligned}
\tilde{C}_T &= \frac{C_T}{C_\perp} = \frac{1.25 \times 10^8}{2.5 \times 10^{-3}}\frac{n_0 T_0}{B_0}\frac{B_0^2 T_0^{\frac{1}{2}}}{n_0^2} && \text{(A.55)}\\
&= 5 \times 10^{10}\frac{B_0 T_0^{\frac{3}{2}}}{n_0} && \text{(A.56)}
\end{aligned}$$

for the above set of values $\tilde{C}_T = 5.6 \times 10^3$.

Then the thermal conduction equation looks like:

$$\begin{aligned}
\frac{d\tilde{T}}{d\tilde{t}} &= \frac{1}{\tilde{n}}\tilde{\nabla} \cdot \left[\tilde{\kappa}_{ll}\tilde{\nabla}_{ll}\tilde{T} + \tilde{\kappa}_\perp \tilde{\nabla}_\perp \tilde{T} + \tilde{\kappa}_T \hat{B} \times \tilde{\nabla}_\perp \tilde{T}\right] && \text{(A.57)}\\
&= \frac{1}{\tilde{n}}\tilde{\nabla} \cdot \tilde{\overrightarrow{\overrightarrow{\kappa}}} \cdot \nabla\tilde{T} && \text{(A.58)}
\end{aligned}$$

where

$$\begin{aligned}
\tilde{\kappa_\perp} &= 4.97\beta_0 \frac{\tilde{n}^2}{\tilde{B}^2 \tilde{T}^{\frac{1}{2}}} && \text{(A.59)}\\
\tilde{\kappa_{ll}} &= 4.97\beta_0 \tilde{C}_{ll}\tilde{T}^{\frac{5}{2}} && \text{(A.60)}\\
\tilde{\kappa_{ll}} &= 4.97\beta_0 \tilde{C}_T \frac{\tilde{n}\tilde{T}}{\tilde{B}} && \text{(A.61)}
\end{aligned}$$

with

$$\tilde{C}_{ll} = 2.36 \times 10^{22} \frac{B_0^2 T_0^3}{n_0^2} \tag{A.62}$$

$$\tilde{C}_T = 5 \times 10^{10} \frac{B_0 T_0^{\frac{3}{2}}}{n_0} \tag{A.63}$$

in frame aligned with magnetic field:

$$\overrightarrow{\overrightarrow{\tilde{\kappa}}} = \begin{pmatrix} \tilde{\kappa}_\perp & \tilde{\kappa}_T & 0 \\ -\tilde{\kappa}_T & \tilde{\kappa}_\perp & 0 \\ 0 & 0 & \tilde{\kappa}_{ll} \end{pmatrix}$$

A.0.2 For the case of Z and μ not equal to 1

In this section we modify this derivation keeping track of our μ's and our Z_{eff}'s. To do this we need to understand why $\tau_r = 1.2 \times 10^{-7} a^2 T_0^{\frac{3}{2}}$. Note that an inconsistency is introduced here in that $n_e = n_i = n$ when it should be $n_e = Zn_i = n$ though this is messed up even more by the fact that we are using Z_{eff} rather than Z so it is unclear whether or not what follows makes sense to use at all.

$$\tau_r = 4\pi a^2 / c^2 \eta_0 \tag{A.64}$$

$$\eta_0 = 1.15 \times 10^{-14} Z ln(\Lambda) T^{-\frac{3}{2}} \; sec \tag{A.65}$$

$$\tau_r = \frac{4\pi}{c^2} \frac{1}{1.15 \times 10^{-14} ln(\Lambda)} \frac{a^2 T^{\frac{3}{2}}}{Z} \tag{A.66}$$

Assuming the speed of light is 3×10^{10} and $ln(\Lambda)$ is 10 we get $\tau_r = 1.21414209 \times$

$10^{-7}\frac{a^2T_0^{\frac{3}{2}}}{Z}$, so let's call it $\tau_r = 1.2\times 10^{-6}\frac{a^2T_0^{\frac{3}{2}}}{ln(\Lambda)Z}$.

With that taken care of we now need to go back and redo the calculation of $C_\perp$ keeping the correct factors of Z and μ. We will probably need to go back into the calculation for C_{ll} as well, but we can do that later.

So for reasons stated at the beginning of this document $\kappa_\perp = \frac{1}{2}\kappa_\perp^i$

$$\kappa_\perp = \frac{1}{2}\kappa_\perp^i = \frac{1}{2}\frac{2nk_BT/2}{m_i\omega_{c_i}^2\tau_i} \qquad \omega_{c_i} = \frac{eB}{m_ic} = 9.58\times 10^3 ZB/\mu \tag{A.67}$$

$$= \frac{1}{2}\frac{nk_BT}{m_i\omega_{c_i}^2\tau_i} \qquad \tau_i = 2.09\times 10^7\frac{T^{\frac{3}{2}}\mu^{\frac{1}{2}}}{n\lambda Z^4} \tag{A.68}$$

$$= \frac{1}{2}\frac{1.6\times 10^{-12}}{1.67\times 10^{-24}\mu}\frac{nT}{(9.58\times 10^3)^2\,\frac{Z^2B^2}{\mu^2}}\frac{n\lambda Z^4}{(2.09\times 10^7)\,T^{\frac{3}{2}}\mu^{\frac{1}{2}}} \tag{A.69}$$

$$= 2.5\times 10^{-4}\frac{n^2\lambda Z^4\mu^{\frac{1}{2}}}{Z^2B^2T^{\frac{1}{2}}} \tag{A.70}$$

$$C_\perp = 2.5\times 10^{-4}\lambda Z^2\mu^{\frac{1}{2}}\frac{n_0^2}{B_0^2T_0^{\frac{1}{2}}} \tag{A.71}$$

$C_\perp$ goes to $2.5\times 10^{-3}\frac{n_0^2}{B_0^2T_0^{\frac{1}{2}}}$ when $\lambda = 10$, and $\mu = Z = 1$. Ok, so we are still defining τ_κ the same way, it just has these extra bits in it.

$$\tau_\kappa = \frac{3}{2}\frac{n_0a^2}{C_\perp} = \frac{3}{2}\frac{n_0a^2B_0^2T_0^{\frac{1}{2}}}{2.5\times 10^{-4}n_0^2}\frac{1}{\lambda Z^2\mu^{\frac{1}{2}}} = 6\times 10^3\frac{B_0^2a^2T_0^{\frac{1}{2}}}{n_0}\frac{1}{\lambda Z^2\mu^{\frac{1}{2}}} \tag{A.72}$$

Finally we do τ_r/τ_κ,

$$
\begin{aligned}
\frac{\tau_r}{\tau_\kappa} &= \frac{1.2\times10^{-6}a^2T_0^{\frac{3}{2}}n_0}{6\times10^3B_0^2a^2T_0^{\frac{1}{2}}}\frac{\lambda Z^2\mu^{\frac{1}{2}}}{\lambda Z} && \text{(A.73)}\\
&= 2\times10^{-10}\frac{n_0T_0}{B_0^2}Z\mu^{\frac{1}{2}} = \frac{2\times10^{-10}}{8\pi k_B}\frac{8\pi n_0k_BT_0}{B_0^2}Z\mu^{\frac{1}{2}} && \text{(A.74)}\\
&= \frac{2\times10^{-10}}{8\pi\left(1.6\times10^{-12}\right)}\beta_0Z\mu^{\frac{1}{2}} && \text{(A.75)}\\
&= 4.97\beta_0Z\mu^{\frac{1}{2}} && \text{(A.76)}
\end{aligned}
$$

now $C_{ll} = 4.8\times10^{20}T_0^{\frac{5}{2}}/Z^2\lambda$ so now we have,

$$
\begin{aligned}
\tilde{C}_{ll} &= \frac{C_{ll}}{C_\perp} = \frac{5.9\times10^{20}T_0^{\frac{5}{2}}B_0^2T_0^{\frac{1}{2}}}{2.5\times10^{-4}n_0^2}\frac{1}{\lambda^2Z^4\mu^{\frac{1}{2}}} && \text{(A.77)}\\
\tilde{C}_{ll} &= 2.36\times10^{24}\frac{B_0^2T_0^3}{n_0^2}\frac{1}{\lambda^2Z^4\mu^{\frac{1}{2}}} && \text{(A.78)}
\end{aligned}
$$

So what does this all mean? At first glance it seems that ckmult should be set to $\mu^{1/2}Z$ as τ_k goes like $C_\perp$. This means ckpar, which is $C_\parallel/C_\perp$, should change like $1/Z^4\mu^{1/2}$ though there is also a factor of $1/\lambda^2$ that in principle should be accounted for as well, so in total the change from what appears in the comments in the code is $100/\lambda^2Z^4\mu^{1/2}$. Alternatively, one could set $n_e = Zn_i = n$. This makes more sense, but is a little funny to compare to the experiment as Z is not equal to Z_{eff} in this sense. Whatever the case, if this second, definition is used, then these relations change such that ckmult becomes $\mu^{1/2}$ and ckpar is multiplied by $100/\lambda^2Z^2\mu^{1/2}$.

Note that an alternate definition of the normalization parameters is described in a pair of papers published in 2000 by Scheffel, *et al.*, which get a similar scaling assuming the conductivities have been normalized by a collision time.

Appendix B

Derivation of the Poynting Flux

B.1 Using Lorentz force

Start with the Lorentz force $\vec{F} = q(\vec{E} + \vec{v} \times \vec{B})$ and dot it with $\vec{v}$ to get the rate of work done. So we have:

$$\dot{Work} = q(\vec{E} + \vec{v} \times \vec{B}) \cdot \vec{v} = \vec{E} \cdot \vec{J} \tag{B.1}$$

Then, we solve ampere's law, $\nabla \times \vec{B} = \mu_0 \left(\vec{J} + \epsilon_0 \frac{d\vec{E}}{dt} \right)$, for $\vec{J}$ and dot it into $\vec{E}$.

$$-\vec{E} \cdot \vec{J} = \vec{E} \cdot \left(\epsilon_0 \frac{d\vec{E}}{dt} - \frac{1}{\mu_0} \nabla \times \vec{B} \right). \tag{B.2}$$

Now we can write the vector identity $\nabla \cdot \left(\vec{E} \times \vec{B} \right) = \vec{B} \cdot \nabla \times \vec{E} - \vec{E} \cdot \left(\nabla \times \vec{B} \right)$ as

$$-\vec{E} \cdot \left(\nabla \times \vec{B} \right) = \nabla \cdot \left(\vec{E} \times \vec{B} \right) - \vec{B} \cdot \nabla \times \vec{E}. \tag{B.3}$$

So we now have

$$-\vec{E}\cdot\vec{J}=\epsilon_0\vec{E}\cdot\frac{d\vec{E}}{dt}+\frac{1}{\mu_0}\nabla\cdot\left(\vec{E}\times\vec{B}\right)-\frac{1}{\mu_0}\vec{B}\cdot\nabla\times\vec{E}. \tag{B.4}$$

Remember Faradays Law can be written $\nabla\times\vec{E}=-\dot{\vec{B}}$

$$-\vec{E}\cdot\vec{J}=\epsilon_0\vec{E}\cdot\frac{d\vec{E}}{dt}+\frac{1}{\mu_0}\nabla\cdot\left(\vec{E}\times\vec{B}\right)+\frac{1}{\mu_0}\vec{B}\cdot\frac{d\vec{B}}{dt}. \tag{B.5}$$

Now we define the Poynting Flux as $\vec{S}=\frac{1}{\mu_0}\left(\vec{E}\times\vec{B}\right)$ and the change in stored electro-magnetic energy (not to be confused with the rate of work done) as $\dot{W}=\frac{d}{dt}\frac{1}{2}\left(\frac{1}{\mu_0}B^2+\epsilon_0E^2\right)$ yielding (finally):

$$\vec{E}\cdot\vec{J}=-\dot{W}-\nabla\vec{S} \tag{B.6}$$

B.2 Maxwell's Equations Only

This is neat. Start by dotting $\vec{E}$ into Ampere's law

$$\vec{E}\cdot\left(\nabla\times\vec{H}\right)=\vec{E}\cdot\left(\vec{J}+\frac{d\vec{D}}{dt}\right) \tag{B.7}$$

Apply the vector identity and Faraday's law as above,

$$\vec{E}\cdot\vec{J}=-\frac{d}{dt}\underbrace{\frac{1}{2}\left(\frac{1}{\mu}B^2+\epsilon E^2\right)}_{\dot{W}}-\nabla\cdot\underbrace{\left(\vec{E}\times\vec{H}\right)}_{\vec{S}}. \tag{B.8}$$

It should be noted that the electric field is generally of order 1V/m reaching 30V/m at the sawtooth. The magnetic field is roughly 0.4T at all times. That said, the $1/\mu_0$ makes the $\dot{B}$ term a 10^6 bigger while the ϵ_0 term makes the $\dot{E}$ term about 10^{11} times smaller. Given that the fields are within an order of magnitude of each other this means the change in the electric field would have to be 10^{17} times that of the magnetic field for it contribute to $\dot{W}$ in a significant way. Therefore, $\dot{W} \approx \frac{1}{2}\frac{d}{dt}\left(\frac{1}{\mu_0}B^2\right)$. The above is simply math. It gives an identity for $E \cdot J$. The interpretation is the tricky bit. This is just a statement of conservation of electro-magnetic energy. The net energy flowing into a volume must either be consumed in that volume or stored in that volume. The storage term is the $\dot{W}$ term, which in almost all cases is simply the change in stored magnetic energy. The dissipation term is $E \cdot J$ which application of a simple Ohm's law can simply be written as $E \cdot J = \eta J^2$. This becomes complicated however when the a more general Ohm's law is used that includes MHD and Hall dynamo terms. These dynamo terms tend to be conservative, simply shifting energy from one region to another so the net dynamo contribution to the entire plasma volume is zero. Very careful accounting of the $\dot{B}$ and $\dot{E}$ terms is needed to ensure that the dynamo contributions are accounted for. Basically, the contribution of the MHD dynamo to the $E \cdot J$ term should be canceled by the local change in stored magnetic energy. This is all fine and good, but often the assumption is made that the rate of work done on the plasma $E \cdot J$ goes into heating the plasma not moving the fields around. This is the fundamental flaw. $E \cdot J$ is the total rate of electro-magnetic work done on the plasma. The local analysis must separate the energy dissipated with the energy shifted out of the region of interest. The energy dissipated locally should be accounted for by ηJ^2 and possibly some of the smaller inertial terms in the generalized Ohm's law. The larger MHD and Hall dynamo terms are conservative and must be removed from $E \cdot J$ before it can be used for estimating the dissipated power. While that is easy to say, it is highly non trivial to do in any meaningful way in experiment. This is perfectly doable in simulation, but it is hard to say how applicable that information is to the experiment. For now, it is probably best to use global arguments for finding the average Z_{eff} and then use ηJ^2 for the determining the heating power.

Appendix C

χ_e Inversion

The heat equation has the following form:

$$\frac{\partial}{\partial t}\left(\frac{3}{2}nT\right) = \nabla \cdot (n\chi\nabla T) + Source \tag{C.1}$$

where all units are MKS and T is temperature in Joules. We would like find $T(\rho)$ over the minor radius of the plasma by specifying $n(\rho)$ and $\chi(\rho)$. The following document show how this can be done using a matrix inversion.

The term Source is typically dominated by the ohmic input ηJ^2 and has units of $J/s/m^3$, i.e. it is the argument of the volume integral done to find the ohmic power. For simplicity we will start by using just this term for the Source term. Furthermore, we will assume a slowly evolving equilibrium, so the left hand side is zero. Now we just need to expand the first term on the right hand side. We will reduce this to a one dimensional problem by assuming axisymmetry and isobaric, isothermal poloidal flux surfaces of radius ρ.

$$\nabla \cdot (n\chi\nabla T) = \frac{1}{\rho}\left(n\chi\nabla T + \rho\frac{\partial}{\partial\rho}n\chi\nabla T\right) \tag{C.2}$$

$$= \frac{1}{\rho}\left[n\chi\nabla T + \rho\left(n\chi\frac{\partial^2 T}{\partial\rho^2} + \nabla T\frac{\partial}{\partial\rho}\left(n\chi\right)\right)\right] \tag{C.3}$$

$$= \frac{1}{\rho}\left[n\chi\nabla T + \rho\left(n\chi\frac{\partial^2 T}{\partial\rho^2} + \nabla T\left(n\frac{\partial}{\partial\rho}\left(\chi\right) + \chi\frac{\partial}{\partial\rho}\left(n\right)\right)\right)\right] \tag{C.4}$$

plugging this all into Equation C.1 and dividing by $n\chi$ we get:

$$\frac{-Source}{n\chi} = \left(\frac{1}{\rho} + \frac{1}{n}\frac{\partial n}{\partial\rho} + \frac{1}{\chi}\frac{\partial\chi}{\partial\rho}\right)\frac{\partial T}{\partial\rho} + \frac{\partial^2 T}{\partial\rho^2} \tag{C.5}$$

which has the second order ODE form of B=CT'+T". We assume that we know the profiles of χ and n as well as ρ and Source so B and C are just known functions of radius. This equation can be solved using a finite difference technique by defining the first and second derivatives as:

$$T' = \frac{T[i+1] - T[i-1]}{2\Delta\rho} \tag{C.6}$$

$$T'' = \frac{T[i+1] - 2T[i] + T[i-1]}{\Delta\rho^2}. \tag{C.7}$$

Plugging this into Equation C.5 we get:

$$B[i] = C[i]\left(\frac{T[i+1] - T[i-1]}{2\Delta\rho}\right) + \frac{T[i+1] - 2T[i] + T[i-1]}{\Delta\rho^2}. \tag{C.8}$$

Gathering the like terms of T together we get:

$$B[i] = \left(\frac{1}{\Delta\rho^2} - \frac{C[i]}{2\Delta\rho}\right) T[i-1] - \frac{2}{\Delta\rho^2} T[i] + \left(\frac{1}{\Delta\rho^2} + \frac{C[i]}{2\Delta\rho}\right) T[i+1]. \tag{C.9}$$

Now we can cast this as usual in the matrix equation $AX = B$ and find the solution vector X by inverting the matrix A. $A^{-1}AX = X = A^{-1}B$. The elements are as follows:

$$\begin{aligned} A[i,i-1] &= \frac{1}{\Delta\rho^2} - \frac{C[i]}{2\Delta\rho} && \text{(C.10)} \\ A[i,i] &= -\frac{2}{\Delta\rho^2} && \text{(C.11)} \\ A[i,i+1] &= \frac{1}{\Delta\rho^2} + \frac{C[i]}{2\Delta\rho}. && \text{(C.12)} \end{aligned}$$

The first and last row have to be handled separately because we have boundary conditions there. For the inner boundary we know that the gradient should be zero. Intuitively this makes sense because one does not expect discontinuities in the temperature gradient at the core of the plasma. The expectation is that, in a natural system, if a sharp peak was created at the core, it would rapidly relax. This is sort of a 'delta function are unphysical' argument, which is similar to the 'Nature abhors a gradient' argument. But I digress.

The zero gradient in the core is handled by explicitly setting A[0,0]=1 and A[0,1]=-1 and B[0]=0. If you think about what this means when the multiplication is done out we have T[0]-T[1]=0 for the first equation.

The second boundary condition is the value of the temperature at the edge. This is done explicitly by setting the last elements in the last row of the matrix, lets say it is an nx x nx matrix, as A[nx,nx-1]=0, A[nx,nx]=1, B[nx]=T_{edge}. These are the first order accurate boundary conditions. It is not uncommon to use second order accurate boundary conditions, which we have implemented, but i will not be using that scheme here so i will not go into the details of it. The nice thing about the first order accurate matrix is that it is tri-diagonal, i.e. only the primary diagonal and the diagonals one above and one below the primary contain non zero elements. This means there are some nifty inversion tricks that one can use which make the computation much, much faster than inverting the entire square matrix. For the second order accurate inversion we used the "invert" function in IDL while for the first order accurate setup we used "trisol".